

THE UNIVERSITY OF HULL

Renewing approaches to understanding the minerals and waters at
alkaline waste sites

being a Thesis submitted for the Degree of

PhD in Geology

in the University of Hull

by

Laura Bastianini, BSc and MSc

December 2021

TABLE OF CONTENTS

FIGURE LIST	9
TABLE LIST	17
ACKNOWLEDGMENTS	19
REMERCIEMENTS	22
THESIS ABSTRACT	25
Chapter 1 – THESIS INTRODUCTION	26
1.1 HYPERALKALINE GEOCHEMICAL SYSTEMS	26
1.1.1 Carbonate geochemistry	26
1.1.2 Natural hyperalkaline systems	28
1.1.3 Bicarbonate-rich carbonate systems	30
1.1.4 Anthropogenic hyperalkaline system	31
1.2 WHAT DO WE KNOW ABOUT THE CARBONATE SEDIMENTOLOGY AT ANTHROPOGENIC HYPERALKALINE SITES?	33
1.2.1 The water chemistry	34
1.2.2 Time-variant mineralogy	36
1.3 THESIS AIMS	37
1.4 THESIS STRUCTURE	37
Chapter 2 – What causes carbonates to form “shrubby” morphologies? An Anthropocene limestone case study.	40
2.1 INTRODUCTION	40
2.2 MATERIAL AND METHODS	42
2.2.1 Field-work methods	42
2.2.2 Hydrochemistry	45

2.2.3 Mineralogy	45
2.2.4 Petrography and terminology	46
2.3 RESULTS	47
2.3.1 Hydrochemistry	47
2.3.2 Mineralogy	49
2.3.3 Site and macroscopic descriptions	50
2.3.4 Facies descriptions	51
2.3.5 Distribution of microfacies	60
2.4 DISCUSSION	61
2.4.1 Hydrochemistry versus distribution of microfacies	61
2.4.2 Kinetic control on shrubby and dendritic carbonate	61
2.4.3 Formation processes of microfacies	63
2.4.4 Co-existence of fabrics within a same site	66
2.4.5 Depositional model	66
2.4.6 Sedimentology in the Anthropocene	67
2.4.7 Comparing natural, alkaline saline lakes with anthropogenic hyperalkaline occurrences	68
2.5 CONCLUSION	70
2.6 AUTHOR CONTRIBUTIONS	70
Chapter 3 – What are the different styles of calcite precipitation within a hyperalkaline leachate? A sedimentological Anthropocene case study.	72
3.1 INTRODUCTION	72
3.1.1 Calcite precipitation within hyperalkaline sites	73
3.1.2 Terrestrial carbonate sedimentology	75

3.2 WHAT DO WE ALREADY KNOW ABOUT ANTHROPOGENIC CARBONATE MICROFACIES?	78
3.3 MATERIAL AND METHODS	81
3.3.1 Field work and data collection	81
3.3.2 Mineralogy	84
3.3.3 Petrographic analyses	84
3.3.4 Terminology	85
3.4 RESULTS	85
3.4.1 Hydrochemistry	85
3.4.2 Depositional environments and carbonate microfacies	90
3.4.3 Macroscopic description	92
3.4.4 Microfacies descriptions	93
3.4.4.1 Microfacies 1: Coated vegetative remains and carbonate rafts (proximal zone)	93
3.4.4.2 Microfacies 2: Micro-peloidal and clotted micritic fabric (distal zone)	94
3.4.4.3 Microfacies 3: Carbonate-coated microbial filament (middle zone)	94
3.4.4.4 Microfacies 4: Globular sparry calcite crust (proximal zone)	96
3.4.4.5 Microfacies 5: Neomorphic sparry calcite crust (distal zone)	97
3.4.4.6 Microfacies 6: Crystal shrub fan (proximal zone)	99
3.4.4.7 Microfacies 7: Dendrite carbonates (proximal zone)	99
3.4.5 Mineralogy	100
3.4.6 Distribution of macrofacies and microfacies	101
3.5 DISCUSSION	101
3.5.1 Depositional model according to macrofacies and microfacies distributions	101

3.5.2 Origin of macrofacies and microfacies	103
3.5.3 Comparison to natural systems	108
3.5.3.1 Resemblance of anthropogenic systems with natural travertine and tufa carbonates	108
3.5.3.2 Macroscopic features	109
3.5.3.3 Microscopic features	110
3.5.3.4 Differences between travertine and anthropogenic systems	112
3.6 CONCLUSION	114
3.7 AUTHOR CONTRIBUTIONS	115
Chapter 4 – Ikaite formation in streams affected by steel waste leachate: first report and potential impact on contaminant dynamics	116
4.1 INTRODUCTION	116
4.1.1 Observations of recent ikaite	117
4.1.2 Formation conditions of ikaite	119
4.1.3 Crystallisation of ikaite	121
4.1.4 Transformation of ikaite to other calcium carbonate polymorphs post-deposition	123
4.1.5 This study	124
4.2 MATERIALS AND METHODS	124
4.2.1 Field work	124
4.2.1.1 Description of the site	124
4.2.1.2 Strategy for finding ikaite	126
4.2.1.3 Collection of the sample	128
4.2.2 XRD	129
4.2.3 Microscopy	130

4.2.4 Trace Element content	130
4.2.5 Laboratory experiments	132
4.3 RESULTS	134
4.3.1 Mineralogy	134
4.3.2 SEM	137
4.3.3 Laser	139
4.3.4 Laboratory experiments	140
4.4 DISCUSSION	142
4.4.1 Discovery of ikaite in steel waste leachate	142
4.4.2 What contaminant phases are likely to be accumulated into a transient ikaite inventory?	144
4.4.3 Why are these elements enriched compared to the solution?	145
4.4.3.1 Laboratory synthesis experiments	146
4.4.4 What is the environmental risk posed by this finding?	147
4.4.5 How harmful would release of these contaminants in a transient mineral inventory likely be?	148
4.5 CONCLUSION	152
4.6 AUTHOR CONTRIBUTIONS	153
Chapter 5 – Improving field alkalinity characterization of waters on anthropogenic alkaline sites	154
5.1 INTRODUCTION	154
5.1.1 Definition of alkalinity for alkaline anthropogenic systems	155
5.1.2 Naturally occurring alkalinity	156
5.1.3 Measuring alkalinity in the field	159

5.1.4 Margin errors resulting from alkalinity titrations	162
5.1.5 The need for further evaluation of methodologies	162
5.2 MATERIAL AND METHODS	163
5.2.1 FEP method	165
5.2.2 Separate expertise testing level for the FEP method	168
5.2.3 IPT method	168
5.2.4 ST method	169
5.2.5 Thermodynamical modelling of the alkalinity data	170
5.3 RESULTS	171
5.3.1 Importance of operator experience for fixed end point alkalinity titrations	171
5.3.2 Comparison between alkalinity methods	173
5.3.3 Saturation index modelling of the alkalinity data	176
5.4 DISCUSSION	179
5.4.1 Comparing Beginner and Expert levels from FEP	179
5.4.2 Comparing FEP versus IP versus ST methods	183
5.4.3 Errors resulting from the different methods	186
5.4.4 Calcite saturation levels of the alkalinity data	186
5.5 CONCLUSION	189
5.6 AUTHOR CONTRIBUTIONS	190
Chapter 6 – THESIS CONCLUSION	191
6.1 INTRODUCTION	191
6.2 KEY FINDINGS AROUND RQ1: What are the dominant carbonate fabrics found in secondary deposits at anthropogenic hyperalkaline sites?	191

6.3 KEY FINDINGS AROUND RQ1: What are the dominant carbonate fabrics found in secondary deposits at anthropogenic hyperalkaline sites? & RQ2: What do differences in carbonate fabrics at hyperalkaline sites tell us about controls on carbonate precipitation?	193
6.4 KEY FINDINGS AROUND RQ3: Through novel coupled field and laboratory analyses, what evidence is there for transient mineral formation at anthropogenic hyperalkaline sites? & RQ4: What are the implications of transient mineral formation on trace metal dynamics?	194
6.5 KEY FINDINGS AROUND RQ5: How can dissolved inorganic carbon be better characterised from anthropogenic hyperalkaline sites?	195
6.6 FUTURE RESEARCH DIRECTIONS	196
6.7 OVERALL FINDINGS AND IMPLICATIONS FOR POLICYMAKERS	198
6.8 THESIS REFERENCES	201

FIGURE LIST

Chapter 2:

Figure 2.1. Location map of the studied samples HU-MR-/3CON1 (C1), HU-MR-/3CON2 (C2), HU-MR-/3CON4 (C4), HU-MR-/3CON5 (C5), HU-MR-/3CON6 (C6), HU-MR-/3CON7 (C7).

Figure 2.2. XRD pattern of the sample HU-MR-/3CON6.

Figure 2.3. FTIR spectra of the sample HU-MR-/3CON6.

Figure 2.4. Geomorphological profile of the downstream transects of Howden Burn and Dene Burn with the localization of the riffle, waterfall and woodland.

Figure 2.5. Macroscopic images of the Consett freshwater samples HU-MR-/3CON1, HU-MR-/3CON2, HU-MR-/3CON4, HU-MR-/3CON5, HU-MR-/3CON6, HU-MR-/3CON7.

Figure 2.6. Thin sections from the Consett freshwater samples HU-MR-/3CON1, HU-MR-/3CON2, HU-MR-/3CON4, HU-MR-/3CON5, HU-MR-/3CON6, HU-MR-/3CON7 with the locations of the optical microscope images where the locations are respectively designed by the number of the figure from this manuscript followed by the letter corresponding to the subsection in the figure.

Figure 2.7. (A), (B), (C) depict the microfacies images by petrographic microscope of clotted micrite (CM) facies. (D) shows a SEM image of clotted micrite facies with diatoms (d). (E) shows a SEM image of the diatom *Gromphomena parvulum*. (F) shows a SEM image of the diatom *Gyrosigma acuminatum*. (G) shows a SEM image of the diatom *Navicula lanceolate*. (H) shows a SEM image of the diatom *Navicula gregaria*. (I) shows a SEM image of the diatom *Navicula gregaria*. (J) shows a SEM image of the diatom *Nitzschia amphibian*. (K) shows a

SEM image of the diatom *Planothidium lanceolatum*. (L) shows a SEM image of the diatom *Sellaphora nigri*.

Figure 2.8. (A), (B), (C), (D), (E) and (F) depict the microfacies images by petrographic microscope of microbial rim (MR) facies.

Figure 2.9. (A), (B), (C), (D), and (E) depict the microfacies images by petrographic microscope of dendrite facies (D).

Figure 2.10. (A), (B), (C) and (D) depict the microfacies images by petrographic microscope of shrub (S) facies. (E) shows a SEM image of shrub facies with diatoms (d) and bacterial filament (bf). (F) shows a SEM image of the diatom *Gromphomena parvulum*. (G) shows a SEM image of the diatom *Gyrosigma acuminatum*. (H) shows a SEM image of the diatom *Navicula lanceolate*. (I) shows a SEM image of the diatom *Navicula gregaria*. (J) shows a SEM image of the diatom *Navicula gregaria*. (K) shows a SEM image of the diatom *Nitzschia amphibian*. (L) shows a SEM image of the diatom *Planothidium lanceolatum*. (M) shows a SEM image of the diatom *Sellaphora nigri*.

Figure 2.11. (A), (B), (C) and (D) show the microfacies images by petrographic microscope of cluster-shaped carbonate (C-SC) facies. (E) shows a SEM image of cluster-shaped carbonate facies with bacterial filament (bf). (F) shows a SEM image of the transition between shrub, cluster-shaped carbonate and clotted micrite.

Figure 2.12. (A), (B) and (C) show the microfacies images by petrographic microscope of multi-shaped calcite (M-SC) facies.

Figure 2.13. (A), (B), (C) and (D): Microfacies images by petrographic microscope of sparry carbonate crust (SCC) and bothryoidal carbonate crust facies (BCC). (E) shows a SEM image of the transition between clotted micrite and sparry carbonate crust facies.

Figure 2.14. (A), (B), (C) and (D): Microfacies images by petrographic microscope of blocky calcite facies (BC).

Figure 2.15. (A) depicts the sample locations versus Calcite Saturation Index, pH, calcite growth rate (R) and distribution of microfacies. (B) shows the depositional model summarizing the lateral changes of the microfacies.

Chapter 3:

Figure 3.1: (A) Location map of the Brook Bottom (BB) samples (BB1, BB13, BB10 fresh, BB10 old deposit, BB16) where the yellow part represents the carbonate deposit. (B) Topographic map with the Brook Bottom samples (BB1, BB13, BB10 fresh, BB10 old deposit, BB16) after Ordnance Survey map. (C) Location map of the Consett (C) freshwater samples in Howden Burn (C6) and Dene Burn (DB) (C4, C5, DB6, DB12, DB18) after Historic OS maps. (D) Topographic map with the Consett freshwater samples in Howden Burn (C6) and Dene Burn (C4, C5, DB6, DB12, DB18) after Ordnance Survey map.

Figure 3.2: Environmental pictures of the downstream transects of Howden Burn, Dene Burn and Brook Bottom with the localisation of the riffle, waterfall, and woodland.

Figure 3.3: (A) Original thin sections from the Brook Bottom (BB) (BB1, BB13, BB10 fresh, BB10 old deposit, BB16) and Consett (C) freshwater samples in Howden Burn (C6) and Dene Burn (DB) (C4, C5, DB6, DB12, DB18) with the locations of the optical microscope images. The locations are respectively designated by the number of the figure from this manuscript followed by the letter corresponding to the subsection in the figure. (B) Interpreted thin-sections with the colours representing the different microfacies. The locations of the optical microscope images are respectively designated by the number of the figure from this manuscript followed by the letter corresponding to the subsection in the figure.

Figure 3.4 Macroscopic images of the Brook Bottom (BB) (BB1, BB13, BB10 fresh, BB10 old deposit, BB16) and Consett (C) freshwater samples in Howden Burn (C6) and Dene Burn (DB) (C4, C5, DB6, DB12, DB18).

Figure 3.5: Coated vegetative remains and carbonate raft (microfacies 1). (A) Assemblage of brown coloured, flat and elongated vegetative remains (arrow) coated by calcite thin films. (B) Some flat remains (arrow) are covered in globular sparry calcite crusts (Gs); interparticle porosity (p) is very abundant. (C) SEM photomicrograph of carbonate rafts (R) covered by multiple arcuate vault structures (Vs) consisting of cloudy, brown-coloured sparry calcite. (D) BSE-SEM image of poorly sorted carbonate rafts covered by vault structures (VS). Some polycrystalline calcite globular aggregates (pcg) can grow laterally to form elongated structures. (E and F) XRD pattern and EDX spot analysis, respectively, indicating a calcite mineralogy.

Figure 3.6: Micro-peloidal and clotted micritic (microfacies 2). (A and B) Patchy micropeloidal micritic textures (pel) alternate with laminated textures (arrows). Filamentous clotted structures can be seen perpendicular to laminae (fil-pel). In some cases, lumpy micropeloidal masses (lum-pel) develop in association with laminated textures. Abundant inter-crystalline porosity (p) is observed in this microfacies. (C and D) SEM images of the microfacies clotted micrite. XRD pattern and EDX spot analysis, respectively, indicating that calcite and quartz are present.

Figure 3.7: Carbonate-coated microbial filament (microfacies 3). (A) Double terminating calcite crystal morphologies agglutinated around organic-rich filamentous structures (arrows) forming crystal lumps. High intercrystalline porosity (p) is recognised between filaments. (B) Double terminating calcite crystals can be detached from microbial filaments forming intraclastic accumulations embedded in organic-rich matrices (o). (C and D) XRD pattern and EDX spot analysis, respectively, indicating that calcite is the predominant mineralogy.

Figure 3.8: Globular sparry calcite crust (microfacies 4). (A and B) Thick isopachous calcite fans with globular arrangements (Gs) growing on top of clotted peloidal templates (arrows). Fans consist of thin darker laminae and thick lighter laminae extending laterally. Competitive growth defines sharp boundaries between fans (cg). This microfacies displays a high intercrystalline porosity (p). (C) SEM image showing the external smooth curved surfaces of the fans (Gs). (D) BSE-SEM image displaying sparry crusts growing on top of organic substrates (arrows). Note thin concentric, darker laminae within fans. (E and F) XRD pattern and EDX spot analysis, respectively, indicating that calcite is the predominant mineralogy.

Figure 3.9: Neomorphic sparry crust (microfacies 5). (A and B) Neomorphic sparry crusts growing on top of organic-rich substrates (arrows). Corroded areas (cor) through irregular surfaces on the external part of the crusts are common. (C and D) BSE-SEM images showing cracking of the crusts where fissures (cr) reach different depths showing no apparent reworking. (E and F) XRD pattern and EDX spot analysis, respectively, indicating that calcite is the predominant mineralogy.

Figure 3.10: Crystal shrub (microfacies 6). (A and B) Light grey-white botryoidal crystal fans 1–3 mm in height and stacked on each other as inverted cones growing on top of discontinuous horizons (arrows). (C and D) BSE-SEM images showing bladed crystal aggregates developing incipient intercrystalline microporosity (arrows). (E and F) XRD pattern and EDX spot analysis, respectively, indicating that calcite and quartz are present.

Figure 3.11: Dendrite carbonates (microfacies 7). (A and B) Light grey calcite polycrystals showing multiple levels of branching (arrows). (C and D) BSE-SEM images showing that each branch consists of numerous thin (up to 0.2 mm thick), plate-like calcite crystals that are stacked en echelon (arrows). (E and -F) XRD pattern and EDX spot analysis, respectively, indicating that calcite and quartz are present.

Figure 3.12: Comparative depositional model between anthropogenic carbonate and travertine systems after Capezuolli et al. (2014) and Mancini et al. (2019).

Figure 3.13: Charts showing the pH, temperature and Calcite Saturation Index (CSI), and the major ions and total carbonate alkalinity for the Brook Bottom and Consett samples.

Figure 3.14: (A) Diagram showing the Calcite Saturation Index (CSI), pH, calcite growth rate (R) versus distribution of microfacies according to the sample locations at Brook Bottom (BB) BB1, BB13, BB10 fresh, BB10 old deposit, BB16 and Consett (C) freshwater samples in Howden Burn (C6) and Dene Burn (DB) (C4, C5, DB6, DB12, DB18). (B) Depositional model summarising the lateral changes of the dominant microfacies: Coated vegetative remains and carbonate raft (R), Micro-peloidal and clotted micritic (CM), Carbonate-coated microbial filament (C), Globular sparry calcite crust (G), Neomorphic sparry crust (N), Crystal shrub (CS) and Dendrite (D).

SUPPLEMENTARY FIGURES

Figure 3.S1: Previous fabrics after Bastianini et al. (2019). (A) Clotted micrite (B) Microbial rim (C) Carbonate Dendrite (D) Calcite shrub (E) Cluster-shaped calcite (F) Multi-shaped carbonate (G) Sparry carbonate crust (H) Blocky calcite.

Chapter 4:

Figure 4.1: Location map of the studied sample HU-MR-/3CON1 (C1).

Figure 4.2: Graph depicting the average air temperatures in Durham versus the dates after CEDA Archive.

Figure 4.3: Figure 3: Macroscopic images of the Consett freshwater sample HU-MR-/3CON1 depicting a scattering of cm-sized euhedral to subhedral white crystals of ikaite (Ik) rising above and cemented to the buff-coloured orange-red oxidated tufa carbonate (Tu).

Figure 4.4: Recovered sample of ikaite (Ik) within the sieve.

Figure 4.5: FTIR spectra of the sample of ikaite C1.

Figure 4.6: One-dimensional diffraction pattern collected from HU-MR-/3CON1 (solid black line). The grey line is the simulated pattern for ikaite (with peak positions highlighted as vertical lines). The two starred peaks correspond to calcite.

Figure 4.7: Coordination about the Ca^{2+} ion with atoms shown as 50% probability ellipsoids. Atoms labelled name i are generated by the symmetry operator $i = 1-x, y, \frac{1}{2}-z$.

Figure 4.8: SEM images of the Consett freshwater sample C1.

Figure 4.9: Trial of making ikaite following the method of Lennie et al. (2004) corresponding to ACC.

Figure 4.10: Trial of making ikaite following the method of Tollefsen et al. (2020) corresponding to ACC.

Figure 4.11: Climatology of annual mean land temperature for 1951-1980 from the Berkeley Earth data after NCAR, ClimateDataGuide with the overlapped localization of the countries with annual mean land temperature lower than 8°C and steel plant sites after World steel plant maps - 2020 Geography (<https://www.steelonthenet.com/maps.html>).

Chapter 5:

Figure 5.1: Distribution diagram for carbonate species as a function of pH, assuming the total carbonate $\text{CT} = 10^{-3}$ M. Concentrations of H^{+} and OH^{-} , which are independent of CT, are shown as dashed straight lines after Langmuir (1997).

Figure 5.2: Location map of the Welton spring-system where was collected the water samples.

Figure 5.3: Graph depicting the data of the Fixed End Point method (Beginner and Expert Level).

Figure 5.4: Graph depicting the data of the Inflection Point method (water 1 and water 2).

Figure 5.5: Graph depicting the comparison of the three methods of titrations.

Figure 5.6: Graph depicting the comparison of the median of the three methods of titrations.

Figure 5.7: Graph depicting the comparison of beginner and expert levels within the FEP.

Figure 5.8: Flow chart describing the process of the FEP method.

TABLE LIST

Chapter 1:

TABLE. 1.1. – Table summarizing the occurrences of hyperalkaline springs with their key chemical characteristics and environments.

TABLE. 1.2. – Summary Table of alkaline residues and annual production after Gomes et al. (2016).

Chapter 2:

TABLE. 2.1. – Hydrochemistry dataset of the samples including pH, temperature, major ion concentrations, total alkalinity, calcite saturation index, ionic strength, activity and calcite growth rate from the research works of Hobson et al., (2018), Hull et al., (2014), Mayes et al., (2008), Mayes et al., (2018), and Riley and Mayes (2015).

Chapter 3:

TABLE. 3.1. – Hydrochemistry data set of the Brook Bottom samples including pH, temperature, major ion concentrations, total alkalinity, calcite saturation index, ionic strength, activity and calcite growth rate.

TABLE. 3.2. – Hydrochemistry data set of the Consett samples including pH, temperature, major ion concentrations, total alkalinity, calcite saturation index, ionic strength, activity and calcite growth rate from the research works of Mayes et al. (2008), Hull et al. (2014), Riley and Mayes (2015), Hobson et al. (2018), and Mayes et al. (2018).

Chapter 4:

TABLE. 4.1. – Reporting template (metadata) for LA-ICP-MS U-(Th-)Pb data.

TABLE. 4.2. – FTIR review with the different peak diagnostic of the CaCO₃ polymorphs.

TABLE. 4.3. – Depicting the different partition coefficients for the elements sequestered in the sample of ikaite versus the partition coefficients of calcite and aragonite from the literature.

TABLE. 4.4. – Depicting the rate of contaminants stored in ikaite per day for each metal.

TABLE. 4.5. – Depicting the potential impacts of the contaminants Cd, Zn, Pb, Cr and Zn classified by primary ecological importance, priority, and secondary hazardous substances.

TABLE. 4.6. – Depicting the potential impacts of the contaminants Ba, Mn and Ni classified by primary ecological importance, priority, and secondary hazardous substances.

Chapter 5:

TABLE. 5.1. – Table depicting the ranges of SI corresponding of the alkalinity values from the different methods.

TABLE. 5.2. – Table depicting the uncertainties (CV) from the FEP, ST and IPT methods applied to alkalinities after Mayes et al. (2008) – Table 1; N/A values correspond to extreme alkalinity values where PHREEQC was unable to compute an SI for calcite.

TABLE. 5.3. – Table depicting the uncertainties (CV) from the FEP, ST and IPT methods applied to alkalinities after Bastianini et al. (2019) – Table 1; N/A values correspond to extreme alkalinity values where PHREEQC was unable to compute an SI for calcite.

TABLE. 5.4. – Table depicting the different sources of error with their nature for each method.

Chapter 6:

TABLE. 6.1. – Summary of research priorities for a better understanding of the geochemistry of hyperalkaline carbonate systems.

ACKNOWLEDGEMENTS

I would like to start these acknowledgements by thanking profusely my supervisors. This work would have never been successful without their everlasting support. I want to express my gratitude to Mike Rogerson for his demanding nature, ambition and passion for his profession, which have allowed me to achieve a level of excellence in research. I am also grateful for his continuous encouragements and humanity in some difficult times of this adventure. I have appreciated all of our regular fruitful discussions and I hope they may continue in the future. I am equally thankful of Will Mayes for his efficiency and kindness. He has always provided me remarkably constructive feedback in a very positive manner. I am particularly appreciative of his constant support during this last stage of my PhD writing where he gave me invaluable advice. They both have been active in supporting my applications to find a position in the near future and I would be delighted to pursue a collaboration with them. Likewise, Tim Prior has been an excellent supervisor and I am recognizant for his reactivity and professionalism. He has always been present when I needed his help and I have benefited from his pedagogy to explain concepts related to a domain where I was novice. I wish to thank warmly Mark Anderson who has been of great support in my laboratory work and in the preparation of my field campaigns.

This incredible opportunity of doctorate could never happen without Bruno Caline, who gives me my first chance to work as a carbonate sedimentologist at TOTAL (Centre scientifique et technique Jean-Féger, Pau, France). He has been a fantastic supervisor. I will never forget his delicateness and kindness in supervising me. He really knew how to give me the confidence I needed at that point. I want to thank you equally François Baudin from Sorbonne Université (Paris, France) for offering me the chance to write my first paper related to my work at TOTAL in the Bulletin de la Société Géologique de France, although I was not

a PhD student at that time. This experience was followed by two amazing Erasmus + internships at the University of Aberdeen (School of Geosciences). It was a great pleasure to meet Alex Brasier and to work with him. I will always feel indebted to him for trusting me and recognizing my work qualities. It was a long process to become a PhD researcher and I am very thankful of him for accompanying me in all my efforts to succeed. Indeed, I had to leave my country to come living in the UK. I discovered a great culture rich of immense human values. I appreciated the welcoming, open-mindedness and loyalty of British people and I hope to be part of them one day.

I want to thank all my family as well. A heartfelt thank you to my father for being the person he is. I could not have dreamed of a better father. I cannot find the words to describe all he represents for me and how I am thankful for all the love I received from him. A special thank you to my mother too for all her love and for believing in me and in my dream of becoming a researcher. I have been touched by her genuine curiosity on what exactly I was doing over the past four years. I would like to give sincere thanks to my sister and brother, including their respective spouses, for all of their support and I want them to know all my love. They are so important to me that I could not imagine life without them. I want to include in these acknowledgements my magic godmother and grandmother for her eternal encouragements. I know she is proud of me and I am very thankful of her for having been always present when I needed her. In addition, I wish to thank all my wonderful nephews: Nino for his tenderness and intelligence, my sweet godson Lohan for his gentleness and brightness, Lola for her kindness and generosity and Axelle for the happiness she brings to us and her beautiful blue eyes.

I will finish these acknowledgments by thanking all my friends for their reassurance in believing in my vocation. Ultimately, I wish to dedicate this thesis to my great and good friend Yannick. I would never obtain this PhD without his patience and unceasingly support. When I

was just a jobseeker and sometimes desperate to succeed, he continues to believe in me every second and he gave me the strength to achieve this fantastic journey! I am forever grateful to him for this, and I hope he will continue for long to light my way.

REMERCIEMENTS

Je voudrais commencer par remercier vivement mes encadrants. Je n'aurais jamais pu réussir ce travail sans leur soutien continu. Je souhaite exprimer ma gratitude à Mike Rogerson pour son exigence, son ambition et sa passion pour sa profession qui m'ont permises d'atteindre un niveau d'excellence dans la recherche. Je suis aussi reconnaissante pour ses encouragements permanents et son sens de l'humanité dans certains moments difficiles de cette aventure. J'ai apprécié toutes nos fructueuses discussions et j'espère qu'elles pourront se poursuivre dans le futur. Je remercie également Will Mayes pour son efficacité et sa gentillesse. Il m'a toujours fourni des commentaires remarquablement constructifs d'une manière très positive. J'ai pu apprécier particulièrement son soutien constant ainsi que les précieux conseils prodigués durant la dernière étape d'écriture de ma thèse. Ils ont aussi tous deux été actifs par leurs soutiens apportés à mes candidatures pour me permettre de trouver un poste dans un avenir proche et je serais ravi de poursuivre une collaboration avec eux. Tim Prior a également été un excellent encadrant et je suis reconnaissante pour sa réactivité et son professionnalisme. Il a toujours été présent lorsque j'avais besoin de son aide et j'ai bénéficié de sa pédagogie pour expliquer des notions liées à un domaine dans lequel j'étais novice. Je tiens à remercier chaleureusement Mark Anderson qui a été d'un grand soutien dans mon travail de laboratoire et dans la préparation de mes campagnes de terrain.

Cette incroyable opportunité de doctorat n'aurait jamais pu avoir lieu sans Bruno Caline, qui m'a donné ma première chance de travailler en tant que sédimentologue des carbonates à TOTAL (Centre scientifique et technique Jean-Féger, Pau, France). Il a été un encadrant fantastique. Je n'oublierai jamais sa délicatesse et gentillesse dans son encadrement. Il a vraiment su me donner la confiance dont j'avais besoin à ce moment-là. Je tiens également à remercier François Baudin de Sorbonne Université (Paris, France) de m'avoir offert la chance

d'écrire mon premier article lié à mon travail chez TOTAL dans le Bulletin de la Société Géologique de France, bien que je n'étais pas encore doctorante. Cette expérience s'est poursuivie par deux formidables stages Erasmus + à l'Université d'Aberdeen (School of Geosciences). Ce fut un grand plaisir de rencontrer Alex Brasier et de travailler avec lui. Je me sentirai toujours redevable envers lui de m'avoir fait confiance et d'avoir reconnu mes qualités professionnelles. Ce fut un long processus pour devenir doctorante et je lui suis très reconnaissante de m'avoir accompagnée dans tous mes efforts pour réussir. En effet, j'ai dû quitter mon pays pour venir vivre au Royaume-Uni. J'ai découvert une formidable culture, riche d'immenses valeurs humaines. J'ai apprécié l'accueil, l'ouverture d'esprit et la loyauté des Britanniques et j'espère pouvoir faire partie d'eux un jour.

Je tiens également à remercier toute ma famille. Un grand merci à mon père d'être la personne qu'il est. Je n'aurais pas pu rêver d'un meilleur père. Je ne trouve pas les mots pour décrire tout ce qu'il représente pour moi et combien je suis reconnaissante pour tout l'amour que j'ai reçu de lui. Un merci tout spécial à ma mère aussi pour tout son amour et pour avoir cru en moi et en mon rêve de devenir chercheur. J'ai été touché par son authentique curiosité envers ce que j'ai étudié au cours de ces quatre dernières années. Je tiens à remercier sincèrement ma sœur et mon frère, ainsi que leurs époux et épouse respectifs, pour tout leur soutien et je veux qu'ils sachent tout mon amour. Ils sont si importants pour moi que je ne pourrais pas imaginer la vie sans eux. Je veux aussi inclure dans ces remerciements ma fabuleuse marraine et grand-mère pour ses encouragements éternels. Je sais qu'elle est fière de moi et je lui suis très reconnaissante d'avoir toujours été présente quand j'avais besoin d'elle. De plus, je souhaite remercier tous mes merveilleux neveux : Nino pour sa tendresse et son intelligence, mon cher filleul Lohan pour sa douceur et sa vivacité d'esprit, Lola pour sa gentillesse et sa générosité et Axelle pour le bonheur qu'elle nous apporte et ses beaux yeux bleus.

Je terminerai ces hommages en remerciant tous mes amis de m'avoir donné la confiance de croire en ma vocation. Pour finir, je souhaite dédier cette thèse à mon grand et bon ami Yannick. Je n'aurais jamais obtenu ce doctorat sans sa patience et son soutien sans relâche. Lorsque j'étais demandeuse d'emploi et parfois désespérée de réussir, il a continué de croire en moi à chaque minute et il m'a donné la force d'accomplir ce fantastique voyage ! Je lui en suis éternellement reconnaissante et j'espère qu'il continuera longtemps d'éclairer mon chemin.

THESIS ABSTRACT

Highly alkaline (pH 9-12) waters can arise from a range of natural and anthropogenic processes. The latter include drainage waters from a range of globally significant anthropogenic by-products such as lime, cement and steel wastes, bauxite processing residue and combustion ashes. Such waste storage sites are often characterised by extreme geochemical conditions that can be hazardous to aquatic life, but are equally an increasing focus for resource recovery and carbon capture initiatives. The very high rates of mineral precipitation at these sites can give rise to the formation of transient minerals that are not currently well understood. As such our estimates of carbon budgets and understanding of trace metal dynamics at highly alkaline sites is currently limited. This thesis aimed to improve the basis for characterising hyperalkaline carbonate systems by (1) understanding the dominant carbonate fabrics found in secondary deposits and their formation processes, (2) identifying transient minerals forming at hyperalkaline sites, and (3) improving methods for characterising dissolved inorganic carbon and secondary mineral phases at high pH sites. Petrographic analysis showed distinctive shrunken carbonates forming in hyperalkaline (pH 9–12) and moderate conductivity (conductivity 425–3200 μ S) solutions at ambient temperature (12.5–13°C) at two disposal sites in the UK. Microfabrics in anthropogenic sites are comparable to travertines but lack the sub-surface facies and at extreme pH exhibit sparry crusts without clear equivalents in travertines. Despite the highly alkaline conditions, significant diatomaceous and cyanobacterial biofilms were reported growing in the presence of these carbonates, suggesting a bio-influence on their formation. This sedimentology of anthropogenic carbonates shows that calcite mineral formation is complex and not homogeneous or purely driven by thermodynamic processes.

Whilst most of the secondary deposits at the study sites appear to be dominated by calcite, this study provides the first account internationally of ikaite ($\text{CaCO}_3 \cdot 6\text{H}_2\text{O}$) crystallization within steel-slag leachate through novel field (Fourier Transform Infra-Red) and laboratory (X-Ray Diffraction) validation. This study suggests that ikaite is a secondary mineral with a primary phase being amorphous calcium carbonate (ACC). The ikaite forming in steel-slag leachate affected waters is incorporating large inventories of potentially harmful metals (e.g. lead and cadmium) which could be of environmental concern given ikaite is not thermally stable and could release a pulse of contamination in short duration warming events. The final component of the study develops a new protocol for assessing dissolved inorganic carbon (DIC) in alkaline waters via strontium carbonate precipitation. This method is compared to established methods for DIC using field and laboratory titration. The strontium method appears to perform much better than the existing methods and is likely to provide more robust estimates of alkalinity and saturation index of carbonate minerals.

The combined findings provide an improved understanding of carbonate precipitation processes at highly alkaline sites which in turn should assist future research endeavours around mineral carbonation, trace metal dynamics and environmental remediation at these sites.

CHAPTER 1 – THESIS INTRODUCTION

1.1 | HYPERALKALINE GEOCHEMICAL SYSTEMS

Hyperalkaline geochemical systems are typically defined as those with a water pH in excess of 10 (Leleu et al., 2016). Such high pH waters are understudied in comparison to extremely acidic systems that arise from mining processes (Gomes et al., 2016). Highly alkaline waters can arise from a range of natural and anthropogenic processes: the natural systems include ophiolite (mafic / ultramafic) spring waters (Chavagnac et al., 2013) whilst the man-made systems include drainage waters from a range of globally significant anthropogenic by-products such as lime, cement and steel wastes, bauxite processing residue and combustion ashes (Gomes et al., 2016). Hyperalkaline sites are therefore of great significance for understanding potential sources of contaminants, sites for resource recovery, and potential mineral carbonation.

1.1.1 | Carbonate geochemistry

Non-clastic carbonates form an important class of sediment, having precipitated from solution either through inorganic precipitation or through a biologically mediated process (Alonso-Zarza & Tanner, 2009). Throughout the sedimentary record of the earth, they comprise an important component of continental sediments, providing insights into paleoenvironmental, paleoecological, and paleoclimatic conditions. Analyses of elemental and isotopic geochemistry are now fundamental to any study of carbonate deposits, subject to the many complexities introduced by the sensitivity of carbonate minerals to early, middle, and late diagenetic alteration. The precipitation of carbonate minerals from continental water is fundamentally controlled by the thermodynamics of the carbonate mineral systems. Even given the dramatic importance of biota in mediating mineral precipitation reactions, such organisms must somehow achieve mineral supersaturation in order for biomineralization to occur, either

within or near cellular tissue (e.g., the proton pump of Lian et al., 2006). Understanding the geochemistry of carbonate minerals, therefore, is fundamentally a question of understanding ionic activities in solution at the time of precipitation.

Despite the simplicity of the thermodynamics, however, carbonate mineral precipitation in near-surface continental environments is tremendously complicated by the geochemical impacts of large and small organisms, and reaction kinetics in an environment with non-ideal ion interactions, variable substrates, fluctuating pH, organic molecules, and gas phase interactions (Alonso-Zarza & Tanner, 2009). With these complications in mind, it is nevertheless helpful to consider that, when we observe sedimentary carbonates, the fundamental reason that solid calcite, for example, exists is because Ca(aq)^{2+} and $\text{CO}_3\text{(aq)}^{2-}$ were present in sufficient concentrations and activities for calcite to be supersaturated. Hence, a lack of calcareous microfossils in a lacustrine deposit may be directly due to limnological processes inhibiting the bioavailability of Ca(aq)^{2+} , rather than to other ecological factors such as pH or salinity. Understanding the genesis of carbonate minerals, therefore, is a question of understanding what processes promote supersaturation and precipitation, be they biotic or abiotic, and what kinetic effects inhibit precipitation (perhaps favoring certain phases). Moreover, understanding how these processes control the incorporation and partitioning of major and trace elements, and stable isotopes (especially of C, O, and Sr) provides a powerful tool for paleoenvironmental reconstruction.

Carbonate minerals represent the largest global store of carbon, making research into carbon dynamics in the carbonate critical zone particularly important. Through numerous reactions and interactions, the inorganic carbon store is linked to organic carbon production, remineralization, and production of various natural acids. Carbonate mineral dissolution by carbonic acid consumes carbon dioxide, contributing to short-term drawing down of atmospheric carbon dioxide levels. However, carbonate mineral dissolution by other acids has

the opposite effect of producing carbon dioxide, coupling the carbonate critical zone and climate (Martin, 2017). Although equilibrium is often assumed between soil carbon dioxide and groundwater, disequilibrium may result from heterogeneous distributions of recharge, flow paths, and respiration often seen in the carbonate critical zone (Alonso-Zarza & Tanner, 2009). Understanding the controls of this disequilibrium, which drives carbon dioxide dissolution or evasion and alters pH, weathering reactions, and carbonate mineral dissolution or precipitation, is critical in linking the carbonate critical zone to the global climate system (Martin, 2017).

Organic carbon cycling is coupled to ecosystem metabolism (the ways that plants, animals, and microorganisms process carbon) through fixation of inorganic carbon to organic matter and remineralization of organic matter to carbon dioxide and nutrients like nitrogen and phosphorous (Lian et al., 2006). This nutrient generation supports ecosystems above and below the land surface, although excess anthropogenic nutrients can alter aquatic ecosystems common in clear-water streams of carbonate terrains. Links between dissolved and gaseous carbon dioxide distributions, organic carbon fixation, and mineral weathering make finding answers to questions about carbon dynamics key to understanding many carbonate critical zone processes (Martin, 2017).

1.1.2 | Natural hyperalkaline systems

Hyperalkaline springs in serpentinizing environments (ophiolite spring systems) constitute an important example of natural hyperalkaline systems. Sites of discharge of such very high pH waters are summarized in Table 1.1. The discharge of these waters is reported at springs where they lead to the formation of carbonate concretions, in the form of tuffs in Oman (Chavagnac et al., 2013a) or submarine pinnacles at Lost City (Kelley et al., 2005) and in the Prony Bay in New Caledonia (Launay and Fontes, 1985; Monnin et al., 2014; Pelletier et al., 2006).

Table 1.1: Table summarizing the occurrences of hyperalkaline springs with their key chemical characteristics and environments.

Site	Key chemical characteristics and environments	Reference
Oman	Very high pH waters on land. Geochemical process: serpentinization of ultramafic rocks.	Chavagnac et al., 2013b; Miller et al., 2016; Paukert et al., 2012; Stanger, 1985
Northern Italy	Very high pH waters on land. Geochemical process: serpentinization of ultramafic rocks.	Boschetti and Toscani, 2008; Chavagnac et al., 2013b; Cipolli et al., 2004
Cyprus	Very high pH waters on land. Geochemical process: serpentinization of ultramafic rocks.	Neal and Shand, 2002
Philippines	Very high pH waters on land. Geochemical process: serpentinization of ultramafic rocks.	Cardace et al., 2015
California	Very high pH waters on land. Geochemical process: serpentinization of ultramafic rocks.	Boschetti et al., 2017; Morrill et al., 2013
Ontario	Very high pH waters on land. Geochemical process: serpentinization of ultramafic rocks.	Sader et al., 2007
Newfoundland	Very high pH waters on land. Geochemical process: serpentinization of ultramafic rocks.	Szponar et al., 2012
Portugal	Very high pH waters on land. Geochemical process: serpentinization of ultramafic rocks.	Marques et al., 2008
Greece	Very high pH waters on land. Geochemical process: serpentinization of ultramafic rocks.	D'Alessandro et al., 2018a
Turkey	Very high pH waters on land. Geochemical process: serpentinization of ultramafic rocks.	Meyer-Dombard et al., 2015; Yuce et al., 2014
New Caledonia	Very high pH waters on land. Geochemical process: serpentinization of ultramafic rocks.	Monnin et al., 2014
Spain	Very high pH waters on land. Geochemical process: serpentinization of ultramafic rocks.	Giampouras et al., 2019
Lost City Hydrothermal Field on the Atlantis massif off the Mid-Atlantic ridge	Hyperalkaline waters at the seafloor where plate tectonics has exposed ultramafic rocks to alteration. Geochemical process: serpentinization of ultramafic rocks.	Kelley et al., 2001; Kelley et al., 2005
Marianna forearc	Hyperalkaline waters in mud volcanoes at the decollement zone of a subducting plate. Geochemical process: serpentinization of ultramafic rocks.	Fryer et al., 1989; Fryer et al., 2018; Mottl et al., 2004
Maqarin site in Jordan	Natural combustion of bituminous marls and alteration of the rocks created by a phenomenon that has been called pyrometamorphism lead to the formation of extremely alkaline water, with pH value up to 12.5	Alexander et al., 1992; Khoury et al., 1992
Cabeço de Vide in Portugal	Hyperalkaline waters in an ultramafic complex created by continental collision. Geochemical process: serpentinization of ultramafic rocks.	Marques et al., 2008; Marques et al., 2018

Serpentinization is a natural process that transforms ferromagnesian minerals such as olivine into serpentine (Monnin et al., 2021). This process is accompanied by the formation of high-pH water, hydrogen and methane (Monnin et al., 2021). This forms a unique ecological niche for microorganisms adapted to extreme pH and/or involved in the hydrogen and/or methane cycles (Monnin et al., 2021). In ophiolite spring systems (from Oman and Liguria), the alteration of mafic/ultramafic rocks by meteoric waters and seawater provides saline, hyperalkaline (pH 10) waters which in-gas carbon dioxide from the atmosphere (Leleu et al., 2016). Circulating groundwaters interact with deep crustal rock and are typically depleted in dissolved inorganic carbon (DIC, e.g., Oman: Neal and Stanger 1983, Chavagnac et al. 2013a; New Caledonia: Launay and Fontes 1985, Monnin et al. 2014; Philippines: Abrajano et al. 1988). In this case, the serpentinization process has led to the conversion of initial Mg-HCO₃ type waters into Ca-OH type hyperalkaline waters depleted both in dissolved inorganic carbon (DIC) and Mg but enriched in Ca (Barnes et al. 1967; Barnes and O'Neil 1969; Barnes et al. 1978; Neal and Stanger 1984; Bruni et al. 2002; Cipolli et al. 2004; Sader et al. 2007; Kelemen and Matter 2008; Chavagnac et al. 2013b; Monnin et al. 2014). Precipitation of calcium carbonate from hyperalkaline spring waters is possible only if carbonate ions are available which is typically accomplished in two ways: 1) mixing between DIC depleted hyperalkaline waters and DIC-rich surface runoff waters, and/or 2) via diffusion and dissolution of atmospheric CO₂(g) into spring waters. As a result, the conditions leading to calcium carbonate formation in hyperalkaline springs is fundamentally different from carbonates that precipitate from bicarbonate-rich waters.

1.1.3 | Bicarbonate-rich carbonate systems

Bicarbonate-rich ambient temperature systems are subtly different to more conventional travertine systems, which are usually located at subaerial hot springs such as Mammoth Hot Springs in Wyoming (Ford and Pedley, 1996; Fouke et al., 2000). In geothermal systems, CO₂

is available from the deep subsurface in surplus to the metals (Minissale et al., 1997), making carbonate production calcium-limited. In contrast, within non-geothermal systems driven by mineral hydrolysis, all CO₂ is provided from atmosphere and the carbonate system tends to be limited by the relatively slow kinetics of CO_{2(g)} dissolution and hydrolysis to CO₃²⁻_(aq) rather than the abundance of calcium (Andrews et al., 1997; Rogerson et al., 2017). Hyperalkaline lake systems which precipitate carbonate, such as the Mono Lake, California (Della Porta, 2015), are essentially the same as these spring systems. In the purely geochemically driven models, this voluminous past tufa formation postulated that calcium carbonate precipitation was caused by mixing of carbonate-rich, high pH lake water with Ca-rich spring water (Cloud & Lajoie, 1980; Dunn, 1953; Rieger, 1992). Similar models have recently been invoked to help explain sublacustrine chimneys of the Afar Rift (Dekov et al., 2014). A popular geochemical model for Mono Lake contends that the dominant primary-formed carbonate mineralogy is ikaite (Bischoff et al., 1993), and that in most cases, this later recrystallises to gaylussite (Bischoff et al., 1993) or calcite (Council & Bennett, 1993). Mound and chimney morphologies in these geochemical models are explained by mineral precipitation from upward rising, low-density sublacustrine plumes of spring waters.

1.1.4 | Anthropogenic hyperalkaline systems

Leachates from anthropogenic residues represent an important geochemical hyperalkaline system equally. Alkaline residues are produced by many industrial processes, such as coal combustion, lime production, chromium ore processing, cement production, alumina extraction, iron and steel manufacture, and waste incineration produce alkaline residues, representing a large and increasing global flux (Table 1.2).

Table 1.2: Summary Table of alkaline residues and annual production after Gomes et al. (2016).

Type	Dominant mineral matrix	Production (t a ⁻¹)
Bauxite residues or red mud (Bayer process in aluminium production)	Iron oxides, Na(Ca)-aluminosilicates, Ti(Fe) oxides, natrite (Na ₂ CO ₃), calcite (CaCO ₃) and NaOH (Gräfe et al., 2011; Xue et al., 2015)	120 million (Power et al., 2011)
Steelworks slags	Free lime (CaO) and periclase (MgO), Ca-silicates, Ca-Fe(Al)-oxides and refractory Mg-Fe(Mn)-oxide phases (Piatak et al., 2015)	170-250 million (USGS, 2015a)
Fly ashes (coal combustion)	Quartz (SiO ₂), magnesioferrite (MgFeO ₄), anorthite (CaAl ₂ Si ₂ O ₈), anhydrite (CaSO ₄), haematite (Fe ₂ O ₃), mullite (Al ₆ Si ₂ O ₁₃) and lime (CaO) (Yilmaz, 2015)	415 (Heidrich et al., 2013) -600 million (Bobicki et al., 2012)
Concrete crusher fines	Quartz (SiO ₂), calcite (CaCO ₃), Na(Ca)-aluminosilicates, albite (NaAlSi ₃ O ₈) and portlandite Ca(OH) ₂ (Somasundaram et al., 2014)	497-2095 million (Renforth et al., 2011)
Flue gas desulphurisation waste	Hannebachite (CaSO ₃ .0.5H ₂ O), calcite (CaCO ₃), lime (CaO), mullite (Al ₆ Si ₂ O ₁₃) quartz (SiO ₂), haematite (Fe ₂ O ₃), magnetite (Fe ₃ O ₄), and ettringite [Ca ₆ Al ₂ (SO ₄) ₃ (OH) ₁₂ .26H ₂ O] (NERC, 1980)	11 million (Córdoba, 2015)
Air pollution control (APC) residues	Calcite (CaCO ₃), gypsum (CaSO ₄), CaClOH, portlandite [Ca(OH) ₂], lime (CaO), ettringite [Ca ₆ Al ₂ (SO ₄) ₃ (OH) ₁₂ .26H ₂ O], Quartz (SiO ₂) (Bogush et al., 2015)	1.2 million (Brunner and Rechberger, 2015)
Solvay process waste	Calcite (CaCO ₃), lime (CaO), gypsum (CaSO ₄ .2H ₂ O), brucite [Mg(OH) ₂] (Steinhauser, 2008)	15.5 thousand (USGS, 2015b)
Chromite ore processing residue (COPR)	Free lime (CaO), portlandite [Ca(OH) ₂], brucite [Mg(OH) ₂], calcite (CaCO ₃), hydrocalumite [Ca ₄ Al ₂ (OH) ₁₂ CrO ₄ .6H ₂ O], periclase (MgO) (Geelhoed et al., 2003)	6 million (Wu et al., 2015)

Whilst there are significant differences in bulk mineralogical composition among these residues, they are all typically the products of high-temperature processes and all are characterised by the presence of Na, Ca or Mg silicates and oxides that rapidly hydrate to produce soluble hydroxides (Gomes et al., 2016). A large range of Ca and Na, aluminate and aluminosilicate phases are also present, hydrating and dissolving to generate alkalinity. Finally, any Ca and Mg carbonates present provide a stable (low solubility) alkaline phase (Gomes et al., 2016). Initially, dissolution of soluble Na or Ca hydroxides tends to dominate ($\text{pH} > 12$) (Gräfe et al., 2011; Mayes et al., 2008; Roadcap et al., 2005). Over time, the more slowly reacting phases (e.g. Ca silicates, Na aluminosilicates, $\text{Mg}(\text{OH})_2$) control leachate quality ($9 < \text{pH} < 12$). On long timescales, carbonate dissolution prevails ($\text{pH} < 9$). Therefore, despite the differences in mineral composition of different alkaline residues, there are clear similarities in terms of the environmental processes apparent at anthropogenic hyperalkaline sites. As such, they have garnered a lot of interest from the research community in recent years on a range of issues that include environmental hazard assessment and remediation (e.g. Hull et al., 2014; Gomes et al., 2019), metal recovery (e.g. Gomes et al., 2017), atmospheric carbon capture (Pullin et al., 2019) and understanding of microbial processes in extreme chemical conditions (e.g. Wormald et al., 2021). However, despite similarities between these anthropogenic sites and both hyperalkaline and bicarbonate natural systems, no systematic effort at comparison has been attempted to date. Consequently, there remains significant knowledge to exchange between communities working on the two types of system.

1.2 | WHAT DO WE KNOW ABOUT THE CARBONATE SEDIMENTOLOGY AT ANTHROPOGENIC HYPERALKALINE SITES?

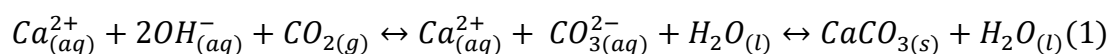
Studies concerning the precipitates at anthropogenic hyperalkaline sites are scarce as most studies have focussed on bulk composition and trace element content, with a focus on environmental risks (Hull et al., 2014; Gomes et al., 2016, 2017, 2020; Renforth, 2019).

However, study of carbonate fabrics at these sites can reveal significant information about biogeochemical processes driving carbonate precipitation in these systems. Although the sedimentology of anthropogenic carbonates has been poorly investigated, significant insight can be gained by comparison with better-known tufa (ambient temperature spring, river, lake and swamp carbonate) and travertine (geothermally influenced) systems (Capezzuoli et al., 2014; Della Porta, 2015; Ford & Pedley, 1996; Pentecost, 2005). At whole-system scales for both tufa and travertine, carbonate sediment forms due to high supersaturation levels with physicochemical precipitation (i.e. that regulated by classic thermodynamic considerations) occurring in a manner analogous to that assumed by hyperalkaline sites. The comparison of anthropogenic carbonates with better-known naturally occurring systems will provide an insight on the potential drivers, precipitation mechanisms, morphological similarities, predictability in 3D facies distributions and depositional models of these systems.

1.2.1 | The water chemistry

Anthropogenic carbonates are pyrotechnological products composed of calcium carbonate, and include wood ash, lime plaster/mortar and hydraulic mortar, in addition to secondary carbonates that arise as a product of weathering a range of globally important industrial residues (Toffolo, 2020). These residues include steel slags (Roadcap et al., 2005), coal combustion residues (Dellantonio et al., 2010), chromite ore processing waste (Stewart et al., 2007), Solvay Process residues from the manufacture of soda ash (Effler et al., 2003), lime spoil (Burke et al., 2012a, b) and bauxite processing residue (Mayes et al., 2011).

The formation of carbonate minerals in alkaline environments occurs when CO₂ gas is dissolved in the solution and reacts rapidly with OH⁻ ions (from portlandite dissolution) to form aqueous carbonate through Eq. (1).



The rate of this reaction is governed by equation 2 (Dietzel et al., 1992):

$$r = C_o \cdot (D \cdot k \cdot [OH^-])^{0.5} \quad (2)$$

In this equation k is the rate constant ($\text{cm}^3 \cdot \text{mol}^{-1} \cdot \text{s}^{-1}$) for hydroxylation, D is the diffusion coefficient of CO_2 through the liquid ($\text{cm}^2 \cdot \text{s}^{-1}$) and C_o the CO_2 concentration in solution ($\text{mol} \cdot \text{cm}^{-3}$).

The dissolution products of alkaline waste materials can raise pH values up to 12.4, well outside the pH range that will be satisfactory for any receiving waters from a regulatory perspective (Mayes et al., 2008).

Andrews et al. (1997) have demonstrated that in Welsh quarry water and carbonate crusts the high pH is caused by dissolution of lime spoil, resulting in high OH^- concentrations. This high alkalinity causes uptake of atmospheric CO_2 and strong fractionation of both carbon and oxygen stable isotopes, resulting in calcite precipitates with unusually negative isotopic compositions. None of their general interpretations, based on near equilibrium partitioning of isotopes (see discussions in Andrews et al., 1993, 1997) could explain these values, suggesting that disequilibrium effects were important at this site.

Microbial communities have been found associated with an anthropogenic, highly alkaline environment of a saline soda lime, in Poland (Kalwasińska et al., 2017). Due to a high salt concentration and alkaline pH, the lime is considered as a potential habitat of haloalkaliphilic and haloalkalitolerant microbial communities. This artificial and unique environment is nutrient-poor and devoid of vegetation, due in part to semi-arid, saline and alkaline conditions. A surprisingly diverse bacterial community was discovered in this highly saline, alkaline and nutrient-poor environment, with the bacterial phyla Proteobacteria (representing 52.8% of the total bacterial community) and Firmicutes (16.6%) showing dominance. Extremophile microbiology has therefore become a major area of research interest around highly alkaline sites, with some researchers reporting that the extreme geochemical conditions present could be useful analogous for primitive Earth-like environments (e.g.

Chavagnac et al., 2013). An improved understanding of carbonate fabrics at highly alkaline sites could help improve our understanding of the importance of microbial processes in these systems.

1.2.2 | Time-variant mineralogy

Hyperalkaline systems with extreme geochemical processes can give rise to a range of transient minerals given the rapid rates of mineral precipitation (e.g. Mayes et al., 2008). These can be of critical importance to trace element dynamics given potential for scavenging by neo-formed and transient precipitates. Such rapid rates of mineral precipitation are analogous to extremely acidic systems where a range of amorphous minerals typically precipitate from solution but alter over time (Nordstrom & Alpers, 1999; Nordstrom et al., 2000). These rapid mineral precipitation processes and transient / amorphous mineral forms create challenges for sampling, with traditional approaches to sampling (solid sample recovery and XRD at some point typically within 2 weeks of sampling) will not adequately characterise amorphous or transient phases. For instance, ikaite (a hexahydrate of calcite: $\text{CaCO}_3 \cdot 6\text{H}_2\text{O}$) is more susceptible to re-dissolution and mechanical abrasion compared to calcite, so a combination of chemical and mechanical processes could cause transient phases like ikaite to vanish rapidly, i.e. probably within a few days in Springtime (Boch et al., 2015). The importance of transient mineral phases in hyperalkaline systems is not currently well-understood. Some studies have noted the presence of polymorphs of calcite (e.g. aragonite and vaterite) at field sites (e.g. Mayes et al., 2008; Milodowski et al., 2013) but their role in mineral carbonation and pollutant uptake have not been studied. The latter is of particular significance given partition coefficients of trace metals vary across carbonate minerals. As such, transient phases which are preferential accumulators of trace metals could become short term pollution sources, for example after warming for carbonates like ikaite that have a narrow thermal window of stability (Boch et al.,

2015). Given these unknowns, improved field assessment of transient mineral phases could help reveal these time-variant mineralogy of hyperalkaline sites.

1.3 | THESIS AIMS

This study aims to improve the basis for characterising hyperalkaline carbonate systems and provide novel insights into the nature of anthropogenic carbonates. To do this, the thesis will answer the following research questions (RQ):

RQ1) What are the dominant carbonate fabrics found in secondary deposits at anthropogenic hyperalkaline sites?

RQ2) What do differences in carbonate fabrics at hyperalkaline sites tell us about controls on carbonate precipitation?

RQ3) Through novel coupled field and laboratory analyses, what evidence is there for transient mineral formation at anthropogenic hyperalkaline sites?

RQ4) What are the implications of transient mineral formation on trace metal dynamics?

RQ5) How can dissolved inorganic carbon be better characterised from anthropogenic hyperalkaline sites?

1.4 | THESIS STRUCTURE

The thesis comprises an Introduction (Chapter 1) highlighting the scope and structure of the thesis. The subsequent chapters are presented in paper format with each containing chapter-specific context, methods, results and discussion. There are four primary data chapters which are:

- Chapter Two: “What Causes Carbonates to Form “Shrubby” Morphologies? An Anthropocene Limestone Case Study.” This chapter explores the nature of secondary

carbonate fabrics at a site receiving drainage from an iron and steel wastes associated with a former steel mill at Consett, County Durham, northern England (Research Question: RQ1). The chapter identifies dominant carbonate fabrics and compares these to analogous natural carbonates found in the South Atlantic Pre-Salt carbonates (Chapter Two).

- Chapter Three: “What are the different styles of calcite precipitation within a hyperalkaline leachate? A sedimentological Anthropocene case study.” This chapter compares anthropogenic carbonates with natural carbonate-precipitating settings (hot-spring and tufa environments) to gain insights on the ultimate processes driving mineral precipitation (RQ2). Chapter three extends the work at Consett to provide a multi-site comparison of carbonate fabrics at systems receiving anthropogenic hyperalkaline drainage (RQ1) and considers similarities in drivers of precipitation processes (RQ2).
- Chapter Four: “Ikaite formation in streams affected by steel waste leachate: first report and potential impact on contaminant dynamics.” This chapter investigates transient minerals produced at hyperalkaline sites with a novel approach for field characterisation and rapid laboratory confirmation of samples of interest (RQ3). The transient minerals identified include the exceptional discovery of the carbonate polymorph ikaite. Through integration of field observations, laboratory characterisation and experimental work, this chapter considers the potential importance of transient mineral phases for trace metal dynamics at hyperalkaline sites (RQ4).
- Chapter Five: “Improving field alkalinity characterization of waters on anthropogenic alkaline sites.” The final data chapter of the thesis critically assesses a range of methods for dissolved inorganic carbon (DIC) characterisation at anthropogenic alkaline sites. DIC is

a crucial measure to assist in understanding carbonate formation processes, trace metal dynamics and carbonation opportunities at these sites, but traditional approaches may not be robust for waters with extreme geochemistry. As such Chapter Five compares a range of methods for assessing dissolved inorganic carbon in alkaline samples and includes the development of a new method for such based-on strontium carbonate precipitation. Traditional methods (manual and automated titrations) are compared against a new strontium carbonate method for accuracy and reliability. The implications of the differing performances in these methods for DIC characterisation are considered for interpreting geochemical processes (notably carbonate saturation) at hyperalkaline sites (RQ5).

The Thesis concludes with Chapter Six, which draws the conclusions of the different data chapters together and revisits the thesis aim and research questions. Chapter Six also discusses future research directions based on the findings and insights presented in the thesis.

CHAPTER 2 – What causes carbonates to form “shrubby” morphologies?

An Anthropocene limestone case study.

Laura Bastianini, Mike Rogerson, Ramon Mercedes-Martín, Timothy J. Prior, Edgley A. Cesar and Will Mayes

This chapter explores the nature of secondary carbonate fabrics at a site receiving drainage from an iron and steel wastes associated with a former steel mill at Consett, County Durham, northern England (RQ1: What are the dominant carbonate fabrics found in secondary deposits at anthropogenic hyperalkaline sites?). The chapter identifies dominant carbonate fabrics and compares these to analogous natural carbonates found in the South Atlantic Pre-Salt carbonates and has been published in *Frontiers in Earth Sciences* on 11th September 2019.

2.1 | INTRODUCTION

The genesis and evolution of Lower Cretaceous, non-marine carbonate hydrocarbon reservoirs in the South Atlantic, with their voluminous shrubby and spherulitic carbonate deposits in a volcanic and alkaline lacustrine setting, remains an enigma (Mercedes-Martin et al. 2016, 2017; Wright and Tosca, 2016). Two main mechanisms for spherulite formation have been presented, with formation within a transient Mg-Si gel (Tosca et al., 2018; Wright and Barnett, 2015; Wright and Tosca, 2016) or as a result of organic acid binding to growing crystal surfaces (Chafetz, and Butler, 1980; Tucker and Wright, 2009; Mercedes-Martin et al. 2016, 2017; Spadafora et al., 2010). Both mechanisms suggest a saline, alkaline environment, and high metal fluxes are required to emplace these large Ca- and Mg-dominated precipitate bodies. The “shrubby” spherulitic boundstones which generally form the best reservoir facies (Ceraldi and Green, 2016; Saller et al., 2016) are less well understood, and are generally assumed to be some local modification of the more common spherular growth-form. Recent examples of shrubby carbonate formation are hard to find, reflecting that the microenvironment in which

these growth-forms develop are not well represented in the modern Earth system. One explanation for the origin of the high flux of metalliferous, alkaline water to the Pre-Salt lakes is hydrolysis of fresh alkaline extrusive igneous materials (Rogerson et al. 2017), and partial analogs of Pre-Salt mineralogies and fabrics do occur in ophiolite spring systems (from Oman and Liguria) (Leleu et al., 2016). Here, the alteration of mafic / ultramafic rocks by meteoric waters and seawater provides saline, hyperalkaline (pH ~ 10) waters which in-gas carbon dioxide from the atmosphere. These ambient temperature systems are subtly different to more conventional travertine systems, which are usually located at subaerial hot springs such as Mammoth Hot Springs in Wyoming (Ford and Pedley, 1996; Fouke et al., 2000). In geothermal systems, CO₂ is available from the deep subsurface in surplus to the metals (Minissale et al., 1997), making carbonate production calcium-limited. In contrast, within non geothermal systems driven by mineral hydrolysis, all CO₂ is provided from atmosphere and the carbonate system tends to be limited by the relatively slow kinetics of CO_{2(g)} dissolution and hydrolysis to CO₃²⁻_(aq) rather than the abundance of calcium (Andrews et al., 1997; Rogerson et al., 2017).

Here, we provide the first report of shrubby carbonates forming today within another carbonate forming system driven by mineral hydrolysis; terrestrial surface waters affected by leachate from steel slag stored in landfill, which are forming significant deposits of Anthropocene Limestone. Our case study, Consett in the UK, exhibits pH even higher than in the ophiolite springs (9-13), and supports exceptional rates of calcite precipitation (up to 100 g m⁻² day⁻¹) (Mayes et al., 2008). The diversity and extremely good preservation of the crystals from these carbonates, exceptionally well constrained local hydrochemical environment (Mayes et al., 2008, 2018; Riley and Mayes, 2015) and the possibility to directly observe the co-occurrence of specific growth-forms and microbial components at sites of deposition provides a unique opportunity to test hypotheses concerning the mechanics of exotic calcium carbonate crystal growth patterns in nature. This study is the first report of carbonate

petrography from this “accidental laboratory” and raises the following question: What carbonate fabrics can emerge from extreme alkaline conditions? Although it is rather unlikely Aptian Pre-Salt lakes were forming downstream of dinosaurian steel works, the probability is high that the lakes were the sinks of calcium and alkalinity sourced by low-temperature mineral hydrolysis, making the geochemistry and sedimentology of these systems cognate. We explore what additional constraints we can now place on Pre-Salt lakes on the basis of discovering the same fabrics within Anthropocene carbonate sediments.

2.2 | MATERIAL AND METHODS

2.2.1 | Field-work methods

Samples were taken during May 2013 along pre-established calcite saturation index transects (Mayes et al., 2008, 2018; Riley and Mayes, 2015) within Dene Burn and Howden Burn (Figure 2.1) for further analyses in the laboratory. In these streams, calcite saturation is enhanced by four alkaline discharges within the former Consett Iron and Steelworks. The site was operational from the middle of the nineteenth century until decommissioning in the early 1980s (Figure 2.1). Waste up to 45 m depth, including slag, flue dusts, ashes and construction and demolition rubble were accumulated after working closure in an area of 2.9 km² (Harber and Forth 2001). These materials are now stored in landfill, and the leachates emerging from them are alkaline ($[\text{OH}^-] = 10\text{-}130 \text{ mg.L}^{-1}$; $[\text{CO}_3^{2-}] = 10\text{-}110 \text{ mg.L}^{-1}$; $[\text{HCO}_3^-] = 110 \text{ mg.L}^{-1}$) because of the bulk chemical composition meteoric waters develop after inter-acting with these materials in the subsurface (Mayes et al., 2008, 2018; Riley and Mayes, 2015).

These landfills can be a source of pollution to surface and ground waters (Mayes et al., 2008) (Figure 2.1). The production of iron results in the emission of sulphur dioxide gas, ore and coke dust particles (Harber and Forth, 2001). Other potential contaminants such as arsenic, chromium, boron and copper are present in iron ore (Harber and Forth, 2001). Coke making

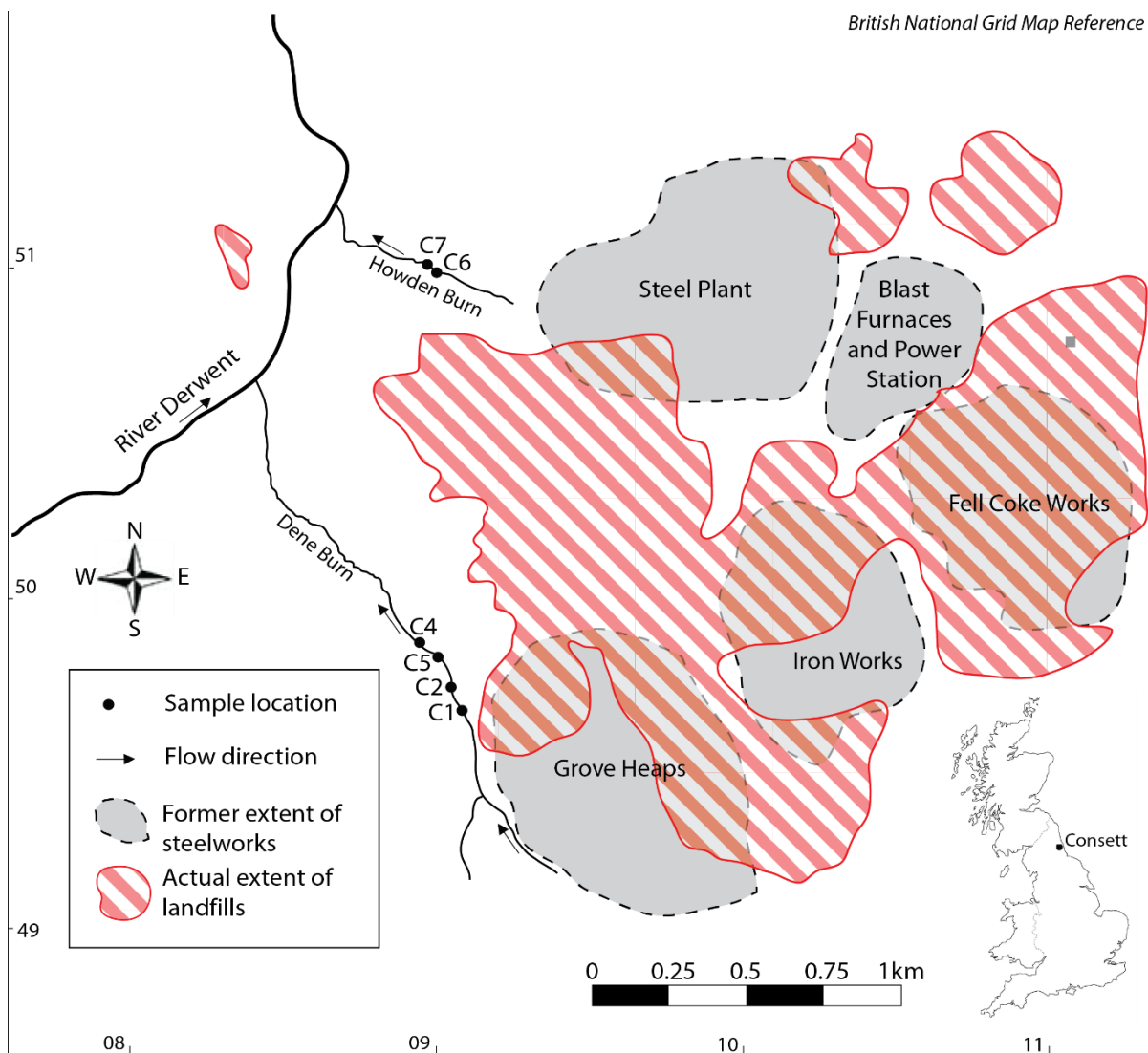


Figure 2.1: Location map of the studied samples HU-MR-/3CON1 (C1), HU-MR-/3CON2 (C2), HU-MR-/3CON4 (C4), HU-MR-/3CON5 (C5), HU-MR-/3CON6 (C6), HU-MR-/3CON7 (C7).

provides inorganic compounds, for example zinc, fluoride, sulphates, phosphates and organic compounds such as fuels and oils (Harber and Forth, 2001). Iron and steel flue dusts contain metals including lead, cadmium, halides, zinc, chromium, arsenic, copper, nickel and alkali metals (Harber and Forth, 2001). Fluoride and zinc are the main pollutants of steel-making wastewaters (Harber and Forth, 2001).

Half of Dene Burn flow comes from a subterranean drainage network beneath the Grove Heaps which consist of blast furnace bottom and steel slag (Mayes et al., 2008), whereas the Howden burn drains an area previously occupied by the working blast furnaces, power station and steel plant (Mayes et al., 2008) (Figure 2.1). The hydrochemical facies of the leachates are

seen to vary notably between the landfills resulting in the streams Howden Burn and Dene Burn (Mayes et al., 2008) (Figure 2.1). Dene Burn leachate source is dominated by Ca, Mg and HCO_3 characteristic of Coal Measures drainage in the region and Ca-OH type leachate from the dissolution of portlandite in the steel slag mounds (Mayes et al., 2008). Dene Burn source leachate also shows elevated Na and Cl concentrations from de-icing salt runoff (Mayes et al., 2008). Howden Burn leachate sources differ considerably from Dene Burn drainage system and are mixed waters rich in K, Na, Ca, and sulphate (Mayes et al., 2008) (Figure 2.1). Sulphate concentrations are exceptionally elevated [$2,500 \text{ mg.L}^{-1}$] typical of a drainage from the former power station and coke works area of the workings (Figure 2.1). Within these locations, coke works spoil, ashes, and iron slags, which have a high sulphur content, were co-deposited with steel and blast furnace slag (Harber and Forth, 2001). The extremely important K content of Howden Burn leachate sources probably derive from highly-soluble potassium oxides associated with flue dusts and ashes deposited with slag (Mayes et al., 2008).

Four samples reported here (HU-MR-/3CON1, HU-MR-/3CON2, HU-MR-/3CON4, HU-MR-/3CON5) are from Dene Burn (Figure 2.1) and further two samples (HU-MR-/3CON6, HU-MR-/3CON7) originate from Howden Burn (Figure 2.1).

During our sampling, on-site measurements of major physico-chemical parameters (pH, electrical conductivity and water temperature) were performed using a Myron L Ultrameter® calibrated on each sample day with pH 4, 7 and 10 buffer solutions and a $1,413 \mu\text{S}$ conductivity standard, to confirm the system had not changed since previous sampling. Sample alkalinity was also obtained in the field using a two-stage titration against $1.6 \text{ N H}_2\text{SO}_4$ with phenolphthalein (to pH 8.3) and bromocresol green-methyl red indicators (to pH 4.6) to facilitate calculation of the constituents of sample alkalinity (i.e. hydroxyl, carbonate and bicarbonate alkalinity using the United States Geological Survey (USGS) Alkalinity calculator

(U.S.G.S. Alkalinity Calculator, 2014)). For each sample, three polypropylene bottles were filled, one of which was acidified with trace analysis grade concentrated nitric acid (for total cation and trace element analysis), one of which was filtered (with 0.45- μm cellulose nitrate filters) prior to acidification (for dissolved cation and trace element analyses) and the other left untreated (for anion analysis).

2.2.2 | Hydrochemistry

Calcite saturation index (CSI), ionic strength and activity of Ca^{2+} and CO_3^{2-} ions were obtained by using the PHREEQC Interactive software. The calcite growth rate (R) was calculated following the formula established by Wolthers et al., 2012:

$$R = I^{-0.004} pH^{-10.71} r_{aq}^{-0.35} (S - 1)^2$$

Where I is the ionic strength, $r_{aq} = \{\text{Ca}^{2+}\} / \{\text{CO}_3^{2-}\}$ activity ratio, S is the saturation ratio ($\Omega^{1/2}$) and R is expressed in m s^{-1} . Growth rate differs from saturation index in that it predicts how quickly crystals will actually assemble, rather than how thermodynamically “favoured” that assembly is. Consequently, this value is intrinsically much more closely linked to crystal assembly controls than saturation is. This parameter was indeed used previously for understanding the precipitation of terrestrial carbonates (Kandianis et al., 2008).

2.2.3 | Mineralogy

X-ray powder diffraction (XRD) data were collected from ground sample (HU-MR-/3CON6) mounted in stainless steel sample holders. Data collection range $5 \leq 2\theta /^\circ \leq 80$ with a step size 0.0262606° and a counting time of 304.725 s per step. Raw data were examined using the program PANalytical HighScore (Plus) which is an implementation of the PDF2 database. This sample was also analysed by Fourier transform infrared (FTIR) spectroscopy

using an Agilent 4300 Handheld Portable FTIR and the peaks were analysed and identified by the MicroLab FTIR Agilent Software.

2.2.4 | Petrography and terminology

Thin-sections (6 x 3 cm) were made for each sample, impregnated with blue-epoxy and were studied with a GXM-MXP Series L3230 optical microscope at the School of Environmental Sciences (University of Hull, England, UK) to determine the mineralogy, texture and the fabric of the studied carbonates. To identify the micro-texture and the micro-scale fabrics, a Scanning Electron Microscope (Zeiss EVO 60) attached to an EDS detector (Oxford Instruments INCA System350 with Silicon Drift Detector) was also used on the same samples for the characterization of their growth and diagenetic processes. The terminology used for petrographic descriptions follow the nomenclature from Flügel (2013), Jones et al., (2005) and Pedley (1992). The definitions of Jones (2017) for single crystal and polycrystal are also employed in this study. Single crystal corresponds to a solid object with only one grain or crystal and hence, no grain boundaries in which an orderly three-dimensional arrangement of the atoms, ions, or molecules is repeated throughout the entire volume. A polycrystal is an aggregate of several crystals or grains where the boundary between the grain is the grain boundary across which the orientation of the crystal changes and the point at which three boundaries meet is called the triple junction.

A key element of the petrographic part of this study is the definition of “shrubby”. We use the definition of Chafetz and Folk (1984): “*three-dimensional, arborescent structures composed of CaCO₃ that expand away from the substrate*”. This differs from dendrites, for which we use the definition of Jones et al., (2005): “*100–200 nm thick calcite fibres that form 3D lattice-like domains and in each dendrite domain, fibres have three structurally equal orientations*”.

2.3 | RESULTS

2.3.1 | Hydrochemistry

Hydrochemistry at each of the sampling sites on the day of sampling is summarised in Table 2.1, and is consistent with previous (Mayes et al., 2008) and more recent (Hobson et al., (2018), Hull et al., (2014), Mayes et al., (2018), and Riley and Mayes (2015)) monitoring of these systems. Some calcium is sourced from background seepage of karst groundwater into both streams, but the majority is derived from steel slag leachate in the form of $\text{Ca}(\text{OH})_2$. Although $\text{Ca}^{2+}(\text{aq})$ is elevated throughout the system, it is dramatically enhanced in the relatively proximal Howden Burn (161-239 mg.L^{-1}) even compared to the more proximal Dene Burn (11 to 14 mg.L^{-1}). CO_2 is supplied to the system from the air, and in-gasses vigorously due to the high pH of the stream waters, and carbonate alkalinity is high where pH is high (7-18 mg.L^{-1} at Dene Burn and 103-109 mg.L^{-1} at Howden Burn). Total alkalinity shows the same enhancement at proximal sites (55-59 mg.L^{-1} in Dene Burn and 264-332 mg.L^{-1} in Howden Burn). Given this water composition, it is unsurprising that calcite saturation index is very high (+0.04 to +2.47), and mineral precipitation is high enough to be lethal to local microbenthos by smothering (Hull et al., 2014).

There is a significant hydrochemical gradient between the Dene Burn and Howden Burn streams (Table 2.1). Parameters such as pH, conductivity, alkalinity, CSI and R ([pH=11.5-11.6]; [conductivity=2160-3190 μS]; [alkalinity=260-330 mg.L^{-1}]; [CSI=2.3-2.5]; [R=4.10-10-5.10-10 m.s^{-1}]) are dramatically more elevated in Howden Burn than in Dene Burn

Table 2.1: Hydrochemistry dataset of the samples including pH, temperature, major ion concentrations, total alkalinity, calcite saturation index, ionic strength, activity and calcite growth rate from the research works of Hobson et al., (2018), Hull et al., (2014), Mayes et al., (2008), Mayes et al., (2018), and Riley and Mayes (2015).

Samples	HU-MR-/3CON1	HU-MR-/3CON2	HU-MR-/3CON4	HU-MR-/3CON5	HU-MR-/3CON6	HU-MR-/3CON7
pH	10.72	10.35	9.06	10.06	11.51	11.64
Temperature (°C)	12.50	12.60	13.40	12.80	12.60	13
Conductivity (µS)	452.40	436.50	438.30	425.70	2165	3193
Major ions (mg.l ⁻¹)						
Ca ²⁺	14.46	11.80	11.18	11.97	161.22	239.82
Mg ²⁺	2.08	0.43	0.75	4.84	0.68	0.03
K ⁺	17.70	21.18	19.19	20.45	183.55	292.46
Na ⁺	24.81	27.53	24.43	27.36	49.88	82.89
OH ⁻	3.30	1.40	0.10	0.70	20.60	28.80
CO ₃ ²⁻	18.30	13.80	1.60	7.30	103.60	139
HCO ₃ ⁻	9.40	16.70	37.20	17.10	8.60	8.50
Total Alkalinity as CaCO ₃ (mg.l ⁻¹)	59	55	66	56	264	332
Calcite Saturation Index	0.96	0.67	0.04	0.25	2.30	2.47
Ionic strength (mol.kgw ⁻¹)	2.01.10 ⁻³	1.73.10 ⁻³	1.48.10 ⁻³	1.95.10 ⁻³	1.11.10 ⁻²	1.65.10 ⁻²
Activity						
Ca ²⁺	2.56.10 ⁻⁴	2.25.10 ⁻⁴	2.36.10 ⁻⁴	2.39.10 ⁻³	1.90.10 ⁻³	2.61.10 ⁻³
CO ₃ ²⁻	1.36.10 ⁻⁴	7.88.10 ⁻⁵	9.68.10 ⁻⁷	2.79.10 ⁻⁵	3.97.10 ⁻⁴	4.25.10 ⁻⁴
Calcite growth rate (m.s ⁻¹)	3.11.10 ⁻¹¹	1.30.10 ⁻¹¹	3.43.10 ⁻¹¹	9.84.10 ⁻¹³	4.39.10 ⁻¹⁰	5.40.10 ⁻¹⁰

([pH=9-10.7]; [conductivity=425-450µS]; [alkalinity=55-66mg.L-1]; [CSI=0.04-1]; [R=9.10-13-3.10-11m.s-1]) (Table 2.1).

Location C4 in Dene Burn describes the lowest CSI (0.04), then followed by location C5 (0.25), C2 (0.67) and C1 respectively (0.96) (Table 2.1). In Howden Burn, the values are almost doubled at the C6 (2.3) and C7 (2.5) sites (Table 2.1) which are correlated with higher concentrations of carbonate (100-140 mg.L-1) and calcium (160-240 mg.L-1) (Table 2.1).

R is the lowest at location C5 (9.10-13m.s-1), then increases quite progressively at locations C2 (1.10-11m.s-1), C1 (3,1.10-11m.s-1), and C4 (3,4.10-11m.s-1) (Table 2.1). In

Howden burn, R faces a major augmentation (C6: R=4.10-10m.s-1; C7: R=5.10-10m.s-1) (Table 2.1).

2.3.2 | Mineralogy

XRD data show that HU-MR-/3CON6 is highly crystalline and corresponds to pure calcite (Figure 2.2). However, FTIR measurements indicate a material which is not calcite via 3 significant peaks ($\lambda=600\text{ cm}^{-1}$; $\lambda=850\text{ cm}^{-1}$; $\lambda=1100\text{ cm}^{-1}$;) (Figure 2.3). These absorptions are consistent with the presence of silica (SiO stretching in silica network defects, symmetric stretching of Si-O-Si bonds and silicon–oxygen covalent bonds vibrations respectively; Al-Oweini and El-Rassy, 2009). The absence of crystalline silica scattering in the XRD patterns indicate that this material must be amorphous, and is present in most samples at >1% concentrations. Consistent with field observations, SEM investigation indicated the presence of a large number of diatom frustules on the sample surface and within the shallow subsurface. The presence of substantial concentrations of these within the limestones explains the persistent presence of amorphous silica in these samples, indicating that the presence of diatomaceous biofilms at these sites during precipitation is persistent.

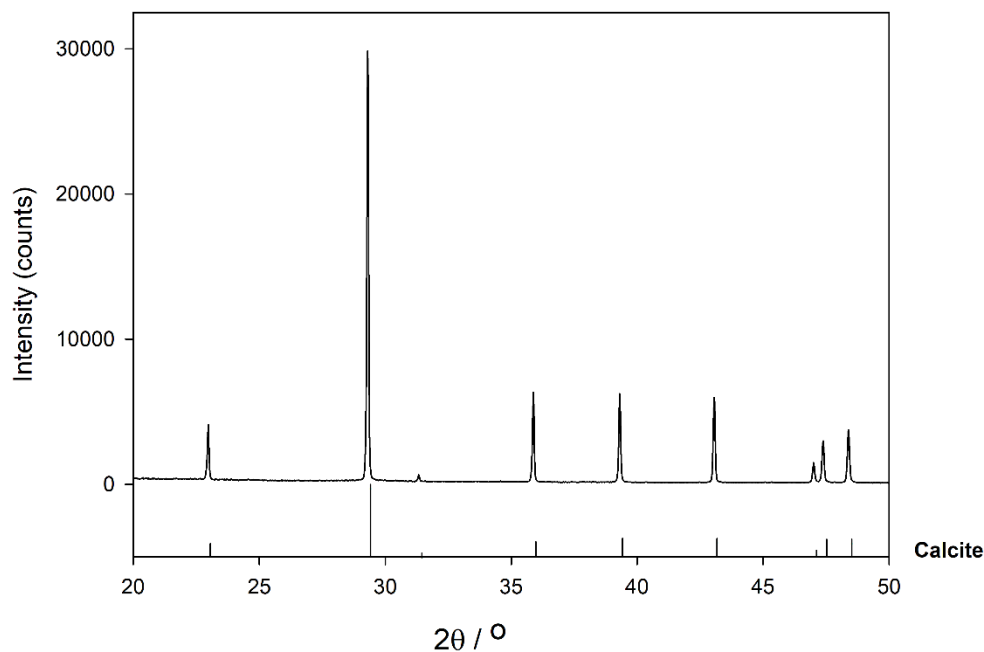


Figure 2.2: XRD pattern of the sample HU-MR-/3CON6.

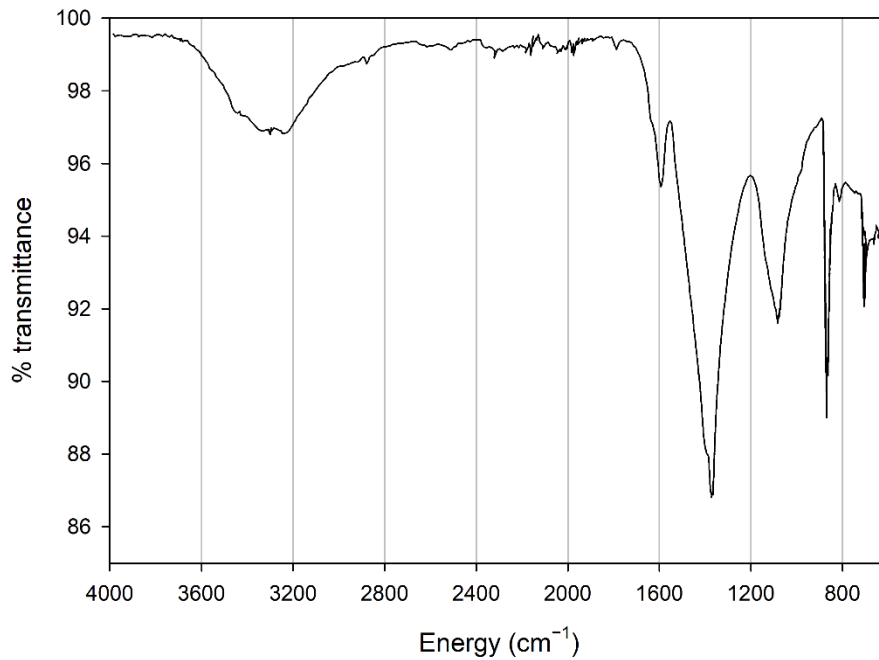


Figure 2.3: FTIR spectra of the sample HU-MR-/3CON6.

2.3.3 | Site and macroscopic descriptions

Precipitation of carbonate material occurs immediately when the water contacts air, and waters seeping from the landfill package precipitate calcite rafts in shallow pools and slow moving water on emergence (Figure 2.4). The meniscus layer mineralisation is a direct consequence of CO₂ in-gassing, but extends for only a few meters downstream. Precipitation is greatest in the environment of waterfalls (Figure 2.4). Fine micrite sediments fill the upper pools within the Howden Burn waterfall-pool system (Figure 2.4). Dark patches on the waterfall surface indicates the presence of substantial diatomaceous biofilms, and a less common yellow discoloration reflects the occurrence of cyanobacteria.

All samples are light brown limestone with clear sedimentary structures corresponding to brown-dark laminations except the HU-MR-/3CON6 sample which is light beige exhibiting a circular ring structure with beige brown laminations (Figure 2.5). In the latter, the beige layers have a fibrous texture (Figure 2.5). This specimen developed as a stalactite growing on the surface of an annual grass and hanging from the roof at the mouth of the drainage tunnel

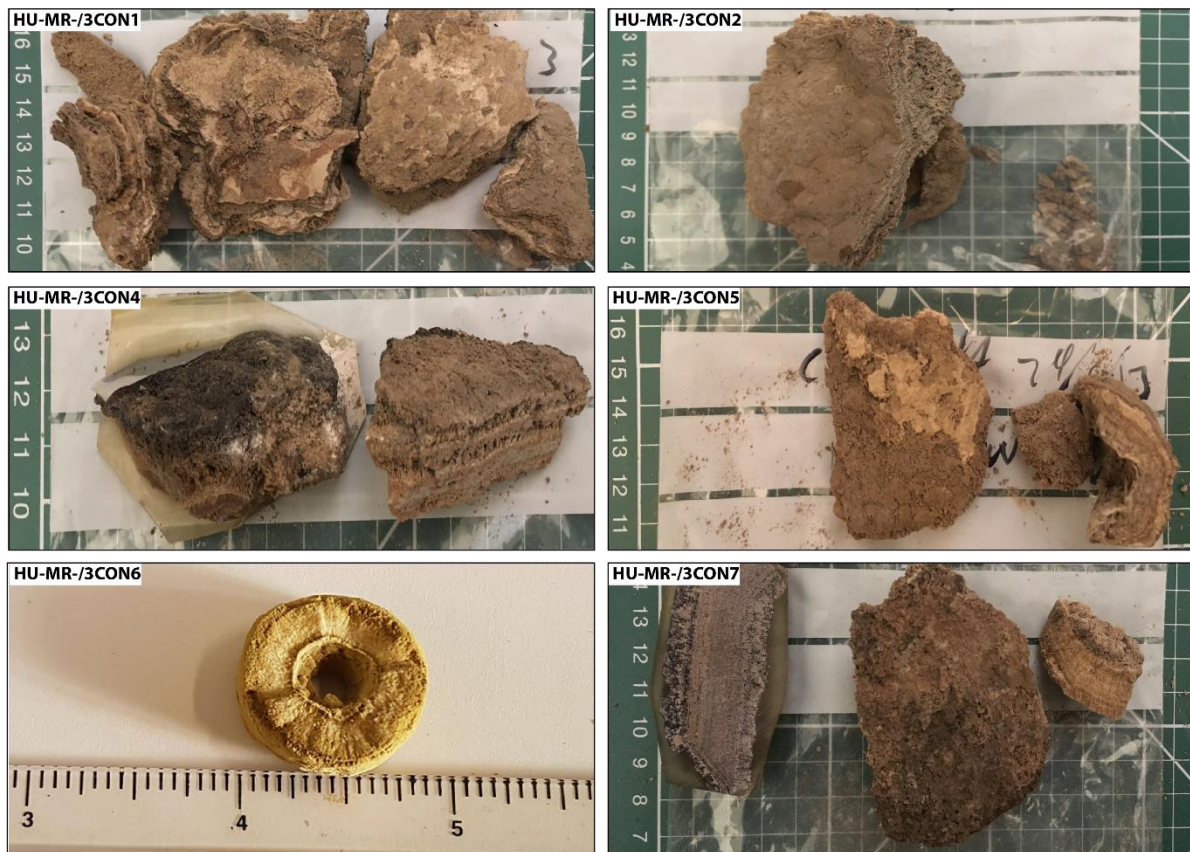


Figure 2.5: Macroscopic images of the Consett freshwater samples HU-MR-/3CON1, HU-MR-/3CON2, HU-MR-/3CON4, HU-MR-/3CON5, HU-MR-/3CON6, HU-MR-/3CON7.

emerging near the top of Howden Burn. The ~8mm of growth of this specimen have therefore occurred within a few months before sampling, and the rate of accumulation at this site is likely $\gg 1\text{cm yr}^{-1}$.

2.3.4 | Facies descriptions

Eight types of microfacies have been identified on the basis of fabric, mineralogy and texture (Figure 2.6). We present a small number of replicates (6), which limits our ability to draw widely applicable conclusions about the distribution of specific features within the sediment. However, they present a wide range of microfabrics, some of which are rarely observed growing in natural environments today. We therefore limit our analysis to identification of these rare features, and to providing a framework for future investigations.

Facies 1: Clotted micrite

Clotted micrite is made up of a brown micritic matrix composed of fine homogeneous rounded micrite peloids (Figs. 2.7A-C). Individual micrite grains reach up to 7 μm in diameter and show (Figure 2.7-D) prismatic tetrahedron-like (70 μm in diameter), and double-terminating calcite crystal morphologies with abundant twinned faces (100 μm in diameter) (Figure 2.7-D). Diatoms are common components within this facies (Figs. 2.7D-7L) (20 μm in diameter) showing elongated and oval external morphologies (*Gromphomena parvulum* (Figure 2.7-E), *Gyrosigma acuminatum* (Figure 2.7-G), *Navicula lanceolata* (Figure 2.7-H), *Navicula gregaria* (Figure 2.7-I), *Navicula gregaria* (Figure 2.7-J), *Nitzschia amphibia* (Figure 2.7-K), *Planothidium lanceolatum* (Figure 2.7-K), *Sellaphora nigri* (Figure 2.7-L)). Micrite shows a clotted distribution (Figs. 2.7A, 2.7B, 2.7C) hosting intercrystalline porosity with cavities between 10-500 μm in diameter) (Figs. 2.7A, 2.7B, 2.7C).

Pedley (1992) described a similar microfacies in freshwater “phytoherm” reef environments where clotted micrite was characterized by anhedral crystals approximately a few micrometres across on average.

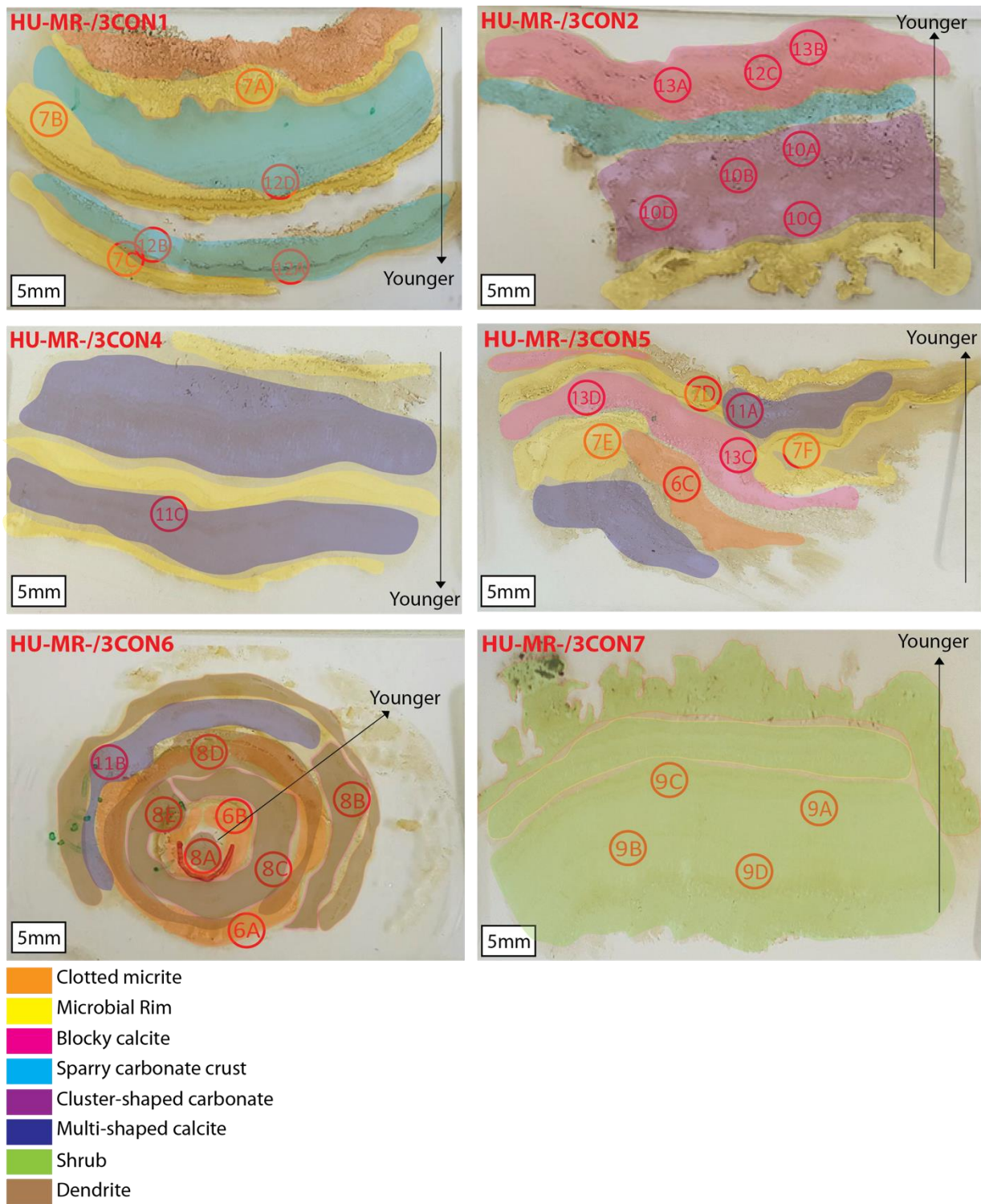


Figure 2.6: Thin sections from the Consett freshwater samples HU-MR-/3CON1, HU-MR-/3CON2, HU-MR-/3CON4, HU-MR-/3CON5, HU-MR-/3CON6, HU-MR-/3CON7 with the locations of the optical microscope images where the locations are respectively designed by the number of the figure from this manuscript followed by the letter corresponding to the subsection in the figure.

Facies 2: Microbial Rim

This facies corresponds to thin black layers (180-250 μm thick) of dense micrite characterized by the presence of a diversity of microbial remains such as biodegraded biofilm or leaf material (Figures 2.8A, 2.8B, 2.8C, 2.8D, 2.8E, 2.8F).

Facies 3: Dendrite

Dendrites are constituted by light grey calcite crystals growing radially forming flower-like geometries (Figures 2.9A, 2.9B, 2.9C, 2.9D, 2.9E) and are made up of radially elongated, polycrystalline calcite giving rise to V-shaped fans that grow upon a surface front. Fans average 580 microns in length and 120 microns in width. Some fans are tightly laterally packed which constraints the growth of the fans themselves. When more space is available for crystals to grow, fans develop preferably in one single direction producing feather-like crystal morphologies (Figs. 2.9B-2.9E).

Similar fabrics were described by Jones et al. (2005) in calcite travertine environments. They defined them as three-dimensional bushes, up to 1 cm high and 1 cm in diameter, with branches that radiate outward and upward from the main branch. Given the relatively loose crystal network, dendrites have high internal porosity (see Jones et al., 2005).

Facies 4: Calcite Shrub

Calcite shrubs are made up of light grey-green botryoidal-like crystal fans 1 to 1.5 mm in height and stacked each other as inverted cones growing on top of discontinuous horizons (Figures 2.10A, 2.10B, 2.10C, 2.10D). Botryoids are internally composed of very coarse sub to euhedral, elongated rhombohedral crystals forming bladed aggregates (60 μm in length). (Figures 2.10A, 2.10B, 2.10C, 2.10D) with their c-axis radiating from a previous substrate (Figures 2.10A, 2.10B, 2.10C, 2.10D). In places, the shrubs are surrounded by diatoms (Figures 2.10-E; 2.10-F; 2.10-G; 2.10-H; 2.10-I; 2.10-J; 2.10-K; 2.10-L; 2.10-M) and bacterial filaments

where bacterial filaments (25 to 60 μm in diameter) are quite rectilinear forming circular tubes (Figure 2.10-E). Bladed crystal aggregates tend to develop a high intercrystalline microporosity (Figure 2.10-E). The SEM confirms the bladed aggregation/ imbrication of rhombohedral polycrystals (Figure 2.10-E).

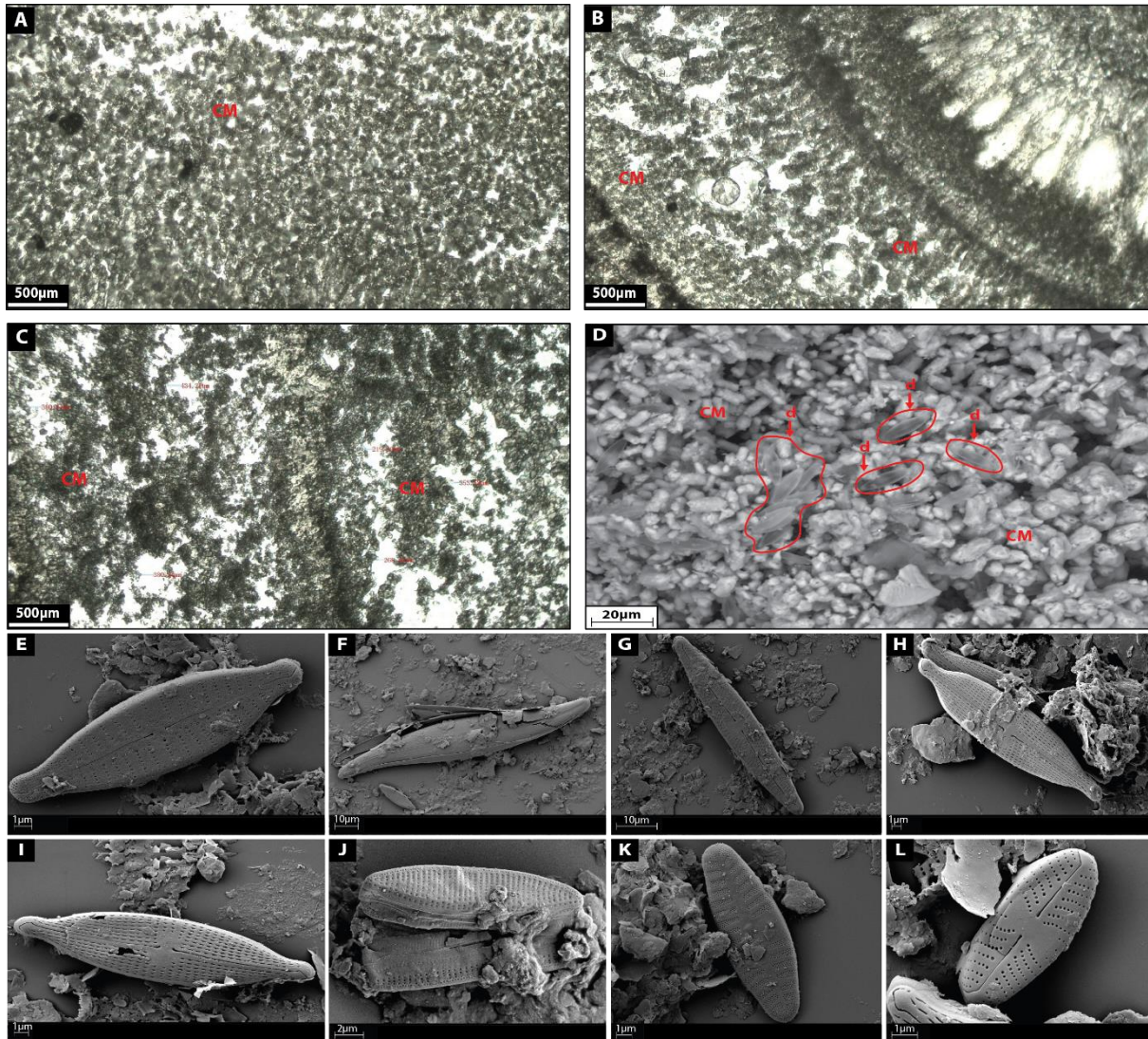


Figure 2.7: (A), (B), (C) depict the microfacies images by petrographic microscope of clotted micrite (CM) facies. (D) shows a SEM image of clotted micrite facies with diatoms (d). (E) shows a SEM image of the diatom *Gromphomena parvulum*. (F) shows a SEM image of the diatom *Gyrosigma acuminatum*. (G) shows a SEM image of the diatom *Navicula lanceolate*. (H) shows a SEM image of the diatom *Navicula gregaria*. (I) shows a SEM image of the diatom *Navicula gregaria*. (J) shows a SEM image of the diatom *Nitzschia amphibian*. (K) shows a SEM image of the diatom *Planothidium lanceolatum*. (L) shows a SEM image of the diatom *Sellaphora nigri*.

Saller et al. (2016) described Pre-Salt calcite shrubs as radiating bundles of fibrous-to-prismatic crystals. Within a shrub branch, upward oriented bundles of radiating crystals have clear growth interference; however, the fibrous, upward-oriented bundles abruptly finish at the

edge of a branch, leaving open vugs between shrubby growths (Saller et al., 2016). The shrubs seem to have grown upward and create positive relief (Saller et al., 2016).

Facies 5: Cluster-shaped carbonate

Cluster-shaped carbonates are here referred as translucent white calcite crystals ranging from 20 to 500 μm in height (Figures 2.11A, 2.11B, 2.11C, 2.11D). They form a matrix made up of coarse euhedral tetrahedron-like and double terminating calcite crystals with many cluster faces, which are surrounded by a black organic substance of biograded biofilm. Cluster-shaped carbonates display an extremely high intercrystalline porosity.

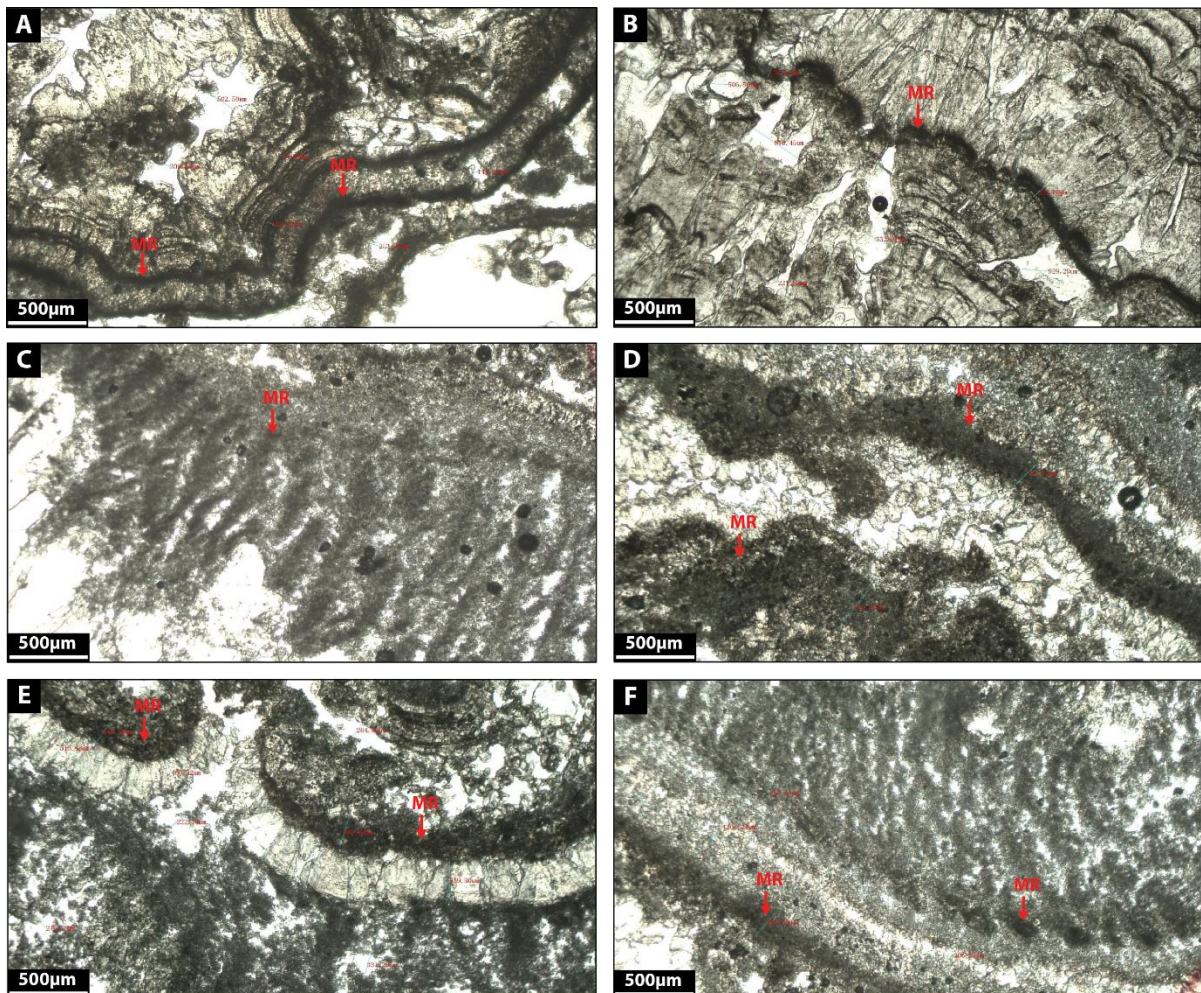


Figure 2.8: (A), (B), (C), (D), (E) and (F) depict the microfacies images by petrographic microscope of microbial rim (MR) facies.

Facies 6: Multi-shaped calcite

Multi-shaped calcite corresponds to translucent white delicate calcite crystals (100-550 μm in diameter) displaying rounded external morphologies and a grain-to-grain contact arrangement (Figures 2.12A, 2.12B, 2.12C). Calcite crystals also exhibit trigonal, arrow and heart-shaped external morphologies (Figures 2.12A, 2.12B, 2.12C) and these crystals seem to correspond to coarse-grained carbonate slightly reworked and stacked together (Figures 2.12A, 2.12B, 2.12C). A black organic substance surrounds some crystals, which appear to be leaf material (Figs. 2.12A, 2.12B, 2.12C) and there is a curved surface below grains (Figures 2.12A, 2.12B, 2.12C) as well as space between crystals displaying porosity (Figures 2.12A, 2.12B, 2.12C).

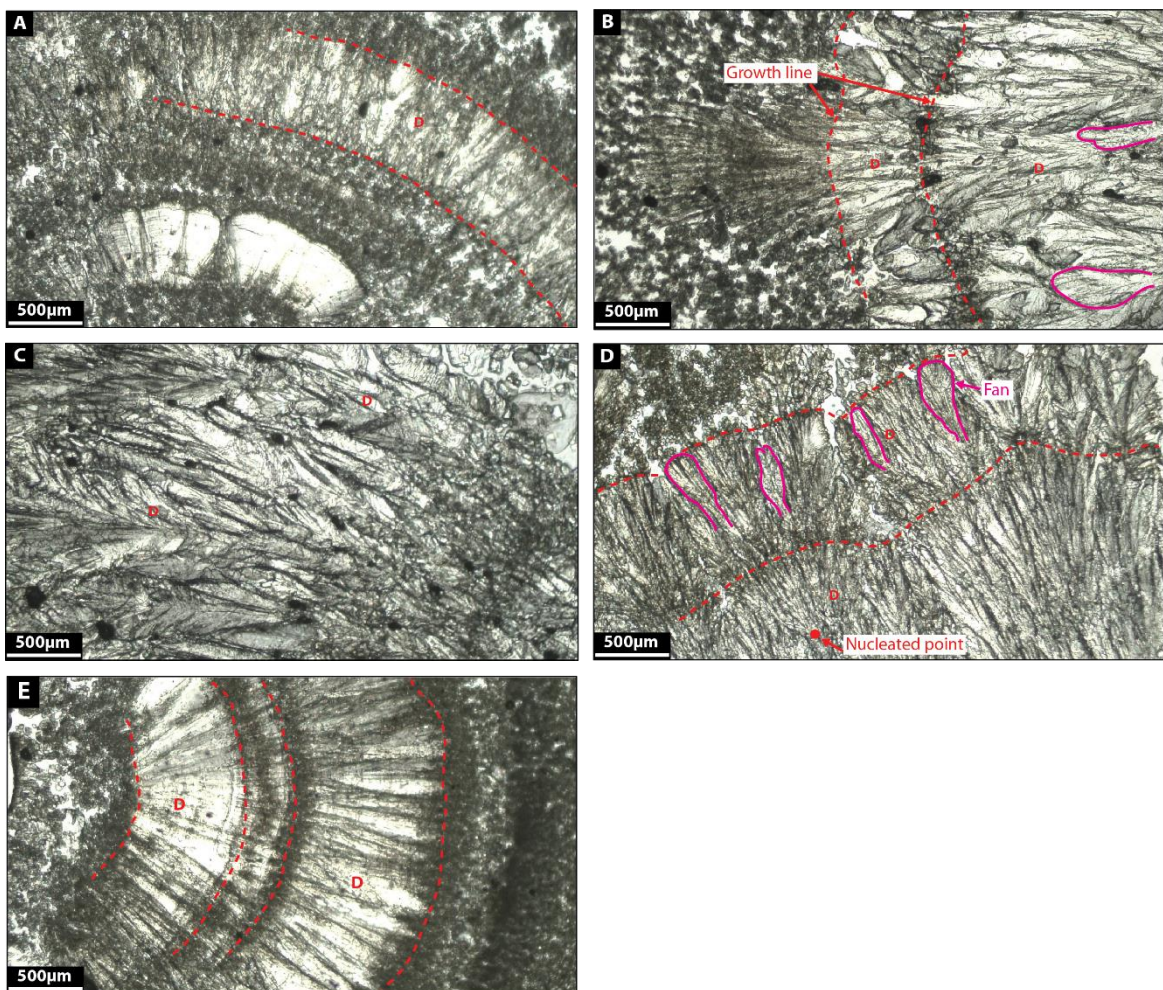


Figure 2.9: (A), (B), (C), (D), and (E) depict the microfacies images by petrographic microscope of dendrite facies (D).

Facies 7: Sparry carbonate crust

Sparry carbonate crust comprises thick sparite crusts (500-2500 mm thick) made up of milky white to grey calcite (Figures 2.13A, 2.13B, 2.13C, 2.13D). The crystals show a very coarse, subhedral morphology as they partly developed crystal faces (Figs. 2.13A, 2.13B, 2.13C, 2.13D). Some crystals are covered by black organic remains corresponding certainly to degraded biofilm (Figures 2.13B, 2.13C). Given the nature of these crystals, they develop very low intercrystalline porosity. Some crusts display several growth zones (Figure 2.13A) and exhibit botryoidal shapes (Figures 2.13A, 2.13B, 2.13C).

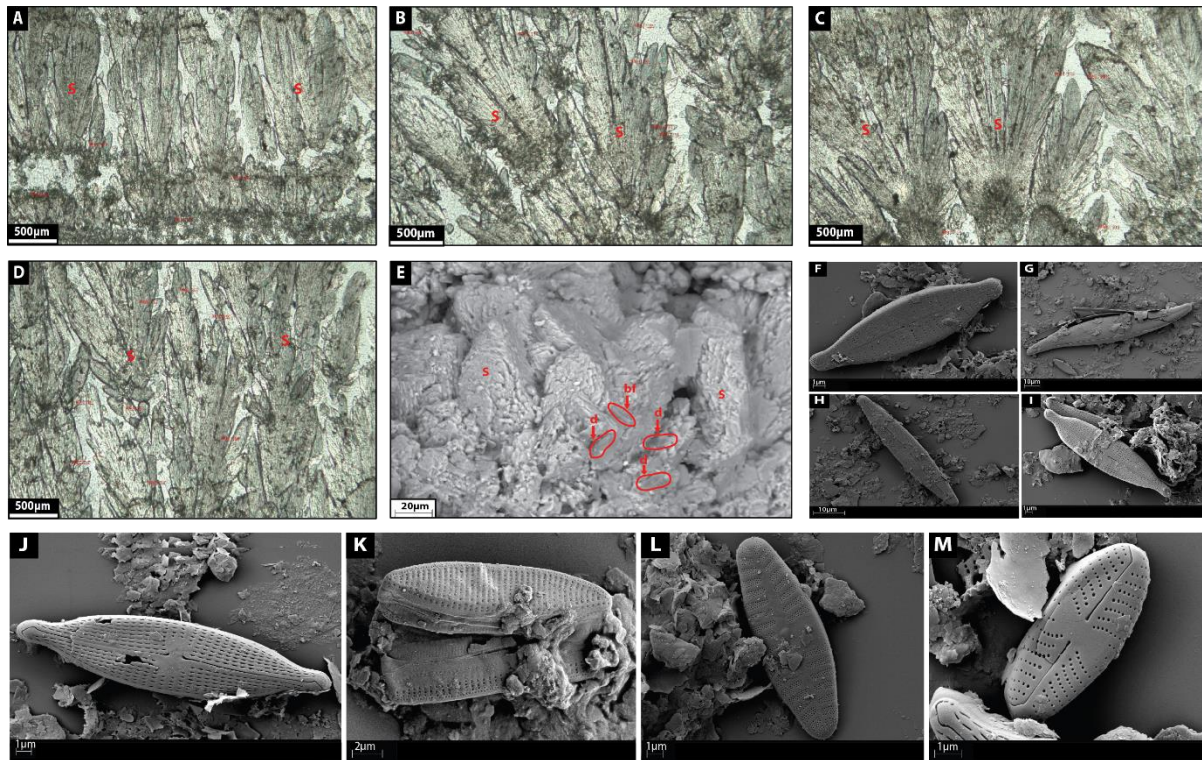


Figure 2.10: (A), (B), (C) and (D) depict the microfacies images by petrographic microscope of shrub (S) facies. (E) shows a SEM image of shrub facies with diatoms (d) and bacterial filament (bf). (F) shows a SEM image of the diatom *Gromphomena parvulum*. (G) shows a SEM image of the diatom *Gyrosigma acuminatum*. (H) shows a SEM image of the diatom *Navicula lanceolata*. (I) shows a SEM image of the diatom *Navicula gregaria*. (J) shows a SEM image of the diatom *Navicula gregaria*. (K) shows a SEM image of the diatom *Nitzschia amphibian*. (L) shows a SEM image of the diatom *Planothidium lanceolatum*. (M) shows a SEM image of the diatom *Sellaphora nigri*.

Facies 8: Blocky calcite

Blocky calcite corresponds to single, very large crystals of calcite (500-1500 μm in diameter), where the crystals are milky white to translucent grey (Figures 2.14A, 2.14B, 2.14C, 2.14D). Coarse-grained euhedral crystals (Figures 2.14A- D) compose the calcite and the crystals show distinct crystal boundaries (Figures 2.14A, 2.14B, 2.14C, 2.14D).

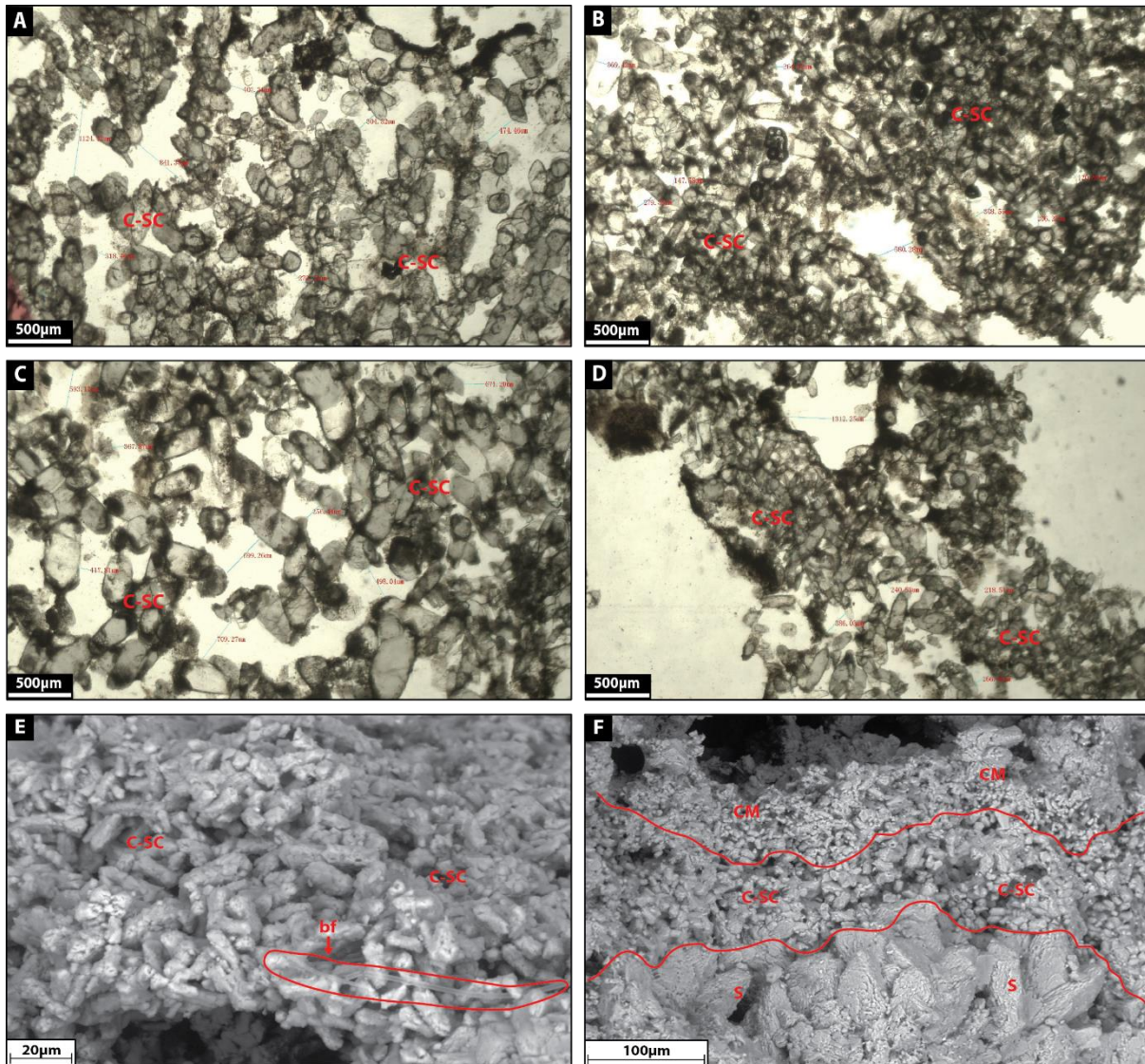


Figure 2.11: (A), (B), (C) and (D) show the microfacies images by petrographic microscope of cluster-shaped carbonate (C-SC) facies. (E) shows a SEM image of cluster-shaped carbonate facies with bacterial filament (bf). (F) shows a SEM image of the transition between shrub, cluster-shaped carbonate and clotted micrite.

2.3.5 | Distribution of microfacies

Shrubs occur exclusively at the most proximal location, C7, and is the only microfacies identified at that site (Figure 2.15A). Dendrite is the most common microfacies represented at location C6, but clotted micrite, sparry carbonate crust and cluster-shaped carbonate are present as well (Figure 2.15A). Microbial rim and sparry carbonate crust are the only microfacies described within location C1 (Figure 2.15A). Cluster-shaped carbonate is abundant at location C2 surrounded by some blocky calcite and sparry-carbonate crust (Figure 2.15A). Location C5 displays the most diverse microfacies, with clotted micrite, microbial rim, blocky calcite and multi-shaped calcite all contributing equal proportions of the sediment (Figure 2.15A). Multi-shaped calcite is a unique microfacies present only at location C4, and even there it is not abundant (Figure 2.15A).

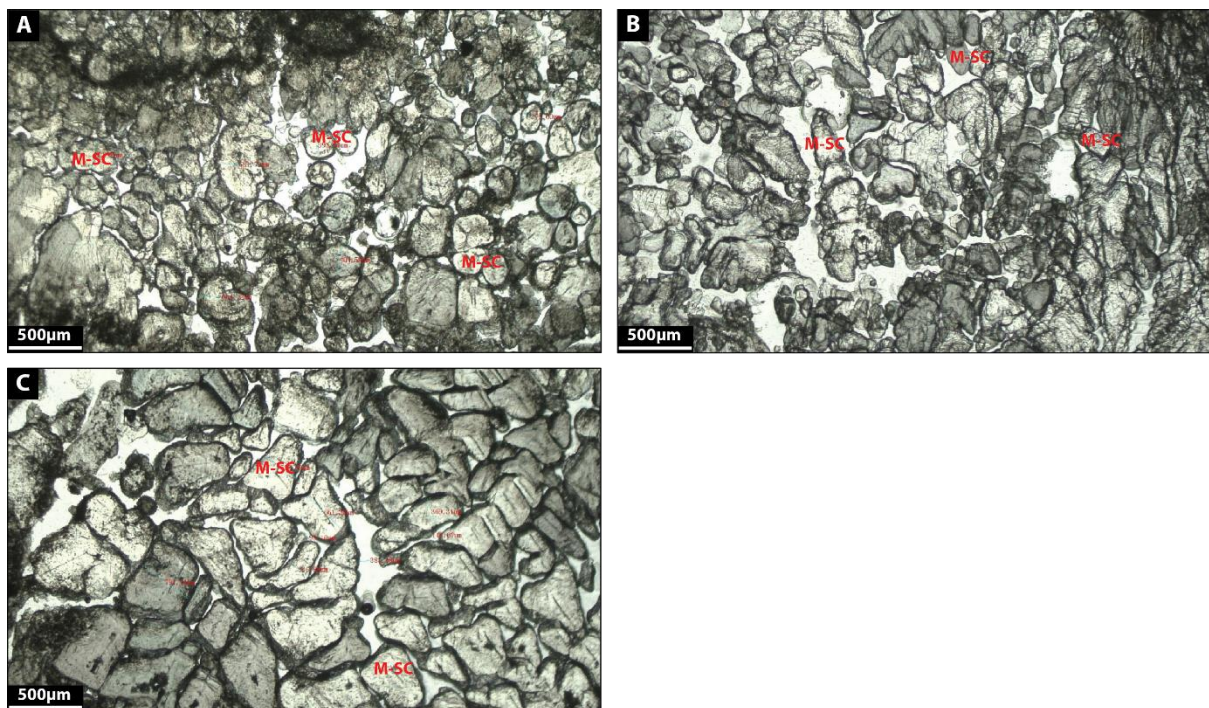


Figure 2.12: (A), (B) and (C) show the microfacies images by petrographic microscope of multi-shaped calcite (M-SC) facies.

2.4 | DISCUSSION

2.4.1 | Hydrochemistry versus distribution of microfacies

In proximal Howden Burn, locations C6 and C7 show deposition principally of shrubby calcite (C7), and dendrite (C6) ($\text{pH}=11.5$; $\text{CSI}=2.5$; $R=5.10^{-10}\text{m.s}^{-1}$) (Figure 2.15A). These sites are characterized by very high pH (11.5-11.6), calcium concentration (161-240 mg.L^{-1}) and carbonate concentration (104-140 mg.L^{-1}) (Table 2.1). Consequently, calcite saturation ($\text{CSI}=2.3$ -2.5) and calcite growth rate ($R=4.4.10^{-10}$ - $5.4.10^{-10}\text{m.s}^{-1}$) are also very elevated (Figure 2.15A). As the solution moves away from the most proximal sites, calcium and alkalinity are consumed steadily reducing CSI. However, this near-linear change in saturation does not well reflect the disappearance of shrub and dendrite microfacies, which do not occur beyond C6. This better reflects R, which is 100-1000 times lower in more distal Dene Burn sites than in Howden Burn (10^{-12} - $3.10^{-13}\text{m.s}^{-1}$) (Figure 2.15A). In locations C1 and C2, despite medium CSI (1-1.3) and high pH (10.3-10.7), R is low (1.10^{-11} - $3.10^{-11}\text{m.s}^{-1}$) (Figure 2.15A), and this relatively weak kinetic forcing corresponds to formation of microbial rim (C1), sparry-carbonate crust (C1) and cluster shaped carbonate (C2). The most distal sites exhibiting significant carbonate deposits (C4 and C5) exhibit the lowest CSI (0.04-0.25), R (3.10^{-11} - 1.10^{-12}) and pH (9-10.3) and are dominated by multi-shaped calcite (C4-C5), clotted micrite (C5), and blocky calcite (C5).

2.4.2 | Kinetic control on shrubby and dendritic carbonate

The juxtaposition of the hydrochemistry and distribution of microfacies shows that shrubby and dendritic crystals develop with high kinetic forcing, blocky calcite at low kinetic forcing and classic “microbialite” rim and clotted micrite forming at moderate-low forcing. We therefore conclude that formation of these microfacies in this system exhibits a kinetic rather than thermodynamic control. This is highly comparable with findings from materials chemistry

summarised by Meldrum and Cölfen (2008). Kinetic control of crystallization arises from enhanced nucleation onto kinetically favoured crystal faces and step-edges Ostwald's step rule. Skeletal biomineral morphologies will self-assemble in such a setting due to Berg effect, where supersaturation over a flat face is low at the center and high near the edges, causing first "hopper like" then true single-crystalline ordered dendrites, disordered polycrystalline side branches, and finally disordered polycrystalline dendrites and dense branching morphologies as the kinetic forcing becomes more extreme. Sunagawa (1999) shows that it is a general rule that growth rate anisotropy will determine the forms of polyhedral crystal, as seen in the development of snow crystals (Libbrecht, 2012), where solid hexagonal plates crystallize at low supersaturation, whereas increasing the supersaturation leads to dendritic growth and flower-like morphologies with six petals. Beck and Andreassen (2012) report similar kinetic control on vaterite formation, where low levels of supersaturation lead to the growth of hexagonal, plate-like crystals while increasing kinetic forcing force causes a shift of the particle growth mechanisms towards dendritic growth.

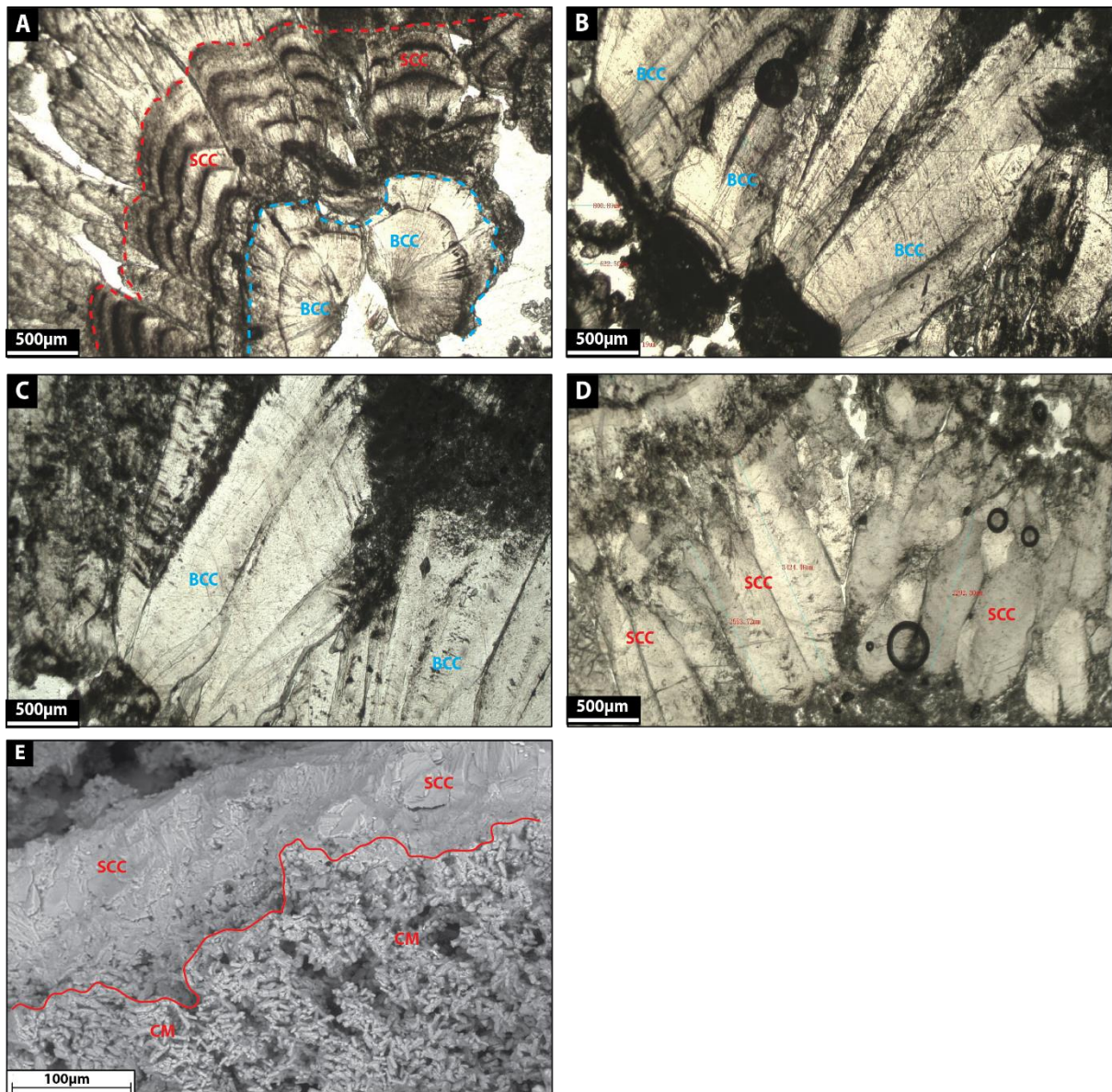


Figure 2.13: (A), (B), (C) and (D): Microfacies images by petrographic microscope of sparry carbonate crust (SCC) and bothryoidal carbonate crust facies (BCC). (E) shows a SEM image of the transition between clotted micrite and sparry carbonate crust facies.

2.4.3 | Formation processes of microfacies

Where kinetic forcing is reduced (lower R), diffusive controls on crystal formation reassert themselves and non-dendritic fabrics occur (blocky calcite which displays a polyhedral shape in a single crystal). This is as would be expected from fundamental crystal assembly controls at relatively low rates of supersaturations (Meldrum and Cölfen, 2008). Curiously, we find the minimum of biofilm and microbe presence within these fabrics, indicating a process of formation dominated by inorganic mineralization, as defined by Dupraz et al. (2009). Classic

“microbialite” fabrics (microbial rim and clotted micrite) occur within the middle and low saturation regime. Diatom and cyanobacterial biofilms are preserved directly as thin brown bands recognised on the thin-section material (Figure 2.6), and indirectly within the biologically-influenced microfacies where the carbonate precipitation is indirectly modified by a precursor organomineral (Dupraz et al., 2009). It is also important to note that the diatoms reported generally develop in environmental conditions of freshwaters and represent biotopes of low to (at most) moderate electrolyte content (Sterrenburg, 1995; Van de Vijver et al., 2013). They were found living epilithically in several smaller rivers and brooks with an almost slightly alkaline pH (7.5) and low specific conductance levels (75–100 $\mu\text{S}\cdot\text{cm}^{-1}$) (Sterrenburg, 1995; Van de Vijver et al., 2013). In our study, it is therefore surprising to find this abundance of diatoms in such very salty and alkaline conditions.

Cluster-shaped carbonate was developed among bacterial filaments with an organic film forming sticky thin black layer around crystals (Figure 2.11A-D) which could correspond to Extracellular Polymeric Substances (EPS). These organic components associated with the micritic matrix of this facies along with its chemical characteristics (high alkalinity, medium pH and SI) suggest that they come from biologically-influenced mineralization as well. The distribution of bio-influenced facies is not ordered with respect to the single-crystal inorganic precipitates, but rather both types of precipitation occur apparently randomly.

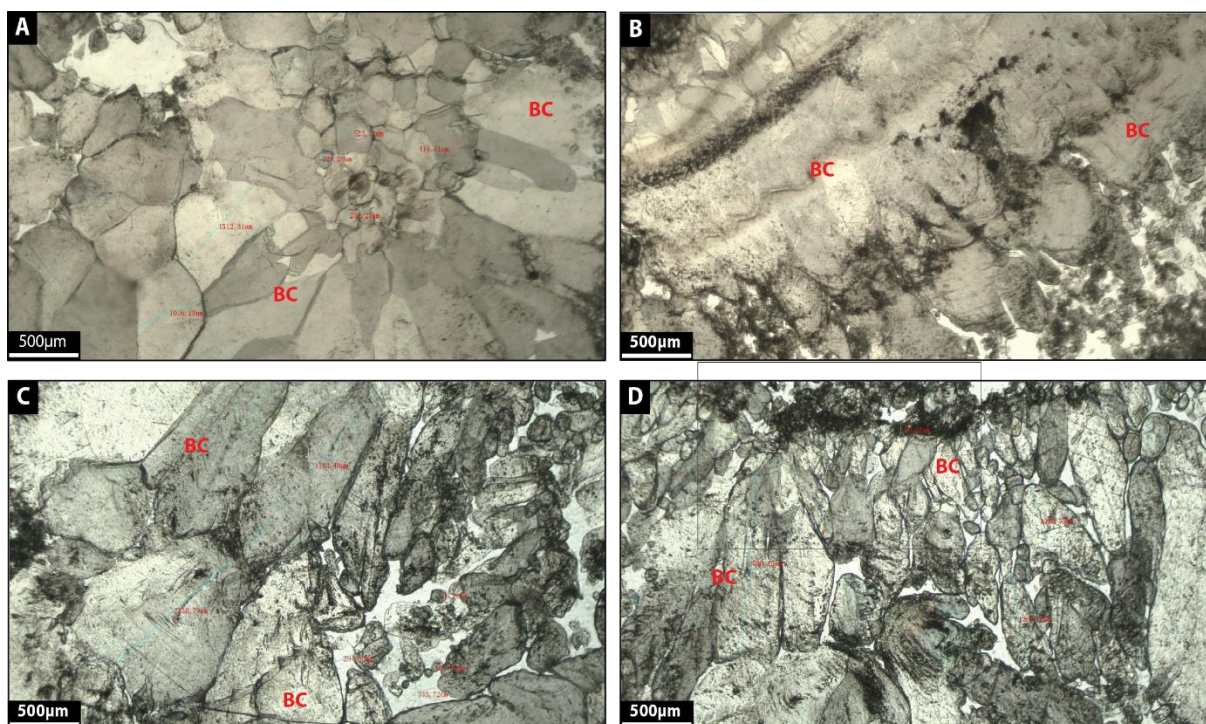


Figure 2.14: (A), (B), (C) and (D): Microfacies images by petrographic microscope of blocky calcite facies (BC).

Kinetic forcing of dendrite growth can be enhanced by “poisoning” of some step-edges by additive molecules, particularly polymerised, polar organic molecules (Meldrum and Cölfen, 2008). We noted that biofilms were common even in proximal sites within Howden and Dene Burns during sampling, and both diatom frustules and organic carbon is pervasive through the majority of samples. Consequently, it is possible that organic additives are promoting the formation of extreme skeletal crystals in these systems at relatively low R. Whether skeletal crystals would form spontaneously in the absence of biofilm EPS was not possible to test during this study. However, we were able to demonstrate that within shrubby fabrics, no indication of microbial biofilm presence (i.e. classic microbialite features) could be identified, even when diatoms were touching the carbonate: it seems that if kinetic forcing is permitted by local hydrochemistry, all the carbonate product generated at that site will comprise skeletal composite crystals. Consequently, the absence of microbial textures does not appear to be a criterion for assuming no microbial influence on precipitation.

2.4.4 | Co-existence of fabrics within a same site

The co-existence of different fabrics at a same location (e.g. at C1, C2, C5 and C6 sites) indicates that the rather “static” analysis we present above is oversimplified, and that some spatial or temporal structure in the environment is present to cause physical association of the mineral products. This will be at least in part due to a variable chemistry caused by weather fluctuations (rainy, dry, low or high temperatures according to season) (Riley and Mayes, 2015) (Figure 2.15A). Mayes et al. (2008) showed that the hydrochemical system in Howden Burn and Dene Burn is relatively stable with a very elevated pH (pH=11-12) over the 36-year data series but when heavy rainfall occurs, the river does adapt very rapidly. Spate flow changes the hydraulics of the flow altering gas exchange, (Gomes et al., 2017), reduces carbonate and calcium concentration and pH, and therefore suppressed CSI and R (Riley and Mayes, 2015). As reduced R will suppress kinetically-forced fabrics and promote diffusion-forced crystal formation, this process alone will explain co-occurrence at any given site. For example, in the case of C6, short phases of reduced R and CSI may produce brief hiatuses in growth, forcing creation of concentric rings of dendritic fabrics (Figure 2.6). In addition to this abiotic forcing, it is likely that the distribution of biofilms is not spatially smooth, and patchy bio-influence will result in patchy occurrence of bio-influenced microfabrics. The apparently random co-occurrence of diffusion-forced and bio-influenced fabrics in Dene Burn likely reflects this spatial complexity within the sites microbiology.

2.4.5 | Depositional model

Although we acknowledge the relatively small sample size in this case and the need for further investigation of such systems, given the hydrogeochemical and facies variation at the site a depositional model can be forwarded. This model is based on the key interpretation that lateral distribution of microfacies at the site relates to geochemical forcing (Figures 2.15A and

2.15B). Shrub and dendrite microfacies disappear with distance from the source, where CSI and R are excessively high (Figure 2.15B). In the most distal part of the river, microbial rim are quite continuous, occurring in most sites (Figure 2.15B). Cluster-shaped carbonate is the only facies represented upstream (C2) and sparry carbonate crust co-appear in C1 and C2 locations (Figure 2.15B). Blocky calcite and multi-shaped calcite are present in the downstream part of Dene Burn (C4 and C5) (Figure 2.15B). Clotted micrite is exclusively represented in both proximal and distal zones of the river (C1, C5, C6) (Figure 2.15B).

2.4.6 | Sedimentology in the Anthropocene

Although this is the first systematic analysis of the sedimentology of an Anthropocene limestone, the Consett site is not unique, and similar hyperalkaline sites occur in most post-industrial landscapes. These extremely alkaline environments have been found for instance in man-made river bed after repository building measures in Austria (Boch et al., 2015), slag-fill aquifers in the Lake Calumet region of Chicago (Roadcap et al., 2005, 2006), and Coatham Marsh steel slag leachate discharges in UK (Mayes et al., 2008). Examples such as non-ferrous metal industry waste disposal sites in Slovakia (Pristas et al., 2015), and technosol contaminated by former mining activity in Slovak Republic (Šimonovičová et al., 2017) can be cited as well. Understanding their operation in terms of mass deposition is a key part of fully constraining their behaviour, and thus being able to manage them successfully. In particular, our finding that precipitation in proximal parts of the system are not diffusion-controlled is likely to result in deviation of element distribution coefficients from empirical values, and higher incorporation of trace metals and metalloids is anticipated in these sites. We recommend that further sedimentological investigation of these “accidental laboratories” is likely to yield further insights, of use both to geoscientists and environmental scientists working with very different scientific motivations.

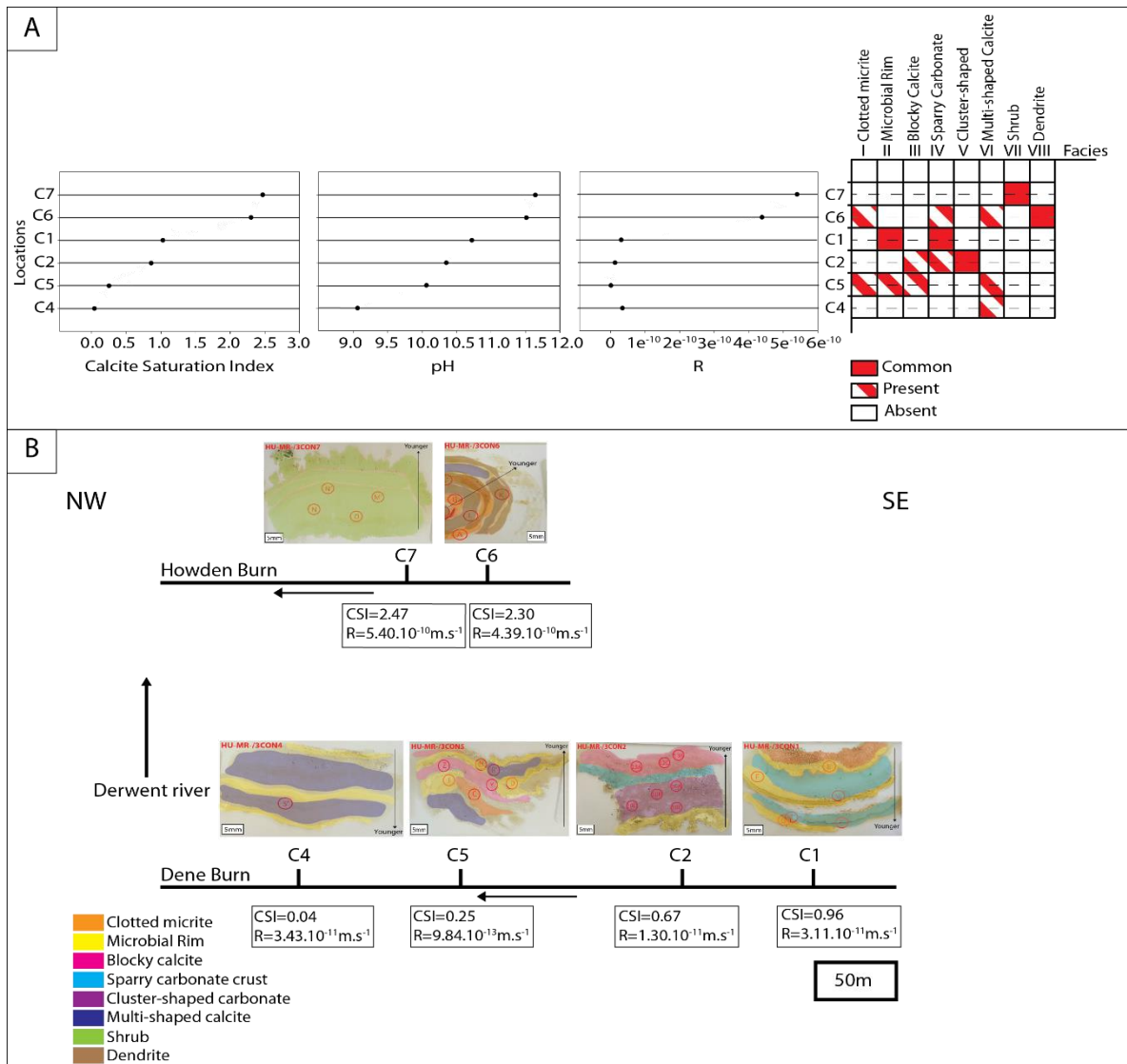


Figure 2.15: (A) depicts the sample locations versus Calcite Saturation Index, pH, calcite growth rate (R) and distribution of microfacies. (B) shows the depositional model summarizing the lateral changes of the microfacies.

2.4.7 | Comparing natural, alkaline saline lakes with anthropogenic hyperalkaline occurrences

A striking feature of recent saline alkaline lakes in rift tectonic settings (such as the East African Rift System, EARS) is the strong dissimilarity between alkaline metal concentration (calcium and magnesium) and the alkalinity of the waters (measured as carbonate and bicarbonate contents). During the evolution of these saline lakes, they tend to become Ca and Mg-poor systems due to the combined effects of the evaporative concentration and the relative

mineral solubility which triggers the sequential precipitation of minerals from carbonates to silicates to complex salts (Eugster and Hardie, 1978; Deocampo and Renault, 2016).

Many recent EARS lakes (e.g., Lake Magadi or Lake Bogoria; Jones et al., 1977; Renault et al., 2002) have been considered tectonically and hydrologically similar to the ancient Pre-Salt lakes. However, they do not show clear evidence of substantial accumulation of spherulitic carbonate sediments, questioning whether EARS usual Ca and Mg-poor chemistries are encouraging spherulitic carbonate precipitation (Rogerson et al., 2017).

Furthermore, the record of anthropogenically-mediated carbonate deposits such as those described here or in an asbestos open pit pond in Yukon, Canada (Power et al., 2011) is increasingly demonstrating that spherulitic carbonate growth can easily arise from waters anomalously enriched in calcium and magnesium, apart from elevated alkalinities and pH. In these sites, the alkalinity engine is thought to be related to the progressive atmospheric CO₂ ingassing (Rogerson et al., 2017) or the dissolution of the carbonate bedrock (Power et al., 2011) rather than increasing evaporation as occurs in alkaline lakes (Eugster and Hardie, 1978).

In addition, both natural alkaline, saline lakes and industrial hyperalkaline ponds are known to precipitate primary aragonite and/or low-Mg calcite minerals. This is mainly driven by the Mg/Ca ratios and the supersaturation state of the precipitating waters (De Choudens-Sánchez and González, 2009; Wang et al., 2012). An interesting observation from the Pre-Salt Aptian carbonate record is the repeated occurrence of Mg-rich and Sr-rich calcites (Saller et al., 2016) which are thought to be primary fabrics due to the lack of an original aragonite precursor. Also, shrubs described in the Kwanza upper case B were interpreted as originally precipitated as Mg-rich calcites and lately transformed to low-Mg calcites (Saller et al., 2016). These features strongly suggest that the Pre-Salt lake waters were likely much richer in Mg and sustained higher supersaturation states than those recorded in both the recent EARS and man-

made alkaline counterparts. Thus, a major future challenge is to constrain the hydrological conditions enabling natural alkaline, saline waterbodies to chemically behave, at least in part, as anthropogenic spherulite-producing sites (Mercedes-Martín et al., 2019).

2.5 | CONCLUSION

A sedimentological, mineralogical and geochemical study was conducted in human-induced carbonate deposits (Consett) including analysis of microfacies (petrographic microscope and SEM), XRD, FTIR analysis and hydrogeochemistry to shed light on the physico-chemical processes forming the analogous Pre-Salt Aptian non-skeletal carbonates. Although the carbonates at Consett arise from low temperature and highly alkaline steel lag leachates, they exhibit strikingly similar primary crystal morphologies to those recognised in the Pre-Salt shrub carbonates. The Consett carbonates developed in a spring waterfall environment in the vicinity of former steelworks and under the influence of constant supplies of calcium and carbonate ions. The shrubby carbonate facies at the site appear to be the result of extreme environmental conditions (elevated pH and alkalinity, high CSI and R) but shrubby and dendritic crystals attest of a kinetic rather than thermodynamic control with high kinetic forcing. Non-dendritic facies (blocky calcite, sparry-carbonate crust and cluster-shaped carbonate) result from a low kinetic forcing and classic “microbialite” rim and clotted micrite form at a moderate-low forcing. Similar hyperalkaline sites, such as the study case of Consett, occur in most post-industrial landscapes. Understanding their operation in terms of mass deposition is a key part of fully constraining their behaviour, and thus being able to manage them successfully.

2.6 | AUTHOR CONTRIBUTIONS

The idea for this manuscript arose from the discussions between all authors. Laura Bastianini executed the petrographic analysis and drafted the manuscript. Mike Rogerson made

improvements through the whole manuscript. Ramon Mercedes-Martín provided insight on the facies descriptions and the discussion. Timothy J. Prior provided the data of XRD pattern and the FTIR spectra. William M. Mayes contributed to the hydrochemical data and their interpretation. Edgley A. Cesar identified the different taxonomies of diatoms.

Chapter 3 – What are the different styles of calcite precipitation within a hyperalkaline leachate? A sedimentological Anthropocene case study.

Laura Bastianini, Mike Rogerson, Ramon Mercedes-Martín, Timothy J. Prior and William M. Mayes.

This chapter compares anthropogenic carbonates with natural carbonate-precipitating settings (hot-spring and tufa environments) to gain insights on the ultimate processes driving mineral precipitation (RQ2: What do differences in carbonate fabrics at hyperalkaline sites tell us about controls on carbonate precipitation?). This chapter extends the work at Consett to provide a multi-site comparison of carbonate fabrics at systems receiving anthropogenic hyperalkaline drainage (RQ1: What are the dominant carbonate fabrics found in secondary deposits at anthropogenic hyperalkaline sites?) and considers similarities in drivers of precipitation processes (RQ2). This chapter has been published in the *Depositional Record* on 2nd November 2021.

3.1 | INTRODUCTION

Anthropogenic carbonates are pyrotechnological products composed of calcium carbonate, and include wood ash, lime plaster/mortar and hydraulic mortar, in addition to secondary carbonates that arise as a product of weathering a range of globally important industrial residues (Toffolo, 2020). These residues include steel slags (Roadcap et al., 2005), coal combustion residues (Dellantonio et al., 2010), chromite ore processing waste (Stewart et al., 2007), Solvay Process residues from the manufacture of soda ash (Effler et al., 2001), lime spoil (Burke et al., 2012a, b) and bauxite processing residue (Mayes et al., 2011). Many of these wastes and by-products are being produced in increasing quantities globally (Dolley,

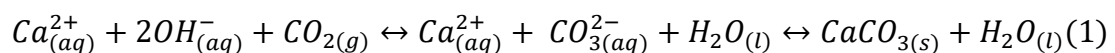
1994), so an understanding of their broader environmental impact and characteristics, either in disposal sites or during after-use (e.g. as aggregates for road fill: (Chaurand et al., 2007)), is required to facilitate their effective management.

The leachates generated by alkaline residues are enriched in a range of metal and metalloid oxyanions which can pose serious risks to the environment, namely As, Cr, Mo, Ni, Ga and V (Burke et al., 2013; Czop et al., 2011; Mayes et al., 2011; Chaurand et al., 2007; Hobson et al., 2017). The treatment of these alkaline leachates by conventional methods (acid dosing and active aeration) is expensive, especially if it is to be continued for many decades after site closure (Evans, 2015).

The dissolution products of alkaline waste materials can raise pH values up to 12.4, well outside the pH range that will be satisfactory for any receiving waters (Mayes et al., 2008). The high pH and calcium loadings of the leachate can also cause high rates of calcium carbonate precipitation when there is contact with atmospheric CO₂, which can smother benthic communities (Hull et al., 2014; Koryak et al., 2002) and restrict light penetration to primary producers (Koryak et al., 2002; Roadcap et al., 2005).

3.1.1 | Calcite precipitation within anthropogenic hyperalkaline sites

Precipitation of carbonates in anthropogenic sites is highly recommended as a carbon sequestration technology (Renforth et al., 2009). The formation of carbonate minerals in alkaline environments occurs when CO₂ gas is dissolved in the solution and reacts rapidly with OH⁻ ions (from portlandite dissolution) to form aqueous carbonate through Eq. (1).



The rate of this reaction is governed by equation 2 (Dietzel et al., 1992):

$$r = C_O \cdot (D \cdot k \cdot [OH^{-}])^{0.5} \quad (2)$$

In this equation k is the rate constant ($\text{cm}^3 \cdot \text{mol}^{-1} \cdot \text{s}^{-1}$) for hydroxylation, D is the diffusion coefficient of CO_2 through the liquid ($\text{cm}^2 \cdot \text{s}^{-1}$) and C_0 the CO_2 concentration in solution ($\text{mol} \cdot \text{cm}^{-3}$).

Post-industrial sites are widespread in the UK as a consequence of the country's industrial heritage and cover approximately 42,000 ha of land. Extrapolating an empirically-determined estimate that 30 kg of carbon per m^2 is being sequestered at these sites, Renforth et al. (2009) suggested that the United Kingdom alone stores approximately 12.7 Mt C as carbonate in brownfield soil, while Riley et al. (2020) estimate a potential carbon store of 138 Mt C in legacy slag deposits in the United Kingdom.

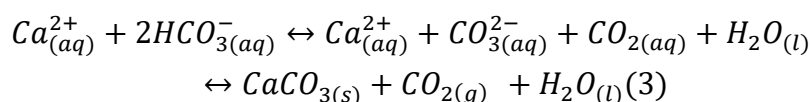
Riley and Mayes (2015) provide an overview of the distribution and mechanisms of calcite production in these sites. Statistical analysis of the physicochemical parameters and elemental composition of samples reveal multiple significant correlations within the streams affected by steel slag leachate. Partial Mann-Kendall (PMK) tests are also used to investigate long-term trends, in particular physical and chemical parameters that had the most complete time series at these sites (pH, alkalinity, Ca). Transient hydrological events control the use of flow as a covariate account for the fluctuations in leachate chemistry. Saturation indices (SI) of polymorphs of calcium carbonate provide a useful measure of the propensity of the hyperalkaline drainage waters to precipitate carbonate on the benthic habitats affected by the slag (Riley & Mayes, 2015).

However, all these approaches assume that the precipitation of calcite through the system is exclusively thermodynamically controlled and is homogeneous in process. More recent research reveals evidence that the mineralization process does not conform to these assumptions. Rather, precipitation mechanisms vary within a site and can be locally controlled by kinetic processes rather than thermodynamic (Bastianini et al., 2019). Microcrystalline, sparry calcite crust forming within the water mass of a pool is unlikely to have an identical rate

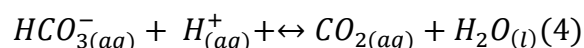
of formation and trace metal incorporation as “snowflake-like” dendritic carbonate crusts forming at the bottom of supercritical flows. Moreover, this study also reports microbial precipitates (clotted micrite and microbial rim carbonates) (Bastianini et al., 2019), which cannot be presumed to be controlled by the thermodynamic properties of the ambient water mass (Dupraz et al., 2009). These different crystallization processes may affect where and how quickly calcite forms, and even affect how effectively it sequesters trace elements (Saunders et al., 2014), including harmful pollutants (Burke et al., 2013; Czop et al., 2011; Mayes et al., 2011; Chaurand et al., 2007; Gomes et al., 2016, 2018; Hobson et al., 2017). Consequently, there is considerable value in investigating the sedimentology of these sites as a means to unlock a more highly resolved and process-based understanding how fast carbonate forms, where it accumulates, how long it will be preserved and how efficiently it coprecipitates contaminants. The origin of carbonate sediments can also impact their post-depositional physical properties (fine powder or lithified crusts) conditioning their use as permanent or transient earth surface carbon and environmental pollution sinks (Renforth et al., 2009).

3.1.2 | Terrestrial carbonate sedimentology

Although the sedimentology of anthropogenic carbonates is in its infancy, significant insight can be gained by comparison with better-known tufa (ambient temperature spring, river, lake and swamp carbonate) and travertine (geothermally influenced) systems (Ford & Pedley, 1996; Capezzuoli et al., 2014; Della Porta, 2015; Pentecost, 2005). At whole-system scales for both tufa and travertine, carbonate sediment forms due to high supersaturation levels with physico-chemical precipitation (i.e. that regulated by classic thermodynamic considerations) occurring in a manner analogous to that assumed by hyperalkaline sites. The primary difference is that carbonate is generated by CO₂ degassing from excess dissolved bicarbonate (eqn. 3; Emeis et al., 1987)) as opposed to CO₂ in-gassing driven by excess dissolved hydroxide (eqn. 1; Clark & Fontes, 1990; Andrews et al., 1997))



Calcite does not precipitate directly from bicarbonate, making the pH-related conversion of $\text{HCO}_{3(aq)}^{-}$ to $\text{CO}_{3(aq)}^{2-}$ a potential limit on precipitation rate (Dreybrodt et al., 1997) rather than hydroxylation of CO_2 as shown in equation 3. This is demonstrated by the observation that precipitation can be slow immediately adjacent to the spring, but rapid a few tens or hundreds of metres downstream (Dandurand et al., 1982). Precipitation rates of CaCO_3 from supersaturated solutions in the $\text{H}_2\text{O} - \text{CO}_2 - \text{CaCO}_3$ system are controlled by three rate-determining processes: the kinetics of precipitation at the mineral surface, mass transport of the reaction species involved to and from the mineral surface, and the slow kinetics of the overall reaction (Benning & Waychunas, 2008; Dreybrodt et al., 1997; Luttge, & Arvidson, 2010; Teng et al., 2000; White, 2020):



Turbulent flow and active agitation increase the area of the air–water interface and therefore promotes gas exchange (Rogerson et al., 2014). Consequently, precipitation may be enhanced at waterfalls and rapids by the same mechanism as occurs at springs (Chen et al., 2004), although physical calculations suggest this change is actually rather small (Hammer et al., 2010). The clear geomorphological evidence for enhanced carbonate precipitation at fast-flowing sites (Arenas et al., 2014) may therefore arise from processes other than gas exchange. At stagnant sites, all supply of ions to or from a growing crystal on the sediment surface is controlled by diffusion. As diffusion may be slower than precipitation, the water reacting with the crystal surface can become depleted in alkalinity, suspending the reaction. At sites with flowing water, vertical movement of ions is mostly by advection, a process that is orders of magnitude more rapid than diffusion. Flow separation occurs at the water–sediment interface forming a "diffusive boundary layer" across which ions are exchanged slowly, but these are thin if the shear velocity in the water is high (Benning & Waychunas, 2008; Liu & Dreybrodt,

1997; Luttge, & Arvidson, 2010; Teng et al., 2000; White, 2020; Zaihua et al., 1995). Consequently, alkalinity supply to the surface of a crystal growing under a rapid flow is sustained by accelerated resupply of alkalinity (Rogerson et al., 2014).

The influence of microbial biofilms further complicates mineral formation in travertine and tufa sites, both via metabolic effects and via the influence of microbially produced extracellular polymeric substances (EPS). The EPS monomers and polymers serve as a physical substrate for carbonate precipitation and, by extension, are passively or actively incorporated within the carbonate mineral product (Bosak & Newman, 2005; Braissant et al., 2007; Dupraz et al., 2009). This results in an array of complex processes, some of which are an active part of microbial ecological mechanisms and others are passive processes resulting from the presence of cells and EPS within sites where carbonate sediment production is already thermodynamically favoured. Following the definitions of Dupraz et al. (2009), biologically-induced mineralization involves an active if indirect action of the biota on the surrounding chemical microenvironment that results in carbonate precipitation. Biologically-influenced mineralization (the passive mineralization of an organic substrate) is a purely chemical process, but not truly abiotic as the organic matter is biologically produced. The source of alkalinity (which could be physicochemical, or metabolic) is also needed to characterise the biogenicity of a carbonate deposit (Gomes et al., 2016, 2018).

Differentiating the influences exerted by abiotic processes and biologically influenced mechanisms in the formation and early diagenesis of non-skeletal carbonates still remains problematic (Fouke, 2011; Wright, 2012; Capezzuoli et al., 2014; Brasier et al., 2015), and non-skeletal carbonates show a wide range of petrographic fabrics due to interactions between physico-chemical and biologically-influenced mechanisms (Arp et al., 2010; Mercedes-Martín et al., 2021a, 2021b). However, these studies provide great insight into what deviation from

thermodynamic equilibrium processes might be expected to experience within hyperalkaline leachate sites and provide a foundation for their investigation.

Here, different styles of calcite precipitation are investigated in anthropogenic carbonates with the aim of comparing them with better-known naturally occurring systems to evidence the potential drivers, precipitation mechanisms, morphological similarities, predictability in 3D facies distributions and depositional models of these systems. This study will focus on two sites (Figure 3.1): Consett, a steel-slag leachate system in County Durham (United Kingdom), and Brook Bottom from Derbyshire (United Kingdom), a cement lime kiln waste environment.

3.2 | WHAT DO WE ALREADY KNOW ABOUT ANTHROPOGENIC CARBONATE MICROFACIES?

An initial investigation of anthropogenic carbonate precipitate facies is reported by Bastianini et al. (2019) for the Consett site further investigated here. The findings of this study were summarised (Supplementary Figure 3.S1) before building on them with further analyses of that site and additional material from Brook Bottom.

Clotted micrite

Clotted micrite is made up of a brown micritic matrix composed of fine homogeneous rounded micrite peloids (Supplementary Figure 3.S1). Individual micrite grains reach up to 7 μm in diameter and under SEM inspection two types of calcite crystals were identified, prismatic tetrahedra *ca* 70 μm in diameter and double-terminated crystals with abundant twinned faces 100 μm in diameter. Intermingling of these heterogeneous fabrics enhance the clotted aspect recognised in thin sections. Diatoms are common components within this

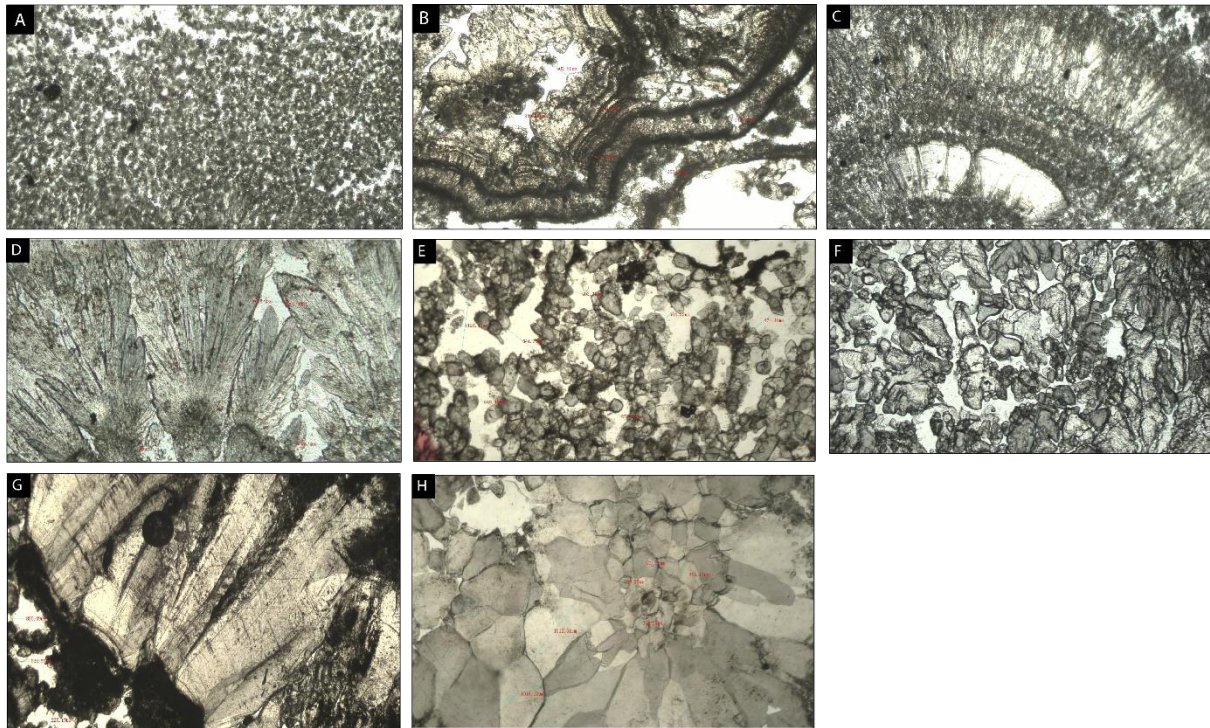


Figure 3.S1: Previous fabrics after Bastianini et al. (2019). (A) Clotted micrite (B) Microbial rim (C) Carbonate Dendrite (D) Calcite shrub (E) Cluster-shaped calcite (F) Multi-shaped carbonate (G) Sparry carbonate crust (H) Blocky calcite.

microfacies. These have a microbial origin, although the balance of bio-influenced and bio-induced is not known (Pedley, 1992).

Microbial Rim

This microfacies corresponds to thin black layers (180–250 μm thick) of dense micrite characterised by the presence of diverse microbial remains such as biodegraded biofilm or leaf material (Supplementary Figure 3.S1). These have a microbial origin, probably from the breakdown of biofilms, so they are considered as being largely bio-influenced.

Carbonate dendrite

Dendrites are constituted by light-grey calcite crystals growing radially forming flower-like geometries and are made up of elongated, polycrystalline calcite giving rise to V-shaped fans that grow upon surface fronts (Supplementary Figure 3.S1). Fans average 580 μm in length and 120 μm in width. These are only found in proximal sites which have very high mineral SI. They are associated with high rates of kinetic mineralization promoting polycrystal formation.

Calcite Shrub

Calcite shrubs are a particular subset of dendritic fabrics made up of light grey-green botryoidal crystal fans, 1–1.5 mm in height and stacked on each other as inverted cones growing on top of discontinuous horizons (Supplementary Figure 3.S1). Botryoids are internally composed of very coarse subhedral to euhedral, elongated rhombohedral crystals forming bladed aggregates (60 μm in length) with their c-axis radiating from a previous substrate. In places, the shrubs are surrounded by diatoms and bacterial filaments. Aggregates of bladed crystals tend to develop a high intercrystalline microporosity.

Cluster-shaped calcite

Cluster-shaped calcite appears as translucent white crystals ranging from 20 to 500 μm in length. They form a matrix made up of coarse euhedral tetrahedrons and double terminating crystals with many cluster faces, which are surrounded by a black biodegraded biofilm. The carbonates of this microfacies display extremely high intercrystalline porosity. Cluster-shaped calcite developed among bacterial filaments with an organic film forming a sticky, thin black layer around crystals which could correspond to EPS. The organic components associated with the micritic matrix of this facies along with its chemical characteristics (high alkalinity, medium pH and SI) suggest that they come from biologically influenced mineralization.

Multi-shaped calcite

The term multi-shaped calcite refers to translucent, white, delicate crystals (100–550 μm in diameter) displaying rounded external morphologies and grain-to-grain contact. These calcite crystals also exhibit trigonal, arrow and heart-shaped morphologies which seem to correspond to coarse-grained carbonate slightly reworked and stacked together. A black organic substance surrounds some crystals, which appears to be leaf material. This reworked microfacies is made up of a mixture of mineralized and organic debris.

Sparry carbonate crust

Sparry carbonate crust comprises thick sparite crusts (500–2,500 μm thick) made up of milky white to grey calcite. The partially developed crystal faces produce a very coarse, subhedral morphology. Some crystals are covered by black organic remains corresponding to degraded biofilm. Given the nature of these crystals, they develop very low intercrystalline porosity. These are diffusively grown single-crystals, associated with relatively low rates of kinetic crystallization.

Blocky calcite

Blocky calcite corresponds to single, very large crystals 500–1,500 μm in diameter, where the crystals are milky white to translucent grey. The coarse-grained euhedral crystals show distinct crystal boundaries. These appear to be a secondary phase, infilling and replacing primary fabrics and dispersed within primary materials.

3.3 | MATERIAL AND METHODS

3.3.1 | Field work and data collection

Samples were collected during May 2013 along pre-established calcite saturation index (CSI) transects (Mayes et al., 2008, 2018; Riley & Mayes, 2015) within Dene Burn, Howden Burn and Brook Bottom (Figure 3.1). In these streams, calcite saturation is enhanced by alkaline discharges within the former Consett Iron Steelworks and Old Lime kiln in Brook Bottom.

The site in Consett was operational from the middle of the nineteenth century until decommissioning in the early 1980s (Figure 3.1). Waste up to 45 m deep, including slag, flue dusts, ashes and construction and demolition rubble were accumulated after closure in an area of 2.9 km² (Harber & Forth, 2001). These materials are now stored in landfill, and the leachates emerging from them are alkaline ($[\text{OH}^-] = 10\text{--}130 \text{ mg L}^{-1}$; $[\text{CO}_3^{2-}] = 10\text{--}110 \text{ mg L}^{-1}$; $[\text{HCO}_3^-] = 110 \text{ mg L}^{-1}$) due to meteoric waters inter-acting with the mixed industrial residue materials in the subsurface (Mayes et al., 2008, 2018; Riley & Mayes, 2015). Five carbonate samples

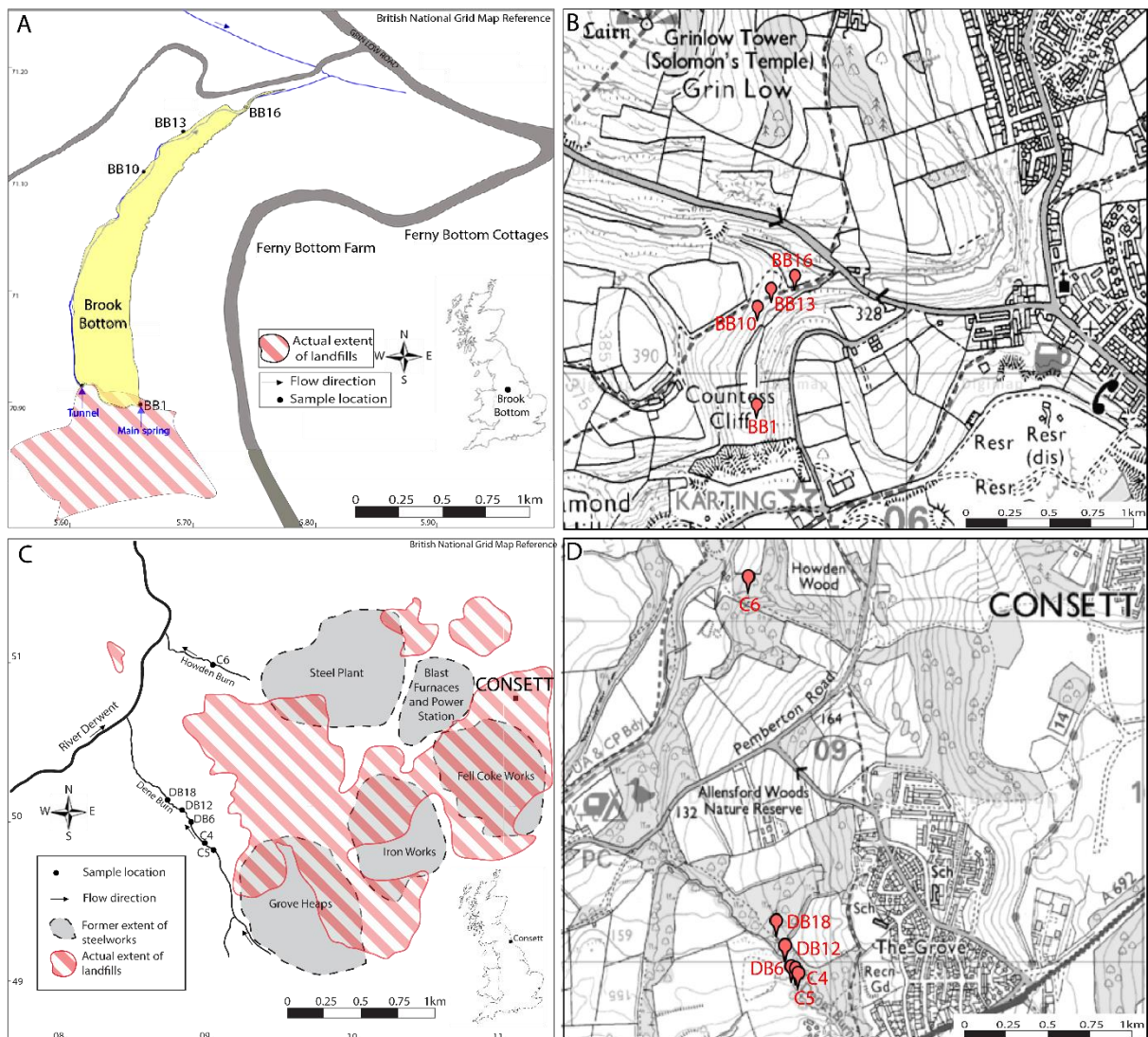


Figure 3.1: (A) Location map of the Brook Bottom (BB) samples (BB1, BB13, BB10 fresh, BB10 old deposit, BB16) where the yellow part represents the carbonate deposit. (B) Topographic map with the Brook Bottom samples (BB1, BB13, BB10 fresh, BB10 old deposit, BB16) after Ordnance Survey map. (C) Location map of the Consett (C) freshwater samples in Howden Burn (C6) and Dene Burn (DB) (C4, C5, DB6, DB12, DB18) after Historic OS maps. (D) Topographic map with the Consett freshwater samples in Howden Burn (C6) and Dene Burn (C4, C5, DB6, DB12, DB18) after Ordnance Survey map.

were studied (C4, C5, DB6, DB12 and DB18) from Dene Burn (Figure 3.1) with a further one (C6) from Howden Burn (Figure 3.1). Partial results from two of these samples (C4 and C5) were reported in an earlier study (Bastianini et al., 2019).

Brook Bottom near Buxton, Derbyshire (53°14'07"N, 001°55'03"W) is a spring-fed flush, the source of which drains (and likely rises in) extensive lime kiln spoil deposits (Gunn, 1998). The Brook Bottom Springs emerge from the base of lime spoil associated with the former Harpur Hill Limeworks which operated between 1835 and 1952 (Milodowski et al., 2013). Highly alkaline leachate emerges at the Brook Bottom Springs with water pH typically in excess of pH 11.3 and dominated by Ca-OH facies (Charles et al., 2019). Four samples of secondary carbonates (BB1, BB10, BB16 and BB16) were collected at Brook Bottom from the extensive deposits in the valley floor between the source zone to the south of the site and the drainage stream to the north (Figure 3.1).

During sampling, on-site measurements of major physicochemical parameters (pH, electrical conductivity and water temperature) were performed using a Myron L Ultrameter® calibrated on each sample day with pH 4, 7 and 10 buffer solutions and a 1,413 μS conductivity standard, to confirm the system had not changed since previous sampling. Sample alkalinity was also obtained in the field using a two-stage titration against 1.6 N H_2SO_4 with phenolphthalein (to pH 8.3) and bromocresol green-methyl red indicators (to pH 4.6) to facilitate calculation of the constituents of sample alkalinity [i.e., hydroxyl, carbonate and bicarbonate alkalinity using the United States Geological Survey alkalinity calculator (U.S. Geological Survey, 2014)]. For each sample, three polypropylene bottles were filled, one of which was acidified with trace analysis grade concentrated HNO_3 (for total cation and trace element analysis), one of which was filtered (with 0.45 μm cellulose nitrate filters) prior to acidification (for dissolved cation and trace element analyses) and the other left untreated (for anion analysis).

The CSI, ionic strength and Ca^{2+} and CO_3^{2-} ion activity were obtained with PHREEQC Interactive software. The kinetic calcite growth rate (R) was calculated following the formula established by Wolthers et al. (2012):

$$R = I^{-0.004} pH^{-10.71} r_{aq}^{-0.35} (S - 1)^2$$

where I is the ionic strength, $r_{aq} = \{\text{Ca}^{2+}\} / \{\text{CO}_3^{2-}\}$ activity ratio, S is the saturation ratio ($\Omega/2$) and R is expressed in m s^{-1} .

3.3.2 | Mineralogy

X-ray powder diffraction (XRD) data were collected from ground samples (BB1, BB10, BB16, C4, C5, C6, DB6) mounted in stainless steel sample holders on a PANalytical Empyrean diffractometer operating with Cu $\text{K}\alpha 1$ radiation. Data were collected between $5 \leq 2\theta / ^\circ \leq 80$ with a step size of 0.0262606° and a counting time of 304.725 s per step. Raw data were examined using the program PANalytical HighScore (Plus) in conjunction with the PDF2 database (Gates-Rector & Blanton, 2019).

3.3.3 | Petrographic analyses

Optical petrography was performed with a GXM-MXP Series L3230 optical microscope at the University of Hull. Twelve thin sections were imaged with a flat-bed scanner to allow textural mapping of microfacies. Seven cuttings were carbon coated and four thin sections were imaged by Scanning Electron Microscopy (SEM) with a Zeiss EVO60 at beam currents of *ca* 40 μA and *ca* 20 kV EHT accelerating voltage (University of Hull). False colour Back-Scattered Electron images (BSE) were taken on four thin-sections to obtain high resolution compositional maps to better characterise the distribution of mineral-organic phases. An Oxford Instruments Peliter-cooled type X-Max 80 Energy Dispersive X-ray Spectroscopy (EDX) system was used to determine the abundance of specific elements in thin-sections and cuttings.

3.3.4 | Terminology

The terminology used for petrographic descriptions follows the nomenclature of Pedley (1992), Jones et al. (2005) and Flügel (2013). The definitions of Mercedes-Martín et al. (2021) for single crystals and polycrystals are also employed in this study. A single crystal corresponds to a solid object with only one grain or crystal and hence, no grain boundaries in which an orderly three-dimensional arrangement of the atoms, ions or molecules is repeated throughout the entire volume (Jones et al., 2005). A polycrystal is an aggregate of several crystals or grains where the boundary between the grain is the grain boundary across which the orientation of the crystal changes and the point at which three boundaries meet is called the triple junction. The term “crystal shrub” was taken from Cook and Chafetz (2017) (see their figure 3C,D): “Shrubs occur in laterally continuous layers commonly 1 to 1.5 cm thick and vertically stacked shrub laminae form accumulations 10’s of centimetres in thickness. Individual laminae are composed of either a layer one shrub high or multiple shrubs stacked on top of each other. Crystal shrubs display a general overall branching outward pattern, and do not display any crystallographic influenced morphology”. These arrangements differ from those recognised in carbonate dendrites, which uses the definition of Jones et al. (2005): “100–200 nm thick calcite fibres that form 3D lattice-like domains and where fibres in each dendrite have three structurally equal orientations.” The terminology of Brasier et al. (2015) is used here for “sparry calcite crusts”.

3.4 | RESULTS

3.4.1 | Hydrochemistry

Hydrochemistry at each of the sampling sites on the day of sampling is summarised in Tables 3.1 and 3.2, and is consistent with previous (Mayes et al., 2008) and more recent (Hull et al., 2014; Riley & Mayes, 2015; Hobson et al., 2018; Mayes et al., 2018) monitoring of these

systems. Some calcium is sourced from background seepage of karst groundwater into both streams, but the majority is derived from steel slag leachate in the form of $\text{Ca}(\text{OH})_2$. Although Ca^{2+} (aq) is elevated throughout all three streams, it is dramatically enhanced in the relatively proximal parts of Howden Burn (161–239 mg L^{-1}) and Brook Bottom (226–745 mg L^{-1}) even compared to the more proximal Dene Burn (11 to 14 mg L^{-1}). Carbon dioxide is supplied to the system from the air, and in-gasses vigorously due to the high pH of the stream waters (Eq. 1). Total alkalinity is thus high where pH is high (55–66 mg L^{-1} at Dene Burn, 264 mg L^{-1} at Howden Burn and 14 to 219 mg L^{-1} at Brook Bottom). Given this water composition, it is unsurprising that the CSI is also very high (+0.04 to +2.71), and mineral precipitation is high enough to be lethal to local microbenthos by smothering (Hull et al., 2014).

Table 3.1: Hydrochemistry dataset of the Brook Bottom samples including pH, temperature, major ion concentrations, total alkalinity, calcite saturation index, ionic strength, activity and calcite growth rate.

Samples	BB1	Tunnel	BB10	BB13	BB14
pH	12.59	12.57	12.34	12.25	12.06
Temperature (°C)	16.9	16.2	17.6	17.4	19
Conductivity (µS)	8273	8290	4648	3410	2374
Major ions (mg.l ⁻¹)					
Al ⁺	0.11	0.13	0.19	0.21	0.19
K ⁺	65.10	92.54	91.91	93.54	91.59
Na ⁺	62.58	35.97	50.77	51.70	51.47
Sr ²⁺	1.27	3.21	2.26	2.16	1.87
Ca ²⁺	744.49	697.52	328.54	225.86	155.94
Ba ²⁺	0.30	2.26	0.88	0.74	0.57
CO ₃ ²⁻	208.20	177.80	71.60	42.40	0.184
HCO ₃ ⁻	10.60	12.40	5.80	5.70	13.316
Total Alkalinity as CaCO ₃ (mg.l ⁻¹)	218.80	190.20	77.40	48.10	13.5
Calcite Saturation Index	2.71	2.65	2.21	1.96	0.43
Ionic strength (mol.kgw ⁻¹)	4.12.10 ⁻²	3.84.10 ⁻²	2.26.10 ⁻²	1.74.10 ⁻²	1.38.10 ⁻²
Activity					
Ca ²⁺	5.72.10 ⁻³	4.59.10 ⁻³	5.59.10 ⁻³	3.40.10 ⁻³	2.10.10 ⁻³
CO ₃ ²⁻	3.31.10 ⁻⁴	2.39.10 ⁻⁴	2.91.10 ⁻⁴	1.73.10 ⁻⁴	6.4.10 ⁻⁷
Calcite growth rate (m.s ⁻¹)	1.87.10 ⁻⁷	1.22.10 ⁻⁷	1.55.10 ⁻⁷	6.38.10 ⁻⁸	2.39.10 ⁻¹⁴

Table 3.2: Hydrochemistry dataset of the Consett samples including pH, temperature, major ion concentrations, total alkalinity, calcite saturation index, ionic strength, activity and calcite growth rates from the research works of Mayes et al. (2008, 2018), Hull et al. (2014), Riley and Mayes (2015), Hobson et al. (2018)

Samples	C4	C5	C6	DB6	DB12	DB18
pH	9.06	10.06	11.51	10.72	10.35	10.50
Temperature (°C)	13.40	12.80	12.60	12.50	12.60	12.90
Conductivity (µS)	438.30	425.70	2165	452.40	436.50	427
Major ions (mg.l ⁻¹)						
Ca ²⁺	11.18	11.97	161.22	14.46	11.80	12.50
Mg ²⁺	0.75	4.84	0.68	2.08	0.43	2.30
K ⁺	19.19	20.45	183.55	17.70	21.18	21.05
Na ⁺	24.43	27.36	49.88	24.81	27.53	28.40
OH ⁻	0.10	0.70	20.60	3.30	1.40	0.80
CO ₃ ²⁻	1.60	7.30	103.60	18.30	13.80	7.50
HCO ₃ ⁻	37.20	17.10	8.60	9.40	16.70	18.20
Total Alkalinity as CaCO ₃ (mg.l ⁻¹)	66	56	264	59	55	60
Calcite Saturation Index	0.04	0.25	2.30	0.96	0.67	0.23
Ionic strength (mol.kgw ⁻¹)	1.48.10 ⁻³	1.95.10 ⁻³	1.11.10 ⁻²	2.01.10 ⁻³	1.73.10 ⁻³	3.50.10 ⁻³
Activity						
Ca ²⁺	2.36.10 ⁻⁴	2.39.10 ⁻³	1.90.10 ⁻³	2.56.10 ⁻⁴	2.25.10 ⁻⁴	2.25.10 ⁻³
CO ₃ ²⁻	9.68.10 ⁻⁷	2.79.10 ⁻⁵	3.97.10 ⁻⁴	1.36.10 ⁻⁴	7.88.10 ⁻⁵	2.65.10 ⁻⁵
Calcite growth rate (m.s ⁻¹)	3.43.10 ⁻¹¹	9.84.10 ⁻¹³	4.39.10 ⁻¹⁰	3.11.10 ⁻¹¹	1.30.10 ⁻¹¹	5.03.10 ⁻¹³

There is a significant hydrochemical gradient between the Dene Burn and Howden Burn streams and between the most proximal sites at Brook Bottom (BB1 and “tunnel” – see Figure 3.1A) and the most distal sites (BB10-BB16; Table 3.1 and 3.2, Figures 3.1 and 3.2). Conductivity, pH, alkalinity, CSI and R are dramatically more elevated in Howden Burn ([pH = 11.5]; [conductivity = 2165 μS]; [alkalinity = 264 mg.L^{-1}]; [CSI = 2.3]; [R = $4.4 \cdot 10^{-10} \text{ m.s}^{-1}$]) than in Dene Burn ([pH = 9 – 10.7]; [conductivity = 425–450 μS]; [alkalinity = 55–66 mg L^{-1}]; [CSI = 0.04–0.96]; [R = $9 \cdot 10^{-13}$ – $3 \cdot 10^{-11} \text{ m.s}^{-1}$]) (Table 3.2). Similarly, the same parameters are considerably elevated in BB1 and “tunnel” ([pH = 12.57-12.59]; [conductivity = 8273-8290 μS]; [alkalinity = 190-219 mg.L^{-1}]; [CSI = 2.65-2.71]; [R = $1.55 \cdot 10^{-7}$ - $1.87 \cdot 10^{-7} \text{ m s}^{-1}$]) compared to BB10, BB13 and BB16 ([pH = 12.06-12.34]; [conductivity = 2374-4648 μS]; [alkalinity = 14-77 mg.L^{-1}]; [CSI = 0.43-2.21]; [R = $2.4 \cdot 10^{-14}$ - $1.2 \cdot 10^{-7} \text{ m.s}^{-1}$]).

Location C4 in Dene Burn has the lowest CSI (0.04), then followed in increasing order by locations C5 (0.25), BB16 (0.43), C2 (0.67) and C1 (0.96) (Tables 3.1 and 3.2). In Howden Burn and Brook Bottom, the values are almost doubled at the C6 (2.3), BB13 (1.96), BB10 (2.21), “tunnel” (2.65) and BB1 (2.71) sites (Tables 3.1 and 3. 2) due to higher concentrations of carbonate (100–208 mg.L^{-1}) and calcium (160–745 mg.L^{-1}) (Tables 3.1 and 3.2, Figures 3.1 and 3.2).

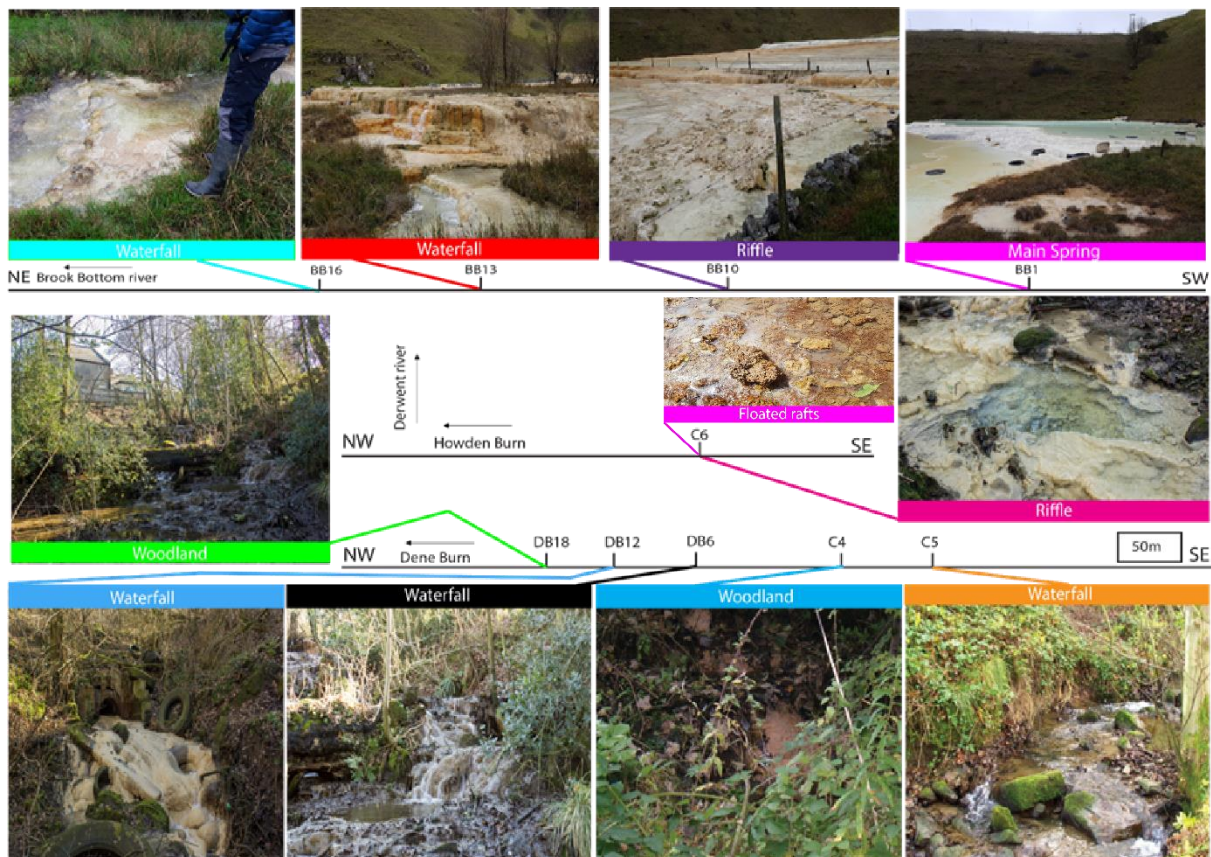


Figure 3.2: Environmental pictures of the downstream transects of Howden Burn, Dene Burn and Brook Bottom with the localisation of the riffle, waterfall, and woodland.

The R is lowest at location DB18 ($5.03 \cdot 10^{-13} \text{m.s}^{-1}$), then increases quite progressively at locations C5 ($9.8 \cdot 10^{-13} \text{m.s}^{-1}$), DB12 ($1.30 \cdot 10^{-11} \text{s}^{-1}$), DB6 ($3.1 \cdot 10^{-11} \text{m s}^{-1}$), C4 ($3.4 \cdot 10^{-11} \text{m.s}^{-1}$) (Table 3.2). In Howden Burn, R is much higher (C6: $R = 4.4 \cdot 10^{-10} \text{m.s}^{-1}$) (Table 3.1). In Brook Bottom, R is high in the more proximal sites BB13 ($1.5 \cdot 10^{-7} \text{m.s}^{-1}$), BB10 ($1.2 \cdot 10^{-7} \text{m.s}^{-1}$), “tunnel” ($1.5 \cdot 10^{-7} \text{m.s}^{-1}$) and BB1 ($1.9 \cdot 10^{-7} \text{m.s}^{-1}$) and is the lowest at the most distal location BB16 ($2.4 \cdot 10^{-14} \text{m.s}^{-1}$). This places proximal Brook Bottom at even higher rates of crystal formation than those reported at Consett, meaning that although the two sites largely overlap in terms of their hydrochemistry the highest rates of mineral formation should occur only at proximal Brook Bottom and the slowest only at distal Dene Burn.

3.4.2 | Depositional environments and carbonate microfacies

Three distinct depositional environments are observed within Consett and Brook Bottom settings, here termed the proximal, middle and distal zones. These sites all extend over

2.5 km in length, and after rising the water is affected by the local temperate climate characterised by relatively dry and high temperatures (average temperature 16°C) during summer and rainy and cold winters (average temperature 4°C) (Riley & Mayes, 2015) developing typical farmland vegetation with grasses, riparian trees and groundcover. A single depositional model can be applied to all three streams, with the tripartite division based on both macro-scale geomorphology and the type and nature of carbonate sediment found within the deposits.

Proximal zone

The proximal zone is characterised by swamp environments with soft barrages (*ca* 30 cm tall) and pools developed (locations BB1, BB10, C6, C5 and C4 on Figure 3.2). The water is milky, and the water is almost stagnant (flow velocity less than 1 cm.s⁻¹). Carbonate precipitation is so high that channels are quickly filled with fine carbonate sediment, and the water spreads and flows like a film no thicker than 10 cm. Accommodation space is quickly

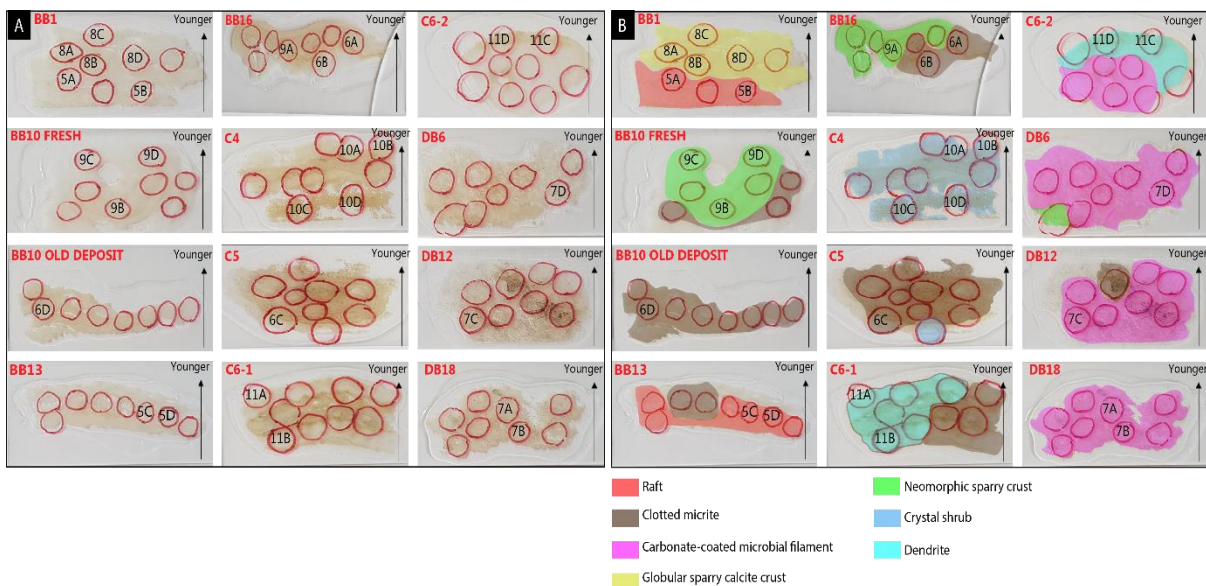


Figure 3.3: (A) Original thin sections from the Brook Bottom (BB) (BB1, BB13, BB10 fresh, BB10 old deposit, BB16) and Consett (C) freshwater samples in Howden Burn (C6) and Dene Burn (DB) (C4, C5, DB6, DB12, DB18) with the locations of the optical microscope images. The locations are respectively designated by the number of the figure from this manuscript followed by the letter corresponding to the subsection in the figure. (B) Interpreted thin-sections with the colours representing the different microfacies. The locations of the optical microscope images are respectively designated by the number of the figure from this manuscript followed by the letter corresponding to the subsection in the figure.

filled by deposits dominated by rafts of globular sparry calcite crust, clotted micrite and shrub carbonates (Figures 3.2 and 3.3; facies discussed below).

Middle zone

High precipitation rates ($3 \cdot 10^{-11}$ – $1.5 \cdot 10^{-7}$ m.s⁻¹) allows for continued rapid crystallization of carbonate, but the style of precipitation changes to favour formation of taller barrages (*ca* 80 cm in height) at BB13 and DB6 (Figure 3.2). These accumulate a range of components including rafts, clotted micrite and cluster-shaped carbonates (see Figure 3.3 and below). The water is still milky, but the water velocity is high (10cm.s⁻¹ – 1m.s⁻¹) when flowing vertically down the barrages.

Distal zone

This zone records the lowest sedimentation rates ($2 \cdot 10^{-14}$ – $1 \cdot 10^{-11}$ m.s⁻¹) which occur in low relief waterfall settings. The water is clearer, and the water velocity becomes slow again overall (*ca* 1 cm.s⁻¹), although water moves nearly vertically on waterfall faces. The carbonate precipitation is just consuming the available accommodation space in BB16, DB12 and DB18, but pools between aggradational barrages may be several tens of centimetres deep. Close to these barrages (*ca* 50 cm in height), the energy in the system is still high depositing carbonate-coated microbial filament, clotted micrite and neomorphic sparry calcite crust microfacies (see Figure 3.3 and below).

3.4.3 | Macroscopic description

All samples are light brown limestone with dark brown laminations except for the C6 sample which is light beige with beige brown laminations in a circular ring structure (Figure 3.4). The samples from Brook Bottom (BB1, BB10 fresh deposit, BB10 old deposit, BB13, BB16) are very friable compared to those of Consett.

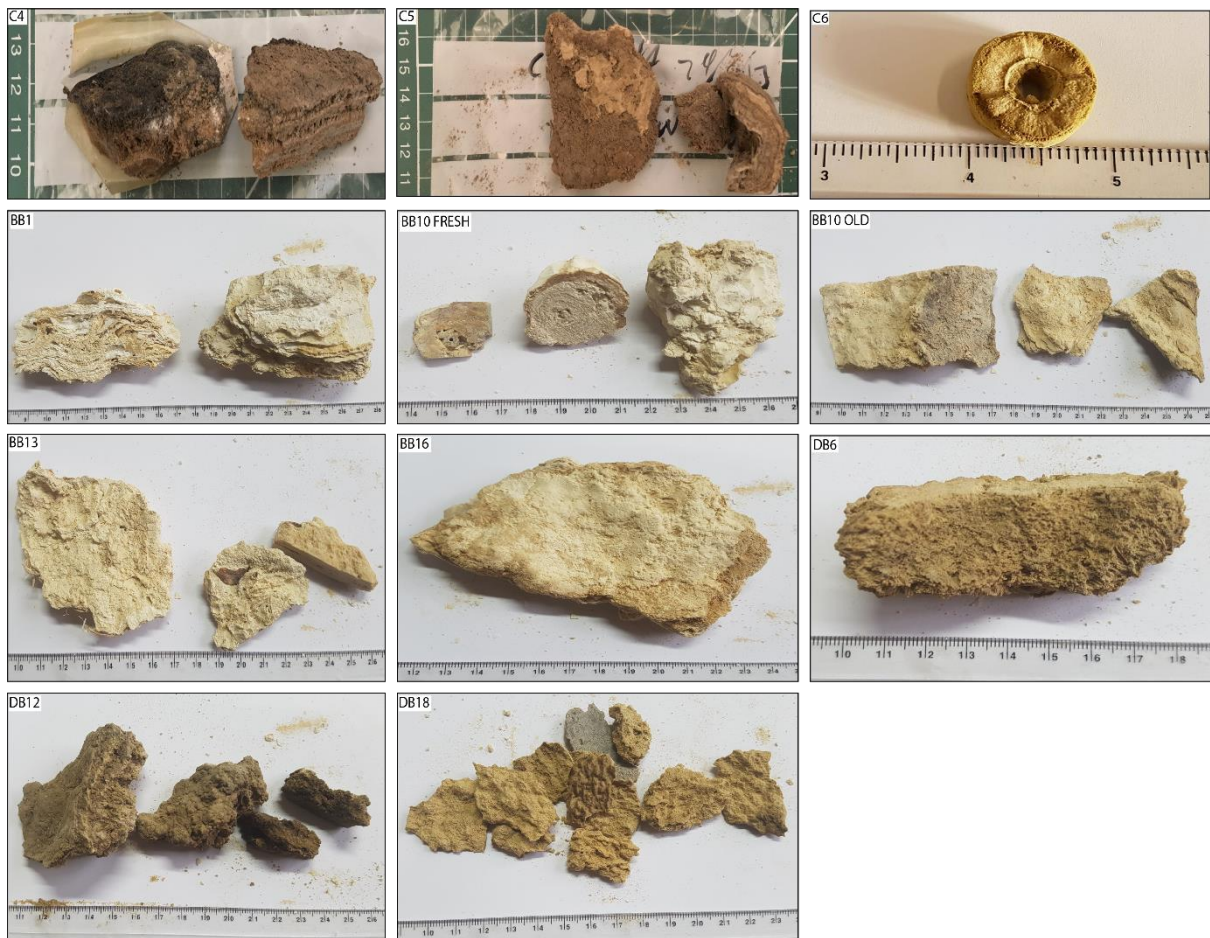


Figure 3.4: Macroscopic images of the Brook Bottom (BB) (BB1, BB13, BB10 fresh, BB10 old deposit, BB16) and Consett (C) freshwater samples in Howden Burn (C6) and Dene Burn (DB) (C4, C5, DB6, DB12, DB18).

3.4.4 | Microfacies descriptions

In addition to those fabrics summarised from previous studies in Section 2, seven additional types of microfacies have been identified on the basis of fabric, mineralogy and texture (Figure 3.3).

3.4.4.1 | Microfacies 1: Coated vegetative remains and carbonate rafts (proximal zone)

This microfacies is made up of a poorly-sorted assemblage of flat vegetative remains coated by calcite (Figure 3.5A), and also carbonate rafts forming intraclastic accumulations with high interparticle porosity (Figures 3.3 and 3.5C,D). Flat organic remains correspond to fragmented and whole specimens of leaves 50 μm to 2 mm in length, and 50 μm to 200 μm in width. The

external surface of these plant fragments shows multiple arcuate vault structures which are internally filled and externally coated by a cloudy, brown-coloured sparry calcite (Figure 3.5C,D) or even coated by globular sparry calcite crust microfacies 3 (Figure 3.5B). In some cases, polycrystalline calcite globular aggregates 50 to 100 μm thick can grow to form elongated structures resembling pure carbonate rafts (*sensu* Taylor & Chafetz, 2004) (Figure 3.5C).

3.4.4.2 | Microfacies 2: Micro-peloidal and clotted micritic fabric (distal zone)

Unlike the previous study of Bastianini et al. (2019), this microfacies is composed of a highly porous and patchy micro-peloidal micritic texture of yellowish and pale brown colour (Figure 3.6A,B)) that can alternate with more laminated textures. Dense clotted fabrics form lumpy masses and, on some occasions protruded filamentous structures are recognised growing perpendicular to the laminae (Figure 3.6A,B). This microfacies host abundant inter-crystalline porosity with cavities between 10 μm and 1 mm in diameter (Figure 3.6A,B).

3.4.4.3 | Microfacies 3: Carbonate-coated microbial filament (middle zone)

This microfacies is here referred to as delicate filamentous structures (ranging from 100 to 2,500 μm in length) coated by translucent white euhedral to anhedral calcite crystals (Figure 3.7A). In some adjacent areas, carbonate grains are clearly detached from microbial filaments forming intraclastic accumulations (Figure 3.7B) already described in Consett (see Figure 7B and cluster-shaped carbonates in figure 11 from Bastianini et al., 2019).

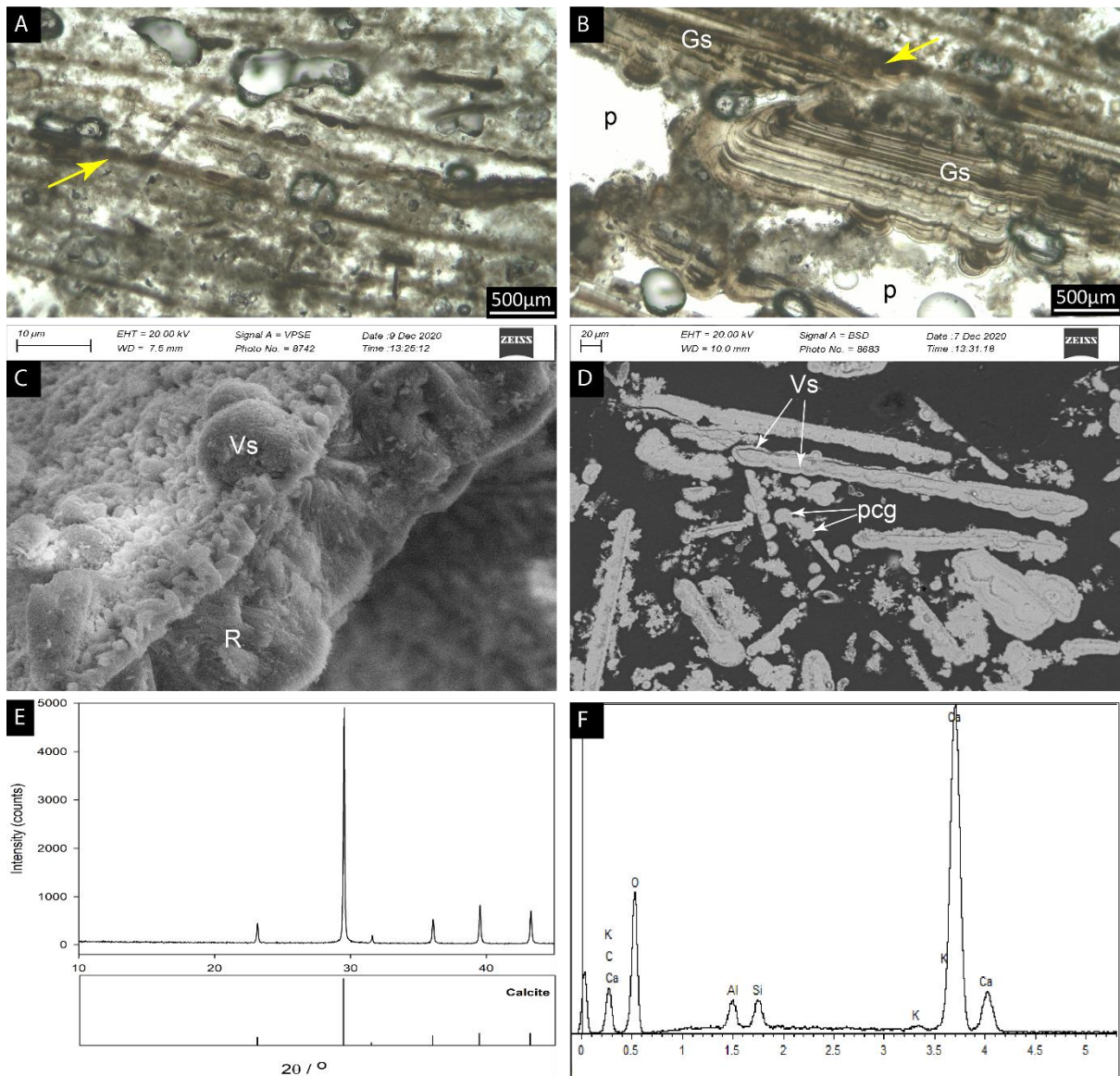


Figure 3.5: Coated vegetative remains and carbonate raft (microfacies 1). (A) Assemblage of brown coloured, flat and elongated vegetative remains (arrow) coated by calcite thin films. (B) Some flat remains (arrow) are covered in globular sparry calcite crusts (Gs); interparticle porosity (p) is very abundant. (C) SEM photomicrograph of carbonate rafts (R) covered by multiple arcuate vault structures (Vs) consisting of cloudy, brown-coloured sparry calcite. (D) BSE-SEM image of poorly sorted carbonate rafts covered by vault structures (VS). Some polycrystalline calcite globular aggregates (pcg) can grow laterally to form elongated structures. (E and F) XRD pattern and EDX spot analysis, respectively, indicating a calcite mineralogy.

Calcite crystals range between 5 to 30 μm in height and agglutinate around organic-rich filaments forming lumps. Coarse, euhedral tetrahedrons and double terminating crystal morphologies are recognised (Figure 3.7A). This microfacies displays an extremely high intercrystalline porosity with cavities fluctuating between 10 μm and 2 mm in diameter.

3.4.4.4 | Microfacies 4: Globular sparry calcite crust (proximal zone)

Similar to the sparry fabrics reported by Bastianini et al. (2019), the sparry carbonate microfacies consists of globular arrangements of isopachous fans within 500 μm to 2 mm thick crusts made up of milky white to pale brown calcite (Figure 3.8A,B). The colour differences in the laminae might be explained by oxidation/reduction conditions changing during spar growth resulting in more or less Mn or Fe trapped in the calcite lattice. However, here sparry crusts nucleated upon clotted organic templates (Figure 3.8A, B), extending upwards and laterally. In some examples, carbonate rafts became coated with sparry carbonate crusts indicating a close relationship between microfacies (Figure 3.5B). Globular sparry calcite fans grew outward and laterally forming homogeneously thick bands punctuated by laminae that

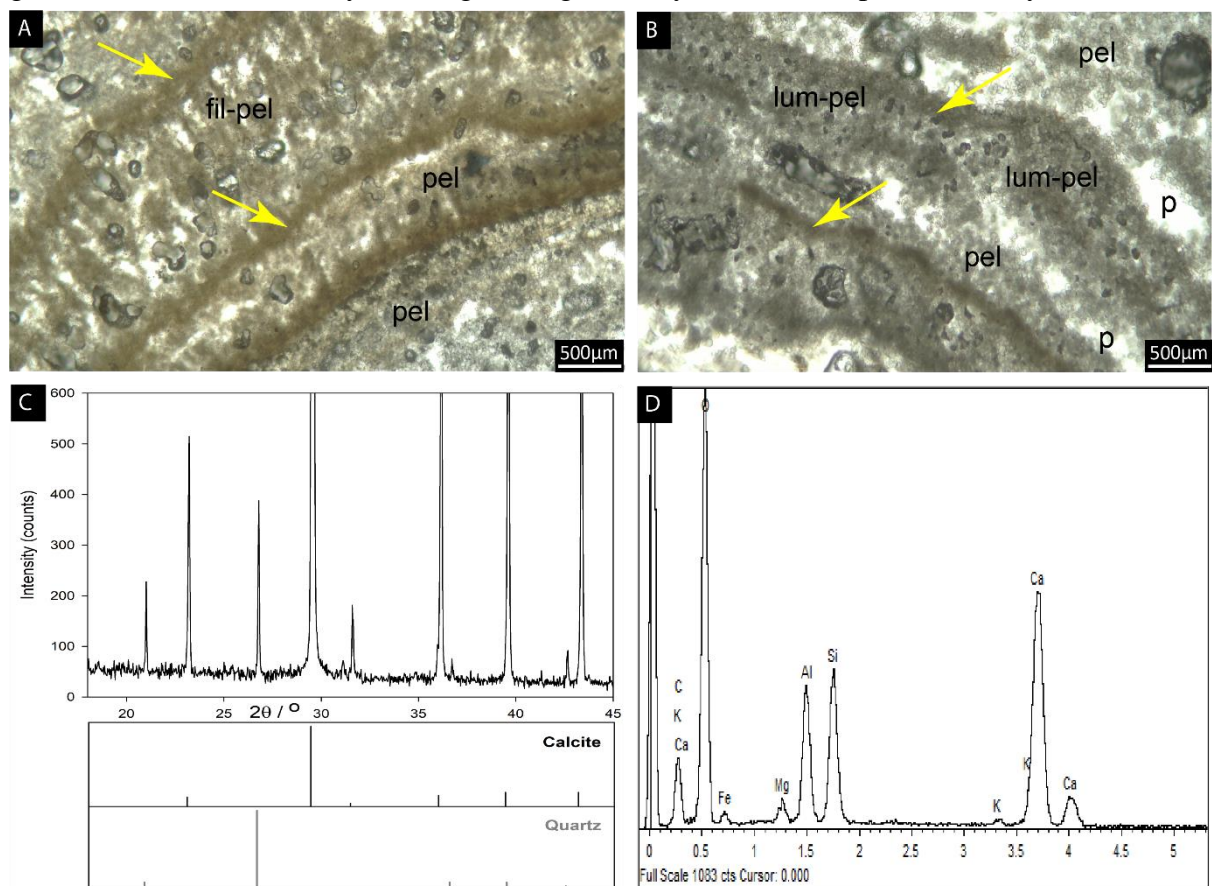


Figure 3.6: Micro-peloidal and clotted micritic (microfacies 2). (A and B) Patchy micropeloidal micritic textures (pel) alternate with laminated textures (arrows). Filamentous clotted structures can be seen perpendicular to laminae (fil-pel). In some cases, lumpy micropeloidal masses (lum-pel) develop in association with laminated textures. Abundant inter-crystalline porosity (p) is observed in this microfacies. (C and D) SEM images of the microfacies clotted micrite. XRD pattern and EDX spot analysis, respectively, indicating that calcite and quartz are present.

can be traceable between fans. Darker laminae tend to be thinner (30 μm to 90 μm in thickness) than lighter laminae (100 μm to 150 μm in thickness). Fans interfered with each other demonstrating that competitive growth took place. Most of the fans terminated in smooth curved surfaces. This microfacies displays a high intercrystalline porosity with cavities between 100 and 2,000 μm in diameter (Figure 3.8A,B).

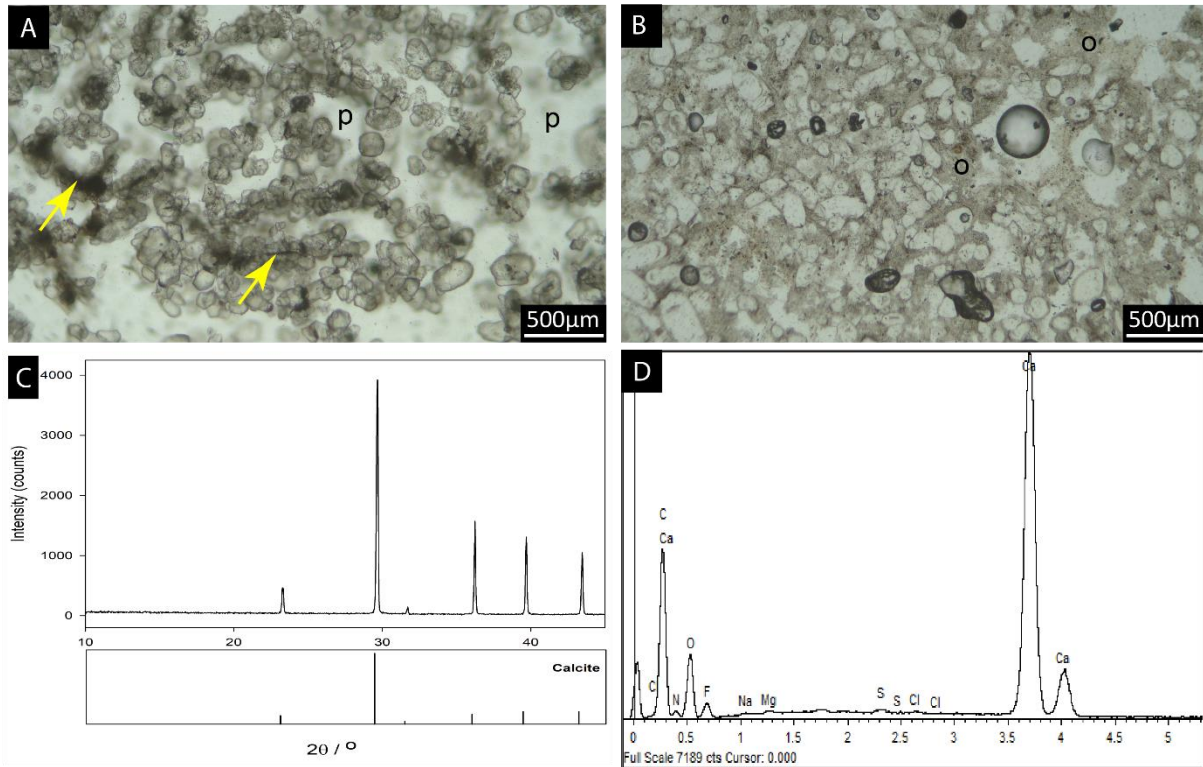


Figure 3.7: Carbonate-coated microbial filament (microfacies 3). (A) Double terminating calcite crystal morphologies agglutinated around organic-rich filamentous structures (arrows) forming crystal lumps. High intercrystalline porosity (p) is recognised between filaments. (B) Double terminating calcite crystals can be detached from microbial filaments forming intraclastic accumulations embedded in organic-rich matrices (o). (C and D) XRD pattern and EDX spot analysis, respectively, indicating that calcite is the predominant mineralogy.

3.4.4.5 | Microfacies 5: Neomorphic sparry calcite crust (distal zone)

Neomorphic sparry crust consists of 500 μm –2.5 mm thick layers of milky white to grey sparry calcite crystals (Figure 3.9A through D). Microbial to micropeloidal and organic-rich substrates are present at the base of the sparry crust, indicating nucleation on top of them (Figure 3.9A). Sparry crusts are made up of isopachous fans where globular arrangements are less well defined. Indeed, EBS-SEM observations (Figure 3.9C, D) indicate that these crystals

underwent dissolution and recrystallization leaving the interstices filled with organic-rich materials. The cracks seen in the crusts are more common at the surface and extend to different depths. The arrangement of the fissures and the overall integrity and continuity of the crusts along the samples advocates towards an authigenic origin rather than a pure intraclastic accumulation of calcite debris. For these reasons, fissures are considered to have formed by dissolution processes.

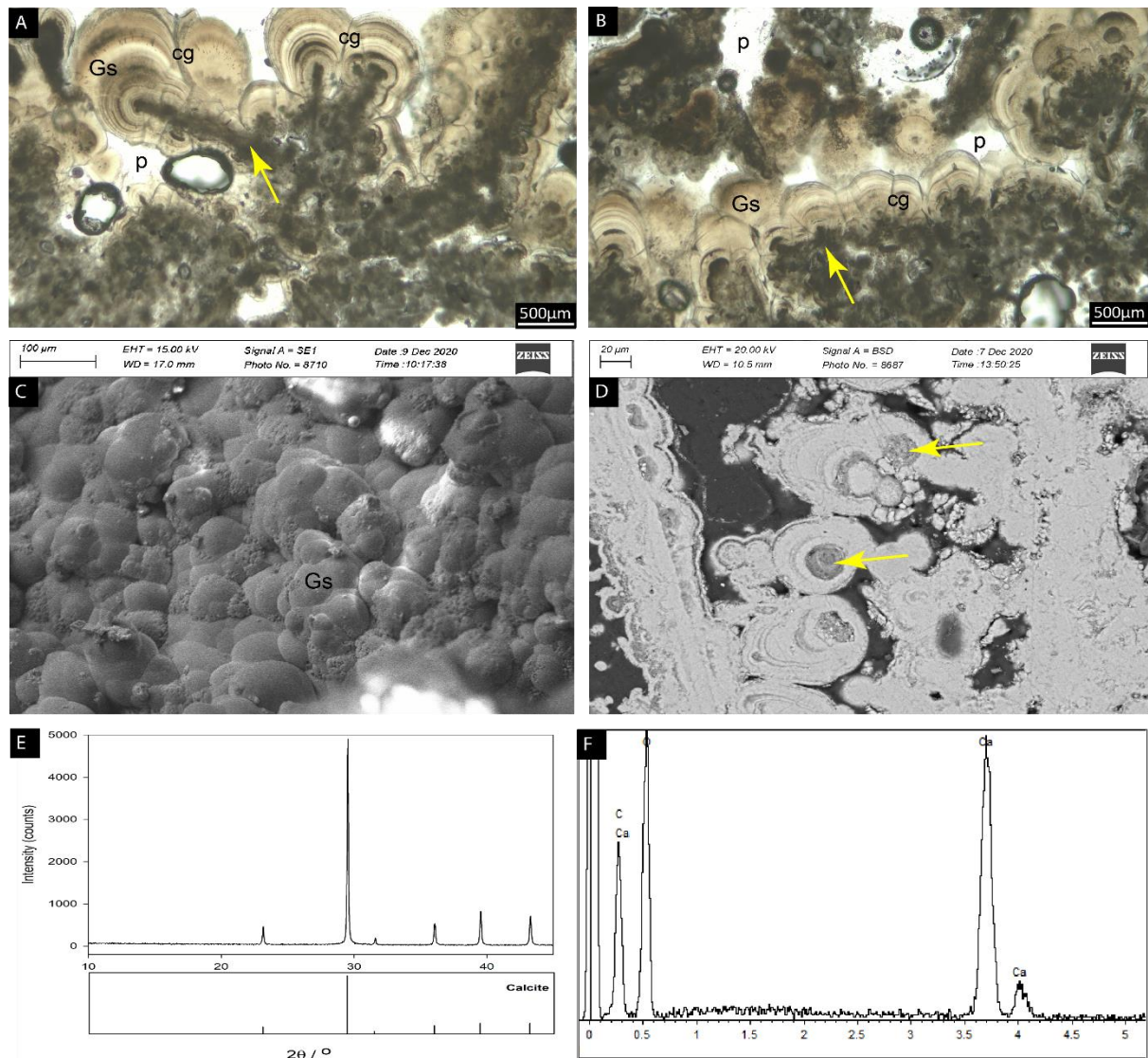


Figure 3.8: Globular sparry calcite crust (microfacies 4). (A and B) Thick isopachous calcite fans with globular arrangements (Gs) growing on top of clotted peloidal templates (arrows). Fans consist of thin darker laminae and thick lighter laminae extending laterally. Competitive growth defines sharp boundaries between fans (cg). This microfacies displays a high intercrystalline porosity (p). (C) SEM image showing the external smooth curved surfaces of the fans (Gs). (D) BSE-SEM image displaying sparry crusts growing on top of organic substrates (arrows). Note thin concentric, darker laminae within fans. (E and F) XRD pattern and EDX spot analysis, respectively, indicating that calcite is the predominant mineralogy.

3.4.4.6 | Microfacies 6: Crystal shrub fan (proximal zone)

The crystal shrub fan microfacies consist of light grey-white botryoidal crystal fans 1–3 mm in height and stacked on each other as inverted cones growing on top of discontinuous horizons (Figure 3.10A through D) (compare with shrub facies in Bastianini et al., 2019, their figure 10). Botryoids are internally composed of very coarse subhedral to euhedral, elongated rhombohedral crystals forming bladed aggregates (60 μm in length) (Figure 3.10A through D) with their c-axis radiating from a previous substrate (Figure 3.10A through D). Bladed crystal aggregates tend to develop incipient intercrystalline microporosity (Figure 3.10A through D).

In this study, analysis of a larger number of samples allows at least three generations of shrubby bands to be recognised throughout the crusts (Figure 3.10A, B). Every shrub generation is interrupted by a thin organic rim which is seen covering previous botryoidal terminations. Shrub bifurcations tend to be more developed in terminal stages where individual shrub branches show more defined limits and sometimes the presence of trapped or infiltrated organic matter (Figure 3.10A, B). A black degraded biofilm and some diatoms are found surrounding the crystals (Bastianini et al., 2019).

3.4.4.7 | Microfacies 7: Dendrite carbonates (proximal zone)

Dendrite carbonates are light grey, tree-shaped calcite polycrystals showing multiple levels of branching (Figure 3.11A through D, see also Bastianini et al., 2019, their figure 9). These crystals, up to 3 cm long and 0.2 cm wide, are compact because they have only short secondary and tertiary branches (Figure 3.11B). Each branch consists of numerous thin (up to 0.2 mm thick), plate-like calcite crystals that are stacked “en echelon” (Figure 3.11A through C) (see Jones et al., 1996). The orientation of these crystals in the primary and secondary branches of the same crystal is analogous. These crystals are surrounded by a dark organic substance (Figure 3.11A, B).

3.4.5 | Mineralogy

The XRD data show that all the samples are highly crystalline and correspond to pure calcite (Figures 3.5E, 3.7C, 3.8E and 3.9E) except C4, C5, C6 (corresponding to shrub, clotted micrite and dendrite microfacies respectively) (Figures 3.6C, 3.10E and 3.11E) which contain a small quantity of quartz (3-5%). The EDS measurements exhibit the limited presence of Al

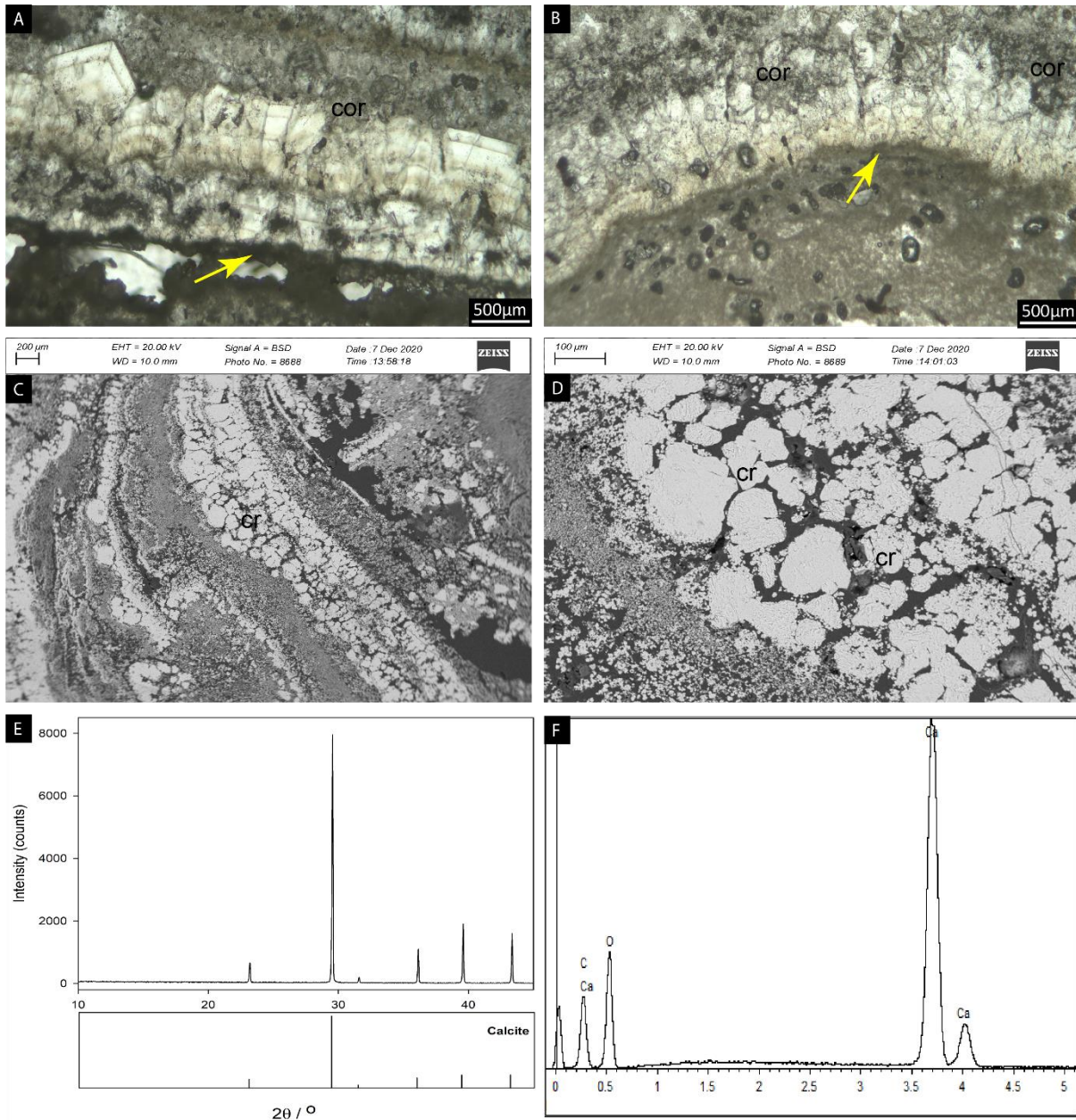


Figure 3.9: Neomorphemic sparry crust (microfacies 5). (A and B) Neomorphemic sparry crusts growing on top of organic-rich substrates (arrows). Corroded areas (cor) through irregular surfaces on the external part of the crusts are common. (C and D) BSE-SEM images showing cracking of the crusts where fissures (cr) reach different depths showing no apparent reworking. (E and F) XRD pattern and EDX spot analysis, respectively, indicating that calcite is the predominant mineralogy.

(1.7%) and Si (1.7%) within the raft facies. Clotted micrite show the highest levels of Al (6%), Si (10,3%) and Mg (1.35%). Shrub and dendrite contain a high quantity of Si (5%), in addition to Al (0.82%) and S (1.10%).

3.4.6 | Distribution of macrofacies and microfacies

The proximal zone in both Brook Bottom and Consett is characterised by low-gradient, swamp environments that favour the development of soft barrages and pools (Figure 3.12). Globular sparry calcite crust, raft, shrub and dendrite calcites constitute the microfacies diagnostic of this zone.

The middle zone corresponds to high barrages allowing the deposition of carbonate-coated microbial filaments and, less importantly, calcite rafts.

The distal zone is recognisable by its lower relief waterfall setting developing pools between aggradational barrages (Figure 3.12). Neomorphic sparry crust, carbonate-coated microbial filament and clotted micritic fabrics are the main deposits of this area. Both Brook Bottom and Consett face a major change in microscopic features at the limit of their proximal-distal zones but the actual microfacies are different depending on the location. In Consett, the microfacies evolve from principally shrub and dendrite and minor raft to reworked carbonates (carbonate-coated microbial filament and neomorphic sparry crust), whereas the microfacies at Brook Bottom evolve from raft and globular sparry calcite crust to neomorphic sparry crust.

3.5 | DISCUSSION

3.5.1 | Depositional model according to macrofacies and microfacies distributions

Macrofacies distribution reveals a common depositional model between Brook Bottom and Consett, a conclusion supported by the observed macroscopic features (Figure 3.12). In

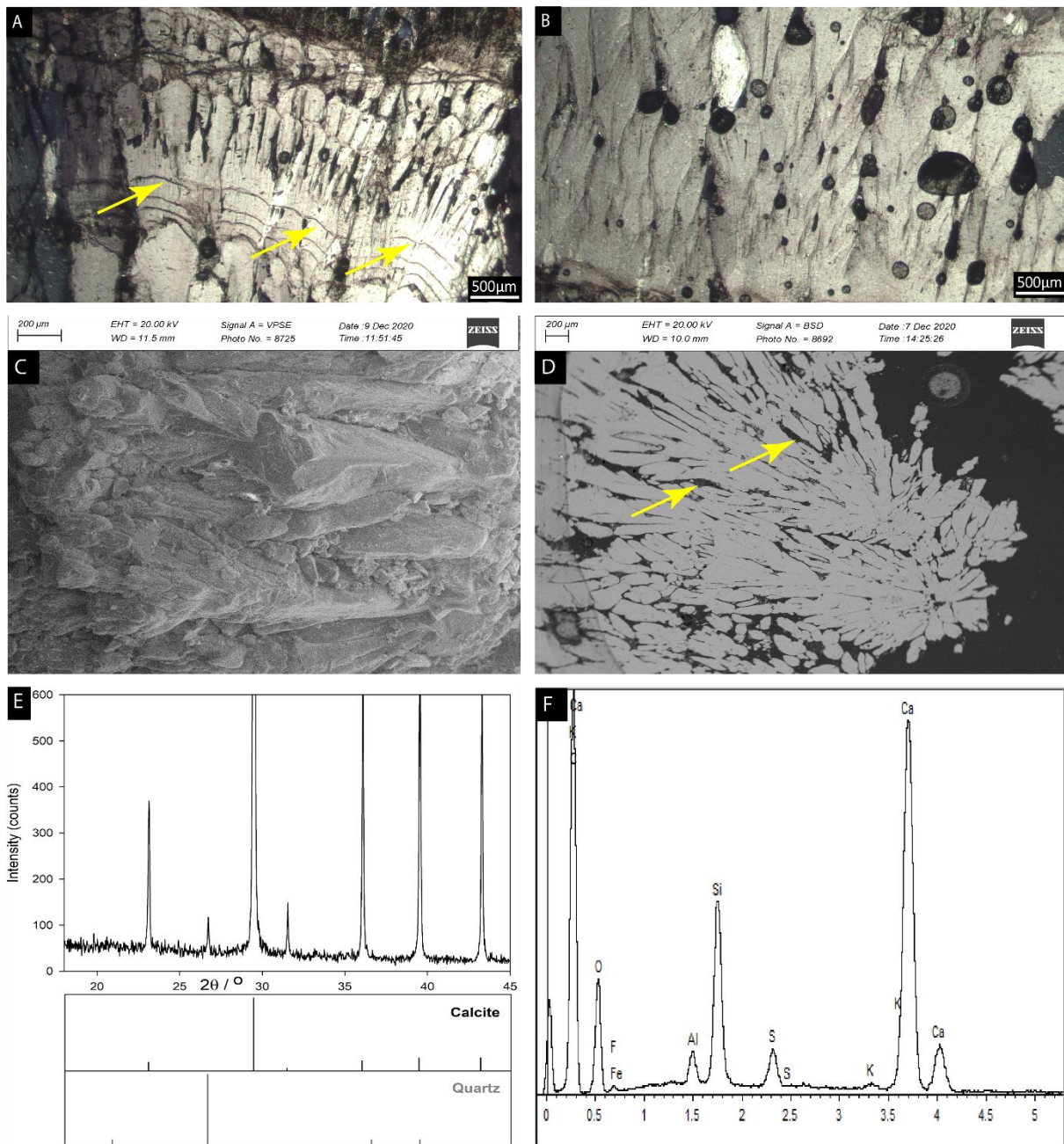


Figure 3.10: Crystal shrub (microfacies 6). (A and B) Light grey-white botryoidal crystal fans 1–3 mm in height and stacked on each other as inverted cones growing on top of discontinuous horizons (arrows). (C and D) BSE-SEM images showing bladed crystal aggregates developing incipient intercrystalline microporosity (arrows). (E and F) XRD pattern and EDX spot analysis, respectively, indicating that calcite and quartz are present.

both cases, the proximal zone is defined by pools and soft barrages, the middle zone by the largest barrages and the distal zone by smaller barrages. It is more challenging to apply a similar depositional model for both sites in microscopic terms. The proximal zone at Brook Bottom consists of rafts, a globular sparry calcite crust and, less importantly, neomorphic sparry crust whereas the Consett microfacies correspond to shrub, dendrite and carbonate-coated microbial

filament. Nevertheless, both sites display intraclastic carbonate-coated microbial filaments or reworked carbonates (neomorphic sparry crusts) in the proximal zone while Consett shows minor deposition of rafts in the most proximal zone, identifiable at the macro-scale (Figure 3.2). The middle zone shows continued deposition of calcite rafts at Brook Bottom and altered carbonates (neomorphic sparry crust and carbonate-coated microbial filament) at Consett. Neomorphic sparry crusts at Brook Bottom and carbonate-coated microbial filaments at Consett are also characteristic of the distal zone in addition to clotted micrite.

While biofilm growth is more developed at Consett, biofilms at Brook Bottom occur only as discoloured pale and homogenous sediment crusts. The higher degree of bio-influence at Consett is confirmed by the SEM images which show more abundant diatoms at Consett, as indicated by the higher Si elemental composition (using EDX), and also the presence of quartz minerals (Goswami et al., 2012) (Figures 3.6, 3.10 and 3.11). This significant difference is probably due to the lethally high pH at Brook Bottom (12-12.6). Indeed, biomolecules have a range of pKa between 6.5 and 9 (Solmaz et al., 2018), significantly below 12, so at this pH biomolecules are completely dissolved and cannot construct EPS (Jones et al., 2015). Therefore, the lack of bio-influence at Brook Bottom is likely to be responsible for the dendritic and shrub fabrics only developing in Consett at a more viable pH (9).

3.5.2 | Origin of macrofacies and microfacies

As the solution moves from the most proximal site, calcium and alkalinity are consumed, steadily reducing CSI (Figure 3.13). The boundary between the proximal and the distal zone (swamp environments to waterfalls) in both Consett and Brook Bottom does not correspond to an unusual change in CSI despite the considerable changes in macromorphology and microfacies (Figure 3.13). However, the proximal-distal transition is well reflected by changes in the predicted kinetic calcite growth rate (R), which shows a sudden decrease of 10^7 between samples BB1, BB10, BB13 and BB16 at Brook Bottom, and 10^3 $\text{m}\cdot\text{s}^{-1}$ between

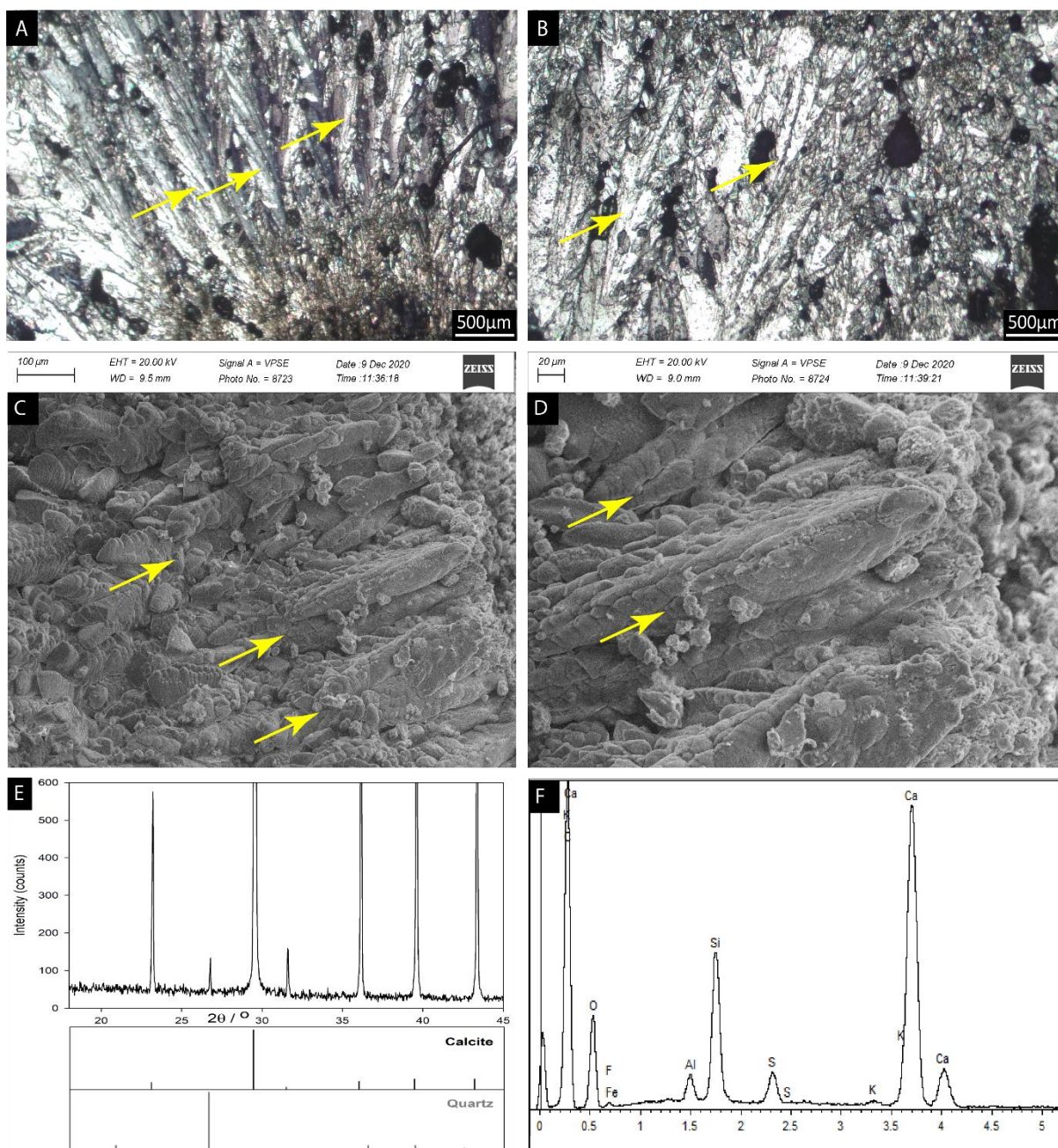


Figure 3.11: Dendrite carbonates (microfacies 7). (A and B) Light grey calcite polycrystals showing multiple levels of branching (arrows). (C and D) BSE-SEM images showing that each branch consists of numerous thin (up to 0.2 mm thick), plate-like calcite crystals that are stacked en echelon (arrows). (E and -F) XRD pattern and EDX spot analysis, respectively, indicating that calcite and quartz are present.

samples C6, C4, C5 and DB6, DB12, DB18 at Consett as calcium and carbonate concentrations drop (Figure 3.13). In proximal Brook Bottom the very high R values promote deposition of rafts and globular sparry calcite crust (Figure 3.14). Howden Burn shows R values which remain high compared to other sites but are lower than proximal Brook Bottom by $10^3 \text{ m}\cdot\text{s}^{-1}$ (Table 3.1). Similarly, pH is much lower at Howden Burn permitting greater development of

biofilm. This difference likely explains the lack of rafts but promotion of kinetically-controlled polycrystal formation at Consett. The most alkaline sites display mineralization in the surface tension layer as well as at the base. However, this requires R values at least higher than the $10^{10} \text{ m}\cdot\text{s}^{-1}$ found in proximal Howden Burn (Table 3.1). When the reaction is no longer able to sustain mineralization in the surface tension layer it switches to precipitation only at the bottom as crusts, with the turbulence of the flow also likely promoting this switch. In the absence of biofilm (as at Brook Bottom) the main fabrics are mostly globular sparry crusts constructed from mono-crystals. This is unexpected due to the very high CSI and R values at these sites. However, this fabric is likely to form as a diffusion-limited equilibrium phase. In the presence of biofilm (as at Consett), polycrystal dendrites and shrubs are formed, with the carbonate precipitation indirectly modified by a precursor organo-mineral (Dupraz et al., 2009).

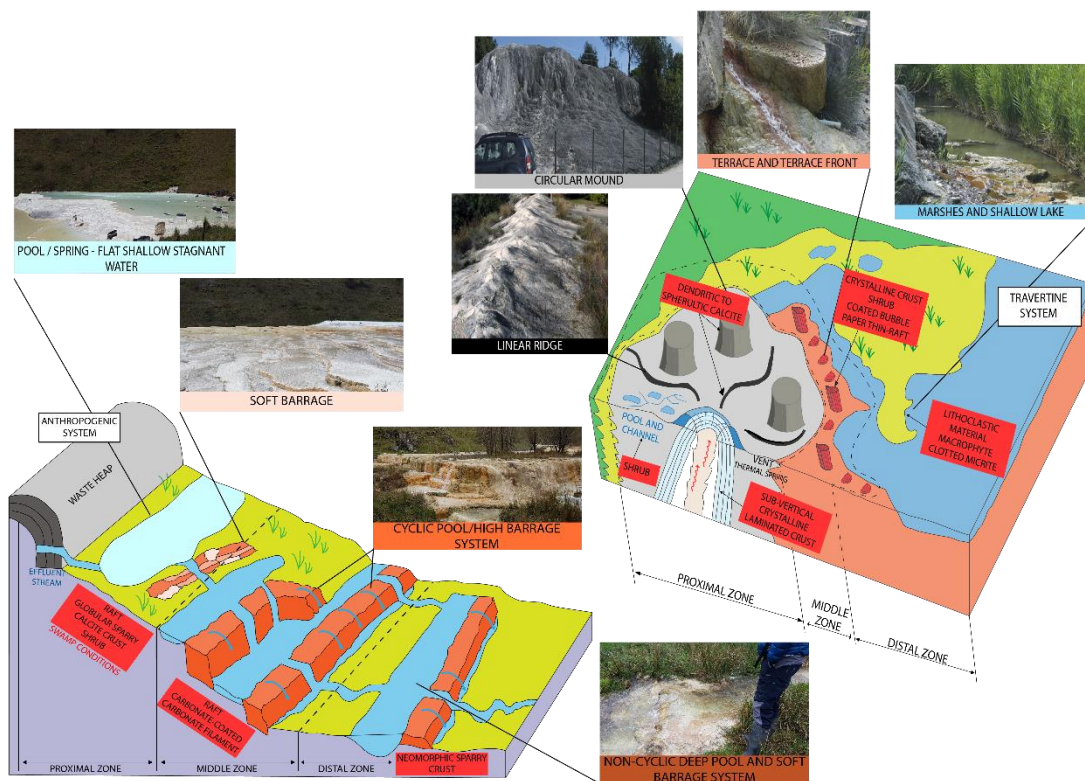


Figure 3.12: Comparative depositional model between anthropogenic carbonate and travertine systems after Capezuolli et al. (2014) and Mancini et al. (2019).

Depending on the context, there are key implications arising from the observation that minerals are forming by three discrete processes in the proximal part of these systems.

Formation of rafts is a direct reflection of equations 1 and 2 and arises from the nucleation of solid crystals within the surface tension layer of the water itself, likely instantaneous with hydration of the ingassing CO₂. Where water is more turbulent and precipitation less rapid downstream, nucleation occurs at the bottom of the water, below a diffuse boundary layer. In this case, the first and second step of equation 1 is no longer instantaneous and may be dependent on the advective mixing timescale of the stream rather than the reaction kinetics of equation 2. The process of carbon sequestration may also be altered by the change in control on reaction speed, with likely reduced rates of mineralization where precipitation is not occurring in the form of carbonate rafts. Where mineralization is decoupled from ingassing and occurs below a diffusive boundary layer at the base, this may also affect pollutant co-precipitation as availability of ions will be controlled by both advective mixing above the boundary layer and diffusion across it, rather than strictly by thermodynamic distribution of ions. Where a precipitate is bio-influenced, the rate, location and even trace element co-precipitation will also be influenced and may depart from strict thermodynamic expectations. Consequently, it is recommended that simple representations of these systems are not used outside of the small area characterised by carbonate raft precipitation at Brook Bottom. Within the middle zone, the carbonate-coated microbial filament deposited at Consett suggests a very low saturation regime and kinetic forcing (Figure 3.13). This microfacies correspond to bio-precipitates creating the close spatial arrangement of the calcite crystals around filamentous structures (Shiraishi et al., 2008). Furthermore, the deposition of this microfacies is characteristic of events possessing high hydraulic energy which break down the microbial filaments leaving detached crystals which are reworked to form intraclastic associations. In Brook Bottom, the middle zone corresponds to the deposition of reworked carbonates as neomorphic-sparry crust microfacies. This would imply that both carbon and pollutants sequestered in these carbonates are being transferred down the system and likely deposited in

distal parts. Similarly to the proximal- distal transition, the middle- distal transition is marked by no change in CSI variance within the zones, but R values show a sudden decrease of 10^7 m.s-1 between samples BB13 and BB16 at Brook Bottom, and of 10^2 m.s-1 between samples DB6 and DB18 at Consett (Figure 3.13). Classic “microbialite” fabrics (micro-peloidal and clotted micritic fabric) arise under low to middle saturation regimes and occur in most locations within the distal zone of Brook Bottom and Consett (BB10, BB13, BB16, C5, C6, DB12), despite the lack of biofilm influence in proximal Brook Bottom (Figures 3.13 and 3.14). Consequently, a high proportion of distal zone precipitation suggests bio-influence and bio-induction. There is further evidence of reworking via abundant polyshaped carbonate facies. In addition, neomorphic sparry crusts occur in all sites within this zone, and EBS-SEM analysis indicate that these crystals underwent dissolution and recrystallization leaving the interstices filled by organic-rich materials (Figures 3.9.C and 3.9.D). Consequently, it is hypothesised that the organic filaments are not primary precipitates. Continued reworking, combined with neomorphism and the assumed thermodynamic linkage between the water and the precipitate at these sites requires careful interpretation. The increasing dominance of microbially altered precipitation will further cause the system to deviate from thermodynamic expectations. Moreover, mass transfer downstream and / or back into solution implies that mass deposited upstream may be transferred out of the system entirely, potentially reducing the effectiveness of the carbonate deposit as a whole to form a stable carbon or pollutant sink. This lends support for future studies to determine whether this loss of mass is a risk to carbon sequestration or passive remediation schemes.

3.5.3 | Comparison to natural systems

3.5.3.1 | Resemblance of anthropogenic systems with natural travertine and tufa carbonates

The depositional systems described here present a stronger resemblance to travertine than tufa systems, although travertines are normally deposited from geothermally heated waters (Pentecost, 2005; Gandin & Capezzuoli, 2008). The dissolved inorganic carbon records are more elevated for travertines ($>10 \text{ mmol.L}^{-1}$) than for tufa carbonates ($<8 \text{ mmol.L}^{-1}$) (Pentecost, 2005; Gandin & Capezzuoli, 2008), which is consistent with the high concentrations of carbonate and bicarbonate reported in this study. Similarly, the depositional rates for anthropogenic systems (3.16 m.year^{-1}) are similar to travertine environments (centimetres to metres annually) but dissimilar to tufa (millimetres to centimetres annually) (Pentecost, 2005; Gandin & Capezzuoli, 2008). This study of anthropogenic systems has revealed the deposition of shrub, dendrite and globular style sparry-calcite crust and rafts, and less importantly clotted micrite micro-crystals. The first array of carbonate styles is similar to the range of crystal types present in travertine systems (where dendritic, bladed, or spherulitic precipitates are common) whereas micritic to micro-sparitic crystals are more common in tufa environments (Pentecost, 2005; Gandin & Capezzuoli, 2008).

Here, anthropogenic carbonate sedimentary systems are compared to the travertine models of Capezzuoli et al. (2014) to further investigate the similarity between these well-studied systems and the relatively limited information available for anthropogenic settings (Figure 3.12). Like anthropogenic systems, travertines are also divided into three different environments: vent environment (proximal), slope environment (middle) and distal environment, facilitating comparisons among them.

3.5.3.2 | Macroscopic features

In proximal environments, travertines accumulate around discrete springs associated with convective hydrothermal systems (Capezzuoli et al., 2014; Fouke, 2001) (Figure 3.12). Depending on the chemical and physical characteristics of these thermal waters, irregular masses of filamentous bacteria may locally colonise pool and channel margins in the vicinity of the vent (Capezzuoli et al., 2014) (Figure 3.12). The resulting macro-morphologies are represented by circular mounds and linear-to-arcuate fissure ridges (Capezzuoli et al., 2014) (Figure 3.12). Travertine fissure ridges mainly develop on brittle-fracturing bedrock exposed at the surface, while isolated thermal springs, such as towers, pinnacles and mounds, generally form on unconsolidated sediments (Hancock et al., 1999; Brogi & Capezzuoli, 2009). At the water surface, travertine might form rapidly and quickly develops into steep-sided constructional morphologies as a result of the nucleation of solid crystals within the surface tension layer. Anthropogenic carbonates also occur within pools and barrages comparable to the steep-sided constructional morphologies and mounds (Figure 3.12), but the swampy raft and polycrystal-rich proximal zone of anthropogenic carbonates are quite unlike the hard proximal deposits of travertines, with their characteristic positive relief. Comparison is straightforward in the middle zone, where terraces (gently inclined slope deposits) and terrace fronts (steep slopes around graben fault margins) (Altunel & Hancock, 1993b) closely resemble the elevated barrages present in the middle zone of anthropogenic carbonates (Figure 3.12). The distal zone of travertines is typically of low relief with the development of marshes (Guo & Riding, 1998), shallow lakes (Sant'Anna et al., 2004) or alluvial plains (Brogi et al., 2012). They are specifically transitional environments where travertine fabrics grade imperceptibly into tufa fabrics and biotic controls on depositional processes progressively increase (Rainey & Jones, 2009). The same gradational transition is found in the distal zone of anthropogenic carbonates, which exhibit low relief within waterfall settings and where the developing

impounded pools and the biomass biofilm significantly influence carbonate precipitation (Figure 3.12).

3.5.3.3 | Microscopic features

Travertines also exhibit carbonate raft microfacies formation at proximal sites reflecting similar coupling of mineral precipitation at the air-water interface as gas exchange, although the gas is exsolving, as in equation 3, rather than dissolving, as in equation 1, and the rate is governed by the dissociation of bicarbonate (Dreybrodt et al., 1997) not equation 2 (Figure 3.12). Large domes forming around vent resurgence points are characterised by a vast array of crystal forms, from coarse dendritic to platy and spherulitic calcite (Jones & Renaut,

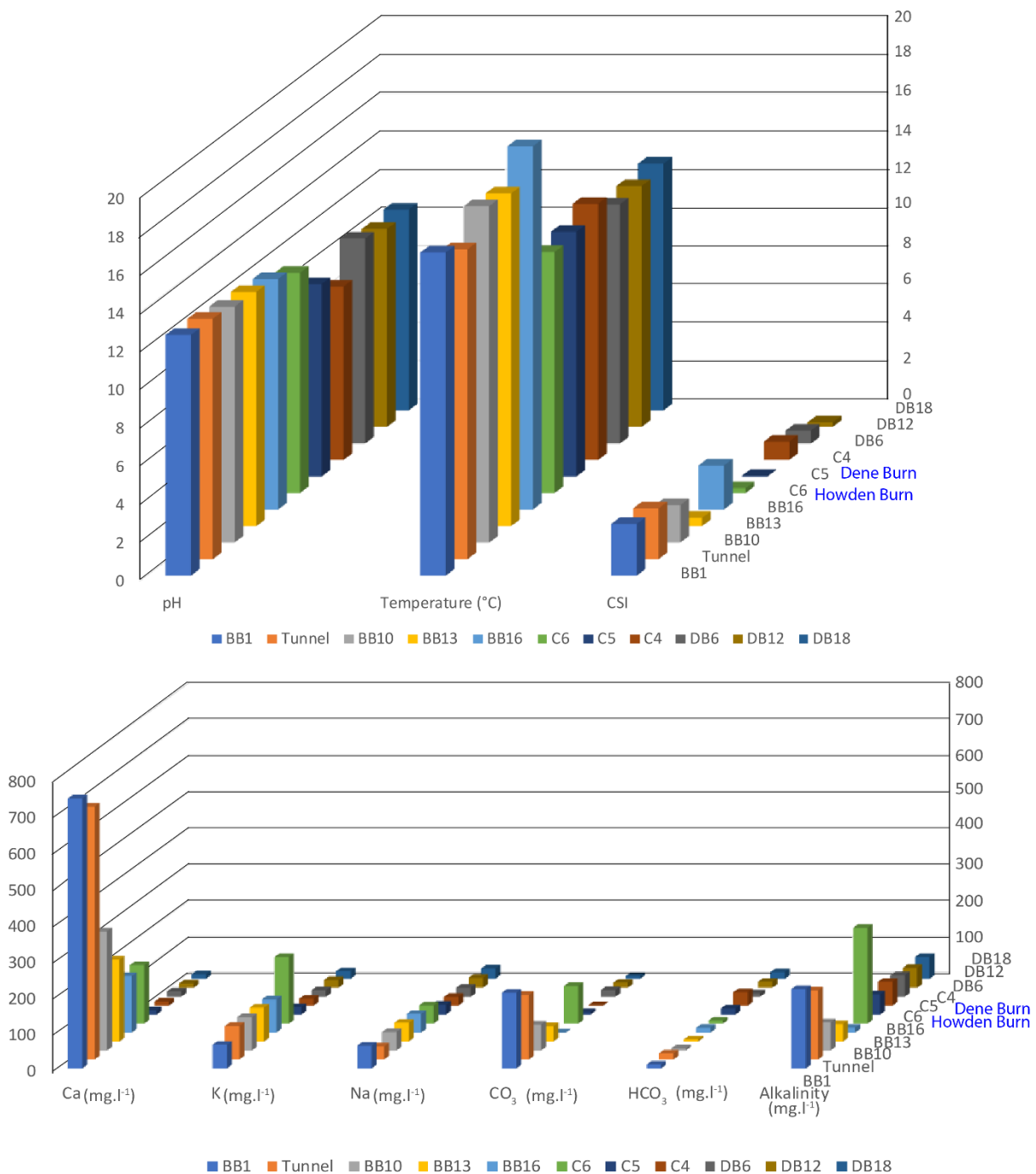


Figure 3.13: Charts showing the pH, temperature and Calcite Saturation Index (CSI), and the major ions and total carbonate alkalinity for the Brook Bottom and Consett samples.

1996, 1998, 2010) (Figure 3.12). Shallow pools in the vicinity of the vent are often associated with micritic to microsparitic laminae which may build up into small (millimetre to centimetre scale) shrubby growths (Capezzuoli et al., 2014) (Figure 3.12). Shrubs are also deposited in the proximal zone of anthropogenic carbonates within shallow pools (Figure 3.12). Chafetz et al. (2018) also report a biogenic influence on the formation of shrubby carbonates. The shallow

plumbing of geothermal systems, representing conduits for the upwelling of thermal water, is lined by variably shaped calcite/aragonite crystals (sparitic, acicular, dendritic and platy) developed into non-porous, sub-vertical crystalline laminated crusts (banded travertine: Altunel & Hancock, 1993a,b, 1996; Della Porta, 2015; Gandin & Capezzuoli, 2014; Uysal et al., 2007, 2009, 2011), but these are not comparable in origin to the crusts forming below open water in the anthropogenic systems (Figure 3.12). The lack of these crusts in travertines may reflect the ubiquitous biofilms, making them more comparable to Consett. In the middle zone, travertines display a diverse range of lithofacies (crystalline crust, shrubs, coated bubbles and paper-thin rafts) (Figure 3.12). Similarly, rafts are also deposited in the middle zone environment in this study. In the distal zone, travertine deposits are often dominated by lithoclastic material (hillwash breccia), but coated grains, in situ coated macrophyte stems and subordinate, massive bedded layers of clotted peloidal micrite may develop (Capezzuoli et al., 2014) (Figure 3.12). This compares well with anthropogenic systems, in which distal sites are characterised by the formation of clotted micrite and reworked/altered material such as carbonate-coated microbial filament and neomorphic sparry crust (Figure 3.12).

3.5.3.4 | Differences between travertine and anthropogenic systems

At the macro-scale, travertines present a more diverse range of environments represented by thermal springs, pools, channels, towers, pinnacles and mounds (Capezzuoli et al., 2014), whereas anthropogenic systems only present pools and low-angle terraced slopes. However, comparatively more research has been performed in natural settings and greater diversity of microfacies can be found in anthropogenic systems. Regardless, the proximal zone within anthropogenic systems is distinctly different from travertine environments. The middle zones are more comparable, but terraces and range-front sheets (Capezzuoli et al., 2014) are not geomorphologically identical to the elevated barrages of anthropogenic systems, which share morphological and possibly microfacies similarities with tufa phytoherm constructions

(Pedley, 1992). The travertine middle zone provides evidence of a wide range of microfacies (crystalline crust, shrub, coated bubbles and raft) (Capezzuoli et al., 2014), while anthropogenic microfacies are considerably more limited (raft and reworked carbonates). As with the overall diversity of systems, this may simply reflect less work carried out in anthropogenic systems. The distal zones are highly similar, despite the continued presence of barrage-like waterfall settings in anthropogenic systems unlikely the alluvial plain and shallow lakes for travertines (Capezzuoli et al., 2014).

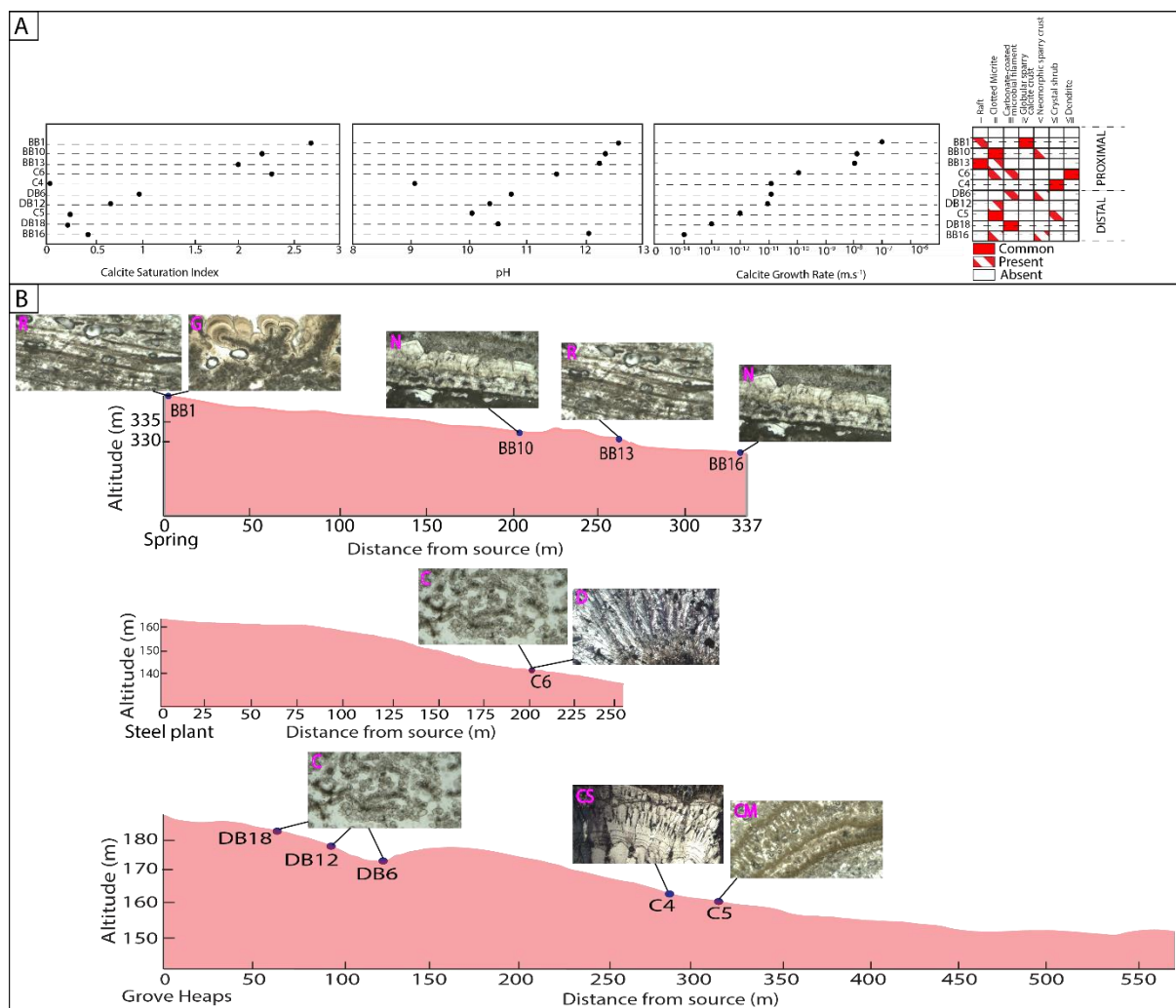


Figure 3.14: (A) Diagram showing the Calcite Saturation Index (CSI), pH, calcite growth rate (R) versus distribution of microfacies according to the sample locations at Brook Bottom (BB) BB1, BB13, BB10 fresh, BB10 old deposit, BB16 and Consett (C) freshwater samples in Howden Burn (C6) and Dene Burn (DB) (C4, C5, DB6, DB12, DB18). (B) Depositional model summarising the lateral changes of the dominant microfacies: Coated vegetative remains and carbonate raft (R), Micro-peloidal and clotted micritic (CM), Carbonate-coated microbial filament (C), Globular sparry calcite crust (G), Neomorphmic sparry crust (N), Crystal shrub (CS) and Dendrite (D).

3.6 | CONCLUSION

Anthropogenic systems show specific sedimentologies which can be partially comparable to those from travertine natural systems although requiring their own depositional models. Like travertines, anthropogenic sites develop in a tripartite division including proximal, middle and distal zones forming partially analogous geomorphologies. The major geomorphological differences are the dominance of swamp environments in the proximal zone, and the prevalence of tufa-like barrage-and-pool sequences in the middle and distal zones. Microfabrics in anthropogenic sites are similar to those from travertine environments but lack the sub-surface facies and, at extreme pH, exhibit a globular sparry crust without a clear equivalent in travertines. An initial depositional model is proposed here for anthropogenic sites as a means of stimulating further international research into these important geosystems.

This sedimentological model of anthropogenic carbonates shows that the formation of calcite minerals is complex and not homogeneous or purely driven by thermodynamic processes. Precipitation within the surface tension layer is reported here, which is likely to be directly controlled by the rate of CO₂ dissolution, but precipitation also occurs below the diffusive boundary layer and this may be influenced by advective transport in the water column. In addition, both diffusively limited and kinetically limited crystal forms are found, indicating differences in crystal assembly style which may alter trace element incorporation and co-precipitation rates. Interestingly, bio-influenced and bio-induced fabrics were identified suggesting that the site, rate, style and trace element incorporation into precipitates can be altered by the presence of microbial biofilms. Anthropogenic systems are as complex as naturally occurring tufa and travertine, and equally approachable to standard sedimentological analysis.

Proper understanding of the sedimentology of these systems will improve our ability to predict and manage the carbon sequestration and pollutant removal which are unique features

of this type of continental carbonate system. Without this knowledge, researchers will be challenged to predict the rates and locations of precipitation and to compare bulk sediment composition to water composition assuming they are driven by thermodynamic equilibrium. Finally, a better understanding of the extent of the reworking processes and the nature of neomorphism and recrystallization is needed to accurately predict the stability of the carbon and pollutant sinks during the temporal and spatial evolution of these systems after deposition.

3.7 | AUTHOR CONTRIBUTIONS

The idea for this manuscript arose from the discussion between all authors. Laura Bastianini executed the petrographic analysis and drafted the manuscript. Mike Rogerson made improvements through the whole manuscript. Ramon Mercedes-Martín provided insight on the facies descriptions and the discussion. Timothy J. Prior collected and interpreted X-ray diffraction data. William M. Mayes contributed to the hydrochemical data and their interpretation.

Chapter 4 – Ikaite formation in streams affected by steel waste leachate: first report and potential impact on contaminant dynamics

Laura Bastianini, Mike Rogerson, Alex Brasier, Timothy J. Prior, Kit Hardman,
Eddie Dempsey, Anna Bird & William M. Mayes.

This chapter investigates transient minerals produced at hyperalkaline sites with a novel approach for field characterisation and rapid laboratory confirmation of samples of interest (RQ3: Through novel coupled field and laboratory analyses, what evidence is there for transient mineral formation at anthropogenic hyperalkaline sites?). The transient minerals identified include the exceptional discovery of the carbonate polymorph ikaite. Through integration of field observations, laboratory characterisation and experimental work, this chapter considers the potential importance of transient mineral phases for trace metal dynamics at hyperalkaline sites (RQ4: What are the implications of transient mineral formation on trace metal dynamics?).

4.1| INTRODUCTION

Ikaite – calcium carbonate hexahydrate ($\text{CaCO}_3 \cdot 6\text{H}_2\text{O}$) – is a rarely-reported hydrous calcium carbonate mineral forming by precipitation from strongly supersaturated, at least marine salinity solutions (Brooks et al., 1950; Pauly, 1963). As a consequence of its limited conditions of formation and its thermal instability, this mineral is poorly documented worldwide. Since ikaite has been reported by Pauly (1963) forming at the bottom of Ikka Fjord in Greenland where cold (3°C) carbonate-rich submarine springs mixed with seawater, recent ikaite has been reported in the SCOPUS database from less than 20 locations worldwide, including inference of its presence from pseudomorphs and cavities. Glendonites, which are considered to be pseudomorphs after calcite, are used in paleoclimate and sedimentology studies to reveal past cold-water environments, although their distribution is highly irregular in

space and time. Rogov et al. (2021) provide an inventory of 700 occurrences of their associated carbonate pseudomorphs (glendonites) through the Phanerozoic. A significant body of evidence suggests that glendonite occurrences are restricted to cold-water settings (Rogov et al., 2021), however they do not occur during every glaciation or cooling event of the Phanerozoic (Rogov et al., 2021). While Quaternary glendonites and ikaite have been described from all major ocean basins, older occurrences have a patchy distribution, which reflects poor preservation potential of both carbonate concretions and older sediments (Tollefsen, 2020).

4.1.1 | Observations of recent ikaite

Glaring et al. (2015) returned to the submarine ikaite columns located in the Ikka Fjord in Southern Greenland to study the permanently cold (less than 6°C) and alkaline (above pH 10) habitat of a microbial community adapted to these extreme conditions where ikaite was first reported. In this study, the function of abundant groups of bacteria in the ikaite columns is unknown, but alkaliphiles, corresponding to obligate methylotrophs common in soda lake environments, may potentially participate in carbon cycling in the ikaite columns by degrading the products of the heterotrophic anaerobes. In addition, sulphate-reducing bacteria (SRB) appear to play an important role in the sulphur cycle in soda lakes and several orders of obligate anaerobic SRB were identified in the ikaite column interior. Rysgaard et al. (2013) significantly extended the Arctic range of ikaite, by discovering crystals of it in sea ice forming from waters with similar properties to those found in the original cold springs. Ikaite crystals have since been observed to precipitate within an hour in frost flowers forming from young Arctic sea ice (Barber et al., 2014). Ikaite also occurs in the anoxic marine sediments of Bransfield Strait on the Antarctic shelf (Suess et al., 1982), in sediment cores recovered from the Nankai Trough south of Japan (Stein, 1986) and the central part of the Zaire deep-sea fan (Jansen et al., 1987). It has been recognised as the parent mineral for thinolite pseudomorphs at the Lahontan and

Mono Lake basins in California (Shearman et al., 1989; Bischoff et al., 1993a). Larsen (1994) identified calcite pseudomorphs formed from ikaite in lacustrine strata and travertine in the Creede caldera of south-central Colorado, and a late Holocene hydrological study of Ohlendorf et al. (2014) show that carbonate crystals occurred in lacustrine sediments of Laguna Chaitel (south-eastern Argentina) indicating a syn- or post-depositional formation of ikaite.

Despite being often short-lived and difficult to analyse, the broad distribution of ikaite in ice and sediment at near-freezing temperatures means it can alter the behaviour of carbon and compatible ions within its environments of growth and alteration. It has been suggested that ikaite precipitation in sea ice may be critical in modifying the quantity of CO₂ dissolved in the surface ocean (pCO₂) (Rysgaard et al., 2013), providing a transient inventory of carbon which could either be retained if ikaite mostly dehydrates to calcite, or else released when the ice melts. As this carbon is released as CO₃²⁻_(aq) rather than as CO_{2(g)}, an increase in total alkalinity has been observed during the summer where dissolution of ikaite crystals is actively occurring (Rysgaard et al., 2013). The pH increase induced by these processes allows surface water to absorb further CO₂, providing a little-known but potentially important sink for carbon at the high latitudes (Ibid). Ikaite may be important for understanding water and carbon cycles on cold rocky planets such as Mars due to the suitability of formation conditions, and present strategies for recognizing hydrous carbonates including ikaite in Compact Reconnaissance Imaging Spectrometer results (Harner & Gilmore, 2015). Ikaite has been reported to have formed during winter months in cold springs waters at Shiowakka, Hokkaido, Japan (Ito, 1996, 1998). Dempster & Jess (2015) reported the occurrence of metamorphic ikaite porphyroblasts during an ultralow- temperature metamorphism with an exceptionally low geothermal gradient in Dalradian calcareous slates and metadolostones of western Scotland.

In a ground-breaking exploration of anthropogenic environments, Boch et al. (2015) describe a similar cold-water process of ikaite formation in an Alpine stream affected by

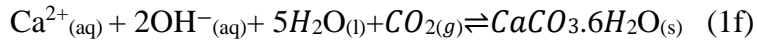
concrete leachates, which extends the observation of this form of calcium carbonate into environments altered by human activity. Within this occurrence, electric conductivity (EC) values ranged from 65 to 3050 mS.cm⁻¹ and sampling sites of the upstream and central sections revealed the overall highest pH (12.9) and EC values (3050 mS.cm⁻¹) in the beginning of the monitoring period during winter (January 2014). They note that metal mass sequestered into ikaite during the winter would be released back into the stream during the spring thaw, which fundamentally changes the hydrochemistry of the system. As the concrete-influence site they report lacks toxic trace metals, the primary influence is on carbonate chemistry. However, they note that were toxic ions present, spring-time ikaite dissolution might result in release as a pulse to the severe detriment of local water quality. These authors note that there is a severe knowledge gap of what this impact would be, or where it would likely be found. Similarly, Milodowski et al. (2013) observed ikaite within a lime-leachate affected site in Derbyshire UK, and Field et al. (2016) observed cavities formed after ikaite within fast growing, hyperalkaline speleothems (forming in tunnels below lime spoil) nearby at Peak Dale, Derbyshire, UK. The issue highlighted by Boch et al. (2015) may therefore be geographically extensive.

4.1.2 | Formation conditions of ikaite

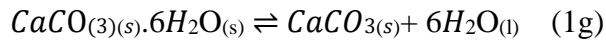
Precipitation of ikaite occurs in aqueous solutions near freezing conditions (temperature range of ca. -4 to 8°C; Boch et al., 2015), extending to negative temperature values where ionic strength is high enough to prevent freezing (down to -8°C; Hu et al., 2014; Papadimitriou et al., 2014). Crystallization of ikaite is also enhanced by elevated pressure conditions (>3 kbar at 25°C) (Marland, 1975; Shahar et al., 2005). However, even under favourable physical conditions, ikaite is characterized by a solubility higher than the anhydrous calcium carbonate polymorphs calcite, aragonite and vaterite (Brečević and Nielsen, 1993; Marion, 2001). These polymorphs are known to be inhibited by dissolved compounds such as magnesium, phosphate, sulfate and organic molecules, whereas the latter promote the nucleation of ikaite (Brooks et

al., 1950; Bischoff et al., 1993; Niedermayr et al., 2013). Bischoff et al. (1993) has shown that ikaite is undersaturated at all temperatures in seawater and in alkaline lakes, but rapidly reaches saturation near 0°C. Its precipitation in near-freezing marine sediments necessitates large additions of $\text{HCO}_3(\text{aq})$ to pore fluids from the diagenetic decomposition of organic matter (Bischoff et al., 1993). However, its crystallisation in tufas or alkaline lakes requires only small additions of Ca from springs (Bischoff et al., 1993). Kinetic experiments have demonstrated that ikaite is stabilized in natural environments by orthophosphate, which prevents the crystallisation of the more stable anhydrous form CaCO_3 but does not interact with the ikaite (Bischoff et al., 1993). Microbial activity associated with anoxic conditions can also induce ikaite formation via recycling of organic compounds in marine sediments (Stougaard et al., 2002; Olcott et al., 2005), and microbial diversity is well developed in ikaite tufa columns in Greenland (Stougaard et al., 2002). This very alkaline (pH 10.4) and cold (4°C) environment favours the development of a wide range of algae and metazoans (Buchardt et al., 1997; Kristiansen & Kristiansen, 1999) but also a diverse bacterial community, both in the column interior and at the surface, and very few archaea (Glaring et al., 2015). Biofilms on the surface of the columns, especially on newly formed ikaite material, is dominated by Cyanobacteria and phototrophic Proteobacteria, whereas Proteobacteria and putative anaerobic representatives of the *Firmicutes* and *Bacteroidetes* are concentrated in the column interior (Glaring et al., 2015). It seems likely therefore that growth of ikaite is significantly favoured by the presence of biofilms, to the extent that growth of this mineral is rare without it. The mechanism is not yet determined but may relate to the role of organic molecules impeding the formation of anhydrous forms in a manner analogous to that already observed in phosphate.

Natural and anthropogenic environmental conditions where there is abundant $\text{OH}(\text{aq})$ may also favour the formation and rapid deposition of ikaite, using calcium directly from the dissolved Ca-OH reservoir (Boch et al., 2015):



Ikaite precipitated by the forward reaction when temperature is low enough for this to be favoured may dissolve again by the reverse reaction (although high pH likely results in the carbon being retained as $\text{HCO}_3^{-}_{(\text{aq})}$ or may alter to calcite by dehydration.



This straightforward equilibrium underlies why ikaite grows so freely where stream waters interact with concrete, or other systems where soluble cement phases such as portlandite ($\text{Ca}(\text{OH})_{2(\text{s})}$) are present. The discovery of pseudomorphs after ikaite in a railway tunnel affected both by concrete leaching and by impacts from surface tips of lime spoil in the UK (Field et al., 2016) shows that Alpine winter conditions are not necessary, but this process can also be significant in low altitude settings. In such carbon-limited conditions such as streams affected by concrete leachates, whenever water temperature is low enough to favour ikaite formation, absorption of gaseous CO_2 into the alkaline solution and its hydroxylation with OH^- are likely the rate-determining parameters (Boch et al., 2015).

4.1.3 | Crystallisation of ikaite

Generally, anhydrous calcium carbonate (calcite, vaterite, or aragonite) occur as the dominant polymorphs throughout the natural environment, compared to hydrated (monohydrocalcite and ikaite), or amorphous forms (amorphous calcium carbonate: ACC) (Chaka, 2018; Chaka, 2019; Hu et al., 2020), which need specific conditions to be favoured as the majority precipitate. Very rapid precipitation favours non-classical mechanisms, where kinetic rather than thermodynamic conditions regulate how the precipitate is assembled (Oaki and Imai, 2003). In this situation, aqueous ions are hypothesized to condense into prenucleation clusters which retain the coordination of dissolved ions and aggregate to form ACC rather than thermodynamically favoured forms with more ordering (Chaka, 2018, Mergelsberg et al.,

2020). For the same reasons, highly hydrated structures such as ikaite, lansfordite, and nesquehonite would be expected to have a higher probability of kinetic formation, even if not thermodynamically favoured, due to the similar cation coordination in the solid and the solution (Hu et al., 2020). The hexahydrate ikaite structure is extensively hydrated with each Ca coordinated to six water molecules and one η^2 carbonate group (Chaka, 2018; Zhou et al., 2020). Demichelis et al. (2011) show this structure is stabilized by an extensive hydrogen bonding network. Formation of ikaite from amorphous prenucleation clusters may be promoted because the Ca–O_{ikaite} ion distances are very similar to the distances in water. Modelled values for the ion distances in ikaite are 2.443 Å (Demichelis et al., 2011), which is in close agreement with measurements from synchrotron X-ray diffraction (Lennie et al., 2004) of 2.469 Å at 243 K and of 2.46 Å for 8-fold Ca coordination in an aqueous environment with large-scale X-ray scattering (Jalilehvand et al. 2001), compared to 2.490 Å for Ca–O_{water} (Demichelis et al., 2011). Ikaite can therefore form directly from amorphous precursors, increasing its likelihood of formation where precipitation is rapid (Jalilehvand et al., 2001). In addition to similar ion distances between aqueous and ikaite Ca–O bonds, calcium coordination is also the same for ikaite and calcium carbonate in solution, and each carbonate ion is oriented in opposing directions to ensure a nonpolar structure (Gebauer et al., 2008; Montes-Hernandez & Renard, 2016). The dipoles are separated by 4.118 Å in both systems due to the coordinated waters in between, and provide an electrostatic driving force for alignment of the complexes in solution (Gebauer et al., 2008; Montes-Hernandez & Renard, 2016).

Thermodynamically, when in equilibrium with water, the free energy of ikaite is far more exothermic than calcite at -131 kJ/mol (Chaka, 2018; Mergelsberg et al., 2020) compared to -48.1 kJ mol⁻¹ (Inskeep and Bloom, 1985). The combination of electrostatic driving force and very exothermic heat of formation for ikaite in water-saturated conditions with high carbonate concentration is sufficient for the ion pairs in solution to self-organize into the ikaite

arrangement and form clusters, which explains the repeated observation that temperature is important in stabilising the structure (Gebauer et al., 2008; Montes-Hernandez & Renard, 2016). At higher temperatures precursor clusters with ikaite-like coordination will dehydrate and lead to formation of ACC, monohydrocalcite, and ultimately anhydrous Ca carbonate (Gebauer et al., 2008; Montes-Hernandez & Renard, 2016). However, at lower temperatures these clusters can grow and precipitate out as ikaite (Gebauer et al., 2008; Montes-Hernandez & Renard, 2016). In combination, the preference for a hydrated form of precursor clusters and the thermodynamic control on what coordination is favoured as order develops explains the occurrence of ikaite in cold conditions with rapid precipitation kinetics.

4.1.4 | Transformation of ikaite to other calcium carbonate polymorphs post-deposition

Monohydrocalcite and ikaite can crystallize from an initial product of ACC as well as precipitating directly. Similarly, ikaite has also been shown to transform to ACC, and subsequently to vaterite, if local conditions favour that sequence (Chaka, 2018). ACC is generally considered a hydrated form of Ca carbonate and has water content typically ranging from 0.5 to 1.4 mol of water per mole of CaCO_3 , although biogenic ACC may have up to 15.25% and an effective stoichiometry of $\text{CaCO}_3 \cdot \text{H}_2\text{O}$ (15.25 wt %) (Chaka, 2018). The reaction in either direction occurs without a change in the coordination of the cation, and are kinetically efficient. Ikaite can thus be considered one possible point in an Ostwald Step Rule sequence, which may occur where kinetic controls regulate precipitation, or where additives within the solution inhibit thermodynamically favoured forms. The order of the steps depends on the same combination of kinetically controlled precipitation determining the initial precipitate phase, and thermodynamic consideration determining stability. In an aqueous solution and under atmospheric pressure and high saturation (400 ppm pCO_2), the sequence of thermodynamic stability is dominated by water temperature (Chaka, 2018). Below 287.7 K, the sequence of thermodynamic stability for ordered forms (i.e. excluding ACC) from lowest

to highest (most stable) is $\text{CaO} \rightarrow \text{portlandite} \rightarrow \text{monohydrocalcite} \rightarrow \text{calcite} \rightarrow \text{ikaite}$. Thus, at low temperatures ikaite will likely form and likely persist. Above 287.7 K, ikaite and calcite change places, and from 292.1 K to 344.7 K, ikaite becomes less stable than monohydrocalcite. This stability switch at $\sim 14.55^\circ\text{C}$ is at slightly higher temperature than the observed upper limit for ikaite stability in the Alps ($\sim 8^\circ\text{C}$) but nevertheless is likely to be the cause of the springtime loss of ikaite observed by Boch et al. (2015).

4.1.5 | This study

Here, we provide the first report of ikaite in a steel waste leachate environment, at 135m altitude and at temperate latitude (54.85°N). This is significant, because there are a range of toxic metals and metalloids available in this system which may be accumulated in the ikaite inventory as it forms, concentrated and then released as the mineral transforms; there is therefore urgent need to close the knowledge gap identified by those authors (Boch et al., 2015; Chaka, 2018; Gebauer et al., 2008; Montes-Hernandez & Renard, 2016). We use novel in-situ and laboratory experimental approaches to address the questions of which ions may be accumulated in transient ikaite inventories, and how this complicates understanding of pollutant dynamics in steel waste-affected sites worldwide.

4.2 | MATERIALS AND METHODS

4.2.1 | Field work

4.2.1.1 | Description of the site

In Howden Burn, calcite saturation is enhanced by four alkaline discharges within the former Consett Iron and Steelworks. The site was operational from the middle of the Nineteenth Century until decommissioning in the early 1980s (Figure 4.1). Waste up to 45 m depth, including slag, flue dusts, ashes and construction and demolition rubble were accumulated after

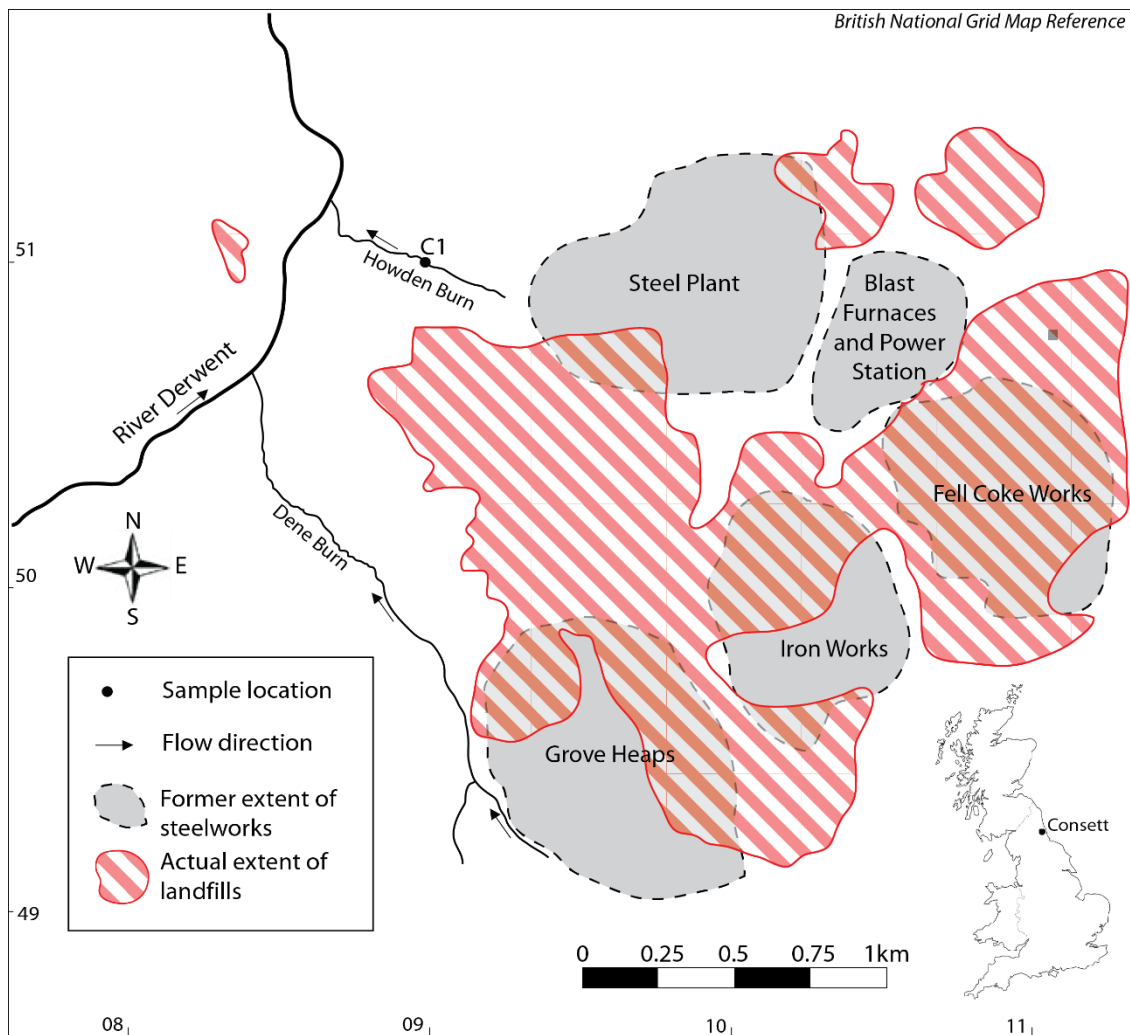


Figure 4.1: Location map of the studied sample HU-MR-/3CON1 (C1).

closure across an area of 2.9 km² (Harber and Forth, 2001). These materials are now stored in landfill, and the leachates emerging from them are alkaline ($[\text{OH}^-] = 10\text{--}130\text{mg.L}^{-1}$; $[\text{CO}_3^{2-}] = 10\text{--}110\text{mg.L}^{-1}$; $[\text{HCO}_3^-] = 110\text{mg.L}^{-1}$) because of the bulk chemical composition meteoric waters develop after interacting with these materials in the subsurface (Mayes et al., 2008, 2018; Riley and Mayes, 2015). These landfills can be a source of pollution to surface and ground waters (Mayes et al., 2008) (Figure 4.1). Iron and steel flue dusts contain metals including boron, lead, cadmium, halides, fluoride, zinc, chromium, arsenic, copper, nickel, and alkali metals and coke making provides inorganic compounds, for example zinc, fluoride, sulfates, phosphates and organic compounds such as fuels and oils (Harber and Forth, 2001).

Howden Burn leachate sources are mixed waters rich in K, Na, Ca, and sulfate (Mayes et al., 2008) (Figure 4.1). Sulfate concentrations are exceptionally elevated [$2,500 \text{ mg.L}^{-1}$] typical of a drainage from the former power station and coke works area of the workings (Figure 4.1). Within these locations, coke works spoil, ashes, and iron slags, which have a high sulfur content, were co-deposited with steel and blast furnace slag (Harber and Forth, 2001). The very high potassium content of Howden Burn leachate sources probably derive from highly soluble potassium oxides associated with flue dusts and ashes deposited with slag (Mayes et al., 2008). The contaminants of most environmental concern are those potentially soluble at high pH, because they form oxyanions (e.g. As, Cr and V), which can be very mobile as they sorb weakly to soils and sediments (Cornelis et al., 2008; Mayes et al., 2011). Alkalinity and high Ca content of emerging waters cause rapid carbonation in streams affected by the leachate, resulting in sediment deposits described elsewhere in this thesis (Chapters I and II). The deposit at Consett comprises a tufa barrage system, with barrages measuring 20 cm in height and predominantly composed of buff-coloured calcitic tufa carbonate (Bastianini et al., 2019, 2021).

4.2.1.2 | Strategy for finding ikaite

WM had previously noticed white growths on the surface of the carbonate deposit when there was snow on the ground one week before collection of the sample (29th January 2019). Consequently, he led a sampling team which visited the site later during the same cold period (average air temperature of 0.9°C on 30th January 2019, -4.35°C on 3rd February 2019 and 1.1°C on 5th February 2019 after CEDA Archive from the nearest station of Durham) (Figure 4.2).

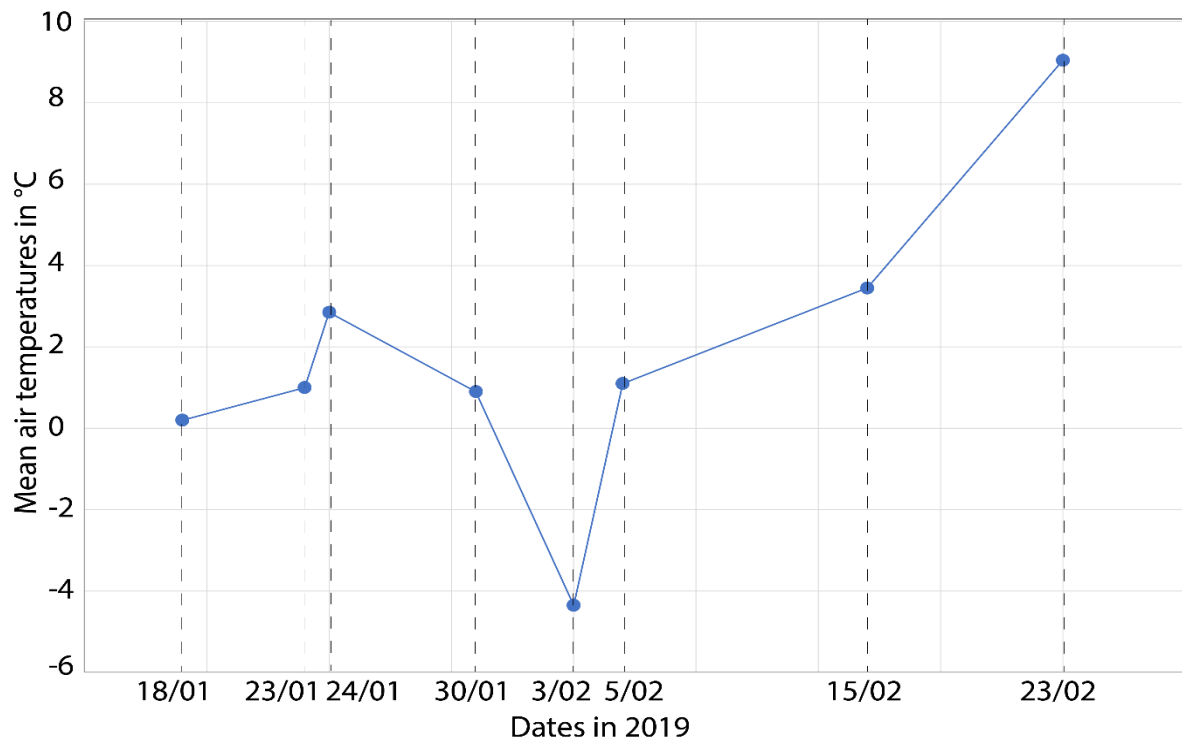


Figure 4.2: Graph depicting the average air temperatures in Durham versus the dates after CEDA Archive.

The sampling team looked for crystalline growths not present in warm weather, focussing on the previously reported scattering of cm-sized euhedral to subhedral white grainy crystals (Figure 4.3), which were suspected ikaite. Rising above (and apparently cemented to) the buff-coloured tufa carbonate during this visit were such a scattering of cm-sized euhedral to subhedral white crystals, dominantly located along the barrage crests (Figure 4.3). The sampled carbonate precipitate described here is a white crystalline material which exhibits a grainy consistency (Figure 4.3) taken from one of these growths. All these precipitates formed within a few days only, and such precipitates are not found at the site outside of similar very brief spells of unusually cold weather.

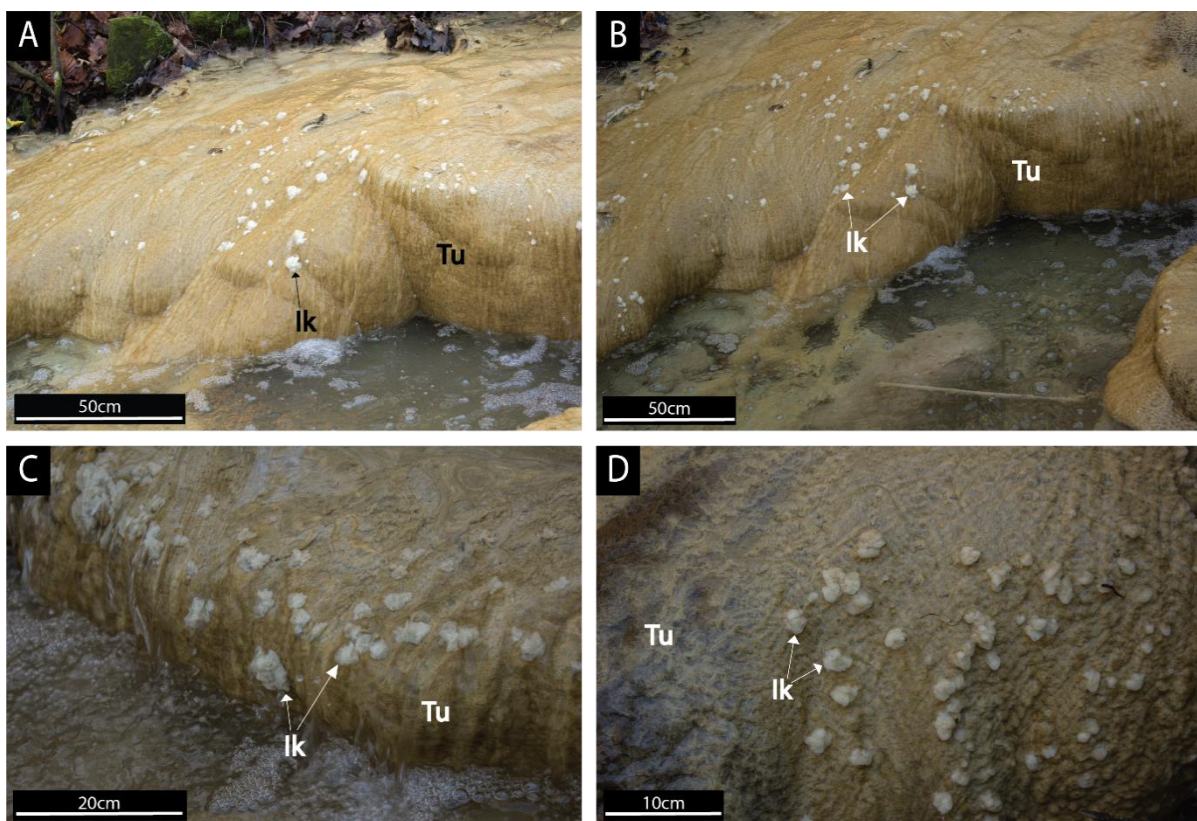


Figure 4.3: Macroscopic images of the Consett freshwater sample HU-MR-/3CON1 depicting a scattering of cm-sized euhedral to subhedral white crystals of ikaite (Ik) rising above and cemented to the buff-coloured orange-red oxidated tufa carbonate (Tu).

4.2.1.3 | Collection of the sample

The sample (HU-MR-/3CON1 — C1) was taken on 5th February 2019 along a pre-established calcite saturation index transect (Mayes et al., 2008, 2018; Riley and Mayes, 2015) within Howden Burn (Figure 4.1). This sample was recovered with a sieve to prevent heating by contact with skin and handled by plastic tweezers (Figure 4.4). Initial identification was by ATR-Fourier Transform Infrared (FTIR) spectroscopy using a portable Agilent 4300 Portable FTIR immediately after sampling, on the stream bank. This innovative approach minimised the risk of alteration of ikaite crystals after sampling, and we are not aware of this approach being previously used. The peaks were analysed and characterized by the MicroLab FTIR Agilent Software. Before identification by ATR-FTIR, the sample was air dried on site and the measurement surface was cleaned with ethanol. Initial scans checks for interferences by water molecules (peak absorption at 3182 cm⁻¹) were undertaken which helps verify that the sample

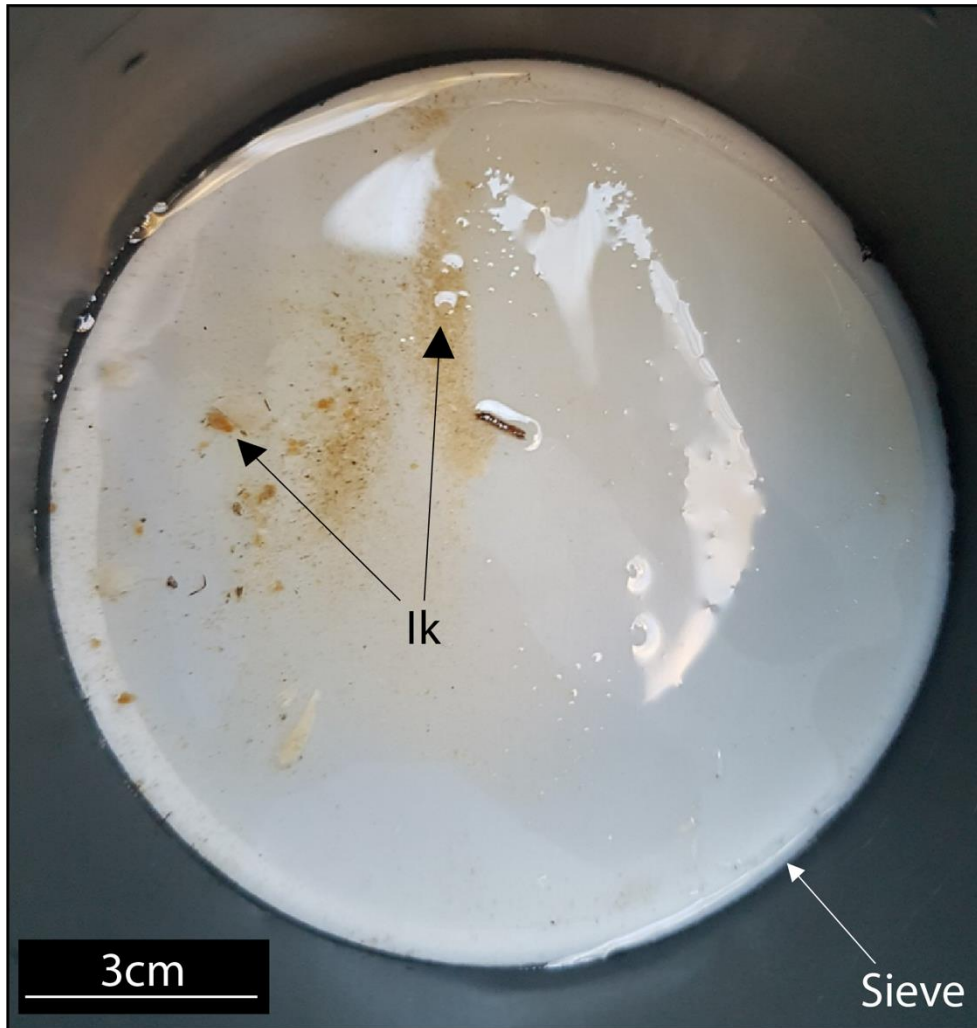


Figure 4.4: Recovered sample of ikaite (Ik) within the sieve.

was dried. The measurement was performed once. The sample of ikaite was subsequently transported in a cooler bag under ice to the laboratory.

During our sampling, on-site measurements of major physico-chemical parameters (pH, electrical conductivity and water temperature) were performed using a Myron L Ultrameter® calibrated with pH 4, 7 and 10 buffer solutions and a 1,413 μS conductivity standard, to confirm the system had not changed since previous sampling.

4.2.2 | XRD

On return to the laboratory, the sample of ikaite was immediately analysed (within 6 hours of sample collection) using a very long collection of single crystal XRD. During

laboratory investigation, the sample was stored over dry ice. A small portion of the sample was removed from the sample bag and placed under a microscope. A portion of this, representative of the bulk, was rapidly mounted at the end of a glass fibre on a goniometer and the sample transferred into a nitrogen gas cryostream at 250 K. The sample was examined by X-ray diffraction; a precession image was recorded while the sample was rotated about ϕ .

Diffraction data were collected using a Stoe IPDS2 image plate diffractometer operating with Mo radiation at the department of Chemistry and Biochemistry, University of Hull. A full hemisphere of diffraction data were collected in a series of omega scans ($180 \times 1^\circ$) with a 120 s exposure time. The data were scaled, merged, and corrected for absorption using the program Sortav. Non-hydrogen atoms were refined using the published positions as the starting model and hydrogen atoms of water were identified from difference Fourier maps and placed subject to chemically-sensible restraints on bond lengths and angles. The program SHELXL-2018 was utilised for least squares refinement of the crystal structure. (Reference is Crystal structure refinement with SHELXL, G. M. Sheldrick, *Acta Cryst.*, 2015 C71, 3-8.)

4.2.3 | Microscopy

To identify the micro-texture and the micro-scale fabrics, a Cryo-Scanning Electron Microscope (Zeiss EVO 60) attached to an EDS detector (Oxford Instruments INCA System350 with Silicon Drift Detector) was used at the department of Chemistry and Biochemistry, University of Hull.

4.2.4 | Trace Element content

Table 4.1 illustrates the different data which are characteristic for the method used (LA-ICP-MS U-(Th-)Pb data). This table is divided into four sections – laboratory and sample preparation, information about the laser ablation system, information about the ICP-MS instrument, and details of the data processing approach.

Trace element partition coefficients, Kd_x , were calculated from the data using:

$$Kd_x = \frac{X_{Solid}/Ca_{Solid}}{X_{Solution}/Ca_{Solution}}$$

where X_{Solid} represents the concentration of a certain trace element in the studied sample of ikaite, $X_{Solution}$ represents the concentration of a certain trace element in the solution (as we do not know precisely when the crystal grew, we use long-term average data from the site; Hull et al., 2014; Riley & Mayes, 2015; Gomes et al., 2018; Bastianini et al., 2019), Ca_{Solid} is the concentration of calcium in the studied sample of ikaite determined by LA-ICP-MS.

Table 4.1: Reporting template (metadata) for LA-ICP-MS U-(Th-)Pb data.

Laboratory and Sample Preparation	
Laboratory name	Geography, Geology and Environment (University of Hull)
Sample type/mineral	Ikaite grains, mounted on milled puck
Sample preparation	Grain mounting
Imaging	None
Laser ablation system	
Make, Model and Type	Applied Spectra, RESolution-SE 193 nm
Ablation cell and volume	Laurin Technic S155 two volume cell
Laser wavelength	193 nm
Pulse width	5 ns
Fluence	5 J.cm ⁻¹
Repetition rate	20 Hz
Ablation duration	Scan length dependent
Spot diameter	100 µm
Sample mode/pattern	Line scans
Scan Speed	0.005 mm.s ⁻¹
Carrier gas	He + N ₂ in the cell, Ar carrier gas to torch
ICP-MS Instrument	
Make, Model and Type	Agilent 8800
Sample introduction	Ablation aerosol mixed with Ar and sent to ICP-MS
RF power	1170 W
Nebuliser gas flow	Ar 0.80 l.min ⁻¹
Detection system	Electron multiplier in counts per second mode
Masses measured	9, 10, 25, 27, 31, 43, 45, 50, 53, 55, 59, 60, 65, 66, 87, 89, 103, 110, 124 135, 206
Integration time	9, 10, 45, 53, 59, 60, 66, 89, 103, 110, 124=0.1s; 135, 206=0.05s; 25, 87=0.002; 43, 50=0.02;27=0.001;31=0.025;55=0.004;65=0.0333
Data Processing	
Calibration strategy	612 used as primary reference material, 610 used as secondary for validation
Internal Reference	Ca43 semiquant
Data processing package	Iolite v4, Data Reduction Scheme - Standard Trace Elements - quantitative (Longerich et al., 1996)

4.2.5 | Laboratory experiments

Many attempts (30 in total) were made to create ikaite according to the method of Lennie et al. (2004) and Tollefsen et al. (2020). This experiment was designed to assess the

partition coefficient and ion substitution of ikaite in order to elucidate the trace elements that can be substituted to ikaite. These trace elements are found in the springs which precipitate ikaite and may cause the waters to become polluted and toxic to aquatic life. Ultimately, this experiment would potentially help in decontamination of these rivers.

According to the recipe of Lennie et al. (2004), LB prepared solution (1) by adding 3.2g of $\text{CaCl}_2 \cdot 2\text{H}_2\text{O}$ dissolved in 100mL of deionized H_2O and solution (2) by adding 4.6g of Na_2CO_3 and 0.5g of $(\text{NaPO}_3)_6$ dissolved in 150mL of deionized H_2O . These two solutions were kept at 3°C for 2 days to allow crystallisation of ikaite. The two solutions were subsequently mixed within an insulated box containing ice to maintain the temperature at 3°C . Sodium polyphosphate was added to inhibit nucleation of calcite. Single crystals formed were recovered by filtration, rinsed in methanol, and dried. Initial identification of precipitated mineral was by ATR-Fourier Transform Infrared (FTIR) spectroscopy using a portable Agilent 4300 Portable FTIR at the Department of Geography, Geology and Environment (University of Hull, UK) followed by an identification by X-ray powder diffraction (XRD) by TJP for confirmation at the Department of Chemistry and Biochemistry (University of Hull, UK).

Based on the method of Tollefsen et al. (2020), LB made a 50–50 mixture of two solutions: Solution 1) was artificial seawater. Solution 2) was prepared by mixing 10.6g of Na_2CO_3 and 8.4g of NaHCO_3 in 1L of deionized water at ambient temperature (15°C). When ~300 ml of mixture was obtained, the experiment was stopped. The resulting mixture was put in the fridge (5°C) overnight. The next day, the mixture was filtered and immediately after the precipitated mineral was collected. It was firstly identified by ATR-Fourier Transform Infrared (FTIR) spectroscopy using a portable Agilent 4300 Portable FTIR at the Department of Geography, Geology and Environment (University of Hull, UK) succeeded by an identification by X-ray powder diffraction (XRD) by TJP for confirmation at the Department of Chemistry and

Biochemistry (University of Hull, UK). Thereafter, the precipitate was stored in a freezer (-18°C).

4.3 | RESULTS

4.3.1 | Mineralogy

The FTIR spectra of the sample immediately after collection showed absorptions at 718 , 1485 , and 3182 cm^{-1} (Figure 4.5), which we compare to reported absorptions in calcium carbonate polymorphs (Table 4.2). The latter peak is typical of O-H stretching, and as the sample was carefully air-dried before analysis indicates the presence of abundant formation water. Absorption at 1485 cm^{-1} reflects asymmetric CO_3 stretching (Gunasekaran et al., 2006), albeit with a small instrument-specific translation from the typical calcite absorption at $\sim 1450\text{ cm}^{-1}$ (Ibid). Absorption at 718 cm^{-1} is symmetric CO_3 deformation, which is correct for ikaite but is not reported from ACC and is present at lower wavenumber in monohydrocalcite.

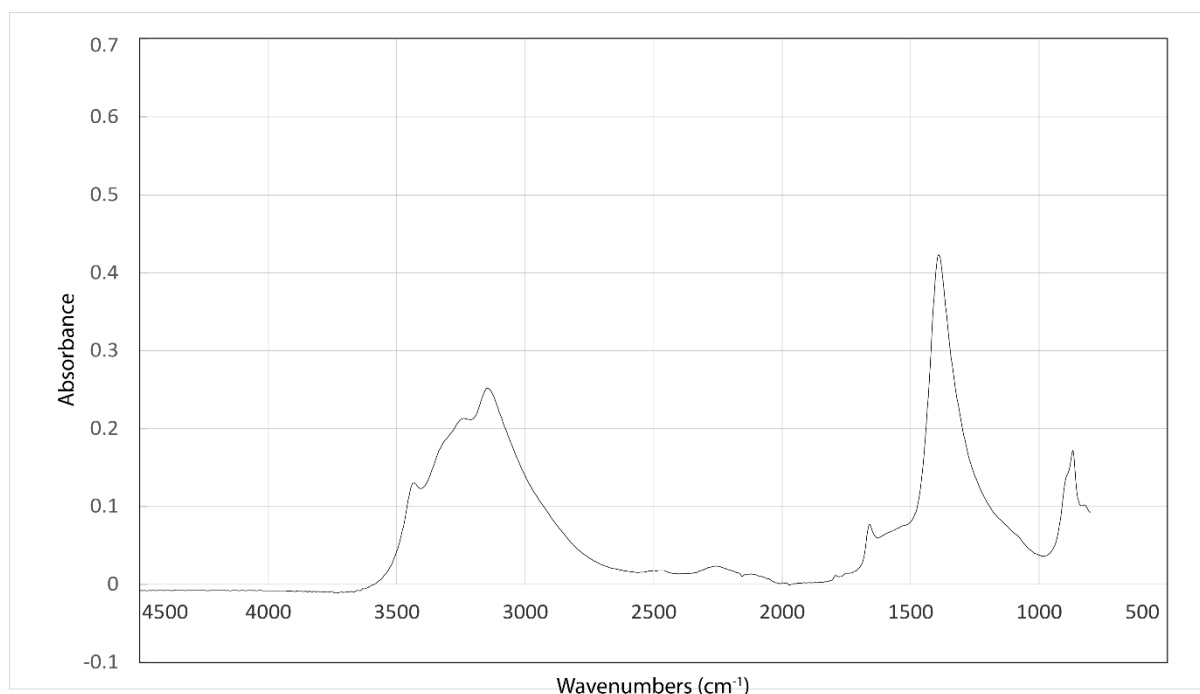


Figure 4.5: FTIR spectra of the sample of ikaite C1.

A white crystalline block (field sample) of size $0.38 \times 0.30 \times 0.28\text{ mm}^3$ was transferred to the single crystal diffractometer and held at 250 K in a nitrogen gas cryostream. The sample

was examined by X-ray diffraction; a precession image was recorded while the sample was rotated about phi. This pattern did not show the presence of rings characteristic of a powder, but a highly symmetric arrangement of spots consistent with a single crystal. The complete hemisphere of data was therefore collected from this crystal sample.

Table 4.2: FTIR review with the different peak diagnostic of the CaCO_3 polymorphs.

Reference	Wavenumber in cm^{-1}					
	Calcite	Aragonite	Vaterite	ACC	Ikaite	Monohydrocalcite
<i>Xyla & Koutsoukos, 1989</i>	714/848/876/1800	842/857/1080	714/745/848/857/1070			
<i>Gauldie et al., 1997</i>		701/1085	713/1066			
<i>Chakrabarty and Mahapatra,</i>	713/874	700/712/844/874/1083	744/844/854/876/1087			
<i>Mikkelsen et al., 1999</i>	712/1086/1436	705/854/1086	738/750/1077/1090		719/1070	
<i>Kontoyamis & Vagenas, 2000</i>	711/1085/1435	700/705/1084/1085	738/750/1074/1084/1089		718/1070/3120/3270/3434	
<i>Tlili et al., 2001</i>					722/873/1072/1485/3182/3240/3425	
<i>Coleyshaw et al., 2003</i>						
<i>Carter et al., 2009</i>	712/1086	701/1085/1431/1531	1075			
<i>Wehrmeister et al., 2010</i>	712/1086	701/1085	1075			
<i>Rodriguez-Blanco et al., 2011</i>	725/874/1090/1409/1805			1460/1645		
<i>Zhang et al., 2012</i>	713/875/1420	700/713/856/875/1440/1490	745/875/1440/1490	866/1418/1475		700/875/1408/1487

The sample examined was dominated by crystalline domain of ikaite, but there were other much smaller crystals present. Spots from several other domains (at least 4 domains) were present in diffraction images, but it was possible to integrate the data for the dominant phase without problems. The R_{int} value of 0.0263 confirms the excellent consistency of data from this domain. It was not possible to identify other phases using the raw diffraction images, but a simulated powder diffraction pattern (Intensity v. 2θ) produced from all of the data frames shows the presence of minor calcite in the block examined (Figure 4.6).

Diffraction data from the single dominant domain were integrated using standard procedures. The structure of ikaite ($\text{CaCO}_3 \cdot 6\text{H}_2\text{O}$) was refined against these data and this unequivocally confirms that ikaite is the dominant component. The structure obtained is in good agreement with earlier structure determinations. The coordination about the calcium ion is shown in Figure 4.7. The diffraction data and structure have been deposited at the CCDC

and are available free of charge from ccdc.cam.ac.uk/structures with the REFcode VIXQEB (1902435).

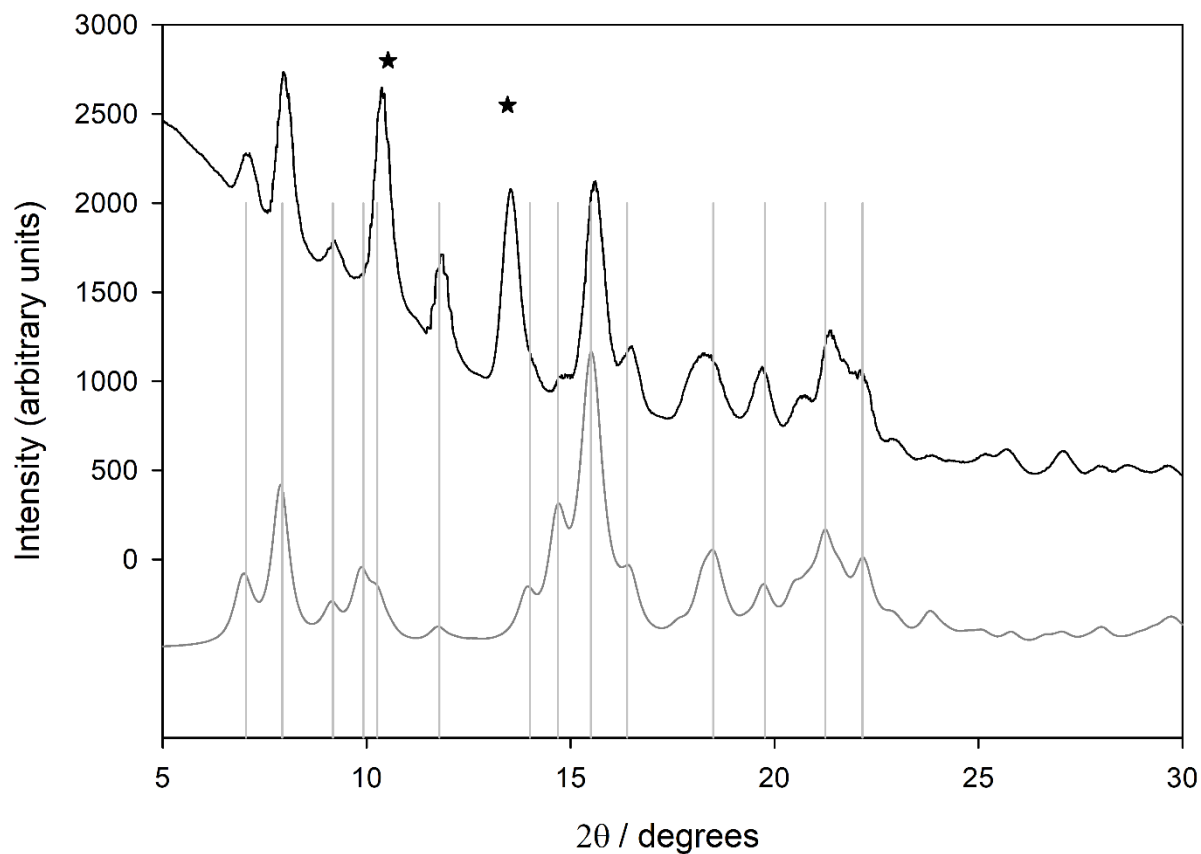


Figure 4.6: One-dimensional diffraction pattern collected from HU-MR-/3CON1 (solid black line). The grey line is the simulated pattern for ikaite (with peak positions highlighted as vertical lines). The two starred peaks correspond to calcite.

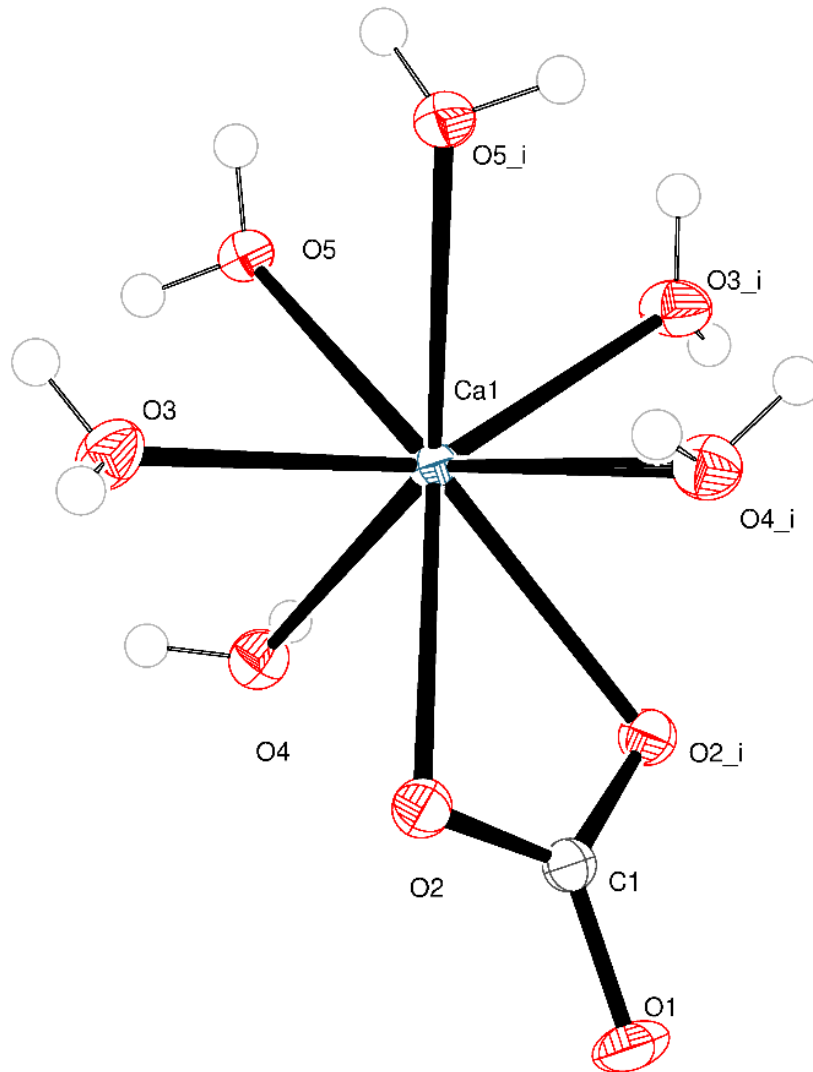


Figure 4.7: Coordination about the Ca^{2+} ion with atoms shown as 50% probability ellipsoids. Atoms labelled name i are generated by the symmetry operator $i = 1-x, y, \frac{1}{2}-z$.

4.3.2 | SEM

SEM images (Figures 4.8A-F) illustrate the shape of crystals from the carbonate crusts. Crystal sizes range from 200 to 1000 μm (Figures 4.8 A-E). Figures 4.8A-B depict smooth surfaces, which have ridges running in straight lines that are quite parallel to the faces on the larger crystal. A striking feature observed is the sigmoidal bending of crystal faces (“s-like”; Figure 4.8F). The SEM images (Figures 4.8A-F) show that the morphologies of these white crystals are consistent with those of monoclinic ikaite (cf. Demichelis et al., 2014), and

observed dimensions and habits are equivalent to those reported by other studies (Bischoff et al., 1993b; Ito, 1996; Omelon et al., 2001; Dieckmann et al., 2008; Rysgaard et al., 2012). However, there are some interesting differences between the crystals observed under the electron microscope in this study and those figured elsewhere. First, most earlier studies have illustrated pitted crystals that have apparently partially transformed into calcite (e.g. Figs 6A and 6D of Ito, 1996; Fig 2 of Tollefsen et al., 2020). This pitting is not evident in crystals we have examined, perhaps because the crystals were kept cold and imaged as soon as possible in a cryoSEM. Rather, Fig. 8 shows ikaite crystals in which some smooth faces are well developed, but there are clearly some stepped and kinked faces that are less favoured and less well developed. This stepping of some faces could either be the result of incomplete growth, or of partial dissolution (Snyder and Doherty, 2007).

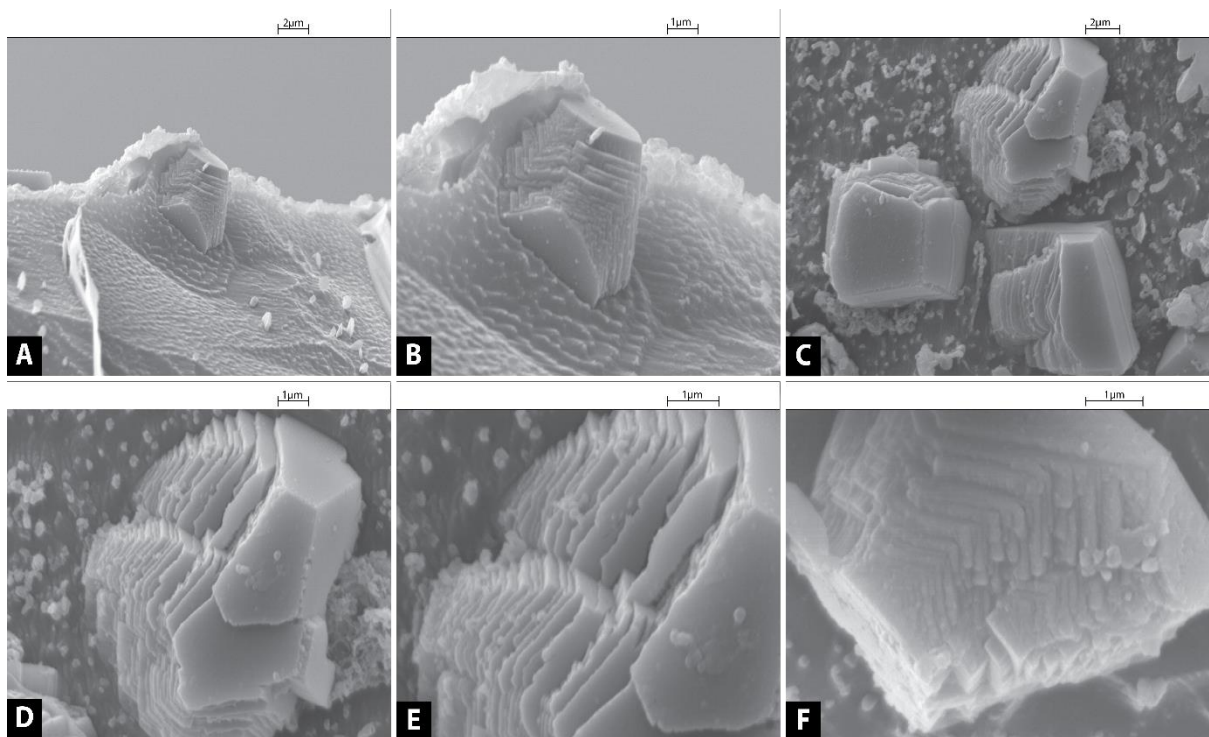


Figure 4.8: SEM images of the Consett freshwater sample C1.

The ridges running parallel to the best developed crystal faces (blue lines on Figure 4.8) could plausibly be interpreted as aligned crystal terminations (c-axis) of numerous small nucleating ikaite crystals. This would be analogous to ‘feather crystals’ of hot-spring

travertines, which align with their tips normal to the substrate to form ‘micro-terraced’ ridges on sloping surfaces, oriented perpendicular to the direction of flow of a thin film of (aragonite or calcite-precipitating) water (Gandin and Capezzuoli, 2014). That the ridges of Fig. 8A-8B are aligned parallel to the favoured faces of larger crystals suggests the stepped and kinked faces of the associated larger crystals (Fig. 8D-E) are likely also reflecting incomplete growth here, rather than dissolution following completed crystal development.

4.3.3 | Laser

Vanadium, chromium, nickel, zinc, cadmium and barium elements are present in trace amounts (median average concentration 0.001-0.17 mMol.Mol⁻¹), whereas manganese, copper and lead are two orders of magnitude more abundant (3.1-7.5 mMol.Mol⁻¹), and Sr is three orders of magnitude more abundant [81.4 mMol.Mol⁻¹]. In terms of dispersion, V, Cr, Mn, Ni, Zn, Cd and Ba attest of a low relative standard deviation lower than 1 [0.0009-0.16] but Cu, Sr and Pb are represented by a high relative standard deviation [26.7-71.19], which indicates values spread out over a wider range.

The trace element partition coefficients for the sample of ikaite are listed in the Table 4.3. All the partition coefficients are much higher than the range of partition coefficients for calcite and aragonite, except for Zn (6.11) which is within the range of calcite partition coefficients (0.9-27), and for Cd (3.13) which is below the range of calcite partition coefficients (4.5-66.1). The partition coefficients for ikaite of Cu, Cr, Mn, and Ni are 10 times higher than those of calcite, whereas Ba and Pb present a partition coefficient 100 times higher, and Sr 100,000 times higher in order of magnitude.

Table 4.3: Depicting the different partition coefficients for the elements sequestered in the sample of ikaite versus the partition coefficients of calcite and aragonite from the literature.

Measured values		Litterature data			
Metal	Partition coefficient (ikaite)	Partition coefficient range (calcite)	Reference	Partition coefficient range (aragonite)	Reference
Ba	3.22	0.04-1.2	Pingitore & Eastman (1984) Olsson et al. (1984)	1.48	Kretz (1982)
Cu	238.38	23.3-50	Kitano et al. (1980) Olsson et al. (1984)		
Cd	3.13	4.5-66.1	Lorens (1981) Olsson et al. (1984)		
Pb	280.30	0.64	Morse et al. (1999)		
Sr	16287.42	0.15-0.40	Mucci & Morse (1983)	0.22-1.83	Kitano et al. (1980) Kretz (1982)
V	0.45				
Cr	1.52	0.10	Kitano et al. (1980)		
Mn	72.03	3.1-13.1	Dromgoole & Walter (1990) Olsson et al. (1984)		
Ni	1.94	0.15-1	Lakshatanov & Kitano (1986) Olsson et al. (1984)		
Zn	6.11	0.90-27	Kitano et al. (1980) Olsson et al. (1984)		

4.3.4 | Laboratory experiments

Figure 4.9 and 4.10 show the FTIR spectra of the trials of making ikaite from the methods of Lennie et al. (2004) and Tollefsen et al. (2020) respectively. These spectra are diagnostic of ACC by two characteristic features: a very smooth and symmetrical peak at the wavenumber 1645cm^{-1} (Table 4.2), corresponding to O-H stretching, instead of a sharp and asymmetrical peak for ikaite at the same wavenumber (Figure 4.5), and the presence of an asymmetrical peak at 1050cm^{-1} (Figures 4.9 and 4.10), which is absent in the ikaite spectra

(Figure 4.5). The non-crystalline nature of these samples was confirmed by XRD, which showed no x-ray scattering and thus very poor crystallinity.

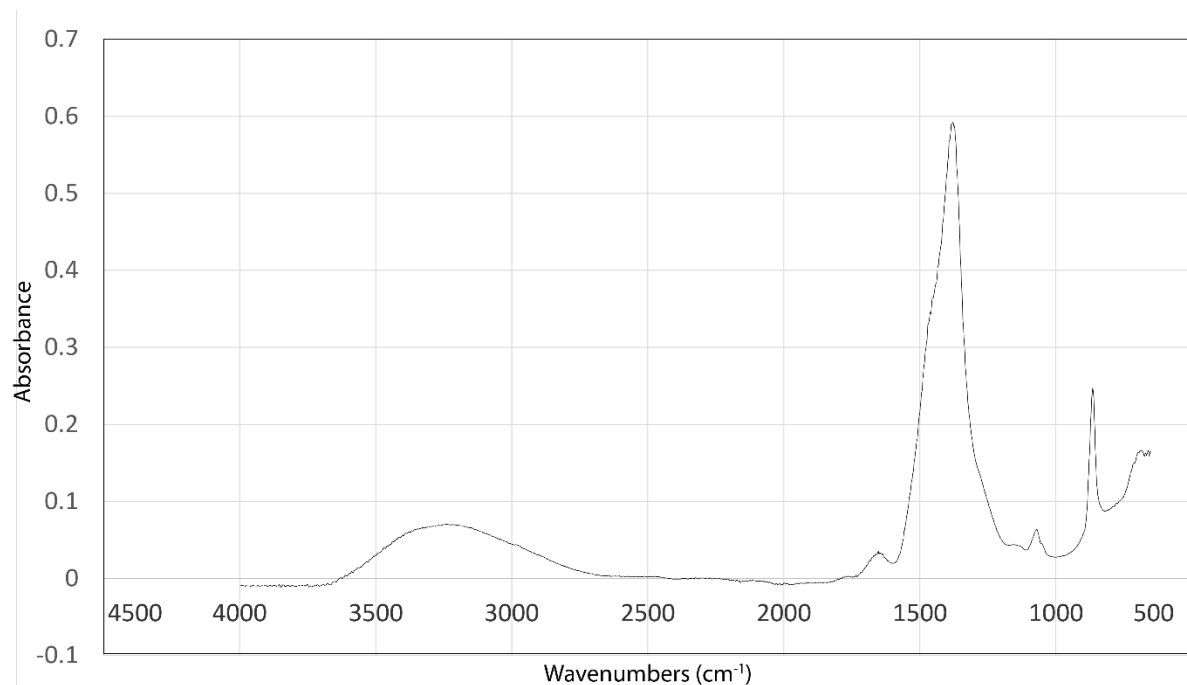


Figure 4.9: Trial of making ikaite following the method of Lennie et al. (2004) corresponding to ACC.

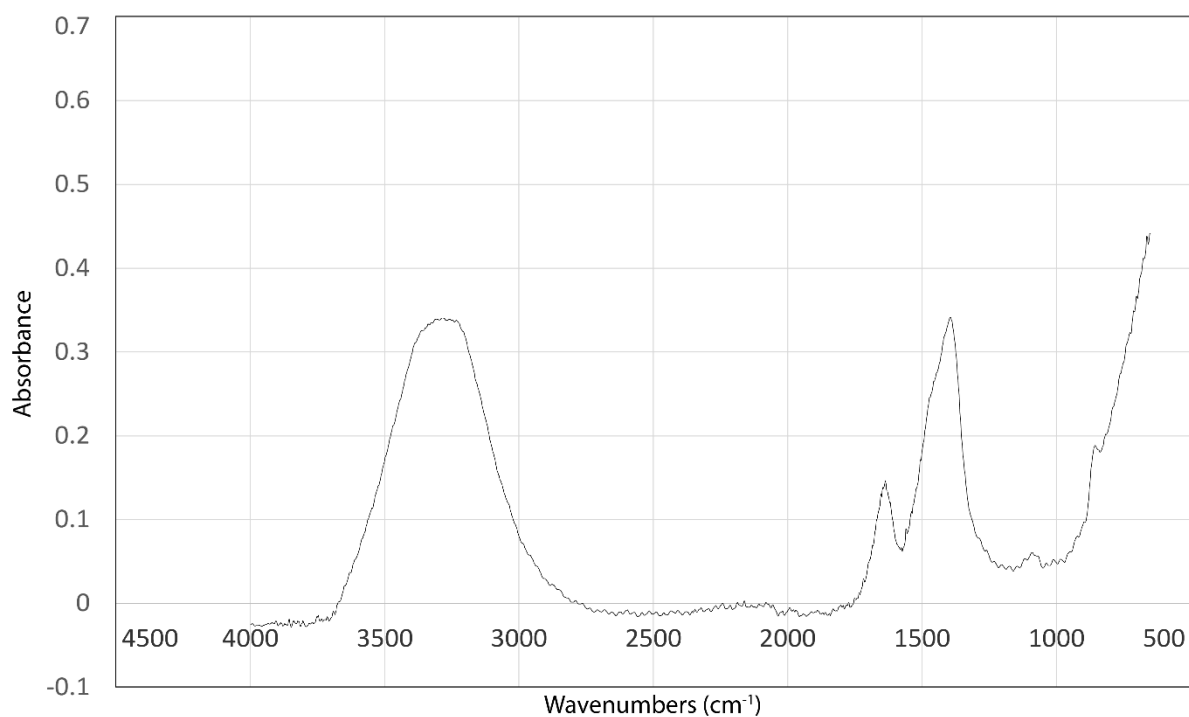


Figure 4.10: Trial of making ikaite following the method of Tollefsen et al. (2020) corresponding to ACC.

4.4 | DISCUSSION

4.4.1 | Discovery of ikaite in steel waste leachate.

We present the first report of ikaite formed in steel slag leachate sites where these transient growths may alter the dynamics of environmentally harmful elements. The sample we describe was recovered during a period with average air temperature of 1.1°C and water temperature of 9.9°C, and the previous two nights had minimum average temperature of -4.1°C (CEDA Archive from the nearest station, Durham).

This is within the stability range for ikaite (<-4–8°C) defined by Boch et al. (2015). Similar transient development of ikaite in steel-waste affected surface water may be very widespread, especially in the northern hemisphere. This potential is illustrated in Figure 4.11, which shows a range of sites at high and mid latitudes which are candidates for this process spanning Canada

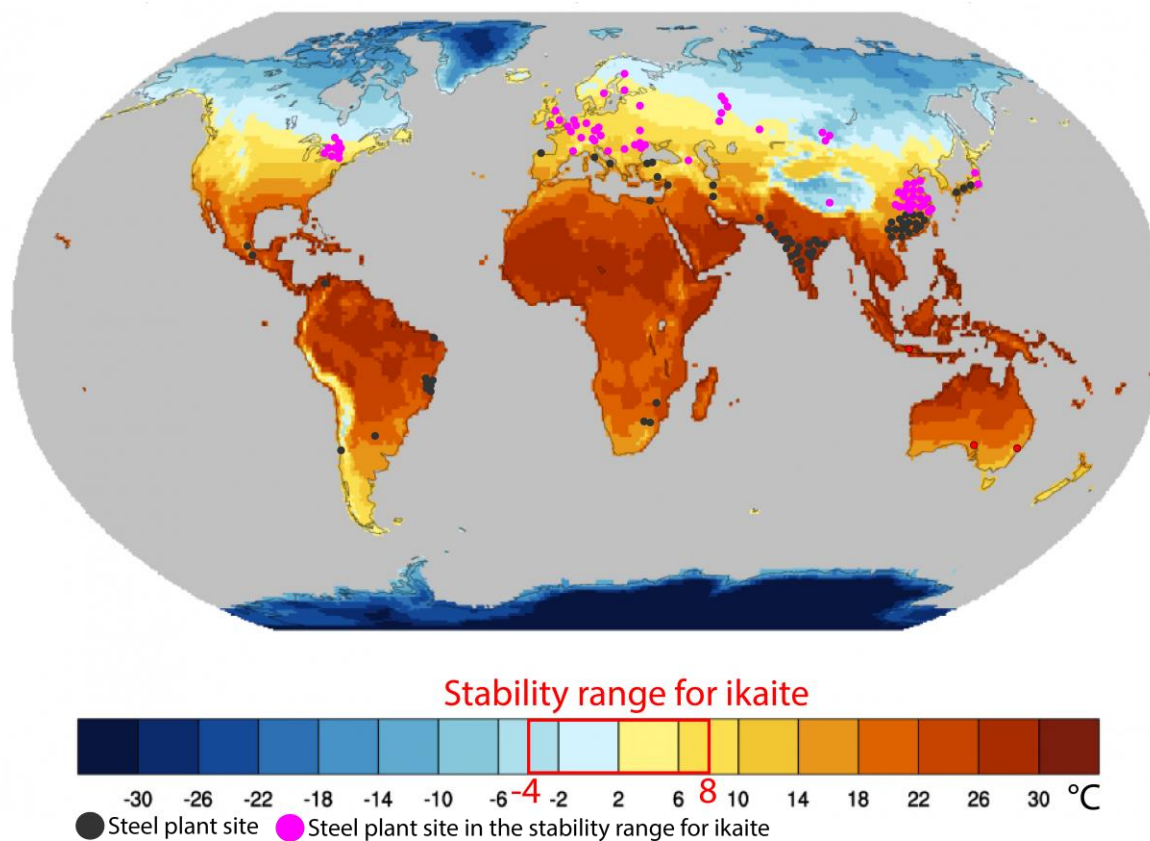


Figure 4.11: Climatology of annual mean land temperature for 1951-1980 from the Berkeley Earth data after NCAR, ClimateDataGuide with the overlapped localization of the countries with annual mean land temperature lower than 8°C and steel plant sites after World steel plant maps - 2020 Geography (<https://www.steelonthenet.com/maps.html>).

(Nova Scotia), Great Lakes of the US, Sweden, Finland, UK, France, Germany, Romania, Russia (Siberia), Ukraine, Kazakhstan, China and Japan. Of particular concern are sites in Russia, Canada, and USA, where the winters are cold enough for ikaite precipitates to accumulate for many months. Indeed, winters are likely to be cold enough to facilitate ikaite precipitation for 5 months at sites in Russia, 3 months in Canada, 3 months in the USA.

The ikaite crystals seen in the field (Figure 4.3) are not embedded within the permanently sedimented calcite. Indeed, the cm-sized euhedral to subhedral white crystals are dominantly located along the barrage crests (Figure 4.3), are thus forming at the water-air interface where low air temperatures will most strongly affect the solution. The sampled carbonate precipitate of white crystalline material exhibits a grainy consistency (Figure 4.3), and although we do find minor calcite within the XRD data we have not found ikaite-shaped cavities, or replacement textures like thinolite or glendonite within these deposits. Therefore, the ikaite must disintegrate, returning its content to solution. Ikaite is more susceptible to re-dissolution and mechanical abrasion compared to calcite due to a combination of chemical and mechanical processes. Consequently, ikaite is subject to vanish rapidly from the barrage crests, i.e. probably within a few days when the cold weather ceases (Boch et al., 2015).

This transient mineral formation is a new type of potential transient contaminant sink for these sites, confirming the hypothesis of Boch et al. (2015). Given that cold periods favourable to ikaite accumulation may occur for 3-5 months of the year in the world's most northerly steel manufacturing sites, the impact of this process could be very severe. Accumulation during cold winter periods followed by rapid increase in spring time temperature will likely result in a "saw tooth" pattern in pollutant dynamics, unlike the behaviour of more permanent inventories.

It remains possible that conversion of ikaite to microcrystalline calcite allows some stable carbonate precipitates to remain in the riverbed, reducing the severity of the rapid mass release

during warming. This is known to occur from other places of original ikaite formation (Omelon et al., 2001; Oehlerich et al., 2013), and after thermal decomposition the solid crusts are easily stripped-off and mobilized in the turbulent water flow (Boch et al., 2015). This will further complicate dynamics at these sites and will require further field and experimental investigation.

4.4.2 | What contaminant phases are likely to be accumulated into a transient ikaite inventory?

Where the ikaite inventory preferentially accumulates an environmental contaminant (i.e. the contaminant has a partition coefficient higher than 1), this will amplify the saw-tooth dynamics by enriching the transient reservoir. In the sample reported here, the partition coefficients are higher than 1 for all investigated contaminants with the exception of vanadium (Table 4.3). Rapid release during warming of an inventory so strongly enriched in a range of contaminants compared to the ambient water would pose a very severe challenge to aquatic and riparian ecosystems, and may extend far downstream of the area exhibiting ikaite growth. These release events would likely evade standard monitoring approaches, which generally focus on sampling at regular, widely spaced intervals. The process of formation-dissolution of ikaite is faster than the spacing between those samplings in our UK site, and at colder sites the release event may be over within a few days during the spring thaw and also be irresolvable. Indeed, the average sampling spacing in recent years (February 2018 until October 2019) is quite infrequent (0.38 per month: 4-5 times in one year) at the nearest site from our UK site, downstream of Consett Sewage Treatment works at Ebchester (Sampling point ID: NE-43400174), within Northumberland Durham and Tees after public sector information licensed under the Open Government Licence v3.0. Since the location of this site (downstream of Consett Sewage Treatment works), it does constitute the closest semi-active station to our UK site, enabling to record a flushing event.

Monitoring of bulk solution properties such as pH may also not respond to the mineral dissolution, as the carbonate release to solution will be masked by already high CO₃ and OH alkalinity. Conductivity monitoring is the most likely bulk parameter to resolve these changes, but as the ratio of contaminant: Ca would be higher during the release event, such measurements would still significantly under-estimate the impact. We find that if ikaite is found within similar systems to that described here, monitoring procedures will need to be redesigned.

It is interesting to note that ikaite could potentially incorporate an element such as Tritium, a rare and radioactive isotope of hydrogen, which has an atomic radius of 53 pm, lower than the atomic radius of Strontium (0.215 nm) (Taylor, 1968), reported in the list of elements sequestered in our ikaite sample (Table 4.3). The study of Kitabata and Kitamura (1997) reported the key issues of heavy water recycling and tritium internal dose reduction for the heavy water handling technology in the Fugen Nuclear Power Station. Dry ikaite might be an alternative to store the pollutant of Tritium in solid state.

4.4.3 | Why are these elements enriched compared to the solution?

The partition coefficients reported here are significantly higher than those reported in the literature for other calcium carbonate polymorphs, and some (e.g. Sr, which is enriched in the mineral by over 150,000 times compared to solution) are very high indeed. It seems likely that were sufficient Sr available in solution, a hydrated strontium carbonate polymorph would have been formed. Although as far as we are aware these are the first partition coefficients of our ikaite field sample provided in the literature, these extreme behaviours demand further investigation.

4.4.3.1 | Laboratory synthesis experiments

Using two different published methodologies for ikaite synthesis, we found the initial precipitate was actually ACC, as determined by FTIR measurements (Figures 4.9 and 4.10). Ikaite was formed as a secondary phase if the precipitate was stored under cool conditions (-4.35 – +1.1°C for at least 7 days). We note 3 months storage is recommended as part of the synthesis for ikaite in the protocol published by Lennie et al. (2004). We also note that Tollefsen et al. (2020) report that ikaite precipitated in their experiments together with ACC at temperatures between 10 °C and 35 °C, and the amount of ACC increased with temperature. At 35 °C, the sample contained 94% ACC. Such formation of ikaite from precursor ACC has previously been reported (Chaka, 2018), and seems a generalisable feature of formation of this mineral in conditions analogous to nature. The electron microscope images of our field sample (Figure 4.8) show ikaite crystals growing, but no clear evidence for ACC. However, replacement may be very rapid and could have completed before our time of sampling, so it remains possible that there was indeed an amorphous pre-cursor at this site.

Initial precipitation as an ACC phase may explain why partition coefficients we report from Consett are very high, as the disordered structure of amorphous mineral permits easy incorporation of trace elements. In an analogous series of experiments, conversion of ACC to calcite by dissolution-precipitation result in final mineral composition with enhanced partition coefficients for Li, Sr, Mg, U, B, Ba, and elements multiplied respectively by up to 3, 4, 8, 16, 565 and 1500 times respectively, (See Table 2 of Ulrich et al., 2021). Since an ordered mineral is not actually being produced direct from solution in these systems, the thermodynamics of aqueous crystal assembly is not relevant to final crystal composition. Rather, composition is set by the sequential partitioning of the water to ACC reaction, and the ACC to ikaite reaction. One potential benefit of this behaviour is that there is potential for very high toxic trace element content to be transferred another Ostwald step forward if ikaite does

dehydrate to calcite during warming, permanently sequestering the pollutants. The Ostwald's step rule states that on the law of successive reactions, it is not the stablest state with the least amount of free energy that is initially obtained, but the least stable one, lying nearest to the original state in free energy (Van Santen, 1984). Further research is needed to determine the balance of heavy metals and barium sequestered to the ikaite inventory which is ultimately transferred to the calcite inventory, or returned to solution.

Table 4.4: Depicting the rate of contaminants stored in ikaite per day for each metal.

Metal	Rate of contaminants stored in ikaite per day (mg.m ⁻² .day ⁻¹)
Ba	59.35
Cr	5.56
Mn	1000.19
Ni	7.49
Zn	23.86
Cd	0.44
Pb	1648.67

4.4.4 | What is the environmental risk posed by this finding?

Mayes et al. (2018) established a maximum rate of carbonate production per day in Howden Burn of 259g.m⁻².day⁻¹. Assuming that under cold conditions as experienced during the fieldwork reported, all of this mass is deposited as ikaite it is possible to use the partition behaviour described above to estimate how much of each contaminant would be stored in ikaite during the cold spell in early 2019. These are shown in Table 4.4. Cadmium, chromium and nickel are likely to be sequestered at a rate close to 0.5-8 mg m⁻² day⁻¹, zinc and barium in a

range of 20-60 mg m⁻² day⁻¹ and manganese and lead at exceptionally high rates of 1000 and 1600 mg m⁻² day⁻¹ respectively (See Table 4.4). If accumulation continued throughout the approximately week-long cold spell, estimates for the amount of lead stored in the transient ikaite inventory may approach 10g m⁻² so long as sufficient Pb was available in the solution. This entire inventory may be released back to solution in a matter of hours during warming.

For specific regions such as Russia, North of America, Canada, Sweden, Finland, Central Europe, where winter can provide conditions at least as cold as Consett for several months, this issue may become acute. Large masses of toxic trace elements accumulated in ikaite and the released in a short duration would cause acute pollution events during thaw periods. We recommend that this impact is investigated, as it may cause river health to be considerably lower than standard monitoring practices would explain. Complicating this further, Tollefsen et al. (2020) demonstrate ikaite forming under ambient temperatures of a much higher range than generally given, extending as high as 35°C. Consequently, it remains possible that minor ikaite formation in steel waste affected sites may be very widespread indeed.

4.4.5 How harmful would release of these contaminants in a transient mineral inventory likely be?

Specific concern arises from this investigation for springtime peaks in contamination with chromium, manganese, nickel, zinc, cadmium, barium, and lead (Table 4.3). There is less preoccupation regarding strontium and copper as for Sr, our system does not infer any radioactivity and for Cu, concentrations are low and usually either around limits of detection (LOD) or if not, there are below aquatic life standards. All aside from manganese and barium are heavy metals which have a marked effect on the aquatic flora and fauna. These toxic metals entering in aquatic environment are adsorbed onto particulate matter, although they can form

free metal ions and soluble complexes that are available for uptake by biological organisms (Lokhande et al., 2011), and through bio-magnification can enter the food chain, ultimately affecting human populations as well (Lokhande et al., 2011). The toxic effects of heavy metals such as chromium, cadmium, zinc, and lead can affect the individual growth rates, physiological functions, mortality and reproduction in fish (Ali et al., 2014). Heavy metals enter in fish bodies by three possible ways: by gills, by digestive track and body surface (Lokhande et al., 2011). The gills are considered as the significant site for direct uptake of metals from the water, though the body surface is normally estimated to take minor part in uptake of heavy metals in fish (Abdul-Wahab et al., 2012).

As reviewed by Ali et al. (2014), heavy metal accumulation, such as Cr and Cd, in fish severely affects their health and are of primary ecological importance (Table 4.5). When passed into the human food supply, fish contaminated with Pb, Cr, Cd and Zn cause great concern for human health (Juberg et al., 1997; Rossi & Jamet, 2008; Healey, 2009). These contaminants constitute priority hazardous substances affecting human health and aquatic life (Table 4.5). The impact of Ba, Mn and Ni is rather different to the heavy metals described above but can be severe for plant and animal systems. These elements correspond to secondary hazardous substances and their toxicity is reported in Table 4.6.

Table 4.5: Depicting the potential impacts of the contaminants Cd, Zn, Pb, Cr and Zn classified by primary ecological importance, priority, and secondary hazardous substances.

PRIMARY ECOLOGICAL IMPORTANCE (Affecting health of fish)	
Element	Potential impacts
Cd	Cadmium can reduce the reproduction rate of aquatic organisms, and continual exposure to cadmium can lead to a gradual extinction of affected taxa (Ali et al., 2014). Cadmium damages the kidney and produces signs of chronic toxicity, including impaired reproductive capacity and kidney function, tumors, hypertension and hepatic dysfunction. Sub-lethal concentrations of Cadmium cause deviations on the electrophoretic arrangements of protein segments in gills and muscle <i>O.mossambicus</i> (ibid) (Ali et al., 2014).
Zn	Zinc is a potential toxicant to fish (Vosyliënė & Mikalajūnė, 2006) which causes disturbances of acid-base and ion regulation, disruption of gill tissue and hypoxia (Murugan et al., 2008). The underlying cause of these impacts is zinc accumulating in the gills and reducing tissue respiration leading to tohypoxia, which results in death. Zinc pollution also promotes changes in ventilator and heart physiology (Olaifa et al., 1998). Sub-lethal levels of zinc have been known to unfavorably affect hatchability, existence and hematological strictures of fish (Olaifa et al., 1998), deficiency of balance since most fins are stationary in the affected fish, restless swimming, air guzzling, periods of dormancy and death (Kori-Siakpere & Ubogu, 2008).
PRIORITY HAZARDOUS SUBSTANCES (Affecting human health and aquatic life)	
Element	Potential impacts
Pb	Lead is a recognised and potent environmental pollutant, which accumulates in muscles, bones, blood and fat (Ali et al., 2014). This results in severe damage to liver, kidneys, brain, nerves and other organs, especially in young individuals and infants. Exposure to lead may also lead to reproductive disorders osteoporosis (brittle bone disease), causes increases in heart disease, high blood pressure, and affects the blood and heart causes anemia and affects the nerves and brain (Ali et al., 2014). Extensive exposure to lead causes memory problems appropriations, behavioral disorders, mental retardation while lesser levels of lead damage the nerves and brain in fetuses and young children, resulting in lowered IQ and learning deficits (ibid).
Cr	Chromium toxicity in humans can cause faded immune system, skin diseases, ulcers and digestive problems, alteration in genetic material, liver and kidney damage, death (Karadede et al., 2004).
Cd	Cadmium can damage the kidneys, causing the excretion of sugars and essential proteins from the body and cause diarrhoea, vomiting, stomach problems, fractures in bone, damage to DNA, failure in reproduction and fertility, cause damage to nervous system, damage to immune system and some cancers (Abdul-Wahab et al., 2012). Elevated levels of zinc can cause skin annoyances, stomach cramps, anemia, vomiting and nausea (Lokhande et al., 2011).
Zn	High levels of Zn damages the pancreas and disturb the protein metabolism, and cause arteriosclerosis (Abdul-Wahab et al., 2012).

Table 4.6: Depicting the potential impacts of the contaminants Ba, Mn and Ni classified by primary ecological importance, priority, and secondary hazardous substances.

SECONDARY HAZARDOUS SUBSTANCES (Affecting plant and animal systems)	
Element	Potential impacts
Ba	It has been shown to reduce photosynthesis, chlorophyll fluorescence and stomatal resistance in plants (Abdul-Wahab et al., 2012). This results in reduced biomass production in beans (Chaudhry et al., 1977; Llugany et al., 2000) and soybeans (Suwa et al., 2008) due to reduced CO ₂ assimilation caused by limited photosynthetic activity (Melo et al., 2011). Barium has also been shown to affect a variety of cellular and developmental processes in both plant and animal systems (Spangenberg & Cherr, 1996). These include perturbation of vitellogenin uptake in insect follicles (Kindle et al., 1990), inhibition of ciliary function in trochophore larvae (Marsden et al., 1986), and structural and functional integrity of flagella in algae (Zmarzly et al., 1986). It has been suggested that these effects result from Ba interaction with cellular Ca homeostasis (Spangenberg & Cherr, 1996).
Mn	Plants have been shown to react to excess Mn with a drop-in photosynthetic rate (Macfie and Taylor, 1992; Macfie et al., 1994). This lowering of photosynthesis occurred as a result of decreases in chlorophyll and the photosynthesis per unit chlorophyll in a sensitive cultivar and only reducing the chlorophyll content in a tolerant cultivar of <i>T. aestivum</i> (Moroni et al., 1991; Macfie and Taylor, 1992). Manganese toxicity has also been associated with swollen chloroplasts in <i>G. max</i> (Wu, 1994).
Ni	Excess Ni has been reported to cause leaf necrosis and chlorosis of plants (Chen et al., 2009). Chlorosis and along-vein necrosis appeared in newly developed leaves of water spinach after plants were treated with 0.085 to 0.255 mM (5 – 15 ppm) Ni for a week (Sun and Yu, 1998). Ni at a concentration of 0.5 mM produced dark brown necrotic spots along the leaf margins and decreased water potential and transpiration rate, resulting in wilting of outer leaves and necrosis of inner leaves of cabbage (Pandey and Sharma, 2002). Barley grown in 0.1 mM Ni for 14 days showed chlorosis and necrosis of leaves (Rahman et al., 2005).

4.5 | CONCLUSION

Ikaite formation presented in this study occurs in an anthropogenic system within steel-slag leachate and is the first documentation worldwide for this setting of ikaite crystallization. This was achieved through a novel combination of in-situ FTIR analysis to inform sample selection for rapid XRD analysis, which could provide a model for identifying ikaite at similar sites in the temperate zone. We deduce from laboratory experiments and very high partition coefficients in the field sample that ikaite is a secondary mineral with a primary phase being ACC. The ikaite forming in steel-slag leachate affected waters is incorporating large inventories of very harmful pollutants such as the heavy metals cadmium and lead which are most toxic to all human beings, animals, fishes, and environment. Chromium, zinc, manganese, barium and nickel are other potent contaminants reported in this study causing various ill effects, which are accumulated in the transient ikaite inventory. Masses accumulated in the ikaite inventory may be very high, with $\text{g}\cdot\text{m}^{-2}\cdot\text{day}^{-1}$ estimated for lead.

As ikaite is thermally unstable, the inventory is lost during warming periods. In our field study area (Consett, County Durham, UK) this is related to synoptic weather, but in colder regions the warming will likely relate to springtime thawing. It is unclear how much ikaite is converted to calcite by dehydration, but at Consett we find no direct evidence of this. Consequently, most of the temporarily stored contaminant mass will be lost back to solution in a short duration, creating a significant peak in toxicity. These short-lived periods of acute pollution may significantly compromise river ecology, and present potential challenges to human health. The regions most exposed to this risk are those with long durations of stable low temperature in the winter, so steel-making and former steel-making locations in Russia, northern North America, Canada, Sweden, Finland and Central Europe should be investigated for this process. Ikaite is considered to have an upper temperature limit of 8°C , providing a key isotherm to guide this investigation spatially and seasonally. However, ikaite has been reported

forming under ambient temperatures (5-35°C), so the 8°C isotherm may significantly underestimate the issue.

4.6 | AUTHOR CONTRIBUTIONS

The idea for this manuscript arose from the discussion between all authors. Laura Bastianini collected the ikaite sample on the field and executed the laboratory experiments to synthesise ikaite. She also drafted the manuscript. Mike Rogerson identified the ikaite sample by FTIR on the field and made improvements through the whole manuscript. Timothy J. Prior collected and interpreted X-ray diffraction data. Kit Hardman, Eddie Dempsey and Anna Bird collected and interpreted the laser data. Mike Rogerson and Laura Bastianini calculated the partition coefficients for ikaite. Alex Brasier provided insight on the interpretation of the SEM images. William M. Mayes had previously noticed ikaite growths on the surface of the carbonate deposit when there was snow on the ground one week before collection of the sample. He subsequently led the sampling team which visited the site later during the same cold period and made improvements through the whole manuscript.

Chapter 5 – Improving field alkalinity characterization of waters on anthropogenic alkaline sites

Laura Bastianini, Mike Rogerson, Timothy J. Prior & William M. Mayes.

This chapter of the thesis critically assesses a range of methods for dissolved inorganic carbon (DIC) characterisation at anthropogenic alkaline sites. DIC is a crucial measure to assist in understanding carbonate formation processes, trace metal dynamics and carbonation opportunities at these sites, but traditional approaches may not be robust for waters with extreme geochemistry. As such, this chapter compares a range of methods for assessing dissolved inorganic carbon in alkaline samples and includes the development of a new method for such based-on strontium carbonate precipitation. Traditional methods (manual and automated titrations) are compared against a new strontium carbonate method for accuracy and reliability. The implications of the differing performances in these methods for DIC characterisation are considered for interpreting geochemical processes (notably carbonate saturation) at hyperalkaline sites (RQ5: How can dissolved inorganic carbon be better characterised from anthropogenic hyperalkaline sites?).

5.1 | INTRODUCTION

Acid Neutralising Capacity (ANC) is a key labile parameter in natural and anthropogenically-influenced waters arising from the combined effect of solutes plus particulates in an unfiltered water sample, reported in equivalents per liter (or milliequivalents or microequivalents) (Radtke et al., 1998). As particulates reflect a broad spectrum of environmental processes, including flow-induced turbidity, it is usually practical to reduce the full ANC to only that of dissolved species by removing the particulate phases. This parameter, alkalinity, therefore reflects the sum of titratable carbonate and noncarbonate chemical species

in a filtered water sample (filter membrane of 0.45- μm or less pore size) (Radtke et al., 1998). In many aqueous systems, alkalinity is controlled by carbonate chemistry, and most is commonly attributable to bicarbonate (HCO_3^-) and less frequently to carbonate (CO_3^{2-}) (Radtke et al., 1998). Carbonate alkalinity represents the acid-neutralizing capacity of carbonate solutes only ($m\text{HCO}_3^- + 2m\text{CO}_3^{2-}$, where m is moles), reported either in equivalents per liter (or milliequivalents or microequivalents) or in milligrams per liter as a carbonate species when titrated from a filtered water sample (Radtke et al., 1998).

At sites impacted by highly alkaline drainage, alkalinity is a key field parameter used to characterise the geochemical processes and potential pollution issues (e.g. Bastianini et al., 2019, 2021; Mayes et al., 2008; Womble et al., 1996). The parameter is crucial to estimates of carbonate precipitation which has been demonstrated to impact macroinvertebrate communities (Koryak, 1998; Hull et al., 2014), and for modelling saturation indices of carbonates in alkaline waters which can feed into carbon capture budgets (e.g. Mayes et al., 2018). In the same manner, alkalinity measurements are key constraints both for geochemical evaluations of processes in natural system such as land surface carbon flux (e.g. Graly et al., 2017), or in sedimentology studies where carbonate minerals are actively precipitating (e.g. Gallagher et al., 2012). Despite these well-established uses of alkalinity data, methods for alkalinity data collection are rarely scrutinised in terms of levels of operator repeatability and rarely collected in replicate in field settings (e.g. Gozzard et al., 2011). This chapter provides a critical appraisal of methods for collecting alkalinity data, with focus on improving the basis for characterisation of geochemical processes at highly alkaline sites.

5.1.1 | Definition of alkalinity for alkaline anthropogenic systems

Alkalinity corresponds to the ability of a sample to neutralize strong acid (Gran, 1950; Rounds, 2012), and in environmental context essentially reflects the presence of dissolved

carbon species (bicarbonate (HCO_3^-), carbonate (CO_3^{2-}) and hydroxide (OH^-)) (Rounds, 2012; Stumm & Morgan, 1981, 1996). The speciation of inorganic carbon in solution acts like a buffer, where the carbonate ion associates (dissociates) with protons as they are provided to the solution (removed from the solution) by addition of a strong acid (by addition of a strong base). The behaviour is determined by the Henderson-Hasselbach equation, which regulates the equilibrium of:



Working from left to right, the first equilibrium is determined by a hydrolysis reaction, and is generally the slowest (rate limiting) reaction in the series (Dreybrodt et al, 1996). The pKa (i.e. hydrogen dissociation coefficient) of the second and third equilibria are ~6.4 and ~10.3 respectively (varying with solution composition, pressure and temperature). Consequently, circumneutral solutions will be dominated by bicarbonate, whereas acid and alkaline solutions will be dominated by carbonic acid and carbonate respectively. Figure 5.1 shows the partitioning of alkalinity generation with pH from Langmuir (1997).

5.1.2 | Naturally occurring alkalinity

In natural water, Total Alkalinity (TA) is defined as the excess of proton acceptors (bases carbonic acid) over proton donors (acids with $K > 10^{-4.5}$) (modified from Dickson, 1981):

$$\begin{aligned} \text{TA} = & [\text{HCO}_3^-] + 2[\text{CO}_3^{2-}] + [\text{B}(\text{OH})_4^-] + 2[\text{HPO}_4^{2-}] + 3[\text{PO}_4^{3-}] + \\ & [\text{SiO}(\text{OH})_3^-] + [\text{HS}^-] + [\text{NH}_3] + [\text{OrgAlk}] + [\text{OH}^-] - [\text{H}^+]_{\text{F}} - [\text{HF}] - \\ & \text{HSO}_4^- - 3[\text{H}_3\text{PO}_4] - [\text{OrgA}] \dots, \end{aligned}$$

where contributions of carbonate (HCO_3^- and CO_3^{2-}) and borate ($\text{B}(\text{OH})_4^-$) species usually dominate. Organic acid charge groups (negatively charged species) can contribute to TA as a base (OrgAlk) and/or an acid (OrgA) depending on their equilibrium constants (Muller

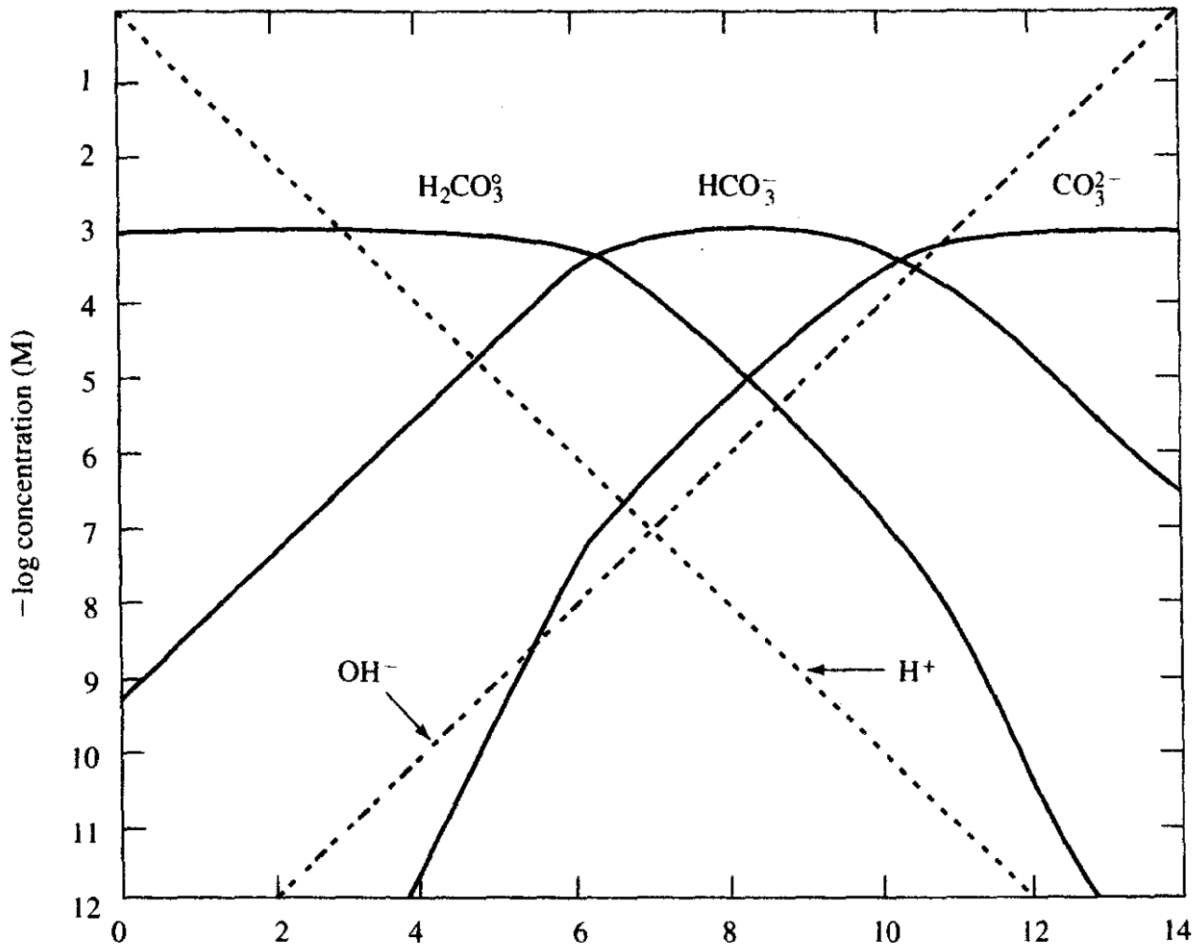


Figure 5.1: Distribution diagram for carbonate species as a function of pH, assuming the total carbonate $CT = 10^{-3}$ M. Concentrations of H^+ and OH^- , which are independent of CT , are shown as dashed straight lines after Langmuir (1997).

and Bleie, 2008; Ulfsbo et al., 2015). In both freshwater and seawater, OrgAlk also affects water pH, carbonate speciation, and buffer capacity (e.g., Cai et al., 1998; Muller and Bleie, 2008; Wang et al., 2013; 2016). Since TA is commonly used as one input parameter in thermodynamic CO₂ system calculations, any uncertainty in the definition or measurement of TA will lead to uncertainty in determining carbonate speciation.

The principal source of carbon dioxide species from which alkalinity is generated in surface or ground water is the CO₂ gas fraction of the atmosphere, or the atmospheric gases present in the soil or in the unsaturated zone lying between the surface of the land and the water table (Wang et al., 2016). The CO₂ content of the atmosphere is near 0.03 percent by volume (Wang et al., 2013). Soil-zone and unsaturated-zone air can be considerably enriched in carbon

dioxide, usually owing to respiration by plants and the oxidation of organic matter. In some natural systems there may be sources of carbon dioxide other than dissolution of atmospheric or soil-zone CO₂ (Muller and Bleie, 2008). Possible major local sources include biologically mediated sulfate reduction and metamorphism of carbonate rocks as well as their weathering. In some areas, outgassing from rocks in the mantle 15 km or more below the surface has been suggested (Irwin and Barnes, 1980). From studies of $\delta^{13}\text{C}$ values in dissolved HCO₃⁻ in 15 oil and gas fields, Carothers and Kharaka (1980) concluded that the decarboxylation of acetate and other short-chain aliphatic acids was an important CO₂ source in these waters. This process also produces methane and other hydrocarbon gases.

Carbon dioxide species are important participants in reactions that control the pH of natural waters. Reactions among the alkalinity-related species, aqueous CO₂, H₂CO₃(aq), HCO₃⁻, and CO₃²⁻, and directly pH related species, OH⁻ and H⁺, are relatively fast and can be evaluated with chemical equilibrium models. Rates of equilibration between solute species and gaseous CO₂ across a phase boundary are slower, and water bodies exposed to the atmosphere may not be in equilibrium with it at all times. The oceans are a major factor in maintaining atmospheric CO₂ contents. It may be of interest to note that carbonic acid, H₂CO₃, is conventionally used to represent all the dissolved undissociated carbon dioxide. In actuality, only about 0.01 percent of the dissolved carbon dioxide is present in this form.

Mass balance calculations indicate that the weathering of Ca-bearing peridotite silicates, such as diopside, is a feasible source of Ca in Ronda Ca–OH hyperalkaline fluids; however, it requires steady-state dissolution rates substantially greater than those determined experimentally (Giampouras et al., 2019). The non-carbonate alkaline species contributions from species of boron, phosphorus, nitrogen and silicon are often dominated by contributions from organic species such as humic acids (Cai and Wang, 1998, Lozovik, 2005, Hunt et al., 2011), which can vary in pK_a and represent a large fraction of TA. Some studies (e.g., Cai et

al., 1998; Tishchenko et al., 2006; Kim and Lee, 2009) have shown that non-carbonate alkaline species are sometimes a significant fraction of TA in estuarine and coastal ocean waters and must be taken into account when analyzing the carbonate system in various environments.

Alkalinity is also generated by many industrial processes, such as coal combustion (Heidrich et al., 2013; Moreno et al., 2005; Yao et al., 2015), lime production (Steinhauser, 2008), chromium ore processing (Darrie, 2001; Freese et al., 2015; Geelhoed et al., 2002), cement production (Adaska and Taubert, 2008), alumina extraction (Burke et al., 2012b; Power et al., 2011), iron and steel manufacture (Mayes et al., 2006; Motz and Geiseler, 2001; Piatak et al., 2015), and waste incineration (Astrup et al., 2006; Bogush et al., 2015; De Boom and Degrez, 2012; Ferreira et al., 2003; Johnson et al., 1999; Quina et al., 2008). All these alkaline residues are characterised by the presence of Na, Ca or Mg oxides that rapidly hydrate to produce soluble hydroxide. A large range of Ca and Na silicate, aluminate and aluminosilicate phases are also represented, hydrating and dissolving to produce hydroxide alkalinity in a manner similar to the natural weathering of alkaline rocks. Any Ca and Mg carbonates present provide a more stable (low solubility) alkaline phase. Initially, dissolution of soluble Na or Ca hydroxides tends to dominate ($\text{pH} > 12$) (Gräfe et al., 2011; Mayes et al., 2008; Roadcap et al., 2005). Over time, the more slowly reacting phases [e.g. Ca silicates, Na aluminosilicates, $\text{Mg}(\text{OH})_2$] control leachate quality ($9 < \text{pH} < 12$). On long timescales, carbonate dissolution prevails ($\text{pH} < 9$).

5.1.3 | Measuring alkalinity in the field

Alkalinity and concentrations of bicarbonate, carbonate, and hydroxide species are most commonly determined by analysing acidimetric-titration data with either the inflection point titration method, the Gran function plot method or the Fixed End Point method (Devlin, 1990; Kirby et al., 2005; USGS, 2012). The Inflection Point Titration (IPT) method, also called

the incremental titration method, is adequate for most waters and study needs (Devlin, 1990; Kirby et al., 2005; USGS, 2012). Difficulty in identifying the inflection points using the IPT method increases as the ratio of organic acids to carbonate species increases and as the alkalinity decreases (Devlin, 1990; Kirby et al., 2005). The Gran function plot (Gran) method is recommended for water in which the alkalinity or ANC is expected to be less than about 0.4 milliequivalents per liter (meq/L) (20 milligrams per liter (mg/L) as CaCO_3), or in which conductivity is less than 100 microsiemens per centimeter ($\mu\text{S}/\text{cm}$), or if there are appreciable noncarbonate contributors or measurable concentrations of organic acids (Kirby et al., 2005). The Fixed-End Point (FEP) method, a widely used technique for alkalinity and acidity determinations, present some specific difficulties when applied to low-pH waters (USGS, 2012). Alkalinity determinations by the fixed end point method are performed by lowering the pH of the sample with acid additions to the carbon-dioxide end point (or methyl-orange end point) of pH 4.5 (Devlin, 1990). This method is based on the principle that when hydroxide, carbonate and bicarbonate are the alkaline-contributing species, carbon dioxide concentration determines the pH at the equivalence point (USGS, 2012). Although the method is straightforward for samples with pH greater than 4.5, the titrations cannot be performed on samples with pH less than 4.5 (Kirby et al., 2005).

With the IPT method, it is possible to obtain the carbonate and bicarbonate endpoints in the titration by determining the highest change in the measured pH per unit volume of acid added (Hem, 1985; Rounds, 2012; U.S. Geological Survey, 2012). The carbonate and bicarbonate equivalence points are respectively near pHs of 8.3 and 4.5, but it is more precise to determine their exact locations from the titration data (Hem, 1985; Rounds, 2012). This could be identified by a distinct inflection point in the measured titration curve (U.S. Geological Survey, 2012). Inflection points correspond to the points of maximum rate of change in pH per volume of titrant added. (Hem, 1985; Rounds, 2012). These endpoints allow

deducing the carbonate alkalinity in mg/L (Rounds, 2012; U.S. Geological Survey, 2012). The relative error of the determinations could be within ± 4 percent if the equivalence point is recognizable within ± 0.3 pH unit of the true equivalence point (U.S. Geological Survey, 2012). This method, also known as the incremental titration with second-derivative calculations, is not useful in alkalinity determination in low-pH waters with negative alkalinities since the calculations cannot yield a negative result.

USGS (2012) does not recommend using the FEP method for determining alkalinity anymore (Rounds, 2012; Stumm & Morgan, 1981, 1996). This technique is indeed less accurate than the IPT method, particularly for low concentrations of total carbonate species and for water with significant organic and other non-carbonate contributors to alkalinity (Rounds, 2012; Stumm & Morgan, 1981, 1996; USGS, 2012). This decrease in accuracy is evident particularly for low concentrations of total carbonate species and for water with significant organic and other noncarbonate contributors to alkalinity or ANC (Rounds, 2012; Stumm & Morgan, 1981, 1996). However, it is a more economical and more easily transportable method in a field campaign than the IPT method (Rounds, 2012; Stumm & Morgan, 1981, 1996). The IPT method can be used for most waters and study needs. It is a very precise method but more expensive than the Fixed End Point Titration method (Rounds, 2012; Stumm & Morgan, 1981, 1996) and it may be difficult to identify the inflection points as the ratio of organic acids to carbonate species increases and (or) as the alkalinity decreases (Rounds, 2012; Stumm & Morgan, 1981, 1996).

Standard references for Alkalinity and Acidity measurements (USEPA, 1983b,a; ASTM, 1998; APHA, 1998b; APHA, 1998a) essentially agree on the major steps in laboratory protocols (Titrate quickly with H_2SO_4 solution to pH 4.5 and use “low Alkalinity” method (a “Gran” titration approach) as necessary) (Kirby and Cravotta, 2005).

5.1.4 | Margin errors resulting from alkalinity titrations

The study of Fritz (1994) shows that there is a broad range of margin errors resulting from alkalinity titrations. The accuracy of the measurement with measuring cylinder and Erlenmeyer flask can be compromised. Temperature effects can have an impact on the alkalinity value as well (Fritz, 1994). Air and water temperature of the sample can change depending on the day. According to Pierce et al. (1948), random or indeterminate errors are caused by inherent limitations of equipment, limitations of observations and lack of care in making measurements. Random errors can never be eliminated (Fritz, 1994). Systematic errors are the most insidious because they are often difficult to detect (Fritz, 1994). They affect each individual result in exactly the same way (Fritz, 1994).

5.1.5 | The need for further evaluation of methodologies

Application of computational and modelling approaches is increasingly a standard part of analysis of natural waters, and re- and meta-analysis of published and “grey literature” data becomes more common. Furthermore, as the implications of this work increasingly determine which passive remediation and carbon management technologies are preferred, our need to consider the real-world analytical uncertainty associated with measurements of alkalinity becomes more acute (Kirby and Cravotta, 2005). In the same manner, the application of these approaches to understanding natural carbon budgets and sedimentological characteristics and processes drives deeper need to consider alkalinity measurement uncertainty for these research communities (Rounds, 2012). This increasing need for understanding of the measurements combines with increasing abilities to take ruggedised automated, semi-automated or completely novel means of measurement to field locations, emphasised by continued drive towards monitoring rather than spot sampling. The result is that it is now appropriate to reconsider whether our approaches taken to making measurements of alkalinity in the field, or

whether we should be seeking methodological innovation to change how this critically important measurement is done.

There are four main objectives in this study:

- Testing operator expertise with the manual approach typically adopted for field alkalinity measurements (FEP).
- Providing an evaluation of the standard manual approach (FEP) to taking alkalinity at field sites and compare it to an automated laboratory device (IPT) which could reasonably be installed to a field station or transportable facility to make measurements close to the point / time of sampling.
- Assessing whether an alternative approach (Strontium titration method) which would be easier to implement into an automated monitoring system provides compatible measurement uncertainty with these established methodologies, which require the presence of a trained operator. This approach carries the additional potential of integration with $\delta^{13}\text{C}_{\text{DIC}}$ measurement, which will be evaluated elsewhere.
- Evaluating how much impact the different uncertainties of the measurements would have on evaluations of mineral supersaturation, and potentially understanding of sites for passive remediation or sedimentology.

5.2| MATERIAL AND METHODS

In this study, spring water samples were collected in Welton (Yorkshire, England) on 13th January 2018 (water 1), 14th May 2019 (water 2) (Figure 5.2). This provides a useful real-world sample with alkalinity concentrations typically in the range of those documented at alkaline waste-impacted sites covered in previous chapters (e.g. Mayes et al., 2008). We used the Welton spring (neutral pH) as opposed to a highly alkaline water as we needed large volumes of water in the laboratory for testing which was not feasible from a distant site such

as Consett or Brook Bottom. Also, if we sampled a highly alkaline water in a barrel, the pH could have dropped from 11.5 to 10 in a few days after collection due to the reaction of the water with the CO₂ in the airspace. Choosing a water close to equilibrium means we had better chance to testing the user performance. Furthermore, we wanted a spring-system of a potential carbonate precipitating water in order to obtain a saturation index level close to saturation. Waters close to saturation with differences in alkalinity could have a major bearing on interpretation. To drive rapid precipitation, high levels of excess dissolved calcium carbonate are necessary in the ambient water (Rogerson and Pedley, 2014).

Carbonate alkalinity titrations were conducted on these samples following both FEP (U.S. Geological Survey, 2012), IPT and Strontium titration (ST) methods (U.S. Geological Survey, 2012) at the Department of Geography, Geology and Environment from the University of Hull (England, UK). A sample size of 33 was completed for all techniques to allow statistical comparison of the different methods. Since we have an unbalanced sample size and non-normal data, it was more robust to apply non-parametric tests (Mann Whitney U or Kruskal Wallis tests). These non-parametric tests are based on the null hypothesis which states that median and distribution are the same across categories (e.g. different alkalinity measurement methods). The null hypothesis is verified if the asymptotic significance value (P) is higher than 0.05.

The alkalinity data have been normalised by obtaining z-scores to reduce the dispersion of the data allowing their comparison. They were calculated by converting a raw score x into a z-score (z) by the formula:

$$z = \frac{x - \mu}{\sigma}$$

Where μ is the mean of the population and σ is the standard deviation of the population.

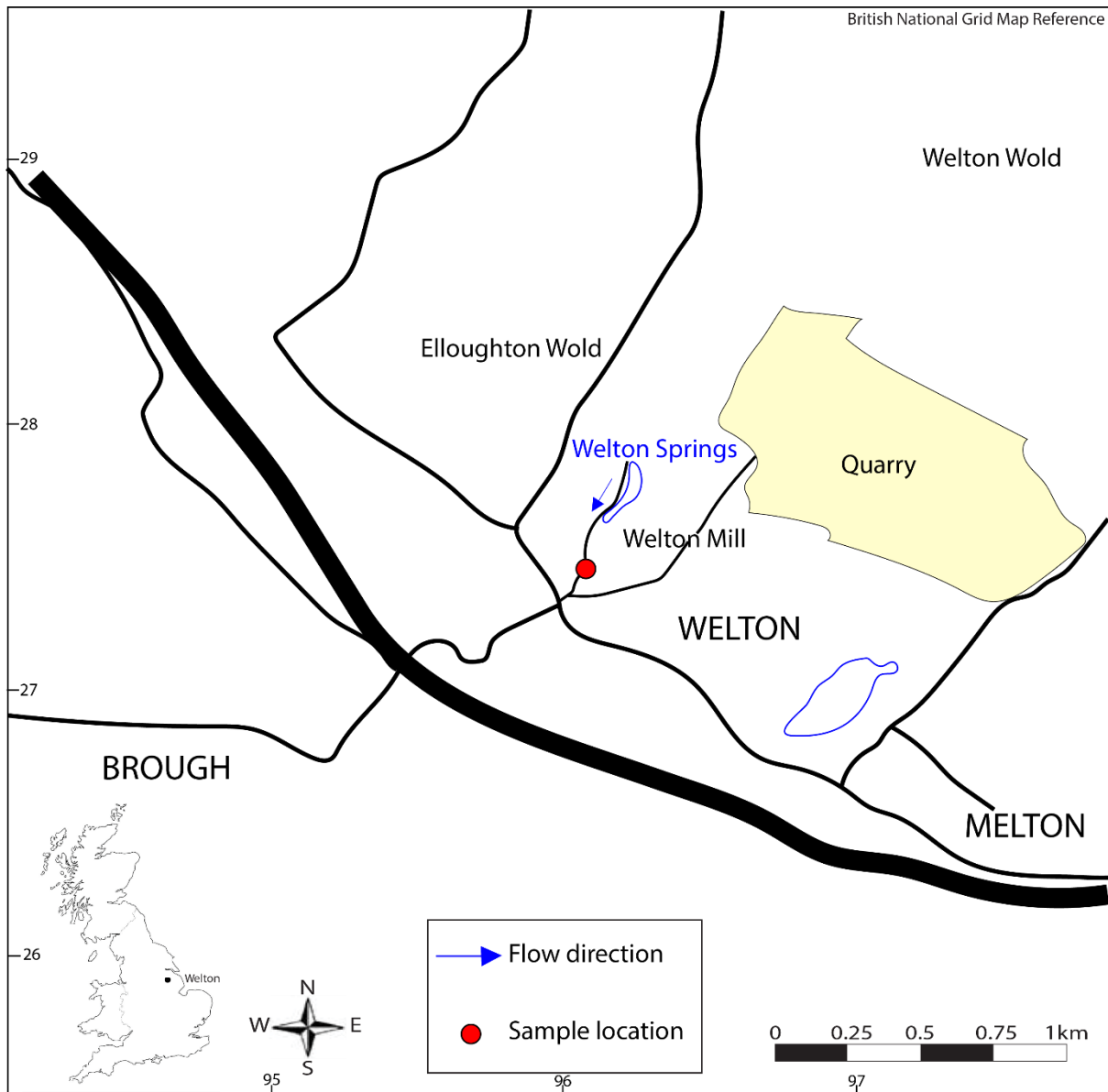


Figure 5.2: Location map of the Welton spring-system where was collected the water samples.

We will use the measurement of coefficient of variation to assess the reproducibility of the three methods of titration. The coefficient of variation, also known as relative standard deviation, is a standardized measure of dispersion of a distribution. It is often expressed as a percentage and is defined as the ratio of the standard deviation to the mean.

5.2.1 | FEP method

The alkalinity of a solution is related to some arbitrary proton reference level or pH, corresponding to the pH at the endpoint of a neutralization carried out by adding strong acid or strong base to the solution in question (Lower, 1999). The main indicators bromocresol blue-

methyl red (pKa = 4.5) and phenolphthalein (pKa = 8.3) are usually employed to detect the endpoints corresponding to solutions of pure H₂CO₃ and pure NaHCO₃, respectively (Lower, 1999). The pH values 4.5 and 8.3, corresponding to the methyl orange and phenolphthalein endpoints respectively, act as operational definitions of two of the three reference points of the acidity-alkalinity scale for the carbonate system (Lower, 1999). The third endpoint, being equivalent to a solution of Na₂CO₃ in pure water, occurs at too high a pH to be considered important in a naturally occurring solution (usually between 10-11). In that sense, carbonate alkalinity can also be described as the quantity of strong acid necessary to titrate the solution to the phenolphthalein endpoint (Lower, 1999). At this stage, all CO₃²⁻_(aq) has been transformed to HCO₃⁻ (Lower, 1999). If the pH of the solution was at or below 8.3 to begin with, the carbonate alkalinity is zero or negative (Lower, 1999). In the same way, calculation of total alkalinity is a simple estimation of the amount of acid used to neutralize the sample to the methyl orange equivalence point (Rounds, 2012; Stumm & Morgan, 1981, 1996), equivalent to the pH point where all carbonate and all bicarbonate have been converted to carbonic acid:

$$Alk \left(\frac{m_{eq}}{L} \right) = \frac{B(m_L)C_a \left(\frac{m_{eq}}{m_L} \right) CF}{V_S(m_L) \left(\frac{1L}{1000m_L} \right)} = 1000(B)(C_a)(CF)/V_S$$

and

$$Alk \left(\frac{m_g}{L} \text{ as } CaCO_3 \right) = Alk \left(\frac{m_{eq}}{L} \right) X \frac{1mmolCaCO_3}{2m_{eq}} X \frac{100.087m_gCaCO_3}{1mmolCaCO_3}$$

$$= 50044(B)(C_a)(CF)/V_S$$

Where Alk is the alkalinity or ANC of the sample.

B is the volume of acid titrant added from the initial pH to the bicarbonate equivalence point (near pH 4.5), in milliliters. Ca is the concentration of acid titrant, in milliequivalents (meq) per millilitre (same as equivalents per litre, or normality N). CF is a correction factor.

The correction factor CF is equal to 1.01 when using the Hach digital titrator cartridges. Vs is the volume of sample, in millilitres and mmol is millimoles, in this case for calcium carbonate.

The concentrations of bicarbonate, carbonate, and hydroxide ($\text{OH}^-_{(aq)}$) constituents in the sample can be determined directly from the sample's pH and alkalinity with the following equations (Rounds, 2012):

$$[\text{HCO}_3^-] \left(\frac{m_{eq}}{L} \right) = \left(\frac{\text{Alk} - K'_w \times 10^{pH} + \frac{10^{-pH}}{\gamma}}{1 + 2K'_2 \times 10^{pH}} \right) \times \left(\frac{1000m_{eq}}{1\text{mol}} \right)$$

$$[\text{CO}_3^{2-}] \left(\frac{m_{eq}}{L} \right) = \left(\frac{\text{Alk} - K'_w \times 10^{pH} + \frac{10^{-pH}}{\gamma}}{2 + \frac{10^{-pH}}{K'_2}} \right) \times \left(\frac{2000m_{eq}}{1\text{mol}} \right)$$

$$[\text{OH}^-] \left(\frac{m_{eq}}{L} \right) = (K'_w \times 10^{pH}) \times \left(\frac{1000m_{eq}}{1\text{mol}} \right)$$

Where Alk is the computed sample alkalinity in equivalents per litre.

pH is the initial sample pH;

K'_w is the acid dissociation constant for water, corrected for the activity of hydroxide;

K'_2 is the second acid dissociation constant for $\text{H}_2\text{CO}_{3(aq)}$, corrected for the activity of carbonate species;

and γ is the activity coefficient for H^+ .

To convert concentrations in meq/L to mg/L, the bicarbonate result is multiplied by 61.0171, the carbonate result by 30.0046, and the hydroxide result by 17.0073 to account for molecular weights (Rounds, 2012).

5.2.2 | Separate expertise testing level for the FEP method

To test the ability of different users of field titration kits, 20 beginners and 15 experts have completed this experiment using a Hach 16900 Manual-Digital Titrator on a sample of 100mL. Each participant had to read a document including the protocol of the FEP method and the main risks associated with this technique. To avoid the risks, they were asked to wear protective gloves, lab coat, and eyes protection as well as washing their skin thoroughly after handling the titrator containing sulphuric acid. LB performed a demonstration of the technique once before the operator started the experiment. The participants were all students/staff members sourced within the Faculty of Science and Engineering (University of Hull, UK), meaning they had some notions of chemistry, especially titration. Each participant has repeated the experiment 10 times. Beginners were defined as though who had brief instruction and supervision in applying the method from an expert. An expert is defined as a participant who has undertaken multiple (>5) field monitoring campaigns using field titration. Given the number of repeats, this experiment has been undertaken 350 times in total. Alkalinity data have been obtained by using the Alkalinity Calculator documented at <http://or.water.usgs.gov/alk/methods.html>.

5.2.3 | IPT method

This method was carrying out 210 times on a sample of 40mL using a T50 Mettler Toledo Titrator, a DL50 Metler Toledo Rondolino and Hydrochloric acid (0.1M).

5.2.4 | ST method

A minimum sample size of 33 replicates was selected for this method. The filter paper was first weighed and 100mL of water solution was collected with a measuring tube. The pH of the solution sample was subsequently measured using a Myron L Ultrameter ® calibrated on each sample day with pH 4, 7, and 10 buffer solutions, to confirm the system had not changed since previous sampling. In this approach, strontium hydroxide, $\text{Sr}(\text{OH})_2 \cdot 8\text{H}_2\text{O}_{(s)}$, reacts with the water sample and $\text{CO}_{2(g)}$ provided from atmosphere to form the strontium carbonate precipitate, $\text{SrCO}_{3(s)}$, following the equation:



Where $\text{DIC}_{(aq)}$ is dissolved inorganic carbon within the sample regardless of state. Despite the presence of calcium in this system, we expect the primary product to be strontianite due to the combined effect of high availability of Sr derived from the hydroxide additive and the lower solubility of strontianite ($K_{sp} = 5.5 \times 10^{-10}$) compared to calcite ($K_{sp} = 3.3 \times 10^{-9}$; both values from www.aqion.de) The high availability of Sr + Ca + Mg and the low solubility of SrCO_3 combine with the hydroxide consumption of $\text{H}^+_{(aq)}$ in the system to ensure that all $\text{DIC}_{(aq)}$ will first be reacted to $\text{CO}_3^{2-}_{(aq)}$ and then almost completely precipitated into solid carbonate mineral with very little residue held in solution. The amount of $\text{Sr}(\text{OH})_2 \cdot 8\text{H}_2\text{O}_{(s)}$ to mix with the water sample therefore needed to be in excess, i.e. at least at double the expected concentration of dissolved carbon. This aqueous residue will result in a small and near-constant underestimate using this methodology which is likely compatible with error found in other approaches. We evaluate the uncertainty of the strontium precipitation approach compared to established methods herein.

As no more than $200\text{mg}\cdot\text{L}^{-1}$ carbon ($0.035\text{mol}\cdot\text{L}^{-1}$) is expected in the samples used, 0.007 moles of Sr are required to provide excess in the sample volume used. Therefore, 0.85g

$\text{Sr}(\text{OH})_{2(s)}$ was added to the water sample in an Erlenmeyer flask. The sample was left for five minutes allowing formation of precipitate, and afterwards filtered, dried and weight. The mass of the filter was subtracted from the total mass in order to obtain the mass of $\text{SrCO}_{3(s)}$. This mass was then reduced to the amount of dissolved inorganic carbon (DIC) in the initial sample using the relative molecular masses of SrCO_3 and CO_2 . Finally, the speciation of the carbonate alkalinity was calculated from the DIC and initial pH using the PHREEQC Interactive software, and assuming the sample was in equilibrium before addition of the reagent.

Although requiring a laboratory step post-fieldwork (filtration and drying), precipitation can be done within a field sampling container and complete, storage is straightforward and requires no special treatment. The approach also requires no specialised laboratory equipment, and $\text{Sr}(\text{OH})_2$ powder is a sufficiently safe material to permit the approach practically, does not pose a strong environmental risk in low masses and is a cheap and widely available reagent. A final advantage is that precipitated solids can be straightforwardly analysed by Isotopic Ratio Mass Spectrometry using the same analysis configuration as calcite powder samples (Singleton et al., 2012). This is not true of any of the other approaches investigated here.

5.2.5 | Thermodynamical modelling of the alkalinity data

It was possible to determine the saturation index (SI) of calcite using the aqueous geochemical modelling software PHREEQC on the Welton water with the range of alkalinities values from the different methods. Saunders (2012) had measured the calcium (132.4mg.L^{-1}) and magnesium (4.6mg.L^{-1}) concentrations of the Welton spring. In our study, we measured the pH (7.5) and temperature (18°C) of this water. These parameters were used for our modelling. This modelling allowed to evidence the different results we can obtain thermodynamically between all the methods and thus compare these data.

It was also interesting to apply the computed uncertainties (CVs) for the different methodologies (expert level of the FEP, ST and IPT) to field data for representative polluted sites. Parameters such as the pH, temperature, major ion concentrations, total alkalinity were computed for each site. This was aimed to show the impact of the errors related to each method on the alkalinities, and consequently on the predicted saturation levels.

5.3 | RESULTS

5.3.1 | Importance of operator experience for fixed end point alkalinity titrations

Within the set of data from the Fixed End Point method, Beginners 1, 6, 7, 8, 14, 15, 19, 20 (40% of the 20 Beginners) present an asymmetrical distribution of results with high CV [CV =15 to 132%]. Results from Beginners 3, 5, 10, 18 (20%) are equally asymmetrical but display a lower CV [CV=-98% to -5%] (Figure 5.3). Beginners 2, 9, 12, 13 (20%) exhibit more symmetrical distribution with moderately high CV [CV =17% to 75%] (Figure 5.3), whereas Beginners 4, 11, 16, 17 (20%) also provide symmetrical results distribution but with low CV [CV =-98% to -6%] (Figure 5.3). Experts 2, 4, 5, 6, 9, 12, 13, 14 (53% of the 15 Experts) provide asymmetrical results with extremely high CV value range [CV=19 to 490%]. Experts 1, 3, 7, 8, 10, 11, 15 (46%) show more symmetrical distribution, with moderately high CV [CV=16 to 169%] (Figure 5.3).

Statistical testing outcome reveals that there is not a significant difference in average normalised alkalinity between the beginner and expert level for the FEP method as the P value is greater than 0.05 (*Mann Whitney U*: 0.061; degree of freedom: 1; $P = 0.805$; Figure 5.3), so the null hypothesis is accepted. This shows there is no significant difference in average alkalinity values recorded on the test waters between beginners and experts. However, the statistical testing outcome shows that there is a significant difference in average normalised alkalinity between operators for the FEP method as the P value is lower than 0.05 (*Kruskal Wallis*: 282.663; degree of freedom: 34; $P = 0$; Figure 5.3), so the null hypothesis is rejected. This suggests there is a significant difference in average alkalinity values recorded on the test waters between operators, but this is not affected by user experience level. This likely arises from the subjectivity in determining the colour change end point, implying different end points.

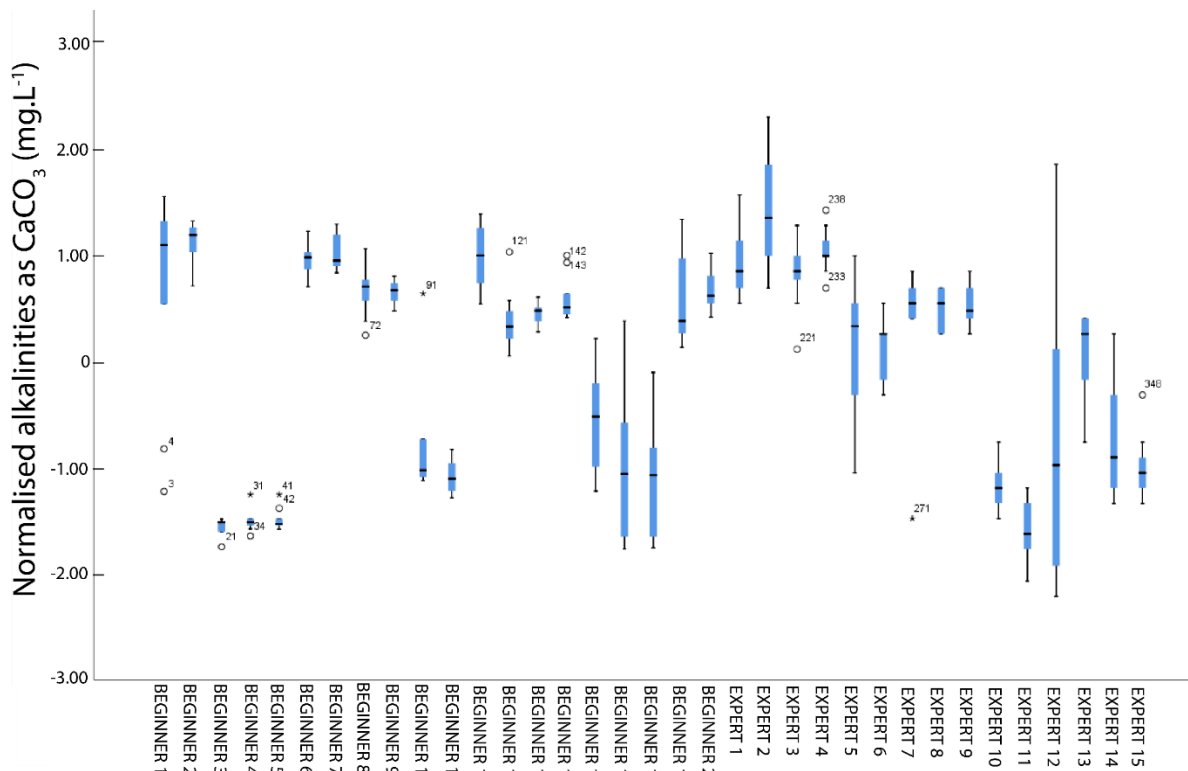


Figure 5.3: Graph depicting the data of the FEP method (Beginner and Expert Level).

Another outcome from the statistical testing shows that there is not a significant difference in average normalised alkalinity between the water 1 and water 2 for the IPT method

as the P value is greater than 0.05 (*Kruskal Wallis*: 2.306; degree of freedom: 1; P = 0.129; Figure 5.4), so the null hypothesis is accepted. This suggests there is no significant difference in average alkalinity values recorded on the test waters between water 1 and water 2.

5.3.2 | Comparison between alkalinity methods

The FEP method shows that among the beginners, 40% present an asymmetrical distribution of results with high CV [CV =15 to 132%], 20% are equally asymmetrical but display a lower CV [CV=-98% to -5%], 20% exhibit more symmetrical distribution with moderately high CV [CV =17% to 75%] (Figure 5.3) and 20% provide symmetrical results distribution but with low CV [CV =-98% to -6%] (Figure 5.3). Regarding the experts, 53% provide asymmetrical results with extremely high CV value range [CV=19 to 490%] and (46%) show more symmetrical distribution, with moderately high CV [CV=16 to 169%] (Figure 5.3). Water 1 from the Inflection Point method reveals a very good symmetry in the results distribution [value range=-2.60 – 1.80; median=0.18] with a very small CV [CV=1.8%] and water 2 also displays a symmetrical distribution [value range=-1.21 – 3.22; median=-0.25] confirmed by a low CV [CV=8%] (Figure 5.4). The ST method attests of a very good symmetry in the boxplot (Figure 5.5) with a CV higher than for the IP method but lower than for FEP [CV=23%]. Comparison between FEP and ST methods, and between IP and ST methods show there is no significant difference in average normalised alkalinity, since the P values are greater than 0.05 (FEP versus ST method: *Kruskal Wallis*: 1.546; degrees of freedom: 2; P = 0.641; IP versus ST method: *Kruskal Wallis*: 0.045; degree of freedom: 2; P = 1.), so the null hypotheses are retained. The low-test statistic values for FEP versus ST (1.546) and IP (0.045) versus ST support this idea further. However, direct comparison of FEP versus IP methods demonstrate that there is a significant difference in average normalised alkalinity (FEP versus IP method: *Kruskal Wallis*: 47.968; degrees of freedom: 2; P = 0) rejecting the null hypothesis. Consequently, we conclude that the IP and FEP methodologies provide statistically different

results for DIC analysis, but neither are statistically distinguishable from the ST method. In addition, the shape of the distributions reveals that ST is highly similar to IPT, but with higher variance (Figure 5.5). FEP has even higher variance, a bias to higher CV and a non-normal distribution (Figure 5.5). Figure 5 confirms the noticeable bias and the non-normal behaviour of FEP. ST is performing slightly better, but there are more easy error distribution to handle (Figure 5.6).

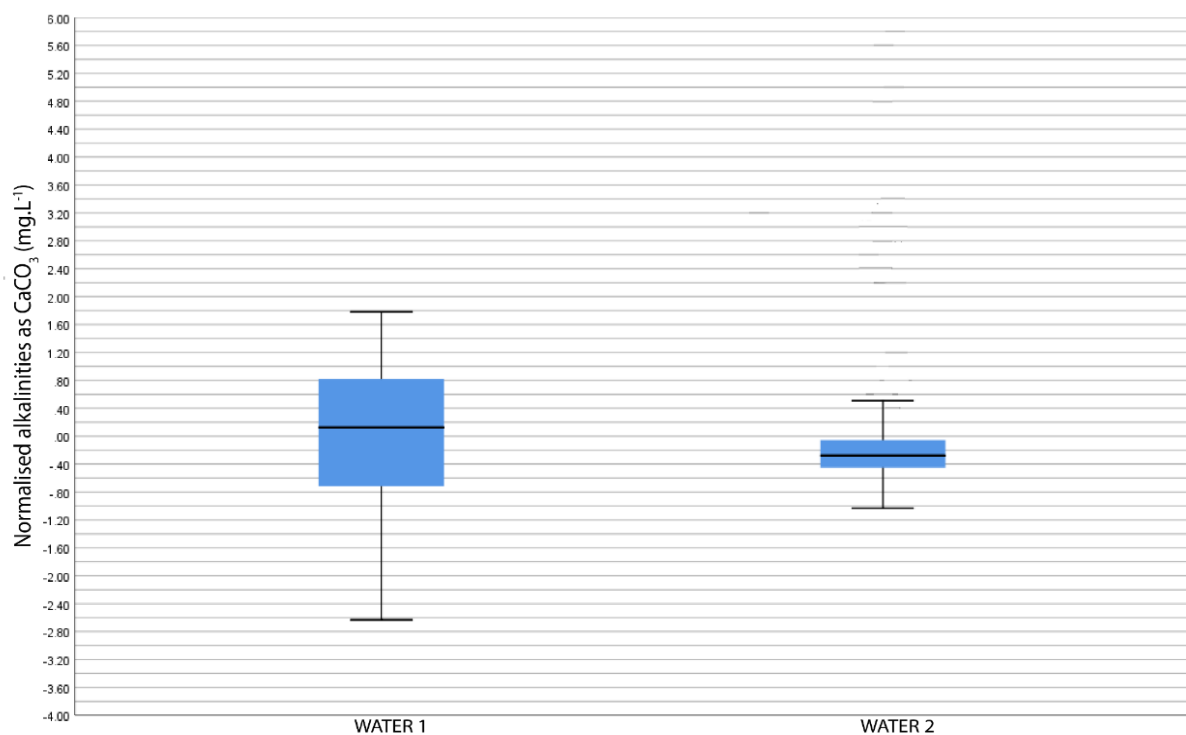


Figure 5.4: Graph depicting the data of the Inflection Point method (water 1 and water 2).

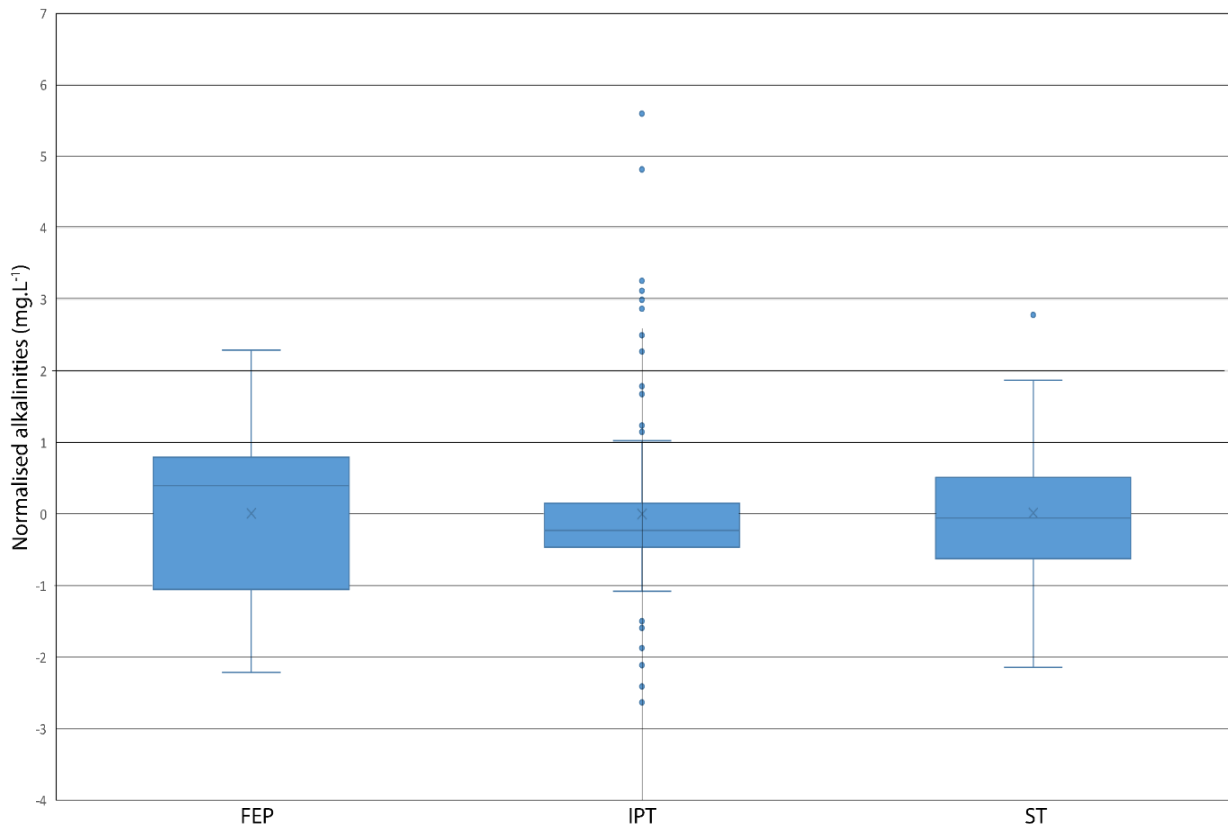


Figure 5.5: Graph depicting the comparison of the three methods of titrations

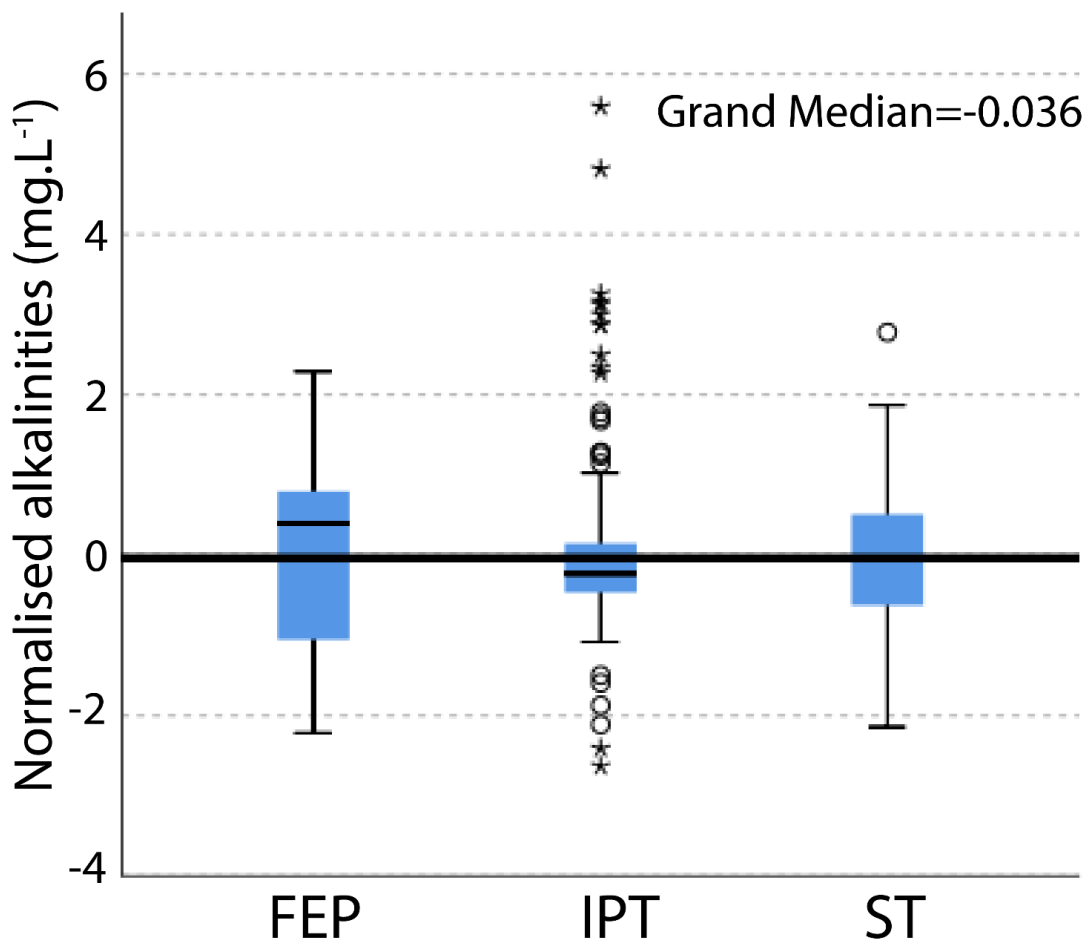


Figure 5.6: Graph depicting the comparison of the median of the three methods of titrations.

The overall comparison between the three methods suggests we can retain the null hypothesis with a P value of 0.059, greater than 0.05. Therefore, there is not globally a difference in average normalised alkalinity. The degree of freedom reaches the value of 2 and the test statistic is of 5.672.

5.3.3 | Saturation index modelling of the alkalinity data

For beginners and experts of the FEP, SI values range from 0.10 to 0.41 and 0.04 to 0.18 respectively (Table 5.1). For FEP, IPT and ST, we obtained the SI range values of 0.04 to 0.41, 0.38 to 0.62 and 0.00 to 0.47 respectively (Table 5.1). When we applied the computed uncertainties (CVs) for the different methodologies (expert level of the FEP, ST and IPT) to field data for representative polluted sites, we obtained much broader ranges of SI for Mayes et al. (2008) (SI=-2.59 to 3.39; see Table 5.2) and Bastianini et al. (2019) (SI=-2.51 to 2.96; see Table 5.3).

Table 5.1: Table depicting the ranges of SI corresponding of the alkalinity values from the different methods.

Alkalinities	Saturation Index (SI) Calcite Range
Beginner (FEP)	0.10-0.41
Expert (FEP)	0.04-0.18
FEP	0.04-0.41
IPT	0.38-0.62
ST	0.00-0.47

Table 5.2: Table depicting the uncertainties (CV) from the FEP, ST and IPT methods applied to alkalinities after Mayes et al. (2008) – Table 1; N/A values correspond to extreme alkalinity values where PHREEQC was unable to compute an SI for calcite.

FEP																		
Alkalinities (mg. L⁻¹) Mayes et al. (2008) – Table 1	95		432		303		85		96		177		174		776		133	
Applied Expert CVs (19 to 490%) to alkalinities	18	466	82	2117	58	1485	16	417	18	470	34	867	33	853	147	3802	25	651
SI Calcite	-1.57	-0.24	N/A	2.89	N/A	2.86	1.08	2.45	1.10	2.37	-0.63	0.70	N/A	2.12	N/A	3.39	1.14	2.35
ST																		
Applied CV (23%) to alkalinities	22		99		70		20		22		41		40		178		31	
SI Calcite	-1.49		N/A		N/A		1.18		1.20		-0.54		- N/A		N/A		1.26	
IPT																		
Applied CVs (1.8 to 8%) to alkalinities	2	8	8	35	6	24	2	7	2	8	3	14	3	14	14	62	2	11
SI Calcite	-2.59	-1.94	N/A	N/A	N/A	N/A	N/A	0.46	N/A	0.50	-1.65	-1.00	N/A	N/A	N/A	N/A	N/A	0.25

Table 5.3: Table depicting the uncertainties (CV) from the FEP, ST and IPT methods applied to alkalinities after Bastianini et al. (2019) – Table 1; N/A values correspond to extreme alkalinity values where PHREEQC was unable to compute an SI for calcite.

FEP												
Alkalinities (mg. L⁻¹) Bastianini et al. (2019) – Table 1	59		55		66		56		264		332	
Applied Expert CVs (19 to 490%) to alkalinities	11	289	10	270	13	323	11	274	50	1294	63	1627
SI Calcite	-0.5	1.61	0.24	1.49	-0.32	0.96	0.14	1.42	N/A	2.73	N/A	2.96
ST												
Applied CV (23%) to alkalinities	14		13		15		13		61		76	
SI Calcite	0.09		0.37		-0.24		0.25		N/A		N/A	
IPT												
Applied CVs (1.8 to 8%) to alkalinities	1	5	1	4	1	5	1	5	5	21	6	27
SI Calcite	N/A	N/A	N/A	-2.51	-1.38	-0.66	N/A	-0.34	N/A	N/A	N/A	N/A

5.4 | DISCUSSION

5.4.1 | Comparing Beginner and Expert levels from FEP

In this study, we are using the International Organization for Standardization (ISO) terms and definitions of precision, trueness, reproducibility, reproducibility standard deviation and bias to provide a framework, which importantly is attached to an external authority of this research work. Precision applies to the closeness of agreement between independent test results obtained under stipulated conditions. Trueness constitutes the closeness of agreement between the average value obtained from a large series of test results and an accepted reference value. Reproducibility corresponds to the precision under conditions where test results are obtained with the same method on identical test items in different laboratories with different operators using different equipment. The reproducibility standard deviation is equivalent to the standard deviation of test results obtained under reproducibility conditions and is obtained by computing the standard deviation of the averages of all the users. Bias signifies the difference between the expectation of the test results and an accepted reference value.

When data are aggregated by beginner and expert levels classifications, there was no significant difference in median value with both showing noisy, but similar distributions (Figure 5.7). Furthermore, the non-parametric test of Kruskal Wallis and Mann-Whitney U reveal that both levels have similar median and distributions (Figure 5.7). Indeed, the adjusted significance is higher than 0.05 (adjusted significance=0.805) allowing the null hypothesis to be retained; in other words, user experience does not alter the distribution of results. This is very helpful for use of grey literature or historical results, as it should be possible to determine a transferrable uncertainty estimate for measurements which can be used with such datasets. It is important to note that the data are overall broadly distributed, especially for the Expert Level

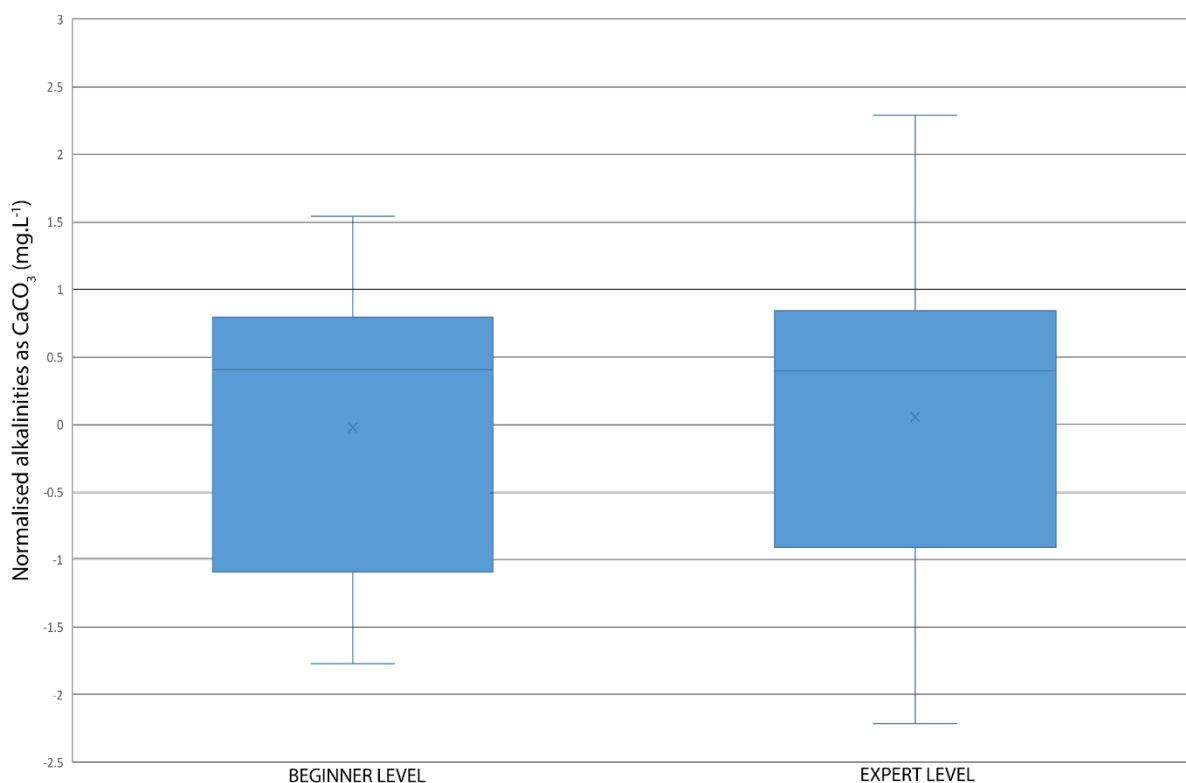


Figure 5.7: Graph depicting the comparison of beginner and expert levels within the FEP.

(~ -2.5 to 2.5 mg.L^{-1}), showing a lower precision and trueness (ISO framework) in comparison to the Beginner Level.

From these tests, we can conclude that the FEP is a useful field instrument as the user does not need much training to get values that are consistent with experts, although the range of results is quite extended. However, there clearly are significant differences between individual operators (Figure 5.3). This is a precision issue from a low reproducibility in the ISO framework arising from differences in reproducibility conditions. The reproducibility standard deviation is very elevated (35.6), which confirms the low reproducibility of this method. The latter might be due to the extended analytical process of FEP (Figure 5.8) and the margins for error that can be introduced throughout the procedure (Table 5.4). Taras et al. (1971) stated that the lack of precision in a titration method can come from the equipment and the measurement. Many water quality laboratories use macroburets that cannot be read with as great precision and accuracy as possible with the microburet used in the current study (Boyd

and Tucker, 1992). This is comparable to the FEP method where measuring the test volume relies on consistency in operator in determining the position of the meniscus. In this test operator-sensitive steps are:

1. Rinsing the test vessel with sample water prior to the test with scope for some residual water to remain in the measuring cylinder or Erlenmeyer flask leading to subtle changes in volume,
2. Measuring the test volume which relies on consistency in operator in determining the position of the meniscus,
3. Entrainment of particulates / biofilm in the sample which would potentially artificially elevate alkalinity if they contained carbonates,
4. Transfer from one vessel to another (measuring cylinder to Erlenmeyer flask) and potential loss of residual sample volume,
5. Air bubbles in the titrator that could lead to an artificially high alkalinity reading,
6. Subjectivity in determining the colour change end point.

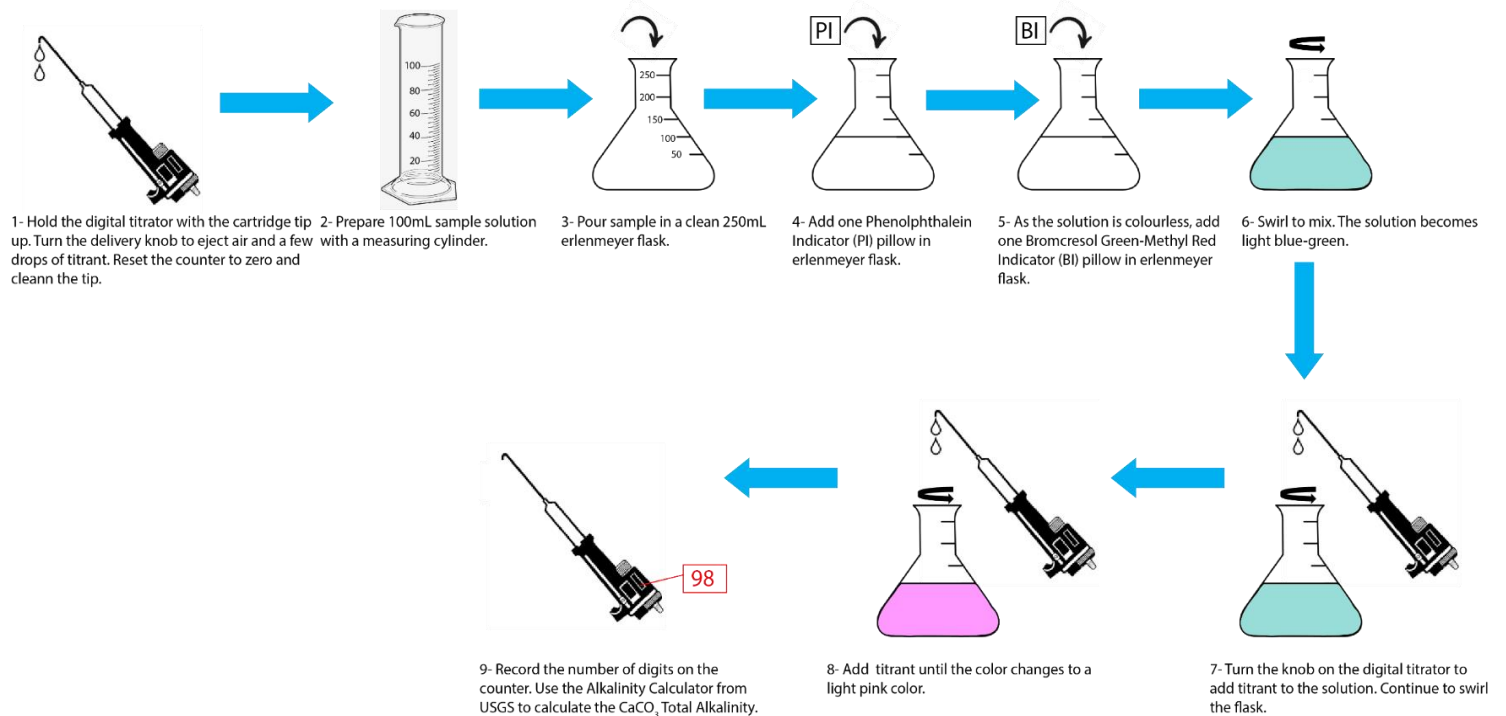


Figure 5.8: Flow chart describing the process of the FEP method.

Whilst operators should be aware of these issues when being trained on the device, subtle differences between operators could aggregate to the relatively large ranges observed in Figure 5.3. The stark differences that are apparent between different consecutive users on the same water sample in Figure 5.3 (e.g. between Beginner 1 / 2 and Beginner 3-5) suggests it may well relate to subjectivity of end-point determination in some cases given the repeated tight clustering of values by individual. The study of Somridhivej & Boyd (2016) shows that the endpoint pH used for the total alkalinity determination can affect the accuracy of results. A titration stopped short of the optimum endpoint pH will underestimate total alkalinity, while one continued beyond the optimum endpoint pH will overestimate total alkalinity. The cause of the variation in endpoint pH is carbon dioxide released during neutralization of alkalinity.

Additionally, Somridhivej & Boyd (2016) reveal that the detection of the endpoint colour is more challenging to recognize than is the measured pH for the endpoint. In the study of Somridhivej & Boyd (2016), the graduate students, comparable to our beginners, generally provided more accurate results than did the participating laboratories. The students had all taken a class on water quality analysis no more than 2 years before. As found here, they also suggest that the accuracy of alkalinity data is highly dependent on the operator. However, in our study, the precision of the alkalinity values is not clearly reliant on the operator (beginner/expert levels) (Figure 5.7). Experts generally produce higher CV than beginners from the same sample, which may reflect inexperienced users ceasing the titration too early. This is consistent with the result of Somridhivej & Boyd (2016), who found that with the the Fixed End Point method, beginners and experts present a CV in the value range of CV = -98 to 132% and CV = 19 to 490% respectively. However, their students (equivalent to our beginner level) reported better precision than obtained by most of the laboratories (equivalent to our expert level). The coefficients of variation for the students ranged from 0.57 to 25.47% (average = 4.64%) for the 20 mg l⁻¹ standard, from 0.14 to 6.49% (average = 0.83%) for the 80 mg l⁻¹

standard, and from 0.10 to 8.54% (average = 1.11%) for the 240 mg l⁻¹ standard (see Table 5 of Somridhivej & Boyd, 2016). This finding is not replicated in the study reported here.

5.4.2 | Comparing FEP versus IP versus ST methods

The global CVs of the beginners from FEP for the two waters used (water 1=22%; water 2=5%) and the experts of FEP (8%) are comparable to the CV of ST (23%), but higher than the CVs of the IPT (water 1=1.8%; water 2=8%). These results demonstrate the excellent precision (ISO framework) of IPT in comparison of FEP and ST which are quite similar. In addition, the non-parametric tests evidence that ST shows the same in distribution and median than FEP and IPT, but IPT has a lower median than FEP (Figures 5.5 and 5.6). However, IPT and FEP have compatible distribution since the null hypothesis is accepted (adjusted significance=0.059 > 0.05) (Figures 5.5 and 5.6).

It seems logical that IPT presents a higher precision, accuracy and reproducibility (ISO framework) than FEP and ST, and a different median than FEP considering the sources of error for these techniques (Table 5.4). IPT is a fully automated method, which involves much less errors (rinsing, measuring, transfer from one vessel to another) than FEP (rinsing, measuring, entrainment of particulates / biofilm, transfer from one vessel to another, air bubbles in titrator, and subjectivity of colour change pattern) as IPT is a mechanised technique and does need only minor intervention from the operator (Table 5.4).

The data clearly show that FEP and ST are giving a positive bias in alkalinity compared to IPT (Figure 5.6). However, FEP provides a much bigger positive bias (ISO framework), therefore the measurement is less precise (Figure 5.6). In addition, FEP is the worst of all methods for quantitative work as its distribution is non-normal (Figure 5.6). It is important to note that ST is showing (in ISO terms) higher precision, accuracy and reproducibility than FEP since ST presents less errors than FEP (Table 5.4). ST errors might come from measuring,

weighing (precision of balance up to 0.0001g), transfer from one vessel to another, loss of precipitate on the edges of the vessel and during filtration (Table 5.4). ST also corresponds to easier data to study than FEP due to the normally distributed data (Figure 5.6). Consequently, for a field campaign if we do not have the possibility to bring an expensive and voluminous automated device such as the IPT, the ST method appear to perform much better than the existing method of FEP.

Table 5.4: Table depicting the different sources of error with their nature for each method.

Type of method	Source of error	Nature of error
FEP	Rinsing.	Indeterminate.
	Measuring.	Random.
	Entrainment of particulates/biofilm.	Random.
	Transfer from one vessel to another.	Indeterminate.
	Air bubbles.	Systemic.
	Subjectivity in determining the colour change endpoint.	Systemic.
ST	Measuring.	Random.
	Weighing.	Systemic.
	Transfer from one vessel to another.	Indeterminate.
	Loss of precipitate.	Indeterminate.
IPT	Rinsing	Indeterminate.
	Measuring.	Random.
	Transfer from one vessel to another.	Indeterminate.

5.4.3 | Errors resulting from the different methods

Unlike the study of Fritz (1994), in our study, the water temperature was measured every day and remained quite constant ranging from 17.9 to 18.5°C. There is a good number of random and indeterminate errors raising from each method such as rinsing, measuring, entrainment of particulates/biofilm, transfer from one vessel to another, loss of precipitate (Table 5.4). Our FEP method induces systematic errors as well, including air bubbles in the titrator, subjectivity in determining the colour change endpoint and weighing due to the precision of the balance (Table 5.4). The elaboration of the different sources of errors and their nature in Table 5.4 suggest that FEP has the greatest change for aggregated errors given its protocol. Indeed, its protocol induces much more steps than the other methods, which must be undertaken by the operator as they are not automated. Furthermore, Figure 5.3 suggests there is a significant difference in average alkalinity values between operators, which might be explained by the subjectivity in determining the colour change end point, involving different end points. Figure 5.1 shows that if we modify the pH values 4.5 and 8.3, corresponding to the methyl orange and phenolphthalein endpoints respectively, we obtain different concentrations of carbonate, bicarbonate and hydroxide ions, hence the discrepancies in total carbonate alkalinity between operators.

5.4.4 | Calcite saturation levels of the alkalinity data

Regarding the saturation levels calculated with the PHREEQC modelling for the Welton water, we have determined the saturation index (SI) of calcite by computing the range of extreme alkalinities values observed from the different methods. There is a large difference between the beginner and expert level. Beginners present much higher range of SI since they have the most elevated range of values with more extreme limits of alkalinities (Table 5.1). All techniques tend to produce undersaturated values, but IPT and ST show the highest levels of

saturation state (Table 5.1). Given the water composition and the neutral pH, it is unsurprising that calcite saturation index is quite low (0.00 to 0.62) (Table 5.1), although these values go across the range of SI where heterogeneous calcite precipitation is often documented ($\sim+0.3$ according to Ford and Williams, 2013). However, IPT presents the largest range of values with more extreme limits of alkalinities and the most elevated alkalinities (Figure 5.5), hence providing the highest range of SI.

To conclude, the experts seem to provide more accurate data than the beginner level as their values are comprised in a minor range of SI. It is more difficult to draw a conclusion for the comparison of the three methods, as they all present quite similar undersaturated values. From this study, we know that IPT is the most reproduceable technique followed by ST, however the large range of alkalinities of IPT inducing the most elevated SI ranges seem to compromise a clear conclusion about which is method is precise enough to address a common research question.

The findings reported above also permit questions concerning whether the approaches used to determine environmental alkalinity are sufficient to answer the research questions they are applied to:

- 1) Are the uncertainties for the different methods so large they may change interpretation of a site?
- 2) Is this outcome the same for all methods?
- 3) Are any of the methods accurate / precise enough to yield answer common research questions at highly alkaline sites?

The data gathered on the range of alkalinity values observed can be informative for thinking about how such variance would translate into geochemical interpretation at other field sites. Here, we are using two case studies at Consett (Mayes et al., 2008; Bastianini et al.,

2019) to address these questions. When we apply high / low permutations of determined methodological errors (CVs) for each alkalinity method to these published data, the differences between alkalinities are extremely elevated. Table 5.2 shows alkalinities ranging from 18 to 3802 mg/L as CaCO₃ for the FEP uncertainties (19% and 490%), from 20 to 178 mg/L as CaCO₃ for the ST error (23%) and from 2 to 62 mg/L as CaCO₃ for the IPT uncertainties (1.8% and 8%). This results in very distinct SI ranges for the different methods (FEP: -1.57 to 3.39; ST: -1.49 to 1.26; IPT: -2.59 to 0.46). Table 5.3 reveals alkalinities ranging from 10 to 1627 mg/L as CaCO₃ for the FEP uncertainties (19% and 490%), from 13 to 76 for the ST error (23%) and from 1 to 27 mg/L as CaCO₃ for the IPT uncertainties (1.8% and 8%), arising disparate SI ranges for the different techniques (FEP: -0.5 to 2.96; ST: -0.24 to 0.37; IPT: -2.51 to -0.34). FEP clearly demonstrates the greatest potential range of SI conditions (from undersaturated to highly supersaturated) due to the extremely high range of uncertainties (19% and 490%). ST comes in second position with a relatively elevated error (23%) giving high range of alkalinities and SI. IPT contribute to extremely low alkalinity values, explaining why the software was unable to compute some SI data. This modelling shows that within a same technique and between two different methods, the assessments of precipitation rate and carbon uptake could be drastically unlike. The uncertainties 1.8%, 8%, 19% and 23% from IPT, FEP and ST respectively generate undersaturated systems whereas the error 490% from FEP cause very high supersaturated systems.

In conclusion, we can state that the uncertainties for the FEP method are so elevated that it does modify our interpretation of the site, but it is less obvious for IPT and ST, which present smaller uncertainties. IPT is certainly accurate and precise enough to utilise their data, but the reliability of those published data could be questioned if they have used a technique inducing many errors, such as FEP and ST. Whilst we may anticipate more consistency in real world sampling conditions where individuals or small sample teams are collecting field

alkalinity data routinely, for long term records with multiple observers (e.g. Riley and Mayes, 2015), there may well be scope for a greater influence of human error in alkalinity and subsequent SI calculations from FEP monitoring. This study established the very important role played by field measurements in influencing our understanding of these systems.

5.5 | CONCLUSION

This study provides an insight into the uncertainties related to field carbonate alkalinity measurements. The comparison of the reproducibility between the beginner and expert level for FEP reveals that there was no significant difference, both are noisy, with similar distributions. Therefore, we conclude that FEP is a useful field instrument as the user does not need much training to get good values, although the range within the results is quite extended. IPT is the most reproduceable technique and presents a different median than FEP due to the sources of error of FEP and ST. IPT is a method which involves much less errors as it is an automated technique and only needs minor intervention from the operator. Regarding FEP and ST, ST is showing higher precision, accuracy and reproducibility than FEP. In addition, ST corresponds to easier data to study than FEP due to the normally distributed data. Therefore, for a field work if we are unable to bring an expensive and voluminous automated device such as the IPT, the ST method appears to perform much better than the existing method of FEP.

When we utilise high / low permutations of alkalinities from the CV data of the FEP, ST and IPT methods on published data, the differences between alkalinities and SI values are extremely elevated. This reveals that within a same technique and between three different methods, the assessments of precipitation rate and carbon uptake might be drastically dissimilar. Some uncertainties generate undersaturated systems whereas other cause very high supersaturated systems. We can consequently question the reliability of those published data if they have used a technique inducing many errors. Therefore, we recommend further

investigation to help potentially understanding hyperalkaline sites for passive remediation or sedimentology.

5.6 | AUTHOR CONTRIBUTIONS

The idea for this manuscript arose from the discussion between all authors. Laura Bastianini conducted the experiment for the FEP method and executed the whole set of experiments for IPT and ST methods. She executed the statistical testing and drafted the manuscript. Mike Rogerson designed the ST method and made improvements through the whole manuscript. William M. Mayes contributed to the experiment of the FEP method (expert level) and provide guidance to perform the statistical testing. He also made improvements through the whole manuscript.

CHAPTER 6 – THESIS CONCLUSION

6.1 | INTRODUCTION

This thesis aimed to better understand the geochemistry of hyperalkaline carbonate systems, particularly those arising from globally important anthropogenic processes such as lime production, cement and steel manufacture, alumina refining and electricity generation. Hyperalkaline sites are of critical importance as potential sources of contaminants, sites for resource recovery, and potential mineral carbonation. An improved understanding of geochemical processes at these sites can therefore be of importance across a breadth of potential applications. This final chapter of the thesis revisits the research questions set in Chapter 1 and considers avenues for future research.

6.2 | KEY FINDINGS AROUND RQ1: What are the dominant carbonate fabrics found in secondary deposits at anthropogenic hyperalkaline sites?

The second chapter of this thesis aimed to identify the dominant carbonate fabrics at a site receiving drainage from iron and steel wastes associated with a former steel mill at Consett, County Durham, northern England and compares these to analogous natural carbonates found in the South Atlantic Pre-Salt carbonates (RQ1). The study of carbonate fabrics at anthropogenic sites is of significant importance to understand biogeochemical processes driving carbonate precipitation in these systems. The dominant carbonate fabrics are clotted micrite, microbial rim, carbonate dendrite, calcite shrub, cluster-shaped calcite, multi-shaped calcite, sparry carbonate crust and blocky calcite. Clotted micrite is made up of a brown micritic matrix composed of fine homogeneous rounded micrite peloids and has a microbial origin, although the balance of bio-influenced and bio-induced is not known (Pedley, 1992). Microbial rim corresponds to thin black layers (180–250 μm thick) of dense micrite characterised by the presence of diverse microbial remains so they are considered as being largely bio-influenced.

Dendrites are constituted by light-grey calcite crystals growing radially forming flower-like geometries associated with high rates of kinetic mineralization promoting polycrystal formation. Calcite shrubs are a particular subset of dendritic fabrics made up of light grey-green botryoidal crystal fans, surrounded by diatoms and bacterial filaments. Cluster-shaped calcite appears as translucent white crystals ranging from 20 to 500 μm in length, developed among bacterial filaments with an organic film forming a sticky, thin black layer around crystals which could correspond to EPS, suggest that this microfacies comes from biologically influenced mineralization. Multi-shaped calcite refers to translucent, white, delicate crystals (100–550 μm in diameter) displaying rounded external morphologies and grain-to-grain contact and this reworked microfacies is made up of a mixture of mineralized and organic debris. Sparry carbonate crust comprises thick sparitic crusts (500–2,500 μm thick) made up of milky white to grey calcite, developing very low intercrystalline porosity. Blocky calcite corresponds to single, very large crystals 500–1,500 μm in diameter, where the crystals are milky white to translucent grey.

Although the carbonates at Consett arise from low temperature and highly alkaline steel lag leachates, they exhibit strikingly similar primary crystal morphologies to those recognized in the Pre-Salt shrub carbonates. The Consett carbonates developed in a spring waterfall environment in the vicinity of former steelworks and under the influence of constant supplies of calcium and carbonate ions. The shrubby carbonate facies at the site appear to be the result of extreme environmental conditions (elevated pH and alkalinity, high CSI and R) but shrubby and dendritic crystals attest to a kinetic rather than thermodynamic control with high kinetic forcing. Non-dendritic facies (blocky calcite, sparry-carbonate crust and cluster-shaped carbonate) result from a low kinetic forcing and classic “microbialite” rim and clotted micrite form at a moderate-low forcing. Carbonate morphology is therefore variable along these gradients and unusual shrubby morphologies are associated with specific chemical and

hydraulic features. These findings are essential for understanding provenance of anthropogenic deposits but also Pre-Salt shrub carbonates.

6.3 | KEY FINDINGS AROUND RQ1: What are the dominant carbonate fabrics found in secondary deposits at anthropogenic hyperalkaline sites? & RQ2: What do differences in carbonate fabrics at hyperalkaline sites tell us about controls on carbonate precipitation?

The third data chapter expands the work at Consett to provide a multi-site comparison of carbonate fabrics at systems receiving anthropogenic hyperalkaline drainage (RQ1) and considers similarities in drivers of precipitation processes (RQ2). This sedimentological study of anthropogenic carbonates shows that the formation of calcite minerals is complex and not homogeneous or purely driven by thermodynamic processes. Precipitation within the surface tension layer is reported here, which is probably directly controlled by the rate of CO₂ dissolution, but precipitation also occurs below the diffusive boundary layer and this may be influenced by advective transport in the water column. In addition, both diffusively limited and kinetically limited crystal forms are found, indicating differences in crystal assembly style which may alter trace element incorporation and co-precipitation rates. Interestingly, bio-influenced and bio-induced fabrics were identified suggesting that the site, rate, style and trace element incorporation into precipitates can be altered by the presence of microbial biofilms. Anthropogenic systems are as complex as naturally occurring tufa and travertine, and equally approachable to standard sedimentological analysis.

6.4 | KEY FINDINGS AROUND RQ3: Through novel coupled field and laboratory analyses, what evidence is there for transient mineral formation at anthropogenic hyperalkaline sites? & RQ4: What are the implications of transient mineral formation on trace metal dynamics?

The fourth chapter explores transient minerals produced at hyperalkaline sites with a novel approach for field characterisation and rapid laboratory confirmation of samples of interest (RQ3). The transient minerals identified include the first discovery worldwide of the hydrated carbonate polymorph ikaite in steel slag leachate. Through integration of field observations, laboratory characterisation and experimental work, this chapter considers the potential importance of transient mineral phases for trace metal dynamics at hyperalkaline sites (RQ4). Based on the laboratory experiments and very high partition coefficients in the field sample, ikaite appears to be secondary mineral with a primary phase being ACC. This may explain why partition coefficients we report from Consett are very high, as the disordered structure of amorphous mineral permits easy incorporation of trace elements. The ikaite forming in steel-slag leachate affected waters is sequestering large inventories of very harmful pollutants such as cadmium and lead which are toxic to flora and fauna as well as being priority hazardous substances for human health. Chromium, zinc, manganese, barium and nickel are other potential contaminants reported in this study causing various ill effects, which are accumulated in the transient ikaite inventory.

As ikaite is thermally unstable, the inventory is lost during warming periods. In our field study area (Consett, County Durham, UK) this is related to synoptic weather, but in colder regions the warming will likely relate to springtime thawing. Therefore, most of the temporarily stored contaminant mass will be lost back to solution in a short duration, potentially creating a significant peak in toxicity. These short-lived periods of acute pollution may significantly compromise river ecology, and present potential challenges to human health. The regions most

exposed to this risk as those with long durations of stable low temperature in the winter, so steel-making and former steel-making locations in Russia, northern North America, Canada, Sweden, Finland and Central Europe should be investigated for this process. Ikaite is considered to have an upper temperature limit of 8°C, providing a key isotherm to guide this investigation spatially and seasonally. However, ikaite has been reported forming under ambient temperatures (5-35°C), so the 8°C isotherm may significantly underestimate the issue.

6.5 | KEY FINDINGS AROUND RQ5: How can dissolved inorganic carbon be better characterised from anthropogenic hyperalkaline sites?

The chapter five evaluates a range of methods for dissolved inorganic carbon (DIC) characterisation at anthropogenic alkaline sites. This chapter compares a range of methods for assessing DIC in alkaline samples and includes the development of a new method for such based-on strontium carbonate precipitation. Traditional methods (manual and automated titrations) are compared against the new strontium carbonate method for accuracy and reliability. The implications of the differing performances in these methods for DIC characterisation are considered for interpreting geochemical processes (notably carbonate saturation) at hyperalkaline sites (RQ5). The comparison of the reproducibility between the beginner and expert level for FEP reveals that there was no significant difference, both are noisy, with similar distributions. Therefore, we conclude that FEP is a useful field instrument as the user does not need much training to get good values, although the range of results is quite extended. IPT is the most reproduceable technique and presents a different median than FEP due to the sources of error of FEP and ST. IPT is a method which involves much less error as it is an automated technique and only needs minor intervention from the operator. Regarding FEP and ST, ST is showing higher precision, accuracy and reproducibility than FEP. Therefore, for a field work if we are unable to bring an expensive and voluminous automated device such as the IPT, the ST method appear to perform much better than the existing method of FEP.

When we apply determined methodological errors of the FEP, ST and IPT methods on published data, the differences between alkalinities and SI values are extremely elevated. This reveals that within a same technique and between three different methods, the assessments of precipitation rate and carbon uptake might be drastically dissimilar. Some uncertainties generate undersaturated systems whereas other cause very high supersaturated systems. We can consequently question the reliability of those published data in terms of quality data if they have used a technique inducing many errors. Therefore, we recommend further investigation to help potentially understanding hyperalkaline sites for passive remediation or sedimentology.

6.6 | FUTURE RESEACH DIRECTIONS

This study raises several future research priorities which are summarised in Table 6.1. These research orientations will be essential to better understand the geochemistry of hyperalkaline carbonate systems, particularly those arising from globally important anthropogenic processes. Hyperalkaline sites constitute potential sources of contaminants, sites for resource recovery, and potential mineral carbonation and a better apprehension of their geochemical processes can be applied to a range of different domains.

Table 6.1: Summary of research priorities for a better understanding of the geochemistry of hyperalkaline carbonate systems.

Key knowledge gaps identified	Research Required	Potential Impact
Lack of evidence of Pre-Salt analogous shrubby carbonates in human-induced carbonate deposits.	Finding more replicates of shrubby carbonates in extreme alkaline environments through extensive fieldworks.	Understanding hyperalkaline sites occurring in most post-industrial landscapes in terms of mass deposition is a key part of fully constraining their behavior, and thus being able to manage them successfully.
Understanding temporal dynamics of trace elements incorporated into transient minerals such as ikaite.	Undertaking seasonal surveys of water quality during melting events to assess dissolved metal concentrations.	Better understanding of potential chronic short term pollution events to advise regulatory authorities on improved monitoring approaches / potential remedial action.
Uncertainty on the first partition coefficients of ikaite elaborated in this study.	Designing an experiment to assess the distribution coefficient and ion substitution of ikaite to elucidate the trace elements that can be substituted to ikaite.	Confirmation of the partition coefficients of ikaite previously established.
Lack of discovery of the transient mineral ikaite in human-induced steel-making settings.	Expanding field campaigns to other hyperalkaline post-industrial settings (e.g. Russia, northern North America, Canada, Sweden, Finland and Central Europe), and to natural hyperalkaline sites (e.g. Newfoundland).	Verification that similar transient development of ikaite in steel-waste affected surface water are very widespread, especially in the northern hemisphere.
Evidencing biological influence on carbonate precipitation in high pH settings.	More extensive surveys of carbonate fabrics from other hyperalkaline sites.	Better indication of bio-influence of carbonates in high pH waters.
Field validation of strontium alkalinity method.	Evaluation of the strontium method during many field studies and comparison with the manual and automated methods in terms of accuracy, reproducibility and reliability.	Confirmation that strontium method is performing much better than the existing methods and is likely to provide more robust estimates of alkalinity and saturation index of carbonate minerals.

6.7| OVERALL FINDINGS AND IMPLICATIONS FOR POLICYMAKERS

Highly alkaline (pH 9-12) sites can arise from a variety of industries, causing significant anthropogenic by-products such as lime, cement and steel wastes, bauxite processing residue and combustion ashes. These sites are of interest to researchers from a whole range of scientists and social scientists because they are important for resource recovery, carbon capture, and potential hydrocarbon deposits. But these sites are under-studied compared to acid sites. This thesis aimed to improve the formation processes of hyperalkaline carbonate systems through petrographical analysis, sedimentological studies linked to hydrochemical data to better constraint the process driving the carbonate precipitation.

In this study, we focussed on two sites, a steel-slag leachate system in Consett, and a cement lime kiln waste environment in Brook Bottom. They are similar in terms of chemistry with a pH between 10-12, and they are both calcium hydroxide dominated. They both take the CO₂ out the atmosphere and precipitate carbonates rapidly.

From the site in Consett, Chapter 2 reports petrographic microfacies and fabrics similar to Pre-Salt shrubby carbonate deposits (Lower Cretaceous, non-marine carbonate reservoirs in the South-Atlantic). This study shows that the analogue Pre-Salt shrubby and dendritic carbonate facies are rather being the result of kinetic than thermodynamic controls with high kinetic forcing.

From Brook Bottom and Consett, Chapter 3 provides an interesting linkage of anthropogenic carbonate precipitation to natural travertine deposits where calcite precipitation rates are similar despite differences in the chemical processes occurring. This study established three distinct zones within the reach scale assessment of precipitation processes.

Chapter 4 presents the first discovery internationally of ikaite ($\text{CaCO}_3 \cdot 6\text{H}_2\text{O}$) crystallization within steel-slag leachate through novel field (Fourier Transform Infra-Red) and laboratory (X-Ray Diffraction) validation. This study suggests that ikaite is a secondary mineral with a primary phase being amorphous calcium carbonate (ACC). The ikaite forming in steel-slag leachate affected waters is incorporating large inventories of potentially harmful metals (e.g. lead and cadmium) which could be of environmental concern given ikaite is not thermally stable and could release a pulse of contamination in short duration warming events. Finally, Chapter 5 develops a new protocol for assessing dissolved inorganic carbon (DIC) in alkaline waters via strontium carbonate precipitation. This method is compared to established methods for DIC using field and laboratory titration. The strontium method appears to perform much better than the existing methods and is likely to provide more robust estimates of alkalinity and saturation index of carbonate minerals.

This work is of great importance for the scientific community including industrial, academic, and broader social beneficiaries. Industrial beneficiaries can learn how to remediate similar hyperalkaline waters and understand the processes of formation and risks associated with them. Industrial beneficiaries such as major steel and lime producers or land owners (often public agencies) containing legacy alkaline wastes can use the improved understanding of carbonate precipitation processes to help manage legacy pollution issues more effectively (Table 6.1). The observations of transient minerals are also of importance, not just to site owners, but also regulatory authorities (e.g. Environment Agency) who could adjust sampling protocols to be aware of potential spring flushing events (Table 6.1). Such issues will be particularly important in high latitude areas with snowmelt controlled hydrological regimes. Industrial beneficiaries could also include those investigating the use of alkaline wastes for mineral carbonation (e.g. lime, steel and cement companies) (Table 6.1). Improved knowledge on precipitation processes could help in estimating atmospheric drawdown rates and potentially

in engineering systems where carbonation can be enhanced (e.g. thin film cascading systems) (Table 6.1). Academic beneficiaries might better understand the formation of hydrocarbon (Pre-Salt shrubby carbonates) and natural carbonate systems (travertines and tufa) through the study of anthropogenic carbonates (Table 6.1). Broader social beneficiaries would gain a better understanding of carbon uptake, bio-processes of carbonate mineralisation, and find better ways to assess the risks of transient mineral release, allowing a better management of pollution at legacy sites where these issues are very long standing (Table 6.1).

6.8 | THESIS REFERENCES

Abdul-Wahab, S., & Marikar, F. (2012). The environmental impact of gold mines: pollution by heavy metals. *Open engineering*, 2(2), 304-313.

Abrajano, T. A., N. C. Sturchio, J. K. Bohlke, G. L. Lyon, R. J. Poreda, and C. M. Stevens (1988), Methane-hydrogen gas seeps, Zambales Ophiolite, Philippines: Deep or shallow origin?, *Chemical Geology*, 71(1-3), 211-222.

Adaska, W. S., & Taubert, D. H. (2008, May). Beneficial uses of cement kiln dust. In 2008 IEEE Cement Industry Technical Conference Record (pp. 210-228). IEEE.

Alexander, W. R., R. Dayal, K. Eagleson, J. Eikenberg, E. Hamilton, C. M. Linklater, I. G. McKinley, and C. J. Tweed (1992), A natural analogue of high pH cement pore waters from the Maqarin area of northern Jordan. II: results of predictive geochemical calculations. *Journal of Geochemical Exploration*, 46(1), 133-146

Ali, A. S., US, S. A., & Ahmad, R. (2014). Effect of different heavy metal pollution on fish. *Research Journal of Chemical and Environmental Sciences, Res. J. Chem. Env. Sci*, 2(1), 74-79.

Alonso-Zarza, A. M., & Tanner, L. H. (2009). Carbonates in continental settings: geochemistry, diagenesis and applications. Elsevier.

Al-Oweini, R., & El-Rassy, H. (2009). Synthesis and characterization by FTIR spectroscopy of silica aerogels prepared using several Si (OR)₄ and R'' Si (OR')₃ precursors. *Journal of Molecular Structure*, 919(1-3), 140-145.

Altunel, E. R. H. A. N., & Hancock, P. L. (1993). Morphology and structural setting of Quaternary travertines at Pamukkale, Turkey. *Geological Journal*, 28(3-4), 335-346.

Altunel, E., & Hancock, P. L. (1996). Structural attributes of travertine-filled extensional fissures in the Pamukkale Plateau, Western Turkey. *International Geology Review*, 38(8), 768-777.

American Public Health Association (APHA), 1998. *Standard Methods for the Examination of Water and Wastewater*, 20th ed. American Public Health Assoc., Washington, DC.

American Society for Testing and Materials (ASTM), 1998. Standard test methods for acidity or alkalinity of water: D 1067-92. In: *Annual Book of ASTM Standards*, Sect. 11, Water and Environmental Technology. ASTM, West Conshocken, PA.

Andrews, J. E., Riding, R., & Dennis, P. F. (1993). Stable isotopic compositions of Recent freshwater cyanobacterial carbonates from the British Isles: local and regional environmental controls. *Sedimentology*, 40(2), 303-314.

Andrews, J. E., Gare, S. G., & Dennis, P. F. (1997). Unusual isotopic phenomena in Welsh quarry water and carbonate crusts. *Terra Nova*, 9(2), 67-70.

Arenas, C., Vázquez-Urbez, M., Pardo, G., & Sancho, C. (2014). Sedimentology and depositional architecture of tufas deposited in stepped fluvial systems of changing slope: lessons from the Quaternary Añamaza valley (Iberian Range, Spain). *Sedimentology*, 61(1), 133-171.

Arp, G., Bissett, A., Brinkmann, N., Cousin, S., de Beer, D., Friedl, T., Mohr, K.I., Neu, T.R., Reimer, A., Shiraishi, F., Stackebrandt, E., Zippel, B. (2010). Tufa-forming biofilms of German karstwater streams: microorganisms, exopolymers, hydrochemistry and calcification. In: Pedley M, Rogerson M (eds) *Tufas and Speleothems*. Geological Society of London Special Publication 336: 83–118.

Astrup, T., Mosbaek, H., & Christensen, T. H. (2006). Assessment of long-term leaching from waste incineration air-pollution-control residues. *Waste management*, 26(8), 803-814.

Barber, D. G., Ehn, J. K., Pućko, M., Rysgaard, S., Deming, J. W., Bowman, J. S., Papakyriakou, T., Galley, R. J., & Sjøgaard, D. H. (2014). Frost flowers on young Arctic sea ice: The climatic, chemical, and microbial significance of an emerging ice type. *Journal of Geophysical Research: Atmospheres*, 119(20), 11-593.

Barnes, I., LaMarche, J. V., & Himmelberg, G. (1967). Geochemical evidence of present-day serpentinization. *Science*, 156(3776), 830-832.

Barnes, I., & O'neil, J. R. (1969). The relationship between fluids in some fresh alpine-type ultramafics and possible modern serpentinization, western United States. *Geological Society of America Bulletin*, 80(10), 1947-1960.

Barnes, I., O'neil, J. R., & Trescases, J. J. (1978). Present day serpentinization in New Caledonia, Oman and Yugoslavia. *Geochimica et Cosmochimica Acta*, 42(1), 144-145.

Bastianini, L., Rogerson, M., Mercedes-Martín, R., Prior, T. J., Cesar, E. A., & Mayes, W. M. (2019). What causes carbonates to form “shrubby” morphologies? An Anthropocene limestone case study. *Frontiers in Earth Science*, 7, 236.

Bastianini, L., Rogerson, M., Mercedes-Martín, R., Prior, T. J., & Mayes, W. M. (2021). What are the different styles of calcite precipitation within a hyperalkaline leachate? A sedimentological Anthropocene case study. *The Depositional Record*.

Beck, R., and Andreassen, J. P. (2012). The influence of crystallization conditions on the onset of dendritic growth of calcium carbonate. *Crystal Research and Technology*, 47(4), 404-408.

Benning, L. G., & Waychunas, G. A. (2008). Nucleation, growth, and aggregation of mineral phases: Mechanisms and kinetic controls. In *Kinetics of Water-Rock Interaction* (pp. 259-333). Springer, New York, NY.

Bischoff, J. L., Stine, S., Rosenbauer, R. J., Fitzpatrick, J. A., & Stafford Jr, T. W. (1993). Ikaite precipitation by mixing of shoreline springs and lake water, Mono Lake, California, USA. *Geochimica et cosmochimica acta*, 57(16), 3855-3865.

Bischoff, W. D., Bertram, M. A., Mackenzie, F. T., & Bishop, F. C. (1993). Diagenetic stabilization pathways of magnesian calcites. *Carbonates and Evaporites*, 8(1), 82-89.

Bobicki, E.R., Liu, Q., Xu, Z., Zeng, H., 2012. Carbon capture and storage using alkaline industrial wastes. *Prog. Energy Combust. Sci.* 38, 302e320.

Boch, R., Dietzel, M., Reichl, P., Leis, A., Baldermann, A., Mittermayr, F., & Pölt, P. (2015). Rapid ikaite ($\text{CaCO}_3 \cdot 6\text{H}_2\text{O}$) crystallization in a man-made river bed: hydrogeochemical monitoring of a rarely documented mineral formation. *Applied geochemistry*, 63, 366-379.

Bogush, A., Stegemann, J. A., Wood, I., & Roy, A. (2015). Element composition and mineralogical characterisation of air pollution control residue from UK energy-from-waste facilities. *Waste Management*, 36, 119-129.

Bosak, T., & Newman, D. K. (2005). Microbial kinetic controls on calcite morphology in supersaturated solutions. *Journal of Sedimentary Research*, 75(2), 190-199.

Boschetti, T., and L. Toscani (2008), Springs and streams of the Taro-Ceno Valleys (Northern Apennine, Italy): Reaction path modeling of waters interacting with serpentinized ultramafic rocks, *Chemical Geology*, 257(1-2), 76-91.

Boschetti, T., L. Toscani, P. Iacumin, and E. Selmo (2017), Oxygen, Hydrogen, Boron and Lithium Isotope Data of a Natural Spring Water with an Extreme Composition: A Fluid from the Dehydrating Slab?, *Aquatic Geochemistry*, doi:10.1007/s10498-017-9323-9.

Braissant, O., Cailleau, G., Duprez, C. and Verrecchia, E.P. (2003) Bacterially induced mineralization of calcium carbonate in terrestrial environments: the role of exopolysaccharides and amino acids. *J. Sed. Res.*, 73, 485–490.

Braissant, O., Decho, A. W., Dupraz, C., Glunk, C., Przekop, K. M., & Visscher, P. T. (2007). Exopolymeric substances of sulfate-reducing bacteria: interactions with calcium at alkaline pH and implication for formation of carbonate minerals. *Geobiology*, 5(4), 401-411.

Brasier, A. T., Rogerson, M. R., Mercedes-Martin, R., Vonhof, H. B., & Reijmer, J. J. G. (2015). A test of the biogenicity criteria established for microfossils and stromatolites on Quaternary tufa and speleothem materials formed in the “Twilight Zone” at Caerwys, United Kingdom. *Astrobiology*, 15(10), 883-900.

Brečević, L., & Nielsen, A. (1993). Solubility of calcium carbonate hexahydrate. *Acta Chemica Scandinavica*, 47, 668-673.

Brogi, A., & Capezzuoli, E. (2009). Travertine deposition and faulting: the fault-related travertine fissure-ridge at Terme S. Giovanni, Rapolano Terme (Italy). *International Journal of Earth Sciences*, 98(4), 931-947.

Brogi, A., Capezzuoli, E., Buracchi, E., & Branca, M. (2012). Tectonic control on travertine and calcareous tufa deposition in a low-temperature geothermal system (Sarteano, Central Italy). *Journal of the Geological Society*, 169(4), 461-476.

Brooks, R., Clark, L. M., & Thurston, E. F. (1950). Calcium carbonate and its hydrates. *Philosophical Transactions of the Royal Society of London. Series A, Mathematical and Physical Sciences*, 243(861), 145-167.

Bruni, J., Canepa, M., Chiodini, G., Cioni, R., Cipolli, F., Longinelli, A., Marini L., Ottonello, G., & Zuccolini, M. V. (2002). Irreversible water–rock mass transfer accompanying the generation of the neutral, Mg–HCO₃ and high-pH, Ca–OH spring waters of the Genova province, Italy. *Applied Geochemistry*, 17(4), 455-474.

Brunner, P. H., & Rechberger, H. (2015). Waste to energy–key element for sustainable waste management. *Waste management*, 37, 3-12.

Buchardt, B., P. Seaman, G. Stockmann, M. Vous, U. Wilken, L. Duwel, A. Kristiansen, C. Jenner, and L. Thorbjorn (1997), Submarine columns of ikaite tufa, *Nature*, 390, 129– 130.

Burke, B., Ghila, A., Fallone, B. G., & Rathee, S. (2012). Radiation induced current in the RF coils of integrated linac-MR systems: The effect of buildup and magnetic field. *Medical physics*, 39(8), 5004-5014.

Burke, I. T., Mortimer, R. J., Palaniyandi, S., Whittleston, R. A., Lockwood, C. L., Ashley, D. J., & Stewart, D. I. (2012). Biogeochemical reduction processes in a hyper-alkaline leachate affected soil profile. *Geomicrobiology Journal*, 29(9), 769-779.

Burke, I.T., Peacock, C.L., Lockwood, C.L., Stewart, D.I., Mortimer, R.J.G., Ward, M.B., Renforth, P., Gruiz, K. & Mayes, W.M. (2013) Behavior of aluminum, arsenic, and vanadium during the neutralization of red mud leachate by HCl, gypsum, or seawater. *Environmental Science & Technology*, 47(12), 6527–6535.

Cai, W. J., & Wang, Y. (1998). The chemistry, fluxes, and sources of carbon dioxide in the estuarine waters of the Satilla and Altamaha Rivers, Georgia. *Limnology and Oceanography*, 43(4), 657-668.

Capezzuoli, E., Gandin, A., & Pedley, M. (2014). Decoding tufa and travertine (fresh water carbonates) in the sedimentary record: the state of the art. *Sedimentology*, 61(1), 1-21.

Cardace, d., D. A. R. Meyer-Dombard, K. Woycheese, and C. A. Arcilla (2015), Feasible Metabolic Schema Associated with High pH Springs in the Philippines, *Frontiers in Microbiology*, 6, doi:10.3389/fmicb.2015.00010.

Carothers, W. W., & Kharaka, Y. K. (1980). Stable carbon isotopes of HCO₃⁻ in oil-field waters—implications for the origin of CO₂. *Geochimica et Cosmochimica Acta*, 44(2), 323-332.

CEDA Archive:

<https://catalogue.ceda.ac.uk/uuid/dbd451271eb04662beade68da43546e1>

Ceraldi, T. S., and Green, D. (2016). Evolution of the South Atlantic lacustrine deposits in response to Early Cretaceous rifting, subsidence and lake hydrology. Geological Society, London, Special Publications, 438, SP438-10.

Chafetz, H. S., and Folk, R. L. (1984). Travertines; depositional morphology and the bacterially constructed constituents. *Journal of Sedimentary Research*, 54(1), 289-316.

Chafetz, H., Barth, J., Cook, M., Guo, X., & Zhou, J. (2018). Origins of carbonate spherulites: implications for Brazilian Aptian pre-salt reservoir. *Sedimentary Geology*, 365, 21-33.

Chaka, A. M. (2018). Ab initio thermodynamics of hydrated calcium carbonates and calcium analogues of magnesium carbonates: implications for carbonate crystallization pathways. *ACS Earth and Space Chemistry*, 2(3), 210-224.

Chaka, A. M. (2019). Quantifying the impact of magnesium on the stability and water binding energy of hydrated calcium carbonates by ab initio thermodynamics. *The Journal of Physical Chemistry A*, 123(13), 2908-2923.

Charles, C.J., Rout, S.P., Wormald, R., Laws, A.P., Jackson, B.R., Boxall, S.A. & Humphreys, P.N. (2019) In-situ biofilm formation in hyper alkaline environments. *Geomicrobiology Journal*, 36(5), 405–411.

Chaudhry, F. M., Wallace, A., & Mueller, R. T. (1977). Barium toxicity in plants. *Communications in soil science and plant analysis*, 8(9), 795-797.

Chaurand, P., Rose, J., Briois, V., Olivi, L., Hazemann, J. L., Proux, O., Domas, J., & Bottero, J. Y. (2007). Environmental impacts of steel slag reused in road construction: A crystallographic and molecular (XANES) approach. *Journal of Hazardous Materials*, 139(3), 537-542.

Chavagnac, V., Monnin, C., Ceuleneer, G., Boulart, C., & Hoareau, G. (2013). Characterization of hyperalkaline fluids produced by low-temperature serpentinization of mantle peridotites in the Oman and Ligurian ophiolites. *Geochemistry, Geophysics, Geosystems*, 14(7), 2496-2522.

Chen, C., Huang, D., & Liu, J. (2009). Functions and toxicity of nickel in plants: recent advances and future prospects. *Clean–soil, air, water*, 37(4-5), 304-313.

Chen, Z., Grasby, S. E., & Osadetz, K. G. (2004). Relation between climate variability and groundwater levels in the upper carbonate aquifer, southern Manitoba, Canada. *Journal of Hydrology*, 290(1-2), 43-62.

Cipolli, F., B. Gambardella, L. Marini, G. Ottonello, and M. Vetuschi Zuccolini (2004), Geochemistry of high-pH waters from serpentinites of the Gruppo di Voltri (Genova, Italy) and reaction path modeling of CO₂ sequestration in serpentinite aquifers, *Applied Geochemistry*, 19(5), 787-802.

Clark, I. D., & Fontes, J. C. (1990). Paleoclimatic reconstruction in northern Oman based on carbonates from hyperalkaline groundwaters. *Quaternary Research*, 33(3), 320-336.

Cloud, P., & Lajoie, K. R. (1980). Calcite-impregnated defluidization structures in littoral sands of Mono Lake, California. *Science*, 210(4473), 1009-1012.

Cook, M. & Chafetz, H.S. (2017) Sloping fan travertine, Belen, New Mexico, USA. *Sedimentary Geology*, 352, 30–44.

Córdoba, P. (2015). Status of Flue Gas Desulphurisation (FGD) systems from coal-fired power plants: Overview of the physic-chemical control processes of wet limestone FGDs. *Fuel*, 144, 274-286.

Cornelis, G., Johnson, C. A., Van Gerven, T., & Vandecasteele, C. (2008). Leaching mechanisms of oxyanionic metalloid and metal species in alkaline solid wastes: A review. *Applied Geochemistry*, 23(5), 955-976.

Cotman, M., Drolc, A., & Končan, J. Z. (2008). Assessment of pollution loads from point and diffuse sources in small river basin: Case study Ljubljana River. *Environmental Forensics*, 9(2-3), 246-251.

Council, T. C., & Bennett, P. C. (1993). Geochemistry of ikaite formation at Mono Lake, California: implications for the origin of tufa mounds. *Geology*, 21(11), 971-974.

Czop, E., Economou, A., & Bobrowski, A. (2011). A study of in situ plated tin-film electrodes for the determination of trace metals by means of square-wave anodic stripping voltammetry. *Electrochimica acta*, 56(5), 2206-2212.

D'Alessandro, W., K. Daskalopoulou, S. Calabrese, and S. Bellomo (2018a), Water chemistry and abiogenic methane content of a hyperalkaline spring related to serpentinization in the Argolida ophiolite (Ermioni, Greece), *Marine and Petroleum Geology*, 89, 185-193, doi:10.1016/j.marpetgeo.2017.01.028.

Dandurand, J. L., Gout, R., Hoefs, J., Menschel, G., Schott, J., & Usdowski, E. (1982). Kinetically controlled variations of major components and carbon and oxygen isotopes in a calcite-precipitating spring. *Chemical geology*, 36(3-4), 299-315.

Darrie, G. (2001). Commercial extraction technology and process waste disposal in the manufacture of chromium chemicals from ore.

De Boom, A., & Degrez, M. (2012). Belgian MSWI fly ashes and APC residues: a characterisation study. *Waste management*, 32(6), 1163-1170.

De Choudens-Sánchez, V., and González, L. A. (2009). Calcite and Aragonite Precipitation Under Controlled Instantaneous Supersaturation: Elucidating the Role of CaCO₃ Saturation State and Mg/Ca Ratio on Calcium Carbonate Polymorphism. *Journal of Sedimentary Research*, 79(6), 363–376.

Dekov, V. M., Egueh, N. M., Kamenov, G. D., Bayon, G., Lalonde, S. V., Schmidt, M., Liebetrau, V., Munnik, F., Fouquet, Y., Tanimizu, M., Awaleh, M. O., Guirreh, I., & Le Gall, B. (2014). Hydrothermal carbonate chimneys from a continental rift (Afar Rift): Mineralogy, geochemistry, and mode of formation. *Chemical Geology*, 387, 87-100.

Della Porta, G. (2015). Carbonate build-ups in lacustrine, hydrothermal and fluvial settings: comparing depositional geometry, fabric types and geochemical signature. *Geological Society, London, Special Publications*, 418(1), 17-68.

Dellantonio, A., Fitz, W. J., Repmann, F., & Wenzel, W. W. (2010). Disposal of coal combustion residues in terrestrial systems: contamination and risk management. *Journal of environmental quality*, 39(3), 761-775.

Demichelis, R., Raiteri, P., Gale, J. D., Quigley, D., & Gebauer, D. (2011). Stable prenucleation mineral clusters are liquid-like ionic polymers. *Nature communications*, 2(1), 1-8.

Demichelis, R., Raiteri, P., & Gale, J. D. (2014). Structure of hydrated calcium carbonates: A first-principles study. *Journal of crystal growth*, 401, 33-37.

Dempster, T., & Jess, S. A. (2015). Ikaite pseudomorphs in Neoproterozoic Dalradian slates record Earth's coldest metamorphism. *Journal of the Geological Society*, 172(4), 459-464.

Deocampo, D. M., & Jones, B. F. (2014). Geochemistry of saline lakes. *Treatise on geochemistry*, 7, 437-469.

Devlin, J. F. (1990). Field evidence for the effect of acetate on leachate alkalinity. *Groundwater*, 28(6), 863-867.

Dickson, A. G. (1981). An exact definition of total alkalinity and a procedure for the estimation of alkalinity and total inorganic carbon from titration data. *Deep Sea Research Part A. Oceanographic Research Papers*, 28(6), 609-623.

Dieckmann, G. S., Nehrke, G., Papadimitriou, S., Göttlicher, J., Steininger, R., Kennedy, H., Wolf-Gladrow, D., & Thomas, D. N. (2008). Calcium carbonate as ikaite crystals in Antarctic sea ice. *Geophysical Research Letters*, 35(8).

Dietzel, M., Usdowski, E., & Hoefs, J. (1992). Chemical and $^{13}\text{C}/^{12}\text{C}$ - and $^{18}\text{O}/^{16}\text{O}$ -isotope evolution of alkaline drainage waters and the precipitation of calcite. *Applied Geochemistry*, 7(2), 177-184.

Dolley, T. P. (1994). *The Mineral Industry of Morocco and Western Sahara*. USGS Mineral Yearbook.

Dreybrodt, W., Lauckner, J., Zaihua, L., Svensson, U., & Buhmann, D. (1996). The kinetics of the reaction $\text{CO}_2 + \text{H}_2\text{O} \rightarrow \text{H}^+ + \text{HCO}_3^-$ as one of the rate limiting steps for the

dissolution of calcite in the system $\text{H}_2\text{O} \cdot \text{CO}_2 \cdot \text{CaCO}_3$. *Geochimica et Cosmochimica Acta*, 60(18), 3375-3381

Dreybrodt, W., Eisenlohr, L., Madry, B., & Ringer, S. (1997). Precipitation kinetics of calcite in the system $\text{CaCO}_3 \cdot \text{H}_2\text{O} \cdot \text{CO}_2$: The conversion to CO_2 by the slow process $\text{H}^+ + \text{HCO}_3^- \rightarrow \text{CO}_2 + \text{H}_2\text{O}$ as a rate limiting step. *Geochimica et Cosmochimica Acta*, 61(18), 3897-3904.

Dunn, J. R. (1953). The origin of the deposits of tufa in Mono Lake [California]. *Journal of Sedimentary Research*, 23(1), 18-23.

Dupraz, C., Reid, R. P., Braissant, O., Decho, A. W., Norman, R. S., and Visscher, P. T. (2009). Processes of carbonate precipitation in modern microbial mats. *Earth Sci. Rev.* 96, 141–162. doi: 10.1016/j.earscirev.2008.10.005

Effler, S. W., Brooks, C. M. M., & Driscoll, C. T. (2001). Changes in deposition of phytoplankton constituents in a Ca^{2+} polluted lake. *Environmental science & technology*, 35(15), 3082-3088.

Effler, S.W., Matthews, D.A. (2003). Impacts of a soda ash facility on Onondaga Lake and the Seneca River, NY. *Lake Reserv. Manag.* 19, 285e306.

Ehrlich HL (1990) *Geomicrobiology*. Marcel Dekker, New York
Felbeck H, Childress JJ, Somero GN (1981) Calvin-Benson cycle and sulfide-oxidation enzymes in animals from sulfide-rich habitats. *Nature* 293:291–293

Emeis, K. C., Richnow, H. H., & Kempe, S. (1987). Travertine formation in Plitvice National Park, Yugoslavia: chemical versus biological control. *Sedimentology*, 34(4), 595-609.

Eugster, H. P., and Hardie, L. A. (1978). Saline lakes. In *Lakes* (pp. 237-293). Springer, New York, NY.

Evans K (2015): Successes and challenges in the management and use of bauxite residue. In: Pontikes Y (Hrsg.), Bauxite residue valorisation and best practices, Leuven, Belgium, pp. 53–60

Ferreira, C., Ribeiro, A., & Ottosen, L. (2003). Possible applications for municipal solid waste fly ash. *Journal of hazardous materials*, 96(2-3), 201-216.

Field, L.P., Milodowski, A.E., Shaw, R.P., Stevens, L.A., Hall, M.R., Kilpatrick, A., Gunn, J., Kemp, S.J., and Ellis, M.A. (2016). Unusual morphologies and the occurrence of pseudomorphs after ikaite ($\text{CaCO}_3 \cdot 6\text{H}_2\text{O}$) in fast growing, hyperalkaline speleothem: *Mineralogical Magazine*, doi:10.1180/minmag.2016.080.111. Flügel, E. (2013). *Microfacies of Carbonate Rocks: Analysis, Interpretation and Application*. Berlin: Springer Science and Business Media.

Ford, D., & Williams, P. D. (2013). *Karst hydrogeology and geomorphology*. John Wiley & Sons.

Ford, T. D., & Pedley, H. M. (1996). A review of tufa and travertine deposits of the world. *Earth-Science Reviews*, 41(3-4), 117-175.

Ford, T. D., & Pedley, H. M. (1996). A review of tufa and travertine deposits of the world. *Earth-Science Reviews*, 41(3-4), 117-175.

Fouke, B. W., Farmer, J. D., Des Marais, D. J., Pratt, L., Sturchio, N. C., Burns, P. C., & Discipulo, M. K. (2000). Depositional facies and aqueous-solid geochemistry of travertine-depositing hot springs (Angel Terrace, Mammoth Hot Springs, Yellowstone National Park, USA). *Journal of Sedimentary Research*, 70(3), 565-585.

Fouke, B. W. (2001). Depositional facies and aqueous-solid geochemistry of travertine-depositing hot springs (angel terrace, mammoth hot springs, yellowstone national park, USA): reply. *Journal of sedimentary research*, 71(3), 497-500.

Fouke, B. W. (2011). Hot-spring Systems Geobiology: abiotic and biotic influences on travertine formation at Mammoth Hot Springs, Yellowstone National Park, USA. *Sedimentology*, 58(1), 170-219.

Freese, K., Abbas, A., Senko, J., & Cutright, T. J. (2015). Assessment of process variables that can impact results of soluble sulfate evaluated by the Tex-145E method. *Journal of Testing and Evaluation*, 43(6), 1472-1478.

Fritz, S. J. (1994). A survey of charge-balance errors on published analyses of potable ground and surface waters. *Groundwater*, 32(4), 539-546.

Fryer, P., J. A. Pearce, and L. B. Stokking (1989), Ocean Drilling Program Leg 125 preliminary report; Bonin/Mariana region, 51 pp., Ocean Drilling Program, Texas A&M University, College Station, TX, United States.

Fryer, P., C. G. Wheat, T. Williams, and t. E. Scientists (2018), Mariana Convergent Margin and South Chamorro Seamount., in *Proceedings of the International Ocean Discovery Program Volume 366*, edited, International Ocean Discovery Program, College Station RX, doi:10.14379/iodp.proc.366.2018.

Gallagher, K. L., Kading, T. J., Braissant, O., Dupraz, C., & Visscher, P. T. (2012). Inside the alkalinity engine: the role of electron donors in the organomineralization potential of sulfate-reducing bacteria. *Geobiology*, 10(6), 518-530.

Gandin, A., & Capezzuoli, E. (2008). Travertine versus calcareous tufa: Distinctive petrologic features and stable isotopes signatures. *Italian Journal of Quaternary Sciences*, 21(1B), 125-136.

Gandin, A., & Capezzuoli, E. (2014). Travertine: distinctive depositional fabrics of carbonates from thermal spring systems. *Sedimentology*, 61(1), 264-290.

Gandin, A., & Capezzuoli, E. (2014). Travertine: distinctive depositional fabrics of carbonates from thermal spring systems. *Sedimentology*, 61(1), 264-290.

Gates-Rector, S., & Blanton, T. (2019). The powder diffraction file: a quality materials characterization database. *Powder Diffraction*, 34(4), 352-360.

Gebauer, D., Völkel, A., & Cölfen, H. (2008). Stable prenucleation calcium carbonate clusters. *Science*, 322(5909), 1819-1822.

Geelhoed, J. S., Meeussen, J. C., Hillier, S., Lumsdon, D. G., Thomas, R. P., Farmer, J. G., & Paterson, E. (2002). Identification and geochemical modeling of processes controlling leaching of Cr (VI) and other major elements from chromite ore processing residue. *Geochimica et Cosmochimica Acta*, 66(22), 3927-3942.

Giampouras, M., C. J. Garrido, J. Zwicker, I. Vadillo, D. Smrzka, W. Bach, J. Peckmann, P. Jimenez, J. Benavente, and J. M. Garcia-Ruiz (2019), Geochemistry and mineralogy of serpentinization-driven hyperalkaline springs in the Ronda peridotites, *Lithos*, 350, 22, doi:10.1016/j.lithos.2019.105215.

Glaring, M. A., Vester, J. K., Lylloff, J. E., Al-Soud, W. A., Sørensen, S. J., & Stougaard, P. (2015). Microbial diversity in a permanently cold and alkaline environment in Greenland. *PloS one*, 10(4).

Gomes, H. I., Jones, A., Rogerson, M., Burke, I. T., & Mayes, W. M. (2016). Vanadium removal and recovery from bauxite residue leachates by ion exchange. *Environmental Science and Pollution Research*, 23(22), 23034-23042.

Gomes, H. I., Mayes, W. M., Rogerson, M., Stewart, D. I., & Burke, I. T. (2016). Alkaline residues and the environment: a review of impacts, management practices and opportunities. *Journal of Cleaner Production*, 112, 3571-3582.

Gomes, H. I., Jones, A., Rogerson, M., Greenway, G. M., Lisbona, D. F., Burke, I. T., & Mayes, W. M. (2017). Removal and recovery of vanadium from alkaline steel slag leachates with anion exchange resins. *Journal of environmental management*, 187, 384-392.

Gomes, H. I., Rogerson, M., Burke, I. T., Stewart, D. I., and Mayes, W. M. (2017). Hydraulic and biotic impacts on neutralisation of high-pH waters. *Science of the Total Environment*, 601, 1271-1279.

Gomes, H. I., Mayes, W. M., Baxter, H. A., Jarvis, A. P., Burke, I. T., Stewart, D. I., & Rogerson, M. (2018). Options for managing alkaline steel slag leachate: A life cycle assessment. *Journal of Cleaner Production*, 202, 401-412.

Gomes, H. I., Mayes, W. M., Whitby, P., & Rogerson, M. (2019). Constructed wetlands for steel slag leachate management: Partitioning of arsenic, chromium, and vanadium in waters, sediments, and plants. *Journal of environmental management*, 243, 30-38.

Gomes, H. I., Funari, V., & Ferrari, R. (2020). Bioleaching for resource recovery from low-grade wastes like fly and bottom ashes from municipal incinerators: A SWOT analysis. *Science of The Total Environment*, 715, 136945.

Goswami, B., Choudhury, A., & Buragohain, A. K. (2012). Luminescence properties of a nanoporous freshwater diatom. *Luminescence*, 27(1), 16-19.

Gozzard, E., Mayes, W. M., Potter, H. A. B., & Jarvis, A. P. (2011). Seasonal and spatial variation of diffuse (non-point) source zinc pollution in a historically metal mined river catchment, UK. *Environmental Pollution*, 159(10), 3113-3122.

Gräfe, M., Power, G., & Klauber, C. (2011). Bauxite residue issues: III. Alkalinity and associated chemistry. *Hydrometallurgy*, 108(1-2), 60-79.

Graly, J. A., Drever, J. I., & Humphrey, N. F. (2017). Calculating the balance between atmospheric CO₂ drawdown and organic carbon oxidation in subglacial hydrochemical systems. *Global Biogeochemical Cycles*, 31(4), 709-727.

Gran, G. Determination of the equivalence point in potentiometric titrations, *Acta Chemica Scandinavica*, 4, 559-577 (1950).

Gunasekaran, S., Anbalagan, G., & Pandi, S. (2006). Raman and infrared spectra of carbonates of calcite structure. *Journal of Raman Spectroscopy: An International Journal for Original Work in all Aspects of Raman Spectroscopy, Including Higher Order Processes, and also Brillouin and Rayleigh Scattering*, 37(9), 892-899.

Gunn, J.G. (1998) The hydrogeology of the carboniferous limestone in the derwent catchment. LRG Report 98/13 for the Environment Agency, Limestone Research Group. Huddersfield: Department of Geographical Sciences, University of Huddersfield.

Guo, L. I., & Riding, R. (1998). Hot-spring travertine facies and sequences, Late Pleistocene, Rapolano Terme, Italy. *Sedimentology*, 45(1), 163-180.

Hammer, Ø., Dysthe, D. K., & Jamtveit, B. (2010). Travertine terracing: patterns and mechanisms. *Geological Society, London, Special Publications*, 336(1), 345-355. Hancock, P. L., Chalmers, R. M. L., Altunel, E. R. H. A. N., & Çakir, Z. (1999). Travitronics: using travertines in active fault studies. *Journal of Structural Geology*, 21(8-9), 903-916.

Hancock, P.L., Chalmers, R.M.L., Altunel, E.R.H.A.N. & Çakir, Z. (1999) Travitronics: using travertines in active fault studies. *Journal of Structural Geology*, 21(8–9), 903–916.

Harber, A. J., & Forth, R. A. (2001). The contamination of former iron and steel works sites. *Environmental Geology*, 40(3), 324-330.

Harber, A. J., & Forth, R. A. (2001). The contamination of former iron and steel works sites. *Environmental Geology*, 40(3), 324-330.

Harner, P. L., & Gilmore, M. S. (2015). Visible–near infrared spectra of hydrous carbonates, with implications for the detection of carbonates in hyperspectral data of Mars. *Icarus*, 250, 204-214.

Hassan, F. M., Saleh, M. M., & Salman, J. M. (2010). A study of physicochemical parameters and nine heavy metals in the Euphrates River, Iraq. *E-Journal of Chemistry*, 7(3), 685-692.

Healey, N. (2009). Lead toxicity, vulnerable subpopulations and emergency preparedness. *Radiation protection dosimetry*, 134(3-4), 143-151.

Heidrich, C., Feuerborn, H. J., & Weir, A. (2013, April). Coal combustion products: a global perspective. In *World of coal ash conference* (pp. 22-25).

Hem, J.D. Study and interpretation of chemical characteristics of natural water: U.S. Geological Survey Water-Supply Paper 2254, 263 p (1985).

Hobson, A. J., Stewart, D. I., Bray, A. W., Mortimer, R. J., Mayes, W. M., Rogerson, M., & Burke, I. T. (2017). Mechanism of vanadium leaching during surface weathering of basic oxygen furnace steel slag blocks: a microfocus X-ray absorption spectroscopy and electron microscopy study. *Environmental science & technology*, 51(14), 7823-7830.

Hobson, A. J., Stewart, D. I., Bray, A. W., Mortimer, R. J., Mayes, W. M., Riley, A. L., Rogerson, M., and Burke, I. T. (2018). Behaviour and fate of vanadium during the aerobic neutralisation of hyperalkaline slag leachate. *Science of the total environment*, 643, 1191-1199.

Hu, Y. B., Wolf-Gladrow, D. A., Dieckmann, G. S., Völker, C., & Nehrke, G. (2014). A laboratory study of ikaite ($\text{CaCO}_3 \cdot 6\text{H}_2\text{O}$) precipitation as a function of pH, salinity, temperature and phosphate concentration. *Marine Chemistry*, 162, 10-18.

Hu, Y., Vasiliu, M., Thanthiriwatte, K. S., Jackson, V. E., Chaka, A. M., & Dixon, D. A. (2020). Thermodynamics of metal carbonates and bicarbonates and their hydrates for Mg, Ca, Fe, and Cd relevant to mineral energetics. *The Journal of Physical Chemistry A*, 124(9), 1829-1840.

Hull, S. L., Oty, U. V., & Mayes, W. M. (2014). Rapid recovery of benthic invertebrates downstream of hyperalkaline steel slag discharges. *Hydrobiologia*, 736(1), 83-97.

Hunt, C. W., Salisbury, J. E., & Vandemark, D. (2011). Contribution of non-carbonate anions to total alkalinity and overestimation of pCO₂ in New England and New Brunswick rivers. *Biogeosciences*, 8(10), 3069-3076.

Inskeep, W. P., & Bloom, P. R. (1985). An evaluation of rate equations for calcite precipitation kinetics at pCO₂ less than 0.01 atm and pH greater than 8. *Geochimica et Cosmochimica Acta*, 49(10), 2165-2180.

Irwin, W. P., & Barnes, I. (1980). Tectonic relations of carbon dioxide discharges and earthquakes. *Journal of Geophysical Research: Solid Earth*, 85(B6), 3115-3121.

ISO 5725-5:—1) , Accuracy (trueness and precision) of measurement methods and results — Part 5: Alternative methods for the determination of the precision of a standard measurement method.

Ito, T. (1996). Ikaite from cold spring water at Shiowakka, Hokkaido, Japan. *J. Mm. Petr. Econ. Geol.*, 91, 209-219.

Ito, T. (1998). Factors controlling the transformation of natural ikaite from Shiowakka, Japan. *Geochemical journal*, 32(4), 267-273.

Jalilehvand, F., Spångberg, D., Lindqvist-Reis, P., Hermansson, K., Persson, I., & Sandström, M. (2001). Hydration of the calcium ion. An EXAFS, large-angle X-ray scattering,

and molecular dynamics simulation study. *Journal of the American Chemical Society*, 123(3), 431-441.

Jansen, J. H. F., Woensdregt, C. F., Kooistra, M. J., & Van der Gaast, S. J. (1987). Ikaite pseudomorphs in the Zaire deep-sea fan: An intermediate between calcite and porous calcite. *Geology*, 15(3), 245-248.

Johnson, C. A., Kaeppli, M., Brandenberger, S., Ulrich, A., & Baumann, W. (1999). Hydrological and geochemical factors affecting leachate composition in municipal solid waste incinerator bottom ash: Part II. The geochemistry of leachate from Landfill Lostorf, Switzerland. *Journal of Contaminant Hydrology*, 40(3), 239-259.

Jones, B., Renaut, R.W. & Rosen, M.R. (1996) High-temperature (> 90 C) calcite precipitation at Waikite hot springs, North Island, New Zealand. *Journal of the Geological Society*, 153(3), 481–496.

Jones, B. and Renaut, R.W. (1996) Skeletal crystals of calcite and trona from hot-spring deposits in Kenya and New Zealand. *J. Sed. Res.*, 66, 265–274.

Jones, B. and Renaut, R.W. (1998) Origin of platy calcite crystals in hot-spring deposits in the Kenya rift valley. *J. Sed. Res.*, 68, 913–927.

Jones, B. and Renaut, R.W. (2010) Calcareous spring deposits in continental settings. In: *Developments in Sedimentology: Carbonates in Continental Settings: Facies, Environments and Processes* (Eds A.M. Alonso-Zarza and L.H. Tanner), pp. 177–224. Elsevier, Amsterdam.

Jones, B. F., Eugster, H. P., & Rettig, S. L. (1977). Hydrochemistry of the lake Magadi basin, Kenya. *Geochimica et Cosmochimica Acta*, 41(1), 53-72.

Jones, B., Renaut, R. W., Bernhart Owen, R., & Torfason, H. (2005). Growth patterns and implications of complex dendrites in calcite travertines from Lýsuhóll, Snæfellsnes, Iceland. *Sedimentology*, 52(6), 1277-1301.

Jones, B. (2017). Review of calcium carbonate polymorph precipitation in spring systems. *Sedimentary Geology*, 353, 64-75.

Jones, E. M., Cochrane, C. A., & Percival, S. L. (2015). The effect of pH on the extracellular matrix and biofilms. *Advances in wound care*, 4(7), 431-439.

Juberg, D. R., Kleiman, C. F., & Kwon, S. C. (1997). Position paper of the American Council on Science and Health: lead and human health. *Ecotoxicology and environmental safety*, 38(3), 162-180.

Kalwasińska, A., Felföldi, T., Szabó, A., Deja-Sikora, E., Kosobucki, P., & Walczak, M. (2017). Microbial communities associated with the anthropogenic, highly alkaline environment of a saline soda lime, Poland. *Antonie van Leeuwenhoek*, 110(7), 945-962.

Kandianis, M. T., Fouke, B. W., Johnson, R. W., Veysey, J., & Inskeep, W. P. (2008). Microbial biomass: A catalyst for CaCO₃ precipitation in advection-dominated transport regimes. *Geological Society of America Bulletin*, 120(3-4), 442-450.

Karadede, H., Oymak, S. A., & Ünlü, E. (2004). Heavy metals in mullet, *Liza abu*, and catfish, *Silurus triostegus*, from the Atatürk Dam Lake (Euphrates), Turkey. *Environment International*, 30(2), 183-188.

Kelemen, P. B., and J. Matter (2008), In situ carbonation of peridotite for CO₂ storage, *Proceedings of the National Academy of Sciences of the United States of America*, 105(45), 17295-17300.

Kelley, D. S., et al. (2001), An off-axis hydrothermal vent field near the Mid-Atlantic Ridge at 30 degrees N, *Nature*, 412(6843), 145-149.

Kelley, D. S., et al. (2005), A serpentinite-hosted ecosystem: The lost city hydrothermal field, *Science*, 307(5714), 1428-1434.

Khoury, H. N., E. Salameh, I. D. Clark, P. Fritz, W. Bajjali, A. E. Milodowski, M. R. Cave, and W. R. Alexander (1992), A natural analogue of high pH cement pore waters from the Maqarin area of northern Jordan. I: introduction to the site, *Journal of Geochemical Exploration*, 46(1), 117-132, doi:[https://doi.org/10.1016/0375-6742\(92\)90103-F](https://doi.org/10.1016/0375-6742(92)90103-F).

Kim, H. C., & Lee, K. (2009). Significant contribution of dissolved organic matter to seawater alkalinity. *Geophysical research letters*, 36(20).

Kindle, H., Lanzrein, B., & Kunkel, J. G. (1990). The effect of ions, ion channel blockers, and ionophores on uptake of vitellogenin into cockroach follicles. *Developmental biology*, 142(2), 386-391.

Kirby, C. S., & Cravotta III, C. A. (2005). Net alkalinity and net acidity 1: theoretical considerations. *Applied Geochemistry*, 20(10), 1920-1940.

Kirby, J. O., Spring, M., & Higgitt, C. (2005). The technology of red lake pigment manufacture: study of the dyestuff substrate. *National Gallery Technical Bulletin*, 26, 71-87.

Kitabata, T., & Kitamura, K. (1997). Heavy water management and radiation protection against tritium in the FUGEN nuclear power station.

Kori-Siakpere, O., & Ubogu, E. O. (2008). Sublethal haematological effects of zinc on the freshwater fish, *Heteroclaris* sp.(Osteichthyes: Clariidae). *African Journal of Biotechnology*, 7(12).

Koryak, M., Stafford, L. J., Reilly, R. J., Hoskin, R. H., & Haberman, M. H. (1998). The impact of airport deicing runoff on water quality and aquatic life in a Pennsylvania stream. *Journal of Freshwater Ecology*, 13(3), 287-298.

Koryak, M., Stafford, L. J., Reilly, R. J., & Magnuson, M. P. (2002). Impacts of steel mill slag leachate on the water quality of a small Pennsylvania stream. *Journal of Freshwater Ecology*, 17(3), 461-465.

Kristiansen, J., & Kristiansen, A. (1999). A new species of *Chroomonas* (Cryptophyceae) living inside the submarine ikaite columns in the Ikkafjord, Southwest Greenland, with remarks on its ultrastructure and ecology. *Nordic Journal of Botany*, 19(6), 747-758.

Langmuir, D. (1997). *Aqueous environmental. Geochemistry* Prentice Hall: Upper Saddle River, NJ, 600.

Larsen, D. (1994). Origin and paleoenvironmental significance of calcite pseudomorphs after ikaite in the Oligocene Creede Formation, Colorado. *Journal of Sedimentary Research*, 64(3a), 593-603.

Launay, J., and J. C. Fontes (1985), Les sources thermales de Prony (Nouvelle Calédonie) et leurs précipités chimiques. exemple de formation de brucite primaire., *Geologie de la France*, 1, 83-100.

Leleu, T., Chavagnac, V., Delacour, A., Noiriel, C., Ceuleneer, G., Aretz, M., Rommevaux, C., & Ventalon, S. (2016). Travertines associated with hyperalkaline springs: evaluation as a proxy for paleoenvironmental conditions and sequestration of atmospheric CO₂. *J. Sediment. Res.* 86, 1328–1343. doi: 10.2110/jsr.2016.79

Lennie, A. R., Tang, C. C., & Thompson, S. P. (2004). The structure and thermal expansion behaviour of ikaite, CaCO₃ · 6H₂O, from T= 114 to T= 293 K. *Mineralogical Magazine*, 68(1), 135-146.

Lian, B., Hu, Q., Chen, J., Ji, J., & Teng, H. H. (2006). Carbonate biomineralization induced by soil bacterium *Bacillus megaterium*. *Geochimica et cosmochimica acta*, 70(22), 5522-5535.

Libbrecht, K. G. (2012). Toward a comprehensive model of snow crystal growth dynamics: 1. Overarching features and physical origins. [Preprint]. Available at: <https://arxiv.org/pdf/1211.5555.pdf>

Liu, Z.H., Dreybrodt, W., 1997. Dissolution kinetics of calcium carbonate minerals in H₂O–CO₂ solutions in turbulent flow. The role of the diffusion boundary layer and the slow reaction $\text{H}_2\text{O} + \text{CO}_2 = \text{H}^+ + \text{HCO}_3^-$. *Geochimica et Cosmochimica Acta* 61, 2879–2889
Luttge, A., & Arvidson, R. S. (2010). Reactions at surfaces: A new approach integrating interferometry and kinetic simulations. *Journal of the American Ceramic Society*, 93(11), 3519-3530.

Llugany, M., Poschenrieder, C., & Barceló, J. (2000). Assessment of barium toxicity in bush beans. *Archives of Environmental Contamination and Toxicology*, 39(4), 440-444.

Lokhande, R. S., Singare, P. U., & Pimple, D. S. (2011). Pollution in water of Kasardi River flowing along Talaja industrial area of Mumbai, India. *World Environment*, 1(1), 6-13.

Lower, S. K. Carbonate equilibria in natural waters. Simon Fraser University, 544 (1999).

Lozovik, P. A. (2005). Contribution of organic acid anions to the alkalinity of natural humic water. *Journal of Analytical Chemistry*, 60(11), 1000-1004.

Luttge, A. & Arvidson, R.S. (2010) Reactions at surfaces: a new approach integrating interferometry and kinetic simulations. *Journal of the American Ceramic Society*, 93(11), 3519–3530.

Macfie, S. M., & Taylor, G. J. (1992). The effects of excess manganese on photosynthetic rate and concentration of chlorophyll in *Triticum aestivum* grown in solution culture. *Physiologia Plantarum*, 85(3), 467-475.

Macfie, S. M., Cossins, E. A., & Taylor, G. J. (1994). Effects of excess manganese on production of organic acids in Mn-tolerant and Mn-sensitive cultivars of *Triticum aestivum* L.(wheat). *Journal of plant physiology*, 143(2), 135-144.

Mancini, A., Capezzuoli, E., Erthal, M., Swennen, R. (2019). Hierarchical approach to define travertine depositional systems: 3D conceptual morphological model and possible applications. *Mar. Pet. Geol.* 103, 549–563. Mayes, W. M., Younger, P. L., and Aumônier, J. (2008). Hydrogeochemistry of alkaline steel slag leachates in the UK. *Water Air Soil Pollut.* 195, 35–50. doi: 10.1007/s11270-008-9725-9

Marion, G. M. (2001). Carbonate mineral solubility at low temperatures in the Na-K-Mg-Ca-H-Cl-SO₄-OH-HCO₃-CO₃-CO₂-H₂O system. *Geochimica et Cosmochimica Acta*, 65(12), 1883-1896.

Marland, G. (1975). The stability of CaCO₃· 6H₂O (ikaite). *Geochimica et Cosmochimica Acta*, 39(1), 83-91.

Marques, J. M., P. M. Carreira, M. R. Carvalho, M. J. Matias, F. E. Goff, M. J. Basto, R. C. Graça, L. Aires-Barros, and L. Rocha (2008), Origins of high pH mineral waters from ultramafic rocks, Central Portugal, *Applied Geochemistry*, 23(12), 3278-3289.

Marques, J. M., G. Etiope, M. O. Neves, P. M. Carreira, C. Rocha, S. D. Vance, L. Christensen, A. Z. Miller, and S. Suzuki (2018), Linking serpentinization, hyperalkaline mineral waters and abiotic methane production in continental peridotites: an integrated hydrogeological-bio-geochemical model from the Cabeço de Vide CH₄-rich aquifer (Portugal), *Applied Geochemistry*, 96, 287-301, doi:<https://doi.org/10.1016/j.apgeochem.2018.07.011>.

Marsden, J. R. (1986). Response to light by trochophore larvae of *Spirobranchus giganteus*. *Marine Biology*, 93(1), 13-16.

Martin, J. B. (2017). Carbonate minerals in the global carbon cycle. *Chemical Geology*, 449, 58-72.

Mayes, W. M., Younger, P. L., & Aumo, J. (2006). Buffering of alkaline steel slag leachate across a natural wetland. *Environmental Science & Technology*, 40(4), 1237-1243.

Mayes, W. M., Younger, P. L., & Aumônier, J. (2008). Hydrogeochemistry of alkaline steel slag leachates in the UK. *Water, air, and soil pollution*, 195(1-4), 35-50.

Mayes, W. M., Jarvis, A. P., Burke, I. T., Walton, M., Feigl, V., Klebercz, O., & Gruiz, K. (2011). Dispersal and attenuation of trace contaminants downstream of the Ajka bauxite residue (red mud) depository failure, Hungary. *Environmental science & technology*, 45(12), 5147-5155.

Mayes, W. M., Riley, A. L., Gomes, H. I., Brabham, P., Hamlyn, J., Pullin, H., and Renforth, P. (2018). Atmospheric CO₂ Sequestration in Iron and Steel Slag: Consett, County Durham, United Kingdom. *Environmental science and technology*, 52(14), 7892-7900.

Meldrum, F. C., and Cölfen, H. (2008). Controlling mineral morphologies and structures in biological and synthetic systems. *Chemical reviews*, 108(11), 4332-4432.

Melo, L. C. A., Alleoni, L. R. F., Carvalho, G., & Azevedo, R. A. (2011). Cadmium- and barium-toxicity effects on growth and antioxidant capacity of soybean (*Glycine max* L.) plants, grown in two soil types with different physicochemical properties. *Journal of Plant Nutrition and Soil Science*, 174(5), 847-859.

Mercedes-Martín, R., Rogerson, M. R., Brasier, A. T., Vonhof, H. B., Prior, T. J., Fellows, S. M., Reijmer J.J.G., Billing, I., and Pedley, H. M. (2016). Growing spherulitic calcite grains in saline, hyperalkaline lakes: experimental evaluation of the effects of Mg-clays and organic acids. *Sedimentary Geology*, 335, 93-102.

Mercedes-Martín, R., Brasier, A. T., Rogerson, M., Reijmer, J. J., Vonhof, H., and Pedley, M. (2017). A depositional model for spherulitic carbonates associated with alkaline, volcanic lakes. *Marine and Petroleum Geology*, 86, 168-191.

Mercedes-Martín, R., Ayora, C., Tritlla, J., and Sánchez-Román, M. (2019). The hydrochemical evolution of alkaline volcanic lakes: a model to understand cyclothems evolution and mineral paragenesis in the South Atlantic Pre-Salt lakes. 16th Bathurst Meeting of Carbonate Sedimentologists, Mallorca, Spain.

Mercedes-Martín, R., Rao, A., Rogerson, M., & Sánchez-Román, M. (2021a). Effects of Salinity, Organic Acids and Alkalinity in the Growth of Calcite Spherulites: Implications for Evaporitic Lacustrine Sedimentation. *The Depositional Record*, (December 2020), 1–22. <https://doi.org/10.1002/dep2.136>

Mercedes-Martín, R., Rogerson, M., Prior, T., Brasier, A., Reijmer, J., Billing, I., Matthews, A., Love, T., Lepley, S. and Pedley, M. (2021b). Towards a morphology diagram for terrestrial carbonates: evaluating the impact of carbonate supersaturation and alginic acid in calcite precipitate morphology. *Geochimica et Cosmochimica Acta*, In press.

Mergelsberg, S. T., De Yoreo, J. J., Miller, Q. R., Michel, F. M., Ulrich, R. N., & Dove, P. M. (2020). Metastable solubility and local structure of amorphous calcium carbonate (ACC). *Geochimica et Cosmochimica Acta*, 289, 196-206.

Meyer-Dombard, D. R., K. M. Woycheese, E. N. Yargicoglu, D. Cardace, E. L. Shock, Y. Gulecal-Pektas, and M. Temel (2015), High pH microbial ecosystems in a newly discovered, ephemeral, serpentinizing fluid seep at Yanartas (Chimera), Turkey, *Frontiers in Microbiology*, 5, doi:10.3389/fmicb.2014.00723.

Miller, H. M., J. M. Matter, P. Kelemen, E. T. Ellison, M. E. Conrad, N. Fierer, T. Ruchala, M. Tominaga, and A. S. Templeton (2016), Modern water/rock reactions in Oman

hyperalkaline peridotite aquifers and implications for microbial habitability, *Geochimica et Cosmochimica Acta*, 179, 217-241, doi:<http://dx.doi.org/10.1016/j.gca.2016.01.033>.

Milodowski, A. E., Shaw, R. P., & Stewart, D. I. (2013). The Harpur Hill Site: its geology, evolutionary history and a catalogue of materials present. British Geological Survey Report. CR/13/104. Available from: <https://rwm.nda.gov.uk/publication/harpur-hill-site-its-geology-evolutionary-history-and-a-catalogue-of-materials-present>.

Minissale, A., Evans, W. C., Magro, G., and Vaselli, O. (1997). Multiple source components in gas manifestations from north-central Italy. *Chemical Geology*, 142(3-4), 175-192.

Monnin, C., et al. (2014), Fluid chemistry of the low temperature hyperalkaline hydrothermal system of Prony Bay (New Caledonia), *Biogeosciences*, 11(20), 5687-5706, doi:10.5194/bg-11-5687-2014.

Montes-Hernandez, G., & Renard, F. (2016). Time-resolved in situ raman spectroscopy of the nucleation and growth of siderite, magnesite, and calcite and their precursors. *Crystal Growth & Design*, 16(12), 7218-7230.

Moreno, N., Querol, X., Andrés, J. M., Stanton, K., Towler, M., Nugteren, H., Janssen-Jurkovicova, M., & Jones, R. (2005). Physico-chemical characteristics of European pulverized coal combustion fly ashes. *Fuel*, 84(11), 1351-1363.

Moroni, J. S., Briggs, K. G., & Taylor, G. J. (1991). Chlorophyll content and leaf elongation rate in wheat seedlings as a measure of manganese tolerance. *Plant and Soil*, 136(1), 1-9.

Morrill, P. L., J. G. Kuenen, O. J. Johnson, S. Suzuki, A. Rietze, A. L. Sessions, M. L. Fogel, and K. H. Nealson (2013), *Geochemistry and geobiology of a present-day*

serpentinization site in California: The Cedars, *Geochimica Et Cosmochimica Acta*, 109, 222-240, doi:10.1016/j.gca.2013.01.043.

Mottl, M. J., C. G. Wheat, P. Fryer, J. Gharib, and J. B. Martin (2004), Chemistry of springs across the Mariana forearc shows progressive devolatilization of the subducting plate, *Geochimica Et Cosmochimica Acta*, 68(23), 4915-4933.

Motz, H., & Geiseler, J. (2001). Products of steel slags an opportunity to save natural resources. *Waste management*, 21(3), 285-293.

Muller, F. L., & Bleie, B. (2008). Estimating the organic acid contribution to coastal seawater alkalinity by potentiometric titrations in a closed cell. *Analytica chimica acta*, 619(2), 183-191.

Murugan SS, Karuppasamy R, Poongodim K, Puvaneswari S, (2008). Bioaccumulation Pattern of Zinc in Freshwater Fish *Channa punctatus* (Bloch.) After Chronic Exposure, *Turk. J. Fisher. Aqu. Sci.* 8:55-59.

Neal, C., and G. Stanger (1983), Hydrogen generation from mantle source rocks in Oman, *Earth and Planetary Science Letters*, 66, 315-320.

Neal, C., & Stanger, G. (1984). Calcium and magnesium hydroxide precipitation from alkaline groundwaters in Oman, and their significance to the process of serpentinization. *Mineralogical Magazine*, 48(347), 237-241.

Neal, C., and P. Shand (2002), Spring and surface water quality of the Cyprus ophiolites, *Hydrology and Earth System Sciences*, 6(5), 797-817.

Niedermayr, A., Köhler, S. J., & Dietzel, M. (2013). Impacts of aqueous carbonate accumulation rate, magnesium and polyaspartic acid on calcium carbonate formation (6–40 C). *Chemical Geology*, 340, 105-120.

Nordstrom, D. K., & Alpers, C. N. (1999). Geochemistry of acid mine waters. *Reviews in economic geology*, 6, 133-160.

Nordstrom, D. K., Alpers, C. N., Ptacek, C. J., & Blowes, D. W. (2000). Negative pH and extremely acidic mine waters from Iron Mountain, California. *Environmental Science & Technology*, 34(2), 254-258.

Oaki, Y., and Imai, H. (2003). Experimental Demonstration for the Morphological Evolution of Crystals Grown in Gel Media. *Crystal Growth & Design* 3(5), 711-716.

Oehlerich, M., Mayr, C., Griesshaber, E., Lücke, A., Oeckler, O. M., Ohlendorf, C., Schmahl, W.W., & Zolitschka, B. (2013). Ikaite precipitation in a lacustrine environment—implications for palaeoclimatic studies using carbonates from Laguna Potrok Aike (Patagonia, Argentina). *Quaternary Science Reviews*, 71, 46-53.

Ohlendorf, C., Fey, M., Massaferro, J., Haberzettl, T., Laprida, C., Lücke, A. Maidana, N., Mayr, C., Oehlerich, M., Ramón Mercau, J., Wille, M., Corbella, G., St-Onge, G., Schäbitz, F., & Zolitschka, B. (2014). Late Holocene hydrology inferred from lacustrine sediments of Laguna Cháltel (southeastern Argentina). *Palaeogeography, palaeoclimatology, palaeoecology*, 411, 229-248.

Olaifa F, Olaifa A, Onwude T (1998). Lethal and sub-lethal effects of copper to the African catfish (*Clarias gariepinus*) Juveniles. *Afri J Biomed. Res.*7:45-53

Olcott, A. N., Sessions, A. L., Corsetti, F. A., Kaufman, A. J., & De Oliveira, T. F. (2005). Biomarker evidence for photosynthesis during Neoproterozoic glaciation. *Science*, 310(5747), 471-474.

Omelon, C. R., Pollard, W. H., & Marion, G. M. (2001). Seasonal formation of ikaite ($\text{CaCO}_3 \cdot 6\text{H}_2\text{O}$) in saline spring discharge at Expedition Fiord, Canadian High Arctic:

Assessing conditional constraints for natural crystal growth. *Geochimica et Cosmochimica Acta*, 65(9), 1429-1437.

Pandey, N., & Sharma, C. P. (2002). Effect of heavy metals Co^{2+} , Ni^{2+} and Cd^{2+} on growth and metabolism of cabbage. *Plant Science*, 163(4), 753-758.

Papadimitriou, S., Kennedy, H., Kennedy, P., & Thomas, D. N. (2014). Kinetics of ikaite precipitation and dissolution in seawater-derived brines at sub-zero temperatures to 265 K. *Geochimica et Cosmochimica Acta*, 140, 199-211.

Paukert, A. N., J. M. Matter, P. B. Kelemen, E. L. Shock, and J. R. Havig (2012), Reaction path modeling of enhanced in situ CO_2 mineralization for carbon sequestration in the peridotite of the Samail Ophiolite, Sultanate of Oman, *Chemical Geology*, 330–331(0), 86-100, doi:10.1016/j.chemgeo.2012.08.013.

Pauly, H. (1963). "Ikaite", a new mineral from Greenland. *Arctic*, 16(4), 263-264.

Pedley, M. (1992). Freshwater (phytoherm) reefs: the role of biofilms and their bearing on marine reef cementation. *Sedimentary Geology*, 79(1-4), 255-274.

Pelletier, B., C. Chevillon, J. L. Menou, J. Butscher, E. Folcher, C. Geoffroy, J. M. Bore, and J. Perrier (2006), Plongées, forage et cartographie Baie du Prony et Banc Gail, lagon Sud de Nouvelle-Calédonie, campagne 2005-NC-PL du N.O. ALIS, 13-17 juin 2005 et cartographie baie du Prony N.O. ALIS, 25-26 septembre 2005. Rapports de missions, , *Sci. Terre, Geol-Geophys.*, 70, 44.

Pentecost, A. (2005). *Travertine*. Springer Science & Business Media.

Piatak, N. M., Parsons, M. B., & Seal II, R. R. (2015). Characteristics and environmental aspects of slag: A review. *Applied Geochemistry*, 57, 236-266.

Power, G., Grčefe, M., Klauber, C., 2011. Bauxite residue issues: I. Current management, disposal and storage practices. *Hydrometallurgy* 108, 33e45.

Power, I. M., Wilson, S. A., Dipple, G. M., and Southam, G. (2011). Modern carbonate microbialites from an asbestos open pit pond, Yukon, Canada. *Geobiology*, 9(2), 180-195.

Pristas, P., Stramova, Z., Kvasnova, S., Judova, J., Perhoacova, Z., Vidova, B., and Godany, A. (2015). Non-ferrous metal industry waste disposal sites as a source of polyextremotolerant bacteria. *Nova Biotechnol. Chim.* 14 (1), 62–68.

Pullin, H., Bray, A. W., Burke, I. T., Muir, D. D., Sapsford, D. J., Mayes, W. M., & Renforth, P. (2019). Atmospheric carbon capture performance of legacy iron and steel waste. *Environmental science & technology*, 53(16), 9502-9511.

Quina, M. J., Bordado, J. C., & Quinta-Ferreira, R. M. (2008). Treatment and use of air pollution control residues from MSW incineration: an overview. *Waste Management*, 28(11), 2097-2121.

Radtke, D. B., Wilde, F. D., Davis, J. V., & Popowski, T. J. (1998). Alkalinity and acid neutralizing capacity. *National Field Manual for the Collection of Water Quality Data* (FD Wilde and DB Radtke, eds.), US Geological Survey TWRI Book, 9.

Rahman, H., Sabreen, S., Alam, S., & Kawai, S. (2005). Effects of nickel on growth and composition of metal micronutrients in barley plants grown in nutrient solution. *Journal of Plant Nutrition*, 28(3), 393-404.

Rainey, D. K., & Jones, B. (2009). Abiotic versus biotic controls on the development of the Fairmont Hot Springs carbonate deposit, British Columbia, Canada. *Sedimentology*, 56(6), 1832-1857.

Renaut, R. W., Jones, B., Tiercelin, J. J., and Tarits, C. (2002). Sublacustrine precipitation of hydrothermal silica in rift lakes: evidence from Lake Baringo, central Kenya Rift Valley. *Sedimentary Geology*, 148(1-2), 235-257.

Renforth, P. (2019). The negative emission potential of alkaline materials. *Nature communications*, 10(1), 1-8.

Renforth, P., Manning, D. A. C., & Lopez-Capel, E. (2009). Carbonate precipitation in artificial soils as a sink for atmospheric carbon dioxide. *Applied Geochemistry*, 24(9), 1757-1764.

Renforth, P., Washbourne, C.L., Taylder, J., Manning, D.A.C., 2011. Silicate production and availability for mineral carbonation. *Environ. Sci. Technol.* 45, 2035e2041.

Rieger, T. (1992). Calcareous tufa formations. Searles Lake and Mono Lake: California Geology, 45(4), 99-109.

Riley, A. L., & Mayes, W. M. (2015). Long-term evolution of highly alkaline steel slag drainage waters. *Environmental monitoring and assessment*, 187(7), 463.

Riley, A.L., MacDonald, J.M., Burke, I.T., Renforth, P., Jarvis, A.P., Hudson-Edwards, K.A., McKie, J. & Mayes, W.M. (2020) Legacy iron and steel wastes in the UK: extent, resource potential, and management futures. *Journal of Geochemical Exploration*, 219, 106630.

Roadcap, G. S., Kelly, W. R., & Bethke, C. M. (2005). Geochemistry of extremely alkaline (pH > 12) ground water in slag-fill aquifers. *Groundwater*, 43(6), 806-816.

Roadcap, G. S., Sanford, R. A., Jin, Q., Pardinias, J. R., and Bethke, C. M. (2006). Extremely alkaline (pH > 12) ground water hosts diverse microbial community. *Groundwater*, 44(4), 511-517.

Rogerson, M., Pedley, H. M., Kelham, A., & Wadhawan, J. D. (2014). Linking mineralisation process and sedimentary product in terrestrial carbonates using a solution thermodynamic approach. *Earth Surface Dynamics*, 2(1), 197-216.

Rogerson, M., Mercedes-Martín, R., Brasier, A. T., McGill, R. A., Prior, T. J., Vonhof, H., Fellows, S.M., Reijmer, J.J.G., McClymont, E., Billing, I., Matthews, A., & Pedley, H. M. (2017). Are spherulitic lacustrine carbonates an expression of large-scale mineral carbonation? A case study from the East Kirkton Limestone, Scotland. *Gondwana Research*, 48, 101-109.

Rogov, M., Ershova, V., Vereshchagin, O., Vasileva, K., Mikhailova, K., & Krylov, A. (2021). Database of global glendonite and ikaite records throughout the Phanerozoic. *Earth System Science Data*, 13(2), 343-356.

Rossi, N., & Jamet, J. L. (2008). In situ heavy metals (copper, lead and cadmium) in different plankton compartments and suspended particulate matter in two coupled Mediterranean coastal ecosystems (Toulon Bay, France). *Marine Pollution Bulletin*, 56(11), 1862-1870.

Rounds, S.A. Alkalinity and acid neutralizing capacity (version 4.0), in National field manual for the collection of water-quality data, Wilde, F.D. and Radtke, D.B., eds., U.S. Geological Survey Techniques of Water-Resources Investigations, Book 9, Chapter A6, Section 6.6, 45 p (2012).

Rysgaard, S., Glud, R. N., Lennert, K., Cooper, M., Halden, N., Leakey, R. J. G., Hawthorne, F. C., & Barber, D. (2012). Ikaite crystals in melting sea ice-implications for pCO₂ and pH levels in Arctic surface waters. *The Cryosphere*, 6(4), 901.

Rysgaard, S., Søgaard, D. H., Cooper, M., Pućko, M., Lennert, K., Papakyriakou, T. N., Wang, F., Geilfus, N.X., Glud, R.N., Ehn, J., McGinnis, D.F., Attard, K., Sievers, J., Deming,

J.W., & Barber, D. (2013). Ikaite crystal distribution in winter sea ice and implications for CO₂ system dynamics. *Cryosphere*, 7, 707-718.

Sader, J. A., M. I. Leybourne, B. McClenaghan, and M. S. Hamilton (2007), Low-temperature serpentinization processes and kimberlite groundwater signatures in the Kirkland Lake and Lake Timiskiming kimberlite fields, Ontario, Canada: implications for diamond exploration, *Geochemistry: Exploration, Environment, Analysis*, 7, 3-21.

Saller, A., Rushton, S., Buambua, L., Inman, K., McNeil, R., and Dickson, J. T. (2016). Pre-Salt stratigraphy and depositional systems in the Kwanza Basin, offshore Angola. *AAPG Bulletin*, 100(7), 1135-1164.

Sant'Anna, L. G., Riccomini, C., Rodrigues-Francisco, B. H., Sial, A. N., Carvalho, M. D., & Moura, C. A. V. (2004). The Paleocene travertine system of the Itaboraí basin, Southeastern Brazil. *Journal of South American Earth Sciences*, 18(1), 11-25.

Saunders, P., Rogerson, M., Wadhawan, J. D., Greenway, G., & Pedley, H. M. (2014). Mg/Ca ratios in freshwater microbial carbonates: Thermodynamic, kinetic and vital effects. *Geochimica et Cosmochimica Acta*, 147, 107-118.

Shahar, A., Bassett, W. A., Mao, H. K., Chou, I. M., & Mao, W. (2005). The stability and Raman spectra of ikaite, CaCO₃· 6H₂O, at high pressure and temperature. *American Mineralogist*, 90(11-12), 1835-1839.

Shearman, D. J., McGugan, A., Stein, C., & Smith, A. J. (1989). Ikaite, CaCO₃·6H₂O, precursor of the thinolites in the Quaternary tufas and tufa mounds of the Lahontan and Mono Lake Basins, western United States. *Geological Society of America Bulletin*, 101(7), 913-917.

Shiraishi, Y., & Hirai, T. (2008). Selective organic transformations on titanium oxide-based photocatalysts. *Journal of Photochemistry and Photobiology C: Photochemistry Reviews*, 9(4), 157-170.

Šimonovičová, A., Ferianc, P., Vojtková, H., Pangallo, D., Hanajík, P., Kraková, L., Feketeová, Z., Čerňanský, S., Okenicová, L., Žemberyová, M., Bujdoš, M., and Pauditšová, E. (2017). Alkaline Technosol contaminated by former mining activity and its culturable autochthonous microbiota. *Chemosphere*, 171, 89–96.

Singleton, G. L., Révész, K., & Coplen, T. B. (2012). Determination of the $\delta^{13}\text{C}$ of dissolved inorganic carbon in water; RSIL Lab Code 1710. *Stable Isotope Ratio Methods*, sec. C of *Methods of the Reston Stable Isotope Laboratory*, 1-28.

Snyder, R. C., & Doherty, M. F. (2007). Faceted crystal shape evolution during dissolution or growth. *AIChE journal*, 53(5), 1337-1348.

Sobolewski, A. (1999). A review of processes responsible for metal removal in wetlands treating contaminated mine drainage. *International Journal of Phytoremediation*, 1(1), 19-51.

Solmaz, K. B., Ozcan, Y., Mercan Dogan, N., Bozkaya, O., & Ide, S. (2018). Characterization and production of extracellular polysaccharides (EPS) by *Bacillus pseudomycoides* U10. *Environments*, 5(6), 63.

Somridhivej, B., & Boyd, C. E. (2016). An assessment of factors affecting the reliability of total alkalinity measurements. *Aquaculture*, 459, 99-109.

Spadafora, A., Perri, E., McKenzie, J. A., and Vasconcelos, C. (2010). Microbial biomineralization processes forming modern Ca: Mg carbonate stromatolites. *Sedimentology*, 57(1), 27-40.

Spangenberg, J. V., & Cherr, G. N. (1996). Developmental effects of barium exposure in a marine bivalve (*Mytilus californianus*). *Environmental Toxicology and Chemistry: An International Journal*, 15(10), 1769-1774.

Stanger, G. (1985), *The hydrogeology of the Oman mountains.*, The Open University, UK.

Stein, C. L. (1986). Authigenic carbonate nodules in the Nankai Trough, Site 583. *Init. Repts. DSDP.*, 87, 659-668.

Steinhauser, G. (2008). Cleaner production in the Solvay Process: general strategies and recent developments. *Journal of Cleaner Production*, 16(7), 833-841.

Sterrenburg, F. A. S. (1995). Studies on the genera *Gyrosigma* and *Pleurosigma* (Bacillariophyceae): *Gyrosigma acuminatum* (Kützing) Rabenhorst, *G. spenceri* (Quekett) Griffith, and *G. rautenbachiae* Cholnoky. *Proceedings of the Academy of Natural Sciences of Philadelphia*, 467-480.

Stewart, D. I., Burke, I. T., & Mortimer, R. J. G. (2007). Stimulation of microbially mediated chromate reduction in alkaline soil-water systems. *Geomicrobiology Journal*, 24(7-8), 655-669.

Stewart, R., Xie, Q., Morneault, K., Sharp, C., Schwarzbauer, H., Taylor, T., Rytina, I., Kalla, M., Zhang, L., & Paxson, V. (2007). Stream control transmission protocol.

Stougaard, P., Jørgensen, F., Johnsen, M. G., & Hansen, O. C. (2002). Microbial diversity in ikaite tufa columns: an alkaline, cold ecological niche in Greenland. *Environmental microbiology*, 4(8), 487-493.

Stumm, W. & Morgan, J.J. *Aquatic chemistry*, 2nd ed.: New York, John Wiley & Sons, 780 p (1981).

Stumm, W. & Morgan, J.J., , *Aquatic chemistry: Chemical equilibria and rates in natural waters*, 3rd ed.: New York, John Wiley & Sons, 1022 p (1996).

Suess, E., Balzer, W., Hesse, K. F., Müller, P. J., UNGERER, C. T., & Wefer, G. (1982). Calcium carbonate hexahydrate from organic-rich sediments of the Antarctic shelf: precursors of glendonites. *Science*, 216(4550), 1128-1131.

Sun, E. J., & Wu, F. Y. (1998). Along-vein necrosis as indicator symptom on water spinach caused by nickel in water culture. *Botanical Bulletin of Academia Sinica*, 39.

Sunagawa, I. (1999). Growth and morphology of crystals. *FORMA-TOKYO-*, 14(1/2), 147-166.

Suwa, R., Jayachandran, K., Nguyen, N. T., Boulenouar, A., Fujita, K., & Saneoka, H. (2008). Barium toxicity effects in soybean plants. *Archives of Environmental Contamination and Toxicology*, 55(3), 397-403.

Szponar, N., W. J. Brazelton, M. O. Schrenk, D. M. Bower, A. Steele, and P. L. Morrill (2012), Geochemistry of a continental site of serpentinization, the Tablelands Ophiolite, Gros Morne National Park: A Mars analogue, *Icarus*, 224(2), 286-296, doi:10.1016/j.icarus.2012.07.004.

Taylor, P. M., & Chafetz, H. S. (2004). Floating rafts of calcite crystals in cave pools, central Texas, USA: crystal habit vs. saturation state. *Journal of Sedimentary Research*, 74(3), 328-341.

Teng, H. H., Dove, P. M., & De Yoreo, J. J. (2000). Kinetics of calcite growth: surface processes and relationships to macroscopic rate laws. *Geochimica et Cosmochimica Acta*, 64(13), 2255-2266.

Tishchenko, P. Y., Wallmann, K., Vasilevskaya, N. A., Volkova, T. I., Zvalinskii, V. I., Khodorenko, N. D., & Shkirnikova, E. M. (2006). The contribution of organic matter to the alkaline reserve of natural waters. *Oceanology*, 46(2), 192-199.

Toffolo, M. B. (2020). Radiocarbon Dating of Anthropogenic Carbonates: What Is the Benchmark for Sample Selection?. *Heritage*, 3(4), 1416-1432.

Toffolo, M. B., Regev, L., Mintz, E., Kaplan-Ashiri, I., Berna, F., Dubernet, S., ... & Boaretto, E. (2020). Structural characterization and thermal decomposition of lime binders allow accurate radiocarbon age determinations of aerial lime plaster. *Radiocarbon*, 62(3), 633-655.

Tollefsen, E., Balic-Zunic, T., Mörth, CM. et al. Ikaite nucleation at 35 °C challenges the use of glendonite as a paleotemperature indicator. *Sci Rep* 10, 8141 (2020). <https://doi.org/10.1038/s41598-020-64751-5>

Tosca, N. J., Tutolo, B., Wood, R., and Huwald, N. (2018). Chemical Constraints on Carbonate Sedimentation and Fabric Development, Barra Velha Formation, Santos Basin, Brazil. In ACE 2018 Annual Convention and Exhibition.

Tucker, M. E., and Wright, V. P. (2009). *Carbonate sedimentology*. John Wiley and Sons.

U.S. Geological Survey. Replacement of the simple speciation method for computation of carbonate and bicarbonate concentrations from alkalinity titrations: Office of Water Quality Technical Memorandum 2012.05, accessed September 16 (2012).

U.S. Geological Survey [USGS] (2014). Alkalinity Calculator. Available at: <http://or.water.usgs.gov/alk/> (accessed January, 2019).

Ulfso, A., Kuliński, K., Anderson, L. G., & Turner, D. R. (2015). Modelling organic alkalinity in the Baltic Sea using a Humic-Pitzer approach. *Marine Chemistry*, 168, 18-26.

Ulrich, R., Guillermic, M., Campbell, J., Hakim, A., Han, R., Singh, S., ... & Eagle, R. (2021). Patterns of element incorporation in calcium carbonate biominerals recapitulate phylogeny for a diverse range of marine calcifiers. *Frontiers in Earth Science*, 9.

US Environmental Protection Agency (USEPA), 1983b. Method 305.1, Acidity (Titrimetric). In: Methods for chemical analysis of water and wastes. US Environm. Prot. Agency EPA/600/4-79-020. also available at: <<http://www.epa.gov/cgi-bin/claritgw?op=Display&document=clserv:ORD:0167; &rank=4&template=epa>>.

USGS, 2015a. Iron and Steel Slag Statistics and Information, Minerals Information. U.S. Department of the Interior, U.S. Geological Survey.

USGS, 2015b. Soda Ash, Minerals Information. U.S. Department of the Interior, U.S. Geological Survey.

Uysal, I. T., Zhao, J. X., Golding, S. D., Lawrence, M. G., Glikson, M., & Collerson, K. D. (2007). Sm–Nd dating and rare-earth element tracing of calcite: implications for fluid-flow events in the Bowen Basin, Australia. *Chemical Geology*, 238(1-2), 63-71.

Uysal, I. T., Feng, Y. X., Zhao, J. X., Isik, V., Nuriel, P., & Golding, S. D. (2009). Hydrothermal CO₂ degassing in seismically active zones during the late Quaternary. *Chemical Geology*, 265(3-4), 442-454.

Uysal, I.T., Feng, Y.-X., Zhao, J.-X., Bolhar, R., Işik, V., Baublys, K.A., Yago, A. & Golding, S.D. (2011) Seismic cycles recorded in late Quaternary calcite veins: geochronological, geochemical and microstructural evidence. *Earth and Planetary Science Letters*, 303(1–2), 84–96.

Van de Vijver, B., Wetzel, C., Kopalová, K., Zidarova, R., & Ector, L. (2013). Analysis of the type material of *Achnanthydium lanceolatum* Brébisson ex Kützing (Bacillariophyta) with the description of two new *Planothydium* species from the Antarctic Region. *Fottea*, 13(2), 105-117.

Van Ginkel, S. W., Hassan, S. H., Ok, Y. S., Yang, J. E., Kim, Y. S., & Oh, S. E. (2011). Detecting oxidized contaminants in water using sulfur-oxidizing bacteria. *Environmental science & technology*, 45(8), 3739-3745.

Van Santen, R. A. (1984). The Ostwald step rule. *The Journal of Physical Chemistry*, 88(24), 5768-5769.

Vosylieniė, M. Z., & Mikalajūnė, A. (2006). Effect of heavy metal model mixture on rainbow trout biological parameters. *Ekologija*, (4), 12-17.

Wang, D., Hamm, L. M., Giuffre, A. J., Echigo, T., Rimstidt, J. D., Yoreo, J. J. and De Dove, P. M. (2012). Revisiting geochemical controls on patterns of carbonate deposition through the lens of multiple pathways to mineralization. *Faraday Discussions*, 371–386. <https://doi.org/10.1039/c2fd20077e>

Wang, Z. A., Bienvenu, D. J., Mann, P. J., Hoering, K. A., Poulsen, J. R., Spencer, R. G., & Holmes, R. M. (2013). Inorganic carbon speciation and fluxes in the Congo River. *Geophysical Research Letters*, 40(3), 511-516.

Wang, Z. A., Kroeger, K. D., Ganju, N. K., Gonnee, M. E., & Chu, S. N. (2016). Intertidal salt marshes as an important source of inorganic carbon to the coastal ocean. *Limnology and Oceanography*, 61(5), 1916-1931.

White, W. B. (2020). Rate processes: chemical kinetics and karst landform development (pp. 227-248). Routledge.

Wolthers, M., Nehrke, G., Gustafsson, J. P., & Van Cappellen, P. (2012). Calcite growth kinetics: Modeling the effect of solution stoichiometry. *Geochimica et Cosmochimica Acta*, 77, 121-134.

Womble, R. N., Driscoll, C. T., & Effler, S. W. (1996). Calcium carbonate deposition in Ca²⁺ polluted Onondaga lake, New York, USA. *Water Research*, 30(9), 2139-2147.

Wormald, R.M., Rout, S.P., Hopwood, J., Mayes, W.M., Gomes, H.I., Humphreys, P.N. (2021). Methanogenesis from mineral carbonates, a potential indicator for life on Mars, *Geosciences*, in review.

Wright, V. P. (2012). Lacustrine carbonates in rift settings: the interaction of volcanic and microbial processes on carbonate deposition. Geological Society, London, Special Publications, 370(1), 39-47.

Wright, V. P., and Barnett, A. J. (2015). An abiotic model for the development of textures in some South Atlantic early Cretaceous lacustrine carbonates. Geological Society, London, Special Publications, 418, SP418-3.

Wright, P., and Tosca, N. (2016). A Geochemical Model for the Formation of the Pre-Salt Reservoirs, Santos Basin, Brazil: Implications for Understanding Reservoir Distribution. In AAPG Annual Convention and Exhibition.

Wu, S. H. (1994). Effect of manganese excess on the soybean plant cultivated under various growth conditions. *Journal of plant nutrition*, 17(6), 991-1003.

Wu, J.N., Li, C.L., Yang, F., 2015. The disposition of chromite ore processing residue (COPR) incorporating industrial symbiosis. *J. Clean. Prod.* 95, 156e162.

Yao, Z. T., Ji, X. S., Sarker, P. K., Tang, J. H., Ge, L. Q., Xia, M. S., & Xi, Y. Q. (2015). A comprehensive review on the applications of coal fly ash. *Earth-Science Reviews*, 141, 105-121.

Yuce, G., et al. (2014), Origin and interactions of fluids circulating over the Amik Basin (Hatay, Turkey) and relationships with the hydrologic, geologic and tectonic settings, *Chemical Geology*, 388, 23-39, doi:<http://dx.doi.org/10.1016/j.chemgeo.2014.09.006>.

Zaihua, L., Svensson, U., Dreybrodt, W., Daoxian, Y., & Buhmann, D. (1995). Hydrodynamic control of inorganic calcite precipitation in Huanglong Ravine, China: Field measurements and theoretical prediction of deposition rates. *Geochimica et Cosmochimica Acta*, 59(15), 3087-3097.

Zhou, Y., Liu, Q., Hu, M., Xu, G., Xu, R., Chong, X., & Feng, J. (2020). Investigation on the stability, electronic, optical, and mechanical properties of novel calcium carbonate hydrates via first-principles calculations. *International Journal of Quantum Chemistry*, 120(10), e26219.

Zmarzly, D. L., & Lewin, R. A. (1986). Cation requirements for autotomy or retention of flagellaby the marine alga *Tetraselmis subcordiformis* (Wille) Hazen (Prasinophyceae, Chlorophyta). *Phycologia*, 25(4), 575-579.